



Bimetallic Complexes for Cooperative Polymerization Catalysis

Dissertation

for the award of the degree
“Doctor rerum naturalium” (Dr. rer. nat.)
of the Georg-August University Göttingen

within the doctoral program
Catalysis for Sustainable Synthesis (CaSuS)
of the Georg-August University School of Science (GAUSS)

submitted by
Mike K. Schütze
from Kassel, Germany

Göttingen 2018

Thesis Committee

Prof. Dr. Franc Meyer

(Institute of Inorganic Chemistry, Georg-August University Göttingen)

Prof. Dr. Philipp Vana

(Institute of Physical Chemistry, Georg-August University Göttingen)

Prof. Dr. Marc D. Walter

(Institute of Inorganic and Analytical Chemistry, TU Braunschweig)

Members of the Examination Board

Reviewer:

Prof. Dr. Franc Meyer

(Institute of Inorganic Chemistry, Georg-August University Göttingen)

Second Reviewer:

Prof. Dr. Philipp Vana

(Institute of Physical Chemistry, Georg-August University Göttingen)

Additional Reviewer:

Prof. Dr. Marc D. Walter

(Institute of Inorganic and Analytical Chemistry, TU Braunschweig)

Further members:

Prof. Dr. Selvan Demir

(Institute of Inorganic Chemistry, Georg-August University Göttingen)

Dr. Matthias Otte

(Institute of Inorganic Chemistry, Georg-August University Göttingen)

Dr. Shoubhik Das

(Institute of Organic and Biomolecular Chemistry, Georg-August University Göttingen)

Date of the oral examination: 25.06.2018

Contents

1. General Introduction to Cooperativity in Catalysis	1
2. Chapter 1: Copolymerization of CO₂ and Epoxides	3
2.1. Introduction	3
2.1.1. Sustainable polymers	3
2.1.2. CO ₂ as a C ₁ building block	4
2.1.3. Polycarbonates from CO ₂	5
2.2. State of the art	8
2.2.1. Mechanisms	9
2.2.2. Stereoselectivity	12
2.2.3. Prominent Catalysts	14
2.3. Aim of this work	18
2.4. Complex design of ONO pincer type ligands for the copolymerization of CO ₂ and Epoxides	18
2.4.1. Synthesis and characterization of the [L ^{ProOH} Zn] ₂ complex	19
2.4.2. Copolymerization experiments applying [L ^{ProOH} Zn] ₂	35
2.4.3. Metal variations of [L ^{ProOH} Zn] ₂ and their activity: Ni, Co and Mg complexes	63
2.4.4. Closely-related ligand variations of L ^{ProOH} , their synthesis, complexation and initial testing for copolymerization	71
2.5. Synthesis and application of macrocyclic pyrazole-based complexes for the CO ₂ /epoxide copolymerization	82
2.5.1. Synthesis and characterization of [L ^{CPI} (Zn-OAc) ₂]	82
2.5.2. Synthesis and characterization of [L ^{CPA} (Zn-Cl) ₂] complex	86
2.5.3. Application of macrocyclic complexes for the CO ₂ /epoxide copolymerization	87
2.6. Synthesis and application of bis(oxazoline)-pyrazole (BOX) complexes for the CO ₂ /epoxide copolymerization	89
2.6.1. Synthesis and characterization of the [L ^{BOX} Zn ₂ (OAc) ₃] ₂ complex	89
2.6.2. Synthesis and characterization of the [L ^{BOX} Co ₂ (OAc) ₃] ₂ complex	92
2.6.3. Application of the [L ^{BOX} Zn ₂ (OAc) ₃] ₂ and [L ^{BOX} Co ₂ (OAc) ₃] ₂ complexes for the CO ₂ /epoxide copolymerization.	98
2.7. Summary of results of the CO ₂ /epoxide copolymerizations	101
2.8. Outlook for the CO ₂ /epoxide copolymerization	102

3. Chapter 2: Study on the Cooperative Effects within a Dinuclear Palladium Complex through the Investigation of the Allyl Exchange	103
3.1. Introduction	103
3.1.1. The cooperative effects that are subject of this investigation . . .	103
3.1.2. Fluxional behavior of allyl moieties: the exchange mechanisms . .	104
3.2. Synthesis and characterization of the Pyrazole-bridged-Imine complexes $[L^{PI}PdX_2Pd(C_3H_5)]$	106
3.2.1. Synthesis of the η^3 -allyl complexes $[L^{PI^{iPr}}PdCl_2Pd(C_3H_5)]$ and $[L^{PI^{Ph}}PdCl_2Pd(C_3H_5)]$	106
3.3. Kinetic measurements through EXSY experiments	112
3.3.1. Reversible complex exchange initiated by the presence of halide ions	119
3.4. Summary and Outlook	122
4. Chapter 3: Copolymerization Experiments of Ethylene and MMA Through a Nickel Complex	124
4.1. Introduction	124
4.1.1. Introduction the to olefin polymerization	124
4.1.2. Copolymerization of ethylene with polar monomers	125
4.1.3. Prominent late transition metal catalysts for the polymerization of olefins and their copolymerization with polar monomers	127
4.2. Objective of this Work on the Copolymerization of Ethylene with Methyl Methacrylate	131
4.3. Synthesis and characterization of the $[L^{PI^{Ph}}Ni_2Br_3]_2$ complex	132
4.4. Application of the $[L^{PI^{Ph}}Ni_2Br_3]_2$ complex for the olefin polymerization and copolymerization	137
4.5. Summary and conclusion	143
5. Summary and Conclusion	144
6. Experimental Section	146
6.1. General Considerations	146
6.2. Copolymerization of CO_2/CHO	148
6.2.1. Synthesis of methyl (<i>S</i>)-3-(2-(hydroxydiphenylmethyl)pyrrolidin- 1-yl)propanoate	148
6.2.2. Synthesis of (<i>S</i>)-3-(2-(hydroxydiphenylmethyl) pyrrolidin-1-yl)- propan-1-ol (H_2L^{ProOH})	148
6.2.3. Synthesis of $[L^{ProOH}Zn]_2$	149
6.2.4. Synthesis of $[L^{ProOH}Ni]_2$	150

6.2.5.	Synthesis of $[L^{\text{ProOH}}\text{Co}]_2$	151
6.2.6.	Synthesis of $\text{H}_2\text{L}^{\text{ProO}_2\text{H}}$	151
6.2.7.	Synthesis of $\text{H}_2\text{L}^{\text{F}_{12}\text{ProOH}}$	152
6.2.8.	Synthesis of $\text{H}_2\text{L}^{\text{ProOHMe}}$	153
6.2.9.	Synthesis of $\text{H}_2\text{L}^{\text{OC}_3\text{NO}^{\text{Ph}}}$	154
6.2.10.	Synthesis of $\text{H}_2\text{L}^{\text{OC}_2\text{NO}^{\text{Ph}}}$	154
6.2.11.	Synthesis of $\text{H}_2\text{L}^{\text{O}^{\text{Ph}}\text{NO}^{\text{Ph}}}$	155
6.2.12.	Synthesis of $[\text{L}^{\text{CPI}}(\text{Zn-OAc})_2]$	155
6.2.13.	Synthesis of $[\text{L}^{\text{CPA}}(\text{Zn-Cl})_2]$	156
6.2.14.	Synthesis of $[\text{L}^{\text{BOX}}\text{Zn}_2\text{-OAc}_3]_2$	157
6.2.15.	Synthesis of $[\text{L}^{\text{BOX}}\text{Co}_2\text{-OAc}_3]_2$	157
6.2.16.	General remarks regarding the CO_2 cyclohexene oxide copolymerization	158
6.3.	Allyl Palladium Chemistry	161
6.3.1.	Synthesis of $[\text{L}^{\text{PI}^{\text{Ph}}}\text{PdCl}_2\text{Pd}(\text{C}_3\text{H}_5)]$	161
6.3.2.	Synthesis of $[\text{L}^{\text{PI}^{\text{iPr}}}\text{PdCl}_2\text{Pd}(\text{C}_3\text{H}_5)]$	162
6.4.	Copolymerization of ethylene and methyl methacrylate	163
6.4.1.	Synthesis of $[\text{L}^{\text{PI}^{\text{Ph}}}\text{Ni}_2\text{Br}_3]_2$	163
6.4.2.	Synthesis of $[\text{L}^{\text{PI}^{\text{Ph}}}\text{Cu}_2\text{Cl}_3]_2$	164
6.4.3.	General remarks regarding the ethylene polymerization	164
6.4.4.	General remarks regarding the MMA polymerization	165
6.4.5.	General remarks regarding the ethylene and methyl methacrylate copolymerization	165
A.	Appendix	166
A.1.	Mass Spectrometry	166
A.1.1.	Complex $[\text{L}^{\text{ProOH}}\text{Zn}]_2$	166
A.2.	NMR Spectroscopy	167
A.2.1.	Complex $[\text{L}^{\text{ProOH}}\text{Zn}]_2$	167
A.2.2.	Complex $[\text{L}^{\text{ProO}_2\text{H}}\text{Zn}]_2$	170
A.2.3.	Complex $[\text{L}^{\text{BOX}}\text{Zn}_2(\text{OAc})_3]_2$	170
A.2.4.	Complex $[\text{L}^{\text{BOX}}\text{Co}_2(\text{OAc})_3]_2$	171
A.2.5.	Determined exchange constants by EXSY experiments	172
A.2.6.	Further Information on the evaluation of the ^1H -EXSY-NMR spectra	172
A.2.7.	Plots associated to the allyl exchanges within the palladium complexes	176
A.2.8.	Complex $[\text{L}^{\text{PI}^{\text{Ph}}}\text{Ni}_2\text{Br}_3]_2$	179

A.3. Polymerization reactions	180
A.3.1. CO ₂ /CHO polymerizations with complex [L ^{ProOH} Zn] ₂	180
A.3.2. CO ₂ /CHO polymerizations with complex [L ^{ProOH} _n Co _n]	184
A.3.3. CO ₂ /CHO polymerizations with complex [L ^{BOX} Zn ₂ (OAc) ₃] ₂ and [L ^{BOX} Co ₂ (OAc) ₃] ₂	185
A.3.4. Further information on the data analysis for determination of the tacticity of the polymers	187
A.4. X-ray crystallography	188
A.4.1. Selected bond lengths and bond angles	193
A.5. Abbreviations	207
B. References	208

1. General Introduction to Cooperativity in Catalysis

The concept of cooperativity is common to many branches of chemistry. One of these is catalysis, where various types of cooperative effects have been observed and described.¹ Indeed, many complexes that hold two metal centers in close proximity have been investigated for their catalytic applicability in the last decades. A desirable synergistic effect at equal metal concentration can be observed for some catalytic systems, where the gain in catalytic activity can be attributed to the cooperative effects between the metals.² These effects can, however, be differentiated depending on the types of interactions. Some of these interactions are depicted by blue arrows in Figure 1.

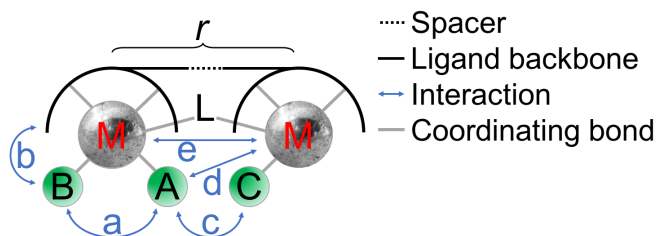


Figure 1: Types of cooperativity that can occur within a dinuclear complex. M represents the metal center and A–C substrates/ligands that coordinate to these centers. r refers to the M–M distance, depending on the spacer or L. While L represents, if present, a bridging ligand moiety between both metal atoms. Selected interactions will be addressed and investigated within this work.

The interactions a–c occur either among the substrates or between the substrate and a chelating backbone ligand. The arrow assigned to d represents the interaction of a substrate to a second metal atom and the arrow e represents the direct interactions between two metal atoms. The latter can either occur through the proximity of metal-oriented molecular orbitals or be mediated by a bridging ligand L. The interaction described by d allows the formation of μ -bridging coordination mode of substrate A. The metal–metal distance r strongly depends on the rigidity and size of the spacer/L. Not represented within Figure 1 are cooperative effects like redox chemical processes in between the M and L that involve non-innocent ligands.^{3,4} However, this work intends to further understand the interactions and synergistic effects in dinuclear systems as depicted in Figure 1. Therefore, this work is focused on studying cooperativity and its application in polymerization catalysis.

The work was developed from three different perspectives. In the first and main chapter of this thesis, the CO₂/epoxides copolymerization was addressed (section 2). For

this the cooperative interaction c (Figure 1) was explored to form polycarbonates. Two metals held in proximity allow the desired catalysis to be more efficient by reducing the order in catalyst within the rate law to one. The aim was to develop new dinuclear catalysts for the CO₂/epoxide copolymerization applying the mentioned cooperative effects.

The second chapter (section 3) provides a deeper understanding of cooperativity based on a study of the interactions a – d (Figure 1) in novel allyl palladium complexes. The objective of this research was to obtain insight on how different ligands (chelating and non-chelating) interact with each other, when coordinating to different metal atoms that are in close proximity.

In the last chapter (section 4), the interaction d in Figure 1 was applied for the copolymerization of olefins with acrylates. While the first metal is intended perform the catalysis, the second one is supposed to interact with the polar monomer to prevent retardation of the polymerization.

Every individual topic will be, nonetheless, preceded by an extensive introduction in the respective sections.

2. Chapter 1: Copolymerization of CO₂ and Epoxides

In order for future generations to live on this planet, solutions for a sustainable use of our resources and waste products need to be found. This long-term aim can only be achieved by scientists and organizations working together to develop truly sustainable processes, with the final goal of entering the anthropogenic carbon cycle.^{5,6}

2.1. Introduction

2.1.1. Sustainable polymers

The pursuit of greener processes for the production of chemical products is becoming of increasing importance. Many research groups from academia and industry put great efforts in finding alternative entry-points into the established chemical value chain, without the use of fossil-based feedstocks. Polymer products, one of biggest sectors in the chemical industry, take an important role in modern society by enabling the development of a vast variety of technologies. The polymer industry produces on average over 300 megatons of polymeric products with an estimated yearly increase of 3–4%.⁷ In 2016, approximately 6% of the oil resources went into the polymer production alone in Europe (not including the use of natural gas).⁸ The current research focuses on finding new methods to replace fossil-based feedstocks with renewable ones, and to increase the fraction of materials that are recyclable or biodegradable. In this respect, the term *bioderived* has been introduced to refer to polymers which are made of monomers originating from plants or other biomass. However, the bioderived polymers are not necessarily biodegradable and *vice versa*.⁹

The term *sustainable polymers* is a general term that applies to plastics produced with the objectives of biodegradability, recyclability, and the usage of bioderived/sustainable building blocks for the synthesis.⁷ Comprehensive reviews have been published on the topic of sustainable polymers.^{10–17} The life cycle analysis of a polymer plays an important factor in evaluating its sustainability.^{18,19}

The market diffusion of the *new* sustainable polymers is, however, still low.²⁰ For example, in 2014, only 1.7 megatons of bioderived polymers were produced, mainly polylactide, bio-sourced polyethylene (bio-PE) and bio-sourced polyethylene terephthalate (bio-PET).^{7,21} The issue with many bioderived polymers is their limitations in versatility of material properties, as well as the costs of monomers and of the process development. For a market introduction *new* polymers will have to compete with established polymeric products, which have been highly optimized over the last decades. At this point, sustainable polymers only fill a niche in the market, yet they are on

the verge of reshaping it. Compound annual growth rate (CAGR) of up to 21% has been predicted until 2021 for this segment.²² Due to their high costs, entering the high-volume-markets (e.g. packaging) will be challenging. The high-value segment seems therefore the likeliest in which they will be encountered first.

Various types of bioderived polymers are associated with poor material properties which can be generally attributed to the higher oxygen atom content of the building blocks. Some solutions for this problem have already been discovered, such as forming polymer blends.^{10,19}

The majority of sustainable polymers is until today still synthesized in research laboratories. In the development of future materials many factors will need to be considered. For instance, on top of the monomer source and life-cycle assessments, social and political aspects must also be considered (e.g. monomers from food sources should be avoided).²³

Another approach of forming sustainable polymers is to utilize the waste product CO₂ and incorporate it into a polymer, similar to what was done in other investigations dealing with the topic of carbon capture and utilization (CCU). Following this approach polycarbonates (PCs) can be formed among other polymers, allowing a long duration of CO₂ fixation. The final aim of CCU is to enter the anthropogenic carbon cycle, leading to fully sustainable productions for all commercial chemicals.⁵

2.1.2. CO₂ as a C₁ building block

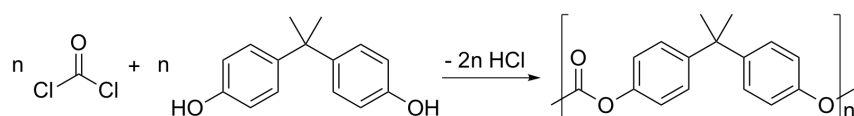
CO₂ is the most stable form of oxidized carbon and has a reputation as green house gas. The increasing levels of CO₂ in the atmosphere originate from the combustion of oil, gas and coal to satisfy the world's energy demands. CO₂ is considered a non-toxic, sustainable, cheap and abundant resource, which is challenging to activate.²⁴



CCU has been in the focus of research for many decades, however, a significant decrease of CO₂ in the atmosphere cannot be expected with current technology. To enter the anthropogenic carbon cycle⁵, many decades of research are still required. Currently, a fair amount of research has already been dedicated to carbon capture and storage (CCS) as well as carbon capture and utilization (CCU). Various research groups have been involved in the topic, and have discovered a great number of reactions for synthesis beyond the use of CO₂ as a solvent.²⁵⁻³⁰

In Figure 2, a selection of reactions is given that can use CO₂ as carbon source.^{27,29,30}

as the production, following similar synthetic approaches as the first discovery. In the beginning of the 1990's the transesterification started to be applied for PC production to avoid phosgene.³⁷ However, phosgene is still applied as well as Bisphenol A, in spite of numerous investigations that suggest avoiding these monomers for PC production. In particular Bisphenol A, an endocrine disruptor³⁸, remains in use due to the fact that the resulting product has outstanding properties.^{37,39} This illustrates the significance of PCs in the world market and the urge for more investigations to be able to reduce or replace the use of Bisphenol A.



Scheme 1: Synthetic path to polycarbonates by the reaction of phosgene with Bisphenol A.

PCs have an exceptional combination of properties including high transparencies, impact resistance, high glass temperatures and a good biological compatibility. Additionally, some PCs are potentially biodegradable.^{40–44} This makes them of interest to biomedical⁴¹ and packaging applications. The latter helps address the issue of the 275 million metric tons of polymeric waste generated, of which approximately 1.7–4.6% (in 2010) end up in the oceans.⁴⁵

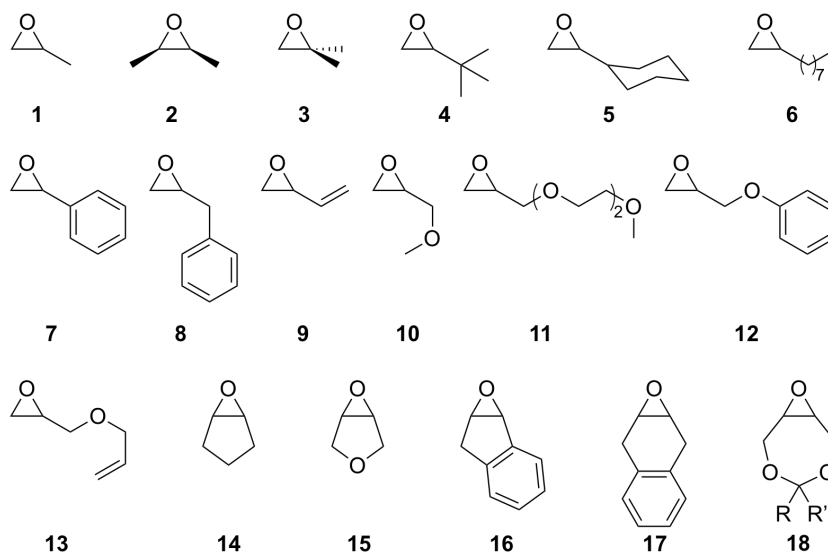


Figure 3: Selected epoxides that have been copolymerized with CO₂.^{46,47}

Based on the information above, the question arises on how the concept of sustainable polymers (including the terms bioderived biodegradable and recyclable) overlaps with the concept of CCU in polycarbonates.

The first part of the answer to this question lies in a discovery by Inoue *et al.* in 1969.⁴⁸ He discovered that the ring-strain of epoxides can be used as the driving force to utilize CO₂ to form polycarbonates.⁴⁸ In fact, the formation of polycarbonates from CO₂ has been described as a *dream reaction* and even the industrial production of polycarbonates from CO₂ has already begun,^{49–54} allowing an uptake of up to 50 wt.% in CO₂, which can drastically reduce production costs.⁴⁹

Although aliphatic PCs are considered to have poor mechanical properties, some applications have been discovered for these new PCs that incorporate CO₂. These include: biodegradable elastomers,^{55–57} drug delivery carriers (micelles),^{58–61} coating material,⁶² binders, foams, polymersomes,^{63,64} hydrogels,^{65–68} and starting material for the synthesis of polyurethanes.³²

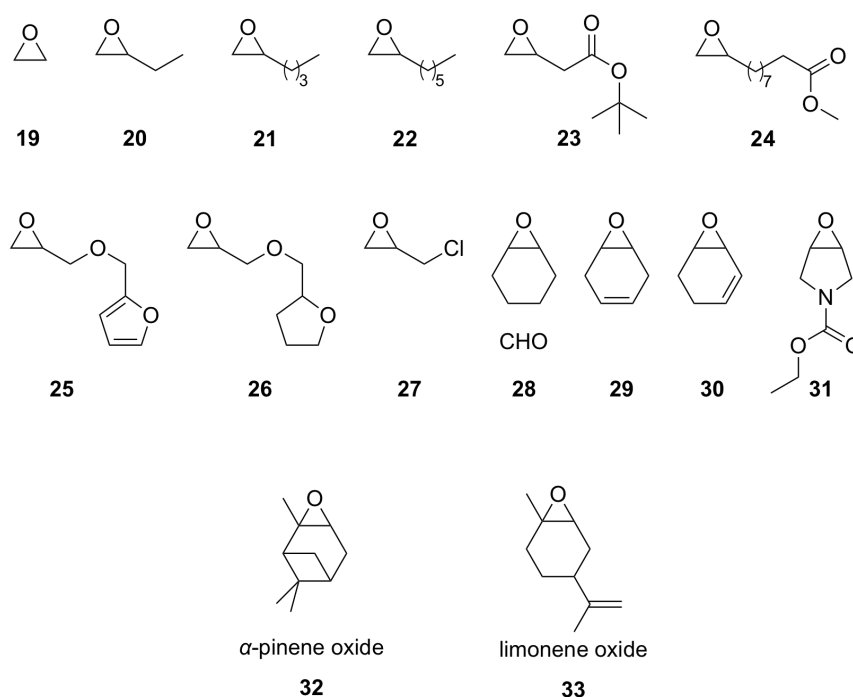


Figure 4: Selected epoxides that have been copolymerized with CO₂. The first and second row derive from metabolites of renewable feedstocks. α -pinene oxide and limonene oxide can be synthesized from precursors of renewable feedstocks directly.^{46,47}

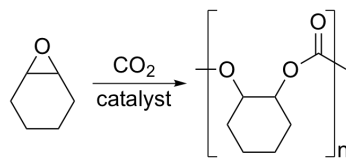
The second part of the answer lies in the origin of the epoxide monomers which will determine the sustainability of the product. In order to generate bioderived copolymers with CO₂ the scope of epoxide monomers has to be broadened. Possible monomers have been discussed and applied for the copolymerization. In Figure 3 and Figure 4, a selection of epoxides which were successfully applied for the CO₂/epoxide copolymerization are depicted.⁴⁶ The ones in Figure 4 origin from metabolites (first and second row) of renewable feedstocks. To name only one example: cyclohexa-1,4-dien, which can be converted to the corresponding epoxide, is obtained from 1,4,7-unsaturated fatty

Yet, even in industrial applications, low pressure reactions are desirable and make a process safer and cheaper, when the TOF is already sufficiently high.

The formation of PCs at 1 bar of CO₂ has proved to be challenging and, even today, only a few catalysts are known to be active under these conditions. The property of stereocontrol addresses the possibility of forming PCs with a defined stereoconfiguration in its primary and secondary structure. Last but not least, the tolerance of catalysts to monomer impurities, especially to water, represents a crucial factor for the applicability of a catalyst.

The following subsections explain the catalytic mechanism that has been proposed for the CO₂/epoxide copolymerization (section 2.2.1), the stereoconfiguration that can be incorporated into the polymer (section 2.2.2), and finally a selection of state-of-the-art catalysts will be shown, describing the properties mentioned above (section 2.2.3).

2.2.1. Mechanisms



Scheme 2: Target reaction of CO₂/CHO copolymerization.

The target reaction of this chapter is the copolymerization of CO₂ and epoxides, in particular using CHO (see Scheme 2). This reaction, under the addition of a catalyst, can form different side products. The most obvious has been the homopolymer, poly(cyclohexene oxid) (PCO), which can also be formed by simple Lewis acids⁷⁶ or a ionic polymerization.⁷⁷ In this case, the activation of CO₂ has failed. The second product is the formation of the corresponding cyclic carbonate, which is the thermodynamic product and can also be used for further synthesis. Excellent progress has been made in this field, yet it is not the objective of this work.⁷⁸⁻⁸⁰ Besides the PCO and cyclic carbonate, the di-CO₂-linked product can also be drawn. However, it is thermodynamically very unfavorable and therefore not formed; it is mentioned only for the sake of completeness. The idealized free energy profile of the CO₂/CHO copolymerization, showing the possible side products, is depicted in Figure 6.^{81,82}

Studies on the barrier for the formation of poly(cyclohexene carbonate) (PCHC) vs. the cyclohexene carbonate showed that for PCHC it was 96.8 kJ/mol, 40.7 kJ/mol lower than for the formation of cyclohexene carbonate (137.5 kJ/mol) (for the specific system of the study).⁸² These barriers do, however, strongly depend on the catalyst of

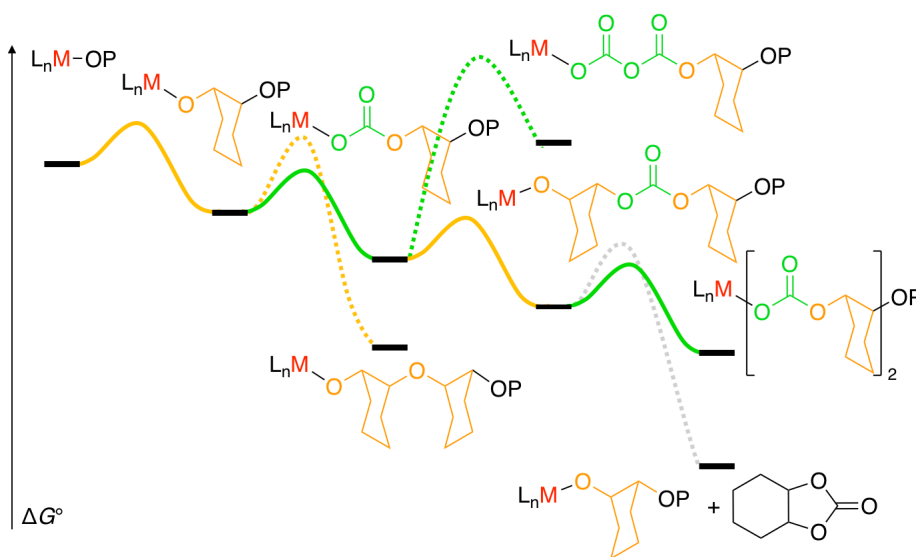
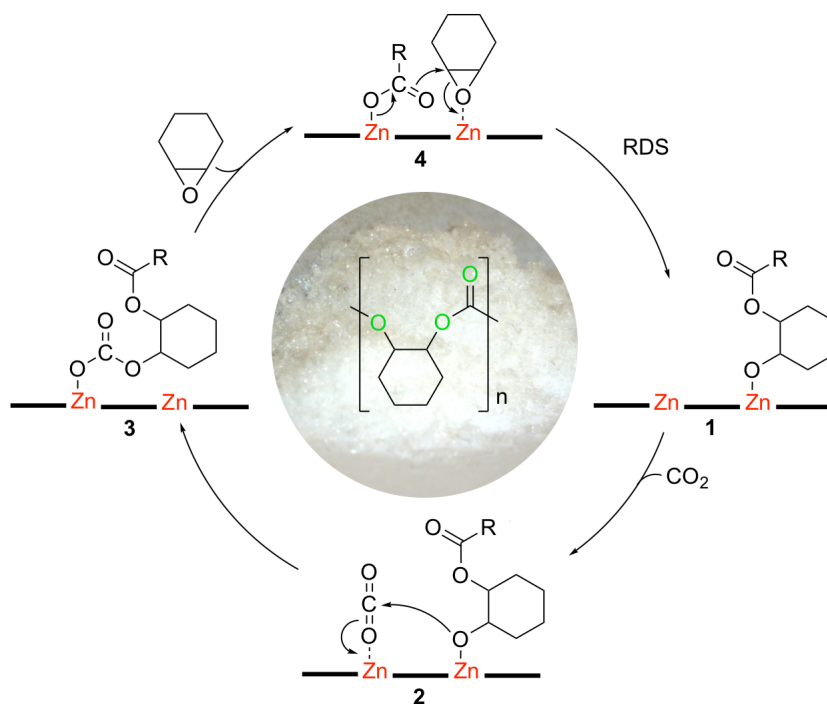


Figure 6: Idealized free energy profile of the CO₂/CHO copolymerization.^{81,82} The relative energies are not based on measured or calculated values and serve only as visualization.

interest. The rigidity of the ligand system plays a crucial role on the barrier of the transition state in a dinuclear system.⁸³ It should be pointed out that usually mixtures of the possible catalytic products are also obtained. Ultimately, the goal is to form the desired PCHO with the highest selectivity possible.

Bimetallic catalysis for the CO₂/CHO copolymerization relies on the interaction *c* depicted in Figure 1, and its proposed mechanism is shown in Scheme 3. This dinuclear mechanism can be described as follows: the alcoholate complex (**1**) allows the coordination of CO₂, forming the species **2**. A nucleophilic-like attack of the alcoholate onto the activated CO₂ allows the formation of the carbonato complex **3**, again leaving one metal site vacant. CHO coordinates to the metal (**4**) and a nucleophilic-like attack, this time by the carbonato ligand onto the CHO, closes the cycle. The latter is the rate-determining step (RDS) and gives the unique opportunity of influencing the stereoconfiguration when the epoxide unit opens.^{82,84} Further details regarding stereocontrol and stereoconfiguration are given in section 2.2.2. The alcoholate species **1** can cause the formation of the abovementioned cyclic carbonate side product through back-biting (Figure 6).

The mechanism in Scheme 3 leads to a first order dependency for the polymerization in the catalyst, following the rate law (eq. 1). In a mononuclear system, a second order in catalyst was observed, therefore a dinuclear system appears to be superior to the mononuclear one.^{85,86} This needs to be considered when designing a possible catalyst. A first order role was observed for CHO, while the order in CO₂ was found



Scheme 3: Proposed dinuclear mechanism for the CO_2/CHO copolymerization.⁸² RDS: Rate-determining step.

to be zero.^{82,87,88}

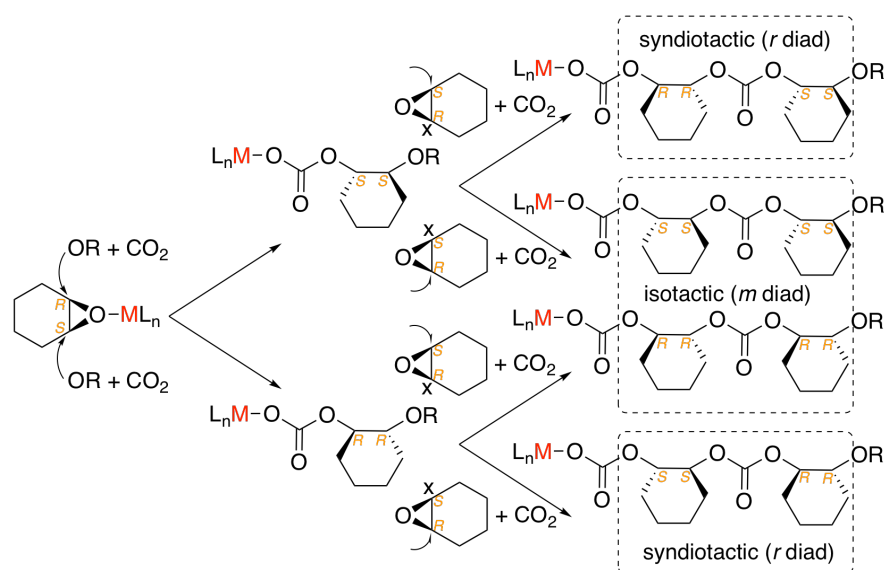
$$r = k[\text{CHO}]^1 \cdot [\text{cat.}]^1 \cdot [\text{CO}_2]^0 \quad (1)$$

In order to enter the catalytic cycle depicted in Scheme 3, an initial step needs to occur to open the first epoxide monomer. A prominent group of catalysts that coordinate one or more initiating ligands such as acetate moieties are zinc and cobalt complexes.⁸⁸ It has been accepted that, in this case, the acetate group is responsible for opening the first epoxide monomer, initiating the catalytic cycle. As a result, the acetate moiety will be found as the end-group of the polymer.^{82,89,90} The initiating group can also be exchanged by a HMDS ligand ($\text{N}(\text{SiMe}_3)_2$),^{91,92} an azide, DMAP, halides, alcoholate or other nucleophiles.^{92,93} Some catalysts depend on a co-catalyst to initiate the reaction,^{94,95} which may occur through an inner- or outer-sphere mechanism.^{84,85,93,96,97} In the case where the initiating group is an alcoholate moiety, findings suggest that this group converts into a carbonato moiety by the insertion of CO_2 into the $\text{M}-\text{O}$ bond. This carbonato unit, similar to the acetate moiety, initiates the first ring opening.⁹⁸⁻¹⁰⁰ Lastly, the depolymerization of the polycarbonate needs to be mentioned. It is assumed that the polymer can degrade *via* back-biting, which is accelerated/initiated by a base (e.g. HMDS).^{95,96,101} This occurs especially at high temperatures, which may result in

a decrease in the molecular weight.

2.2.2. Stereoselectivity

In this section the stereoselectivity that can form during the copolymerization of CO₂ and CHO will be explained. In reference to Scheme 3, the RDS is crucial in order to transfer the stereoinformation from the catalyst into the PCHC. The possible stereoconfigurations, including tacticity and absolute stereoconfiguration, are summarized in Scheme 4. The opening of the *meso*-compound CHO is displayed in two subsequent steps. In each step the CHO can undergo a nucleophilic attack in a *trans* fashion onto the pro-*R*- or pro-*S*-carbon atom, thereby forming a di-*S*- or di-*R*-configured cyclohexenyl moiety, respectively. In this manner, two monomer units can either be connected in a syndiotactic or an isotactic fashion. In the syndiotactic configuration the monomeric units were opened into the opposite configuration, while in the isotactic configuration they were opened in the same. In the latter case it can be differentiated between an all-*R*- or all-*S*-configured isotactic polymer.¹⁰²



Scheme 4: Scheme illustrating the formation of tacticity and possible stereoisomers in the CO₂/CHO copolymerization.¹⁰²

The established method used to determine the tacticity of a polymer is NMR spectroscopy. ¹³C-NMR measurements of the PCHC product can be used for this purpose. Tetrad sequences (four connected monomer units) are experimentally distinguished in the carbonyl region, allowing a determination of tacticity from the fit relative to their abundance. The following statistical expressions apply for the formation of tetrad sequences^{103,104}:

$$[rrr] = P_r^3$$

$$[rrm] = 2(P_r^2(1 - P_r))$$

$$[rmr] = P_r^2(1 - P_r)$$

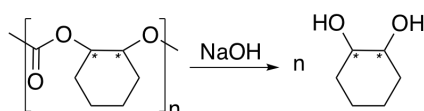
$$[mrm] = P_r(1 - P_r)^2$$

$$[mmr] = 2((1 - P_r)^2 P_r)$$

$$[mmm] = (1 - P_r)^3$$

The P_r or P_m values are the corresponding probabilities of the formation of a racemic (r) or a mesomeric (m) diad ($P_r = 100\% - P_m$) and can be used to quantify the stereo-control of a catalytic system.¹⁰²⁻¹⁰⁵ In this work, the assignment of the tetrad sequences was done according to literature.¹⁰³ It should be pointed out that the assignment of the r - and m -centered tetrads has been updated. In older references¹⁰⁶ the m -centered tetrads were thought to be in the range of 153.0–153.4 ppm in the ^{13}C -NMR spectrum. Today they are assigned to the signals at 153.7–153.8 ppm (in CDCl_3). The different definitions for the diads need to be considered and evaluated for each publication, especially in older ones. In more recent publications the definition of a racemic and a mesomeric diad have become more congruent. For this reason, the determination of the r/m configuration in this work was done by considering the carbon atom at which the main chain enters and leaves the cyclohexene units.¹⁰³

More details, also for the data analysis, can be found in Appendix A.3.4 and in the sections where this method is applied.



Scheme 5: Hydrolysis of PCHC with a solution of NaOH to obtain the corresponding *trans*-cyclohexane-1,2-diol.

To differentiate between the R - and S -configured isotactic polymer, the polymer can be hydrolyzed with a NaOH solution to obtain the corresponding *trans*-cyclohexane-1,2-diol, preserving the absolute stereoconfiguration (see Scheme 5). Subsequently, a chiral GC analysis can be used to determine the absolute configuration and the enantiomeric excess within the diol. Racemic and enantiomerically pure cyclohexane-1,2-diol should be used for calibrating the GC.

Regarding the introduction of stereoinformation into the polymer chain, the enantiomeric-site control or chain-end control mechanism needs to be evaluated.¹⁰⁷ The

symmetry/stereoinformation within the catalyst will determine the stereoconfiguration within the PCHC in an enantiomorphic-site control scenario. In the chain-end control mechanism, the configuration of the last incorporated monomeric unit influences the subsequent unit. The site control mechanism is more frequently observed. The first publication proposing a chain-end controlled mechanism was published by Coates *et al.* in 2006, where they observed the formation of a syndiospecific CO₂/CHO copolymer *via* this mechanism.¹⁰³

2.2.3. Prominent Catalysts

In this section, a selection of prominent catalysts in the field of CO₂/epoxides copolymerization will be illustrated and some of their catalytic performances and characteristics will be pointed out. Not all noteworthy catalysts can be presented here. For more details, the reader should refer to the cited literature of the corresponding catalyst or to comprehensive reviews.^{47,70,81,88,96,108–112}

A selection of important catalysts are presented in Figure 7 and Figure 8. In Figure 7 the first catalyst displayed (**1**) is a zinc-cobalt-Double Metal Cyanide (DMC) catalyst.¹¹⁹ It represents one of the heterogeneous catalysts known to copolymerize CO₂ and epoxides; zinc glutarates are also known for this.¹¹³ Heterogeneous catalysts are not the topic of this work, but potential immobilization of a homogeneous catalyst can unite the benefits of both. Immobilization can even allow to reuse a homogeneous catalyst.¹¹⁵

Catalyst (**2**) was introduced by Sugimoto *et al.* and consists of a tetraphenylporphyrin (TPP) ligand coordinated to a cobalt atom. The (TPP)CoCl-DMAP system relies on a co-catalyst, *viz.* DMAP (4-Dimethylaminopyridine).¹¹⁴ It is a representative of the porphyrin complexes that have been applied with different metals, some of which are even active at 1 bar of CO₂.^{120–123}

In Figure 7 a β -diiminato (BDI) zinc complex (**3**) is shown, which was published in 2003 by Coates *et al.*⁸⁶ They investigated various BDI-type catalysts and many other catalysts over the years. The catalyst depicted showed a TON of 306 and a TOF of 917 h⁻¹ ($T = 50\text{ }^\circ\text{C}$, 20.6 bar CO₂ (300 psi) in toluene) forming PCHC with 90% carbonate linkages. Even more impressive are their works on the stereoselective polymerization, which will be discussed in context with Figure 8.

Complex **4** in Figure 7 is a member of the salen type complexes from Lee *et al.*¹¹⁵ Several salen catalysts have been published over the years,^{83,124–126} yet this particular complex demonstrated outstanding catalytic activities and properties. A TON of 13000 after 30 min. resulting in a TOF of 26000 h⁻¹ was achieved ($T = 80\text{ }^\circ\text{C}$, 17–20 bar

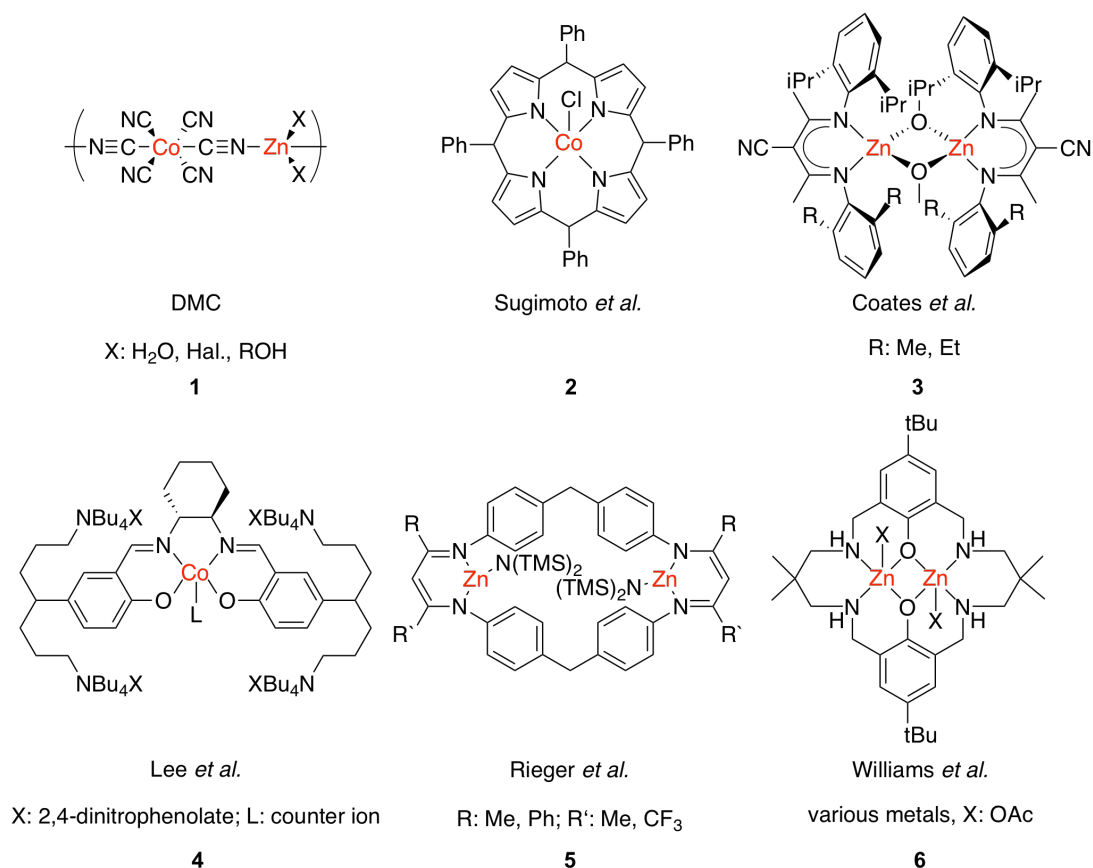


Figure 7: Selection of catalysts from literature for the copolymerization of CO₂ and epoxides. **1**: repeat unit of Zn-Co-DMC, representative for the heterogeneous catalysts¹¹³. **2**: Sugimoto *et al.* investigated a (TPP)CoCl-DMAP system¹¹⁴ which is displayed as representative of the porphyrin-like complexes. **3**: β -diiminato (BDI) zinc complex from Coates *et al.*⁸⁶ one out of many BDI-catalysts investigated by the group, **4**: Salen-type complexes represented by an outstanding catalyst from Lee *et al.*¹¹⁵. **5**: System by Rieger *et al.* which holds the current record for the most active system^{116,117}. **6**: Catalyst systems by Williams *et al.* that is highly active at 1 bar CO₂ with great tolerance to water.¹¹⁸

CO₂ in neat propylene oxide (PO)) yielding in a 99 % carbonate-linked poly(propylene carbonate) (PPC). Furthermore, it maintained activity down to 2 bar in PO.

However, the current record for the most active system is held by a catalyst which was published in 2015 by Rieger *et al.* (**5** in Figure 7).^{116,117} A TON of 6740 (over 20 min.) was reported, producing 88 % carbonate linkages in the PCHC product (80 °C, 30 bar CO₂, CHO in toluene). During the polymerization an unbeaten initial TOF of 155000 h⁻¹ was observed (over the 20 min. duration of the experiment this corresponds to an average TOF of 20220 h⁻¹).

In terms of high activity at 1 bar of CO₂, the current benchmark is a versatile system by Williams *et al.* (**6**).^{118,127} The complex in Figure 7 showed a TON of 527 and a TOF of 25 h⁻¹ at only 1 bar of CO₂ (100 °C, neat CHO) forming 94 % carbonate linkages. After the first publication in 2009, the complex was developed and tested further. Today, this ligand system has also been applied as an iron catalyst¹²⁸ (TON of 2570 and TOF of 107 h⁻¹ at 80 °C, 10 bar CO₂ in neat CHO, 99 % carbonate linkages), a cobalt catalyst¹²⁹ (TON of 340 and TOF of 172 h⁻¹ at 80 °C, 1 bar CO₂ in neat CHO, >99 % carbonate linkages), and a magnesium catalyst¹³⁰ (TON of 360 and TOF of 103 h⁻¹ at 100 °C, 1 bar CO₂ in neat CHO, with O₂CF₃ instead of OAc). These systems are outstanding for their high activity at 1 bar CO₂ and their good tolerability to water. In fact, water can be used as a chain-transfer agent to control the molecular weight.^{118,130}

In Figure 8, a second selection of catalysts is depicted. Here the focus is on the stereoselective polymerization of CO₂ and epoxides. Catalyst **7** was published in 1999 by Nozaki *et al.*^{106,131} Its TON value is relatively low with 40 and a TOF of 2 h⁻¹ (40 °C, 30 bar CO₂, CHO in toluene). However, it forms PCHC with good *P_r* values down to 15 % (calculated from *ee* = 73 %).¹⁰⁶

In 2005 Ding *et al.* used the Trost-type ligand^{135,136} forming a zinc catalyst (**8**) that is active even under 1 bar of CO₂.¹³² The displayed zinc catalyst provided a TON of 285 and TOF of 142 h⁻¹ (*T* = 80 °C, *p* = 20 bar CO₂, neat CHO).¹³² Coordination of a magnesium atom showed a TON of 86 and TOF of 43 h⁻¹ (*T* = 60 °C, *p* = 1 bar CO₂, CHO in toluene).⁸⁷ More research has been put into the ligand design, and the zinc system was further developed. By applying an azetidine ring instead of a pyrrolidine one, *ee* values of >90 % were observed in the obtained PCHC.¹³⁷

The last two displayed systems were developed, again, by the group of Coates *et al.* Compound **9** represents a variety of imine-oxazoline zinc-based catalysts. The one depicted produced an *ee* value of 72 %.¹³³ The axially chiral cobalt system **10** (which was also published as a binaphthyl system) allowed to form polycarbonates with an optimal *ee* > 99 %.¹³⁴

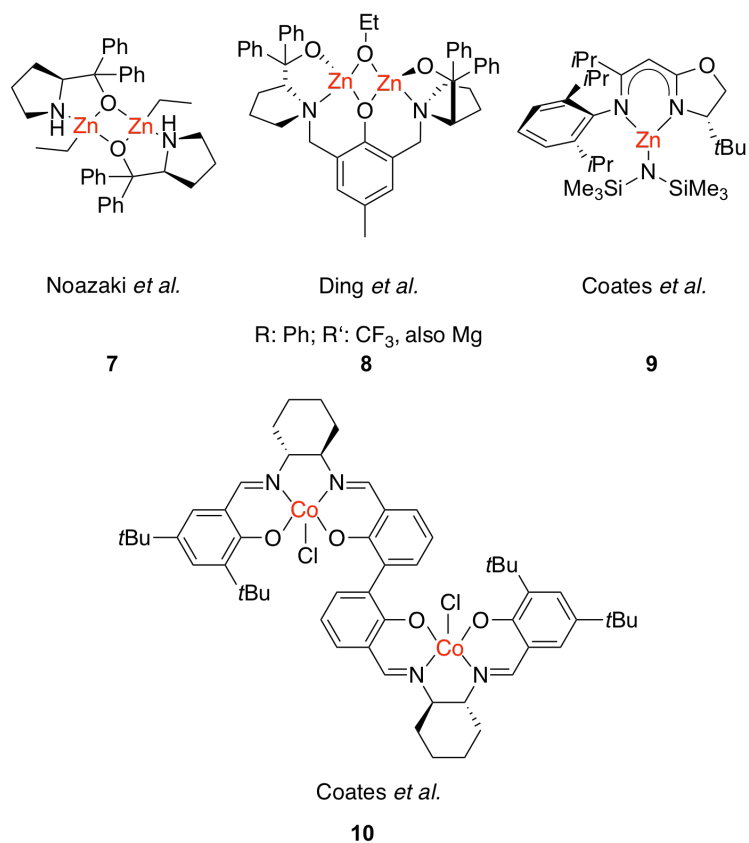


Figure 8: Selection of catalysts from literature for the copolymerization of CO₂ and epoxides with focus on influencing the stereoregularity within the polymer. **7**: Nozaki *et al.*¹³¹ formed PCHC with $P_r = 15\%$ (calculated from $ee = 73\%$).¹⁰⁶, **8**: Trost-type ligand applied by Ding *et al.*^{87,132}, **9**: Imine-oxazoline zinc-based catalysts from Coates *et al.* (this one: $ee = 72\%$).¹³³ **10**: Axially chiral systems by Coates *et al.* achieved $ee > 99\%$.¹³⁴

Overall, a selection of state-of-the-art catalysts have been described, illustrating the current achievements in the field of CO₂/epoxide copolymerization. This PhD thesis aims at expanding this current knowledge.

2.3. Aim of this work

The objective of this work is the discovery of novel catalysts for the copolymerization of CO₂ and epoxides to form greener, more sustainable polymers. For that purpose new complexes have been synthesized and tested for their activity. The selected complex design is inspired by the previous presented complexes in Figure 7 and Figure 8. The overall aim is to combine high activities with good chemo- and stereoselectivity at low CO₂ pressures. Therefore, after a catalyst has been found to be active, the reaction conditions were optimized. The main focus will lie on decreasing the reaction pressure while maintaining high activity and selectivity.

2.4. Complex design of ONO pincer type ligands for the copolymerization of CO₂ and Epoxides

In pursuit of the objective and inspired by the work of Nozaki *et al.* and Ding *et al.* (see Figure 8), the idea of a novel ligand arose. In order to influence the stereochemistry of the PCHC, a sterodirecting ligand holding a chiral moiety is required. The complex of Nozaki *et al.* showed good stereoselectivity and Ding *et al.* demonstrated that their complex could be active at 1 bar of CO₂ pressure. The challenging task to increase the activity of this type of system has remained unsolved. However, the design of a chiral ONO pincer should, in principle, address this question with a general structure depicted in Figure 9.

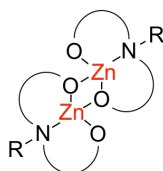


Figure 9: General design of ONO pincer type catalysts.

Two ONO pincer units are connected relying on self-assembly to form a dinuclear complex. This should enter the mechanism depicted in Scheme 3, following a rarte law

that is first order in catalyst (eq. 1). The idea was to alter the Trost ligand design to from a complex as depicted in Figure 10.

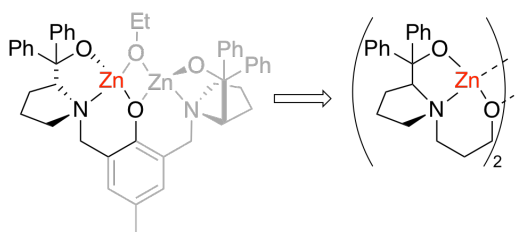


Figure 10: Design idea for a new complex.

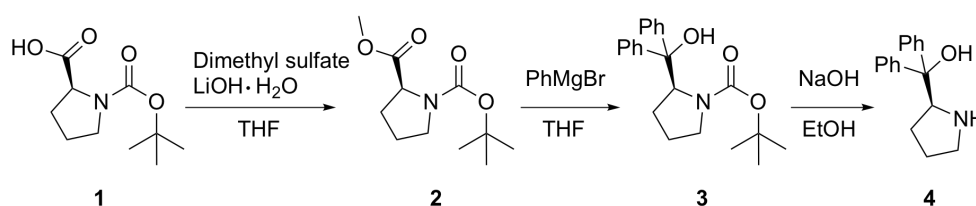
Below, the synthesis of this ligand as well as the corresponding complexes and their characterization are discussed (section 2.4.1). In section 2.4.2 the complex's potential as catalysts will be explored. Some of these contents have already been published.¹³⁸

2.4.1. Synthesis and characterization of the [L^{ProOH}Zn]₂ complex

In this section, the synthesis and characterization of [L^{ProOH}Zn]₂ is discussed. First, the preparation and analytic data of the ligand H₂L^{ProOH} is presented, followed by the synthesis and characterization of [L^{ProOH}Zn]₂. The application of the catalyst for the CO₂/CHO copolymerization will be illustrated in section 2.4.2.

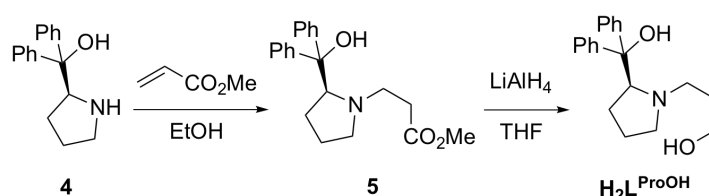
Synthesis and characterization of the H₂L^{ProOH} ligand

The synthesis of the prolin-based ligand H₂L^{ProOH} started from *N*-(*tert*-butoxycarbonyl)-L-proline **1** (Scheme 6), following literature procedures in the initial steps. The methyl ester **2** was formed with dimethyl sulfate and lithium hydroxide, preparing the substrate for the introduction of the phenyl groups.¹³⁹ Phenylmagnesium bromide in THF was used to introduce the phenyl groups, forming **3**.^{140,141} The Boc-protecting group was removed under basic conditions to form **4**.¹⁴⁰

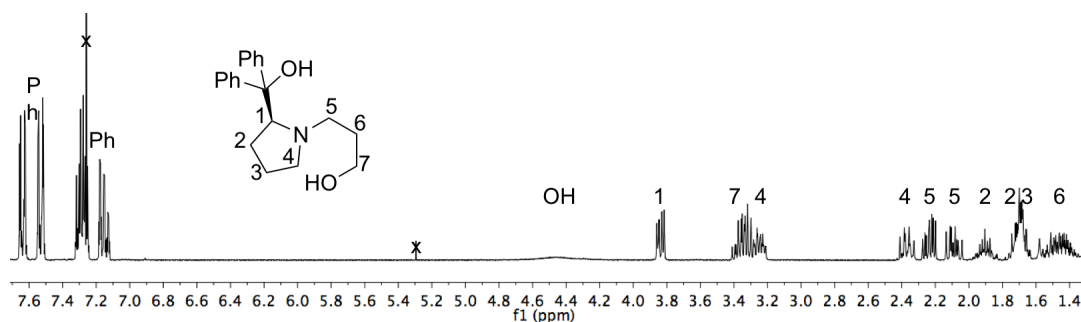
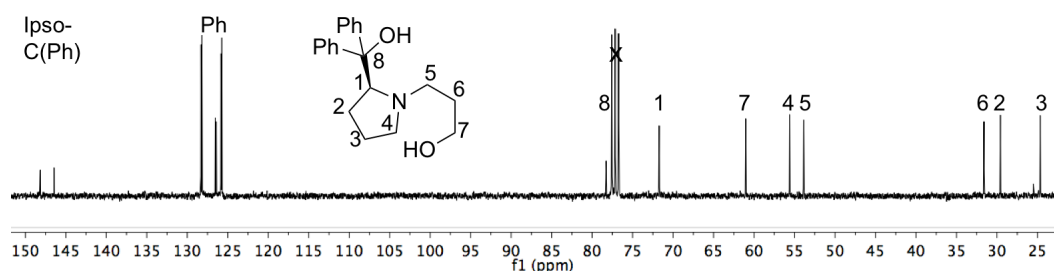


Scheme 6: Established synthetic routes for (*S*)-diphenyl(pyrrolidin-2-yl)methanol.^{139–141}

An aza-Michael addition was performed with the commercially-available compound **4**, with an excess of methyl acrylate.¹⁴² After 3 hours of heating at reflux, compound **5** was obtained quantitatively (see Scheme 7). If the reaction solution is heated for longer periods of time, the methyl ester will react with the solvent to the corresponding ethyl ester, which can be neglected, since it does not interfere with the subsequent synthetic steps. As the last step, **5** was reduced with lithium aluminium hydride and the reaction mixture quenched with water. After the removal of all volatile substances, the desired product was extracted from the residual salts with DCM. Application of an ultrasonic bath during extraction is recommended to obtain a higher yield. After repeated extraction cycles, the ligand H₂L^{ProOH} is obtained in 97% yield.

Scheme 7: Synthesis of H₂L^{ProOH}.

1D- and 2D-NMR spectra of H₂L^{ProOH} were recorded in CDCl₃. The ¹H-NMR spectrum with assignment of the protons, based on 2D-NMR experiments, is displayed in Figure 11. The assignment of the ¹³C-NMR signals can be found in Figure 12.

Figure 11: ¹H-NMR spectrum of H₂L^{ProOH} in CDCl₃.Figure 12: ¹³C-NMR spectrum of H₂L^{ProOH} in CDCl₃.

The ligand was further analyzed by ESI-MS in methanol, showing the molecular ion peak $[M+H]^+$ at 312.2 m/z with 100 % intensity. Single crystals suited for X-ray diffraction experiments were obtained by slow evaporation from a DCM solution. The resulting molecular structure of the ligand H_2L^{ProOH} in the crystal is displayed in Figure 13. An assembly of two ligand molecules to a dimeric unit through hydrogen bonds can be observed within the crystal structure.

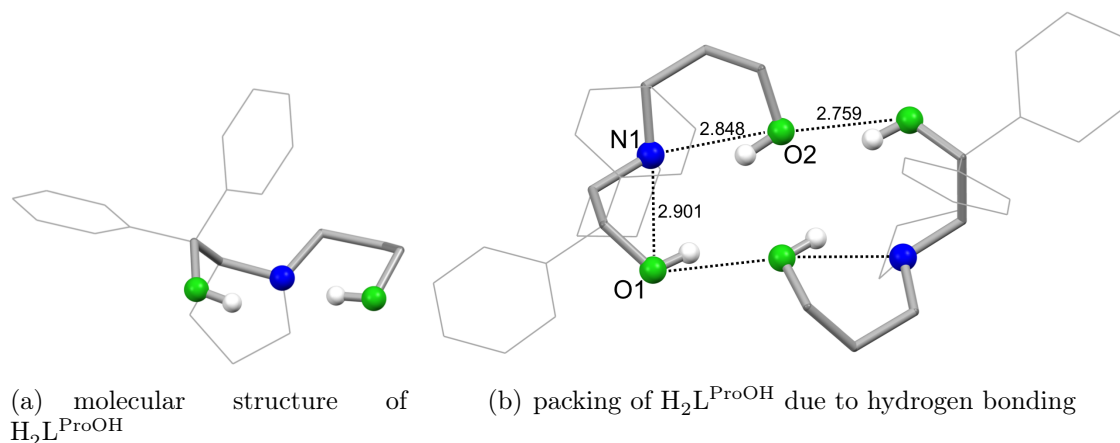
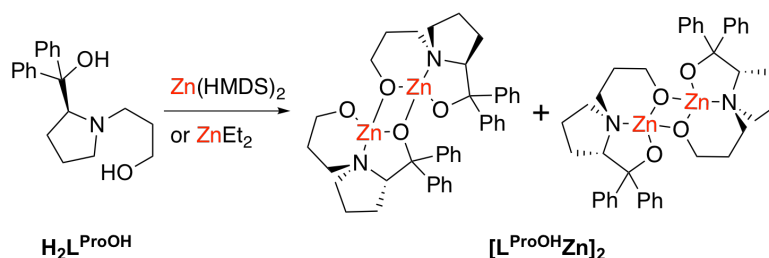


Figure 13: Molecular structure of H_2L^{ProOH} . Most hydrogen atoms were omitted for clarity.

To summarize, it was possible to isolate the target molecule in a high yield and all of the obtained data are conclusive.

Synthesis and characterization of the $[L^{ProOH}Zn]_2$ complex

Zinc(II) complexation with H_2L^{ProOH} was performed in dry DCM or THF under in-



Scheme 8: Synthesis of $[L^{ProOH}Zn]_2$ performed in DCM or THF. Different bridging modes as possible product are depicted. The corresponding stoichiometry is not displayed in this Scheme.

ert conditions. As zinc sources and deprotonating agents, $Zn(HMDS)_2$ or $ZnEt_2$ were used. Both allow the easy removal of the byproducts by evaporation. In the case of

the more costly Zn(HMDS)₂, the formed bis(trimethylsilyl)amine, with a boiling point of 126 °C, is more challenging to remove. Thus the cheaper and more atom-economic choice, ZnEt₂, is recommended for synthesis. The complex was analyzed by means of X-ray diffraction, NMR spectroscopy, elemental analysis, and mass spectrometry, which will be discussed in this section. The discussion will focus on the successful isolation of the [L^{ProOH}Zn]₂ complex and on the study of its aggregation properties in solution. The latter is of special interest since this ONO-pincer ligand relies on self-assembly in order to form the desired dinuclear complexes for the CO₂/epoxide copolymerization.

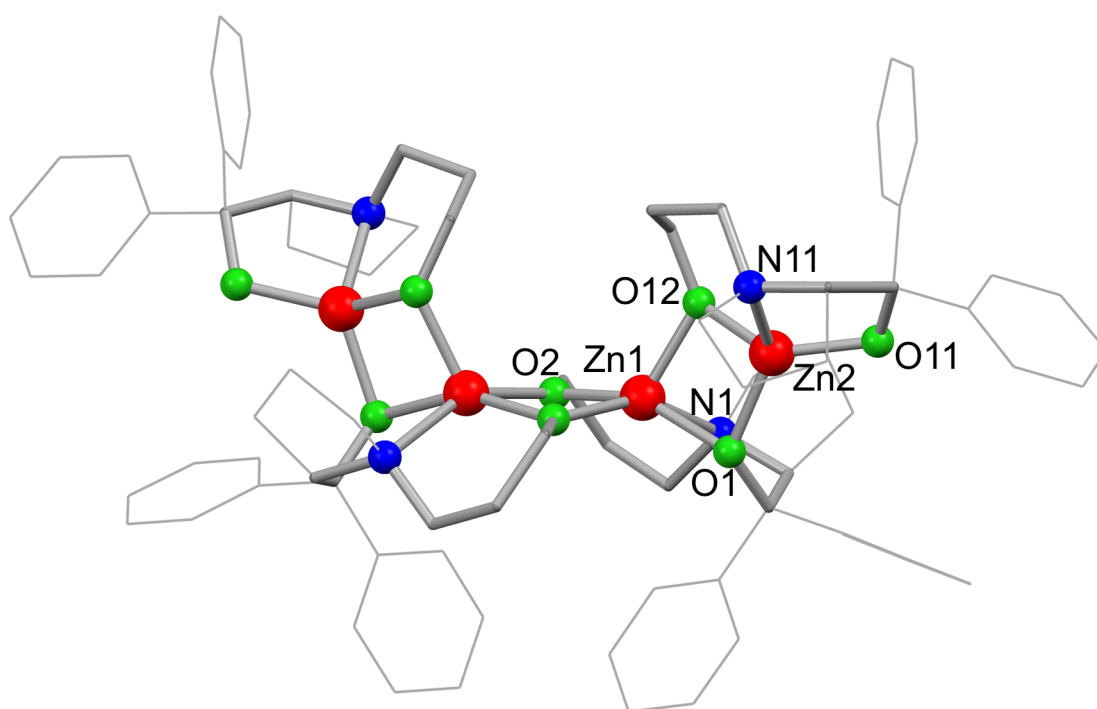


Figure 14: Molecular structure of [L^{ProOH}Zn]₂ in solid state forming a {[L^{ProOH}Zn]₂]₂ unit. Hydrogen atoms were omitted for clarity.

Complex [L^{ProOH}Zn]₂ was found to crystallize in the space group *P*4₃2₁2, with an L₂Zn₂ asymmetric unit and a tetranuclear molecular structure as seen in Figure 14. Relevant bond angles, selected distances and atom labels of the asymmetric unit are displayed in Figure 15 and Table 1.

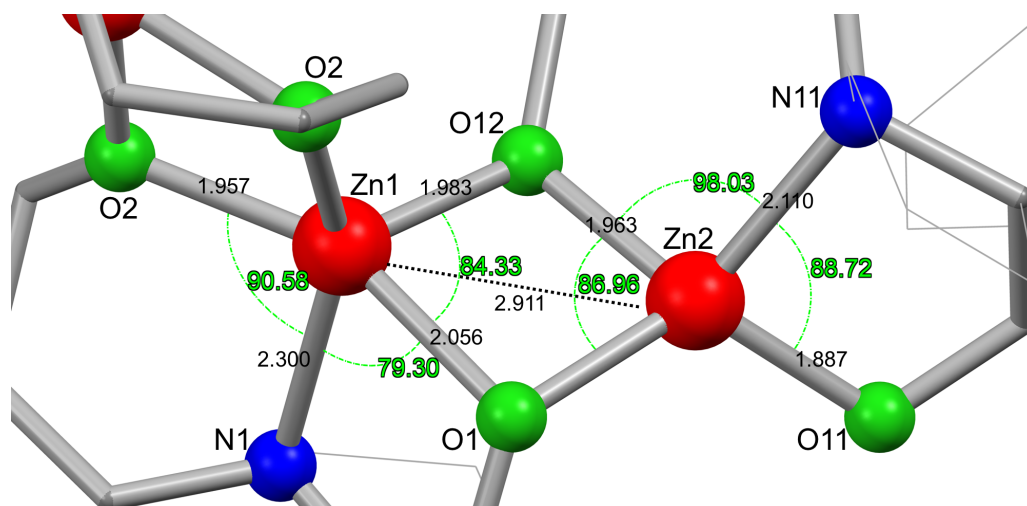
Within the structure, a terminal and a central [LZn] unit can be found. The zinc in the terminal unit (Zn2) coordinates four atoms in a strongly distorted tetrahedral geometry, while the central zinc atom (Zn1) has a coordination number of five, in a strongly distorted trigonal-bipyramidal geometry. The different coordination geometries result in smaller bond angles and longer Zn–ligand bond distances in the central [LZn] unit. In the terminal unit, the five-membered ring shows an angle ∠(O11–Zn2–N11) of 88.7°,

Table 1: Selected atom distances [Å] and bond angles [°] (sorted) for [L^{ProOH}Zn]₂.

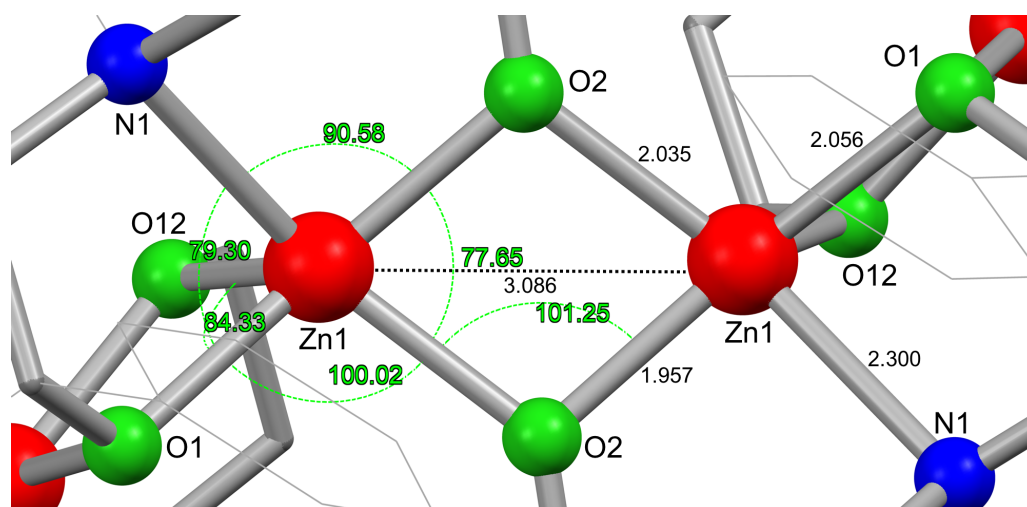
Atoms	Distance	Atoms	Bond angles
Zn2–O11	1.8865(15)	O1–Zn1–N1	79.30(6)
Zn1–O2	1.9568(15)	O12–Zn1–O1	84.33(6)
Zn2–O12	1.9634(15)	O12–Zn2–O1	86.97(6)
Zn2–O1	1.9778(14)	O11–Zn2–N11	88.72(7)
Zn1–O12	1.9830(15)	O2–Zn1–N1	90.58(6)
Zn1–O2'	2.0344(15)	Zn2–O1–Zn1	92.34(6)
Zn1–O1	2.0565(14)	Zn2–O12–Zn1	95.06(6)
Zn2–N11	2.1097(18)	O12–Zn1–N1	96.14(6)
Zn1–N1	2.3001(17)	O12–Zn2–N11	98.03(7)
Zn1–Zn2	2.9110(3)	O2'–Zn1–O1	100.02(6)
Zn1–Zn1'	3.0855(5)	O12–Zn1–O2'	113.17(6)
		O2–Zn1–O12	119.93(7)
		O11–Zn2–O1	121.14(6)
		O1–Zn2–N11	132.34(7)
		O11–Zn2–O12	133.68(7)
		Zn2–Zn1–Zn1'	138.204(12)
		O2'–Zn1–N1	150.55(6)

while in the central unit this angle is more acute by ca. 10° and measures $\angle(\text{O1–Zn1–N1}) = 79.3^\circ$. The six-membered rings show a duller bite angle ($\angle(\text{O12–Zn2–N11}) = 98.0^\circ$), in the terminal unit than in central unit ($\angle(\text{O2–Zn1–N1}) = 90.6^\circ$). The Zn–N distance is 0.190 Å shorter in the terminal unit. The Zn–O distances show the same trend as observed for the Zn–N distances ($d(\text{Zn1–O1}) > d(\text{Zn2–O1})$, $d(\text{Zn1–O12}) > d(\text{Zn2–O12})$ and $d(\text{Zn1–O1}) > d(\text{Zn2–O11})$). The only exception is the distance of $d(\text{Zn1–O2})$, which is slightly smaller than $d(\text{Zn2–O12}) = 1.963$ Å. However, Zn1 coordinates to a second oxygen atom O2 (asymmetric unit) with $d(\text{Zn1–O2}) = 2.035$ Å (see Figure 15, Zn1 to O2 (wire frame style)). More important are the Zn–Zn distances resulting from the angles and bond lengths. Within the asymmetric unit the Zn1–Zn2 distance measures 2.911 Å and between two asymmetric units the distance between the alcoholate-bridged Zn1–Zn1' measures 3.086 Å. The 0.175 Å longer Zn–Zn distance indicates a probable splitting point of the tetranuclear structure, if it were to split into two dinuclear L₂Zn₂ units, e.g. in solution.

Besides the molecular structure shown in Figure 14, a distinctive coordination motif in a second crystal structure has been observed. The crystal showed a $P2_1$ space group and the molecular structure of the complex within the crystal is displayed in Figure 16 (coordination motif **B**). Selected atom distances for the second coordination motif **B** can be found in Table 2. The corresponding bond angles can be found in the Appendix. Structure **B** differs from the more symmetric one in Figure 14 by the presence of a bond



(a) Asymmetric unit of the molecular structure



(b) Central unit of the molecular structure

Figure 15: Molecular structure of $[L^{\text{ProOH}}\text{Zn}]_2$ displayed as dimer of either the asymmetric or central unit with selected distances (formate n.nnn), angles (formate nnn.nn) and labels displayed. Hydrogen atoms were omitted for clarity.

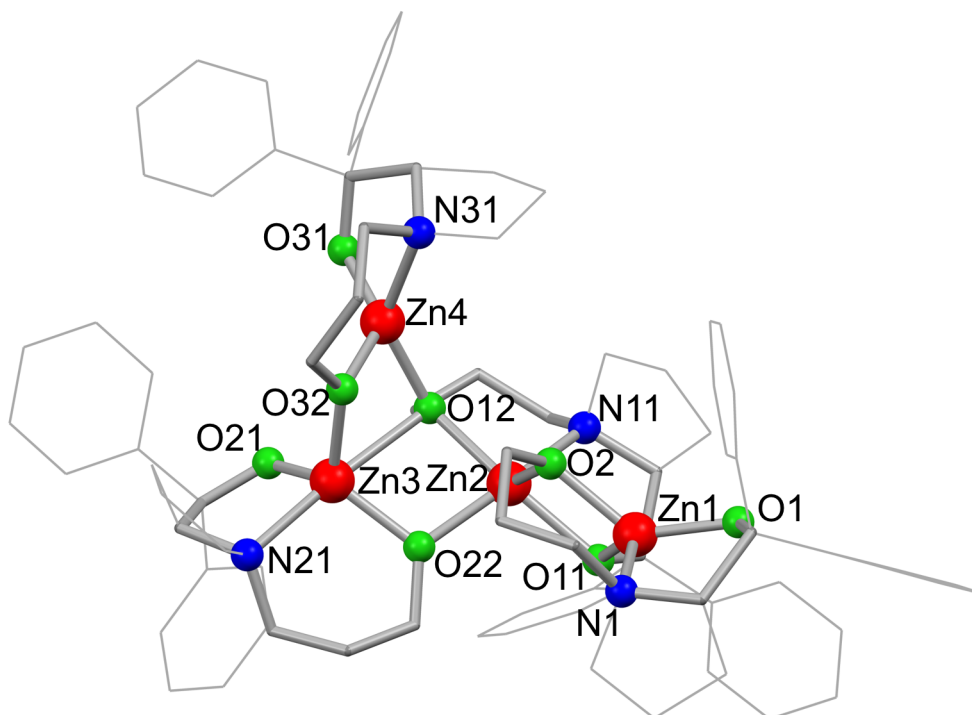


Figure 16: Molecular structure of $[L^{\text{ProOH}}\text{Zn}]_2$ with a second coordination motif forming a $[L^{\text{ProOH}}\text{Zn}]_4$ unit in solid state. Hydrogen atoms were omitted for clarity.

Table 2: Selected atom distances [\AA] (sorted) for the second coordination motif of $\{[L^{\text{ProOH}}\text{Zn}]_2\}_2$. The corresponding bond angles can be found in the Appendix.

Atoms	Distance	Atoms	Distance
Zn4–O31	1.883(3)	Zn2–O22	2.008(3)
Zn1–O1	1.898(3)	Zn2–O12	2.059(3)
Zn3–O21	1.906(3)	Zn2–O11	2.099(3)
Zn4–O32	1.932(3)	Zn1–N1	2.102(4)
Zn3–O22	1.951(3)	Zn4–N31	2.106(3)
Zn4–O12	1.960(3)	Zn3–N21	2.133(3)
Zn1–O11	1.972(3)	Zn2–N11	2.262(3)
Zn1–O2	1.975(3)	Zn3–O12	2.423(3)
Zn2–O2	1.987(3)	Zn1–Zn2	2.9750(6)
Zn3–O32	1.992(3)	Zn3–Zn4	2.9779(6)

between Zn4–O12 and a missing bond between Zn4–O21. Thus, in this structure, four different coordination motifs of individual $[L\text{Zn}]$ units can be observed. The motif of Zn1, however, is the same as of the terminal Zn2 in Figure 14. For better visualization and comparison of the coordination motifs a colored drawing is displayed in Figure 17.

For a better comparison of the two obtained molecular structures **A** and **B** a selection of atom distances of both motifs is given in Table 3. Just as in Figure 14 (Zn2), the two terminal zinc(II) ions in Figure 16 (Zn1 and Zn4) have a coordination number of four,

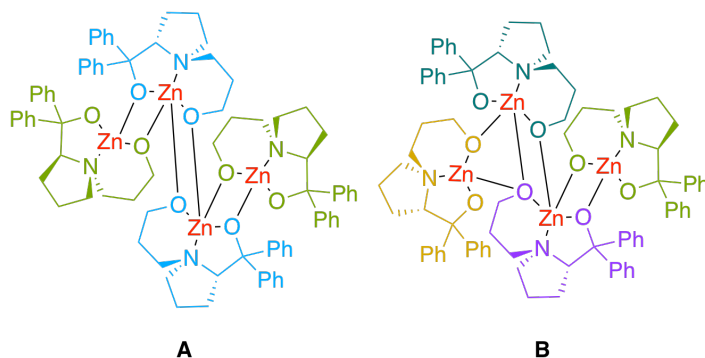


Figure 17: Coordination motifs in the molecular structures of $\{[L^{\text{ProOH}}\text{Zn}]_2\}_2$, drawn for better illustration and comparison. Each coordination motif is displayed in one color. **A** is the molecular structure of Figure 14 and **B** of Figure 16.

Table 3: Comparison of angles and bond lengths from the molecular structures displayed in Figure 14 and Figure 16. Described are only bonds and angles within the $[\text{LZn}]$ units with threefold coordination of the ligand to its coordinating Zn. The color-code refers to Figure 17. Zn2 in Figure 14 and Zn1 & Zn4 in Figure 16 are considered the terminal $[\text{LZn}]$ units.

		Figure 14, A		Figure 16, B			
		Zn1	Zn2	Zn1	Zn2	Zn3	Zn4
$\angle \text{O}^{\text{CPh}_2}\text{-Zn-N}$	[°]	79.30	88.72	88.60	78.84	86.22	87.72
$\angle \text{O}^{\text{C}_3\text{H}_6}\text{-Zn-N}$	[°]	90.58	98.03	100.40	84.80 [†]	100.91	100.84
$d(\text{Zn-N})$	[Å]	2.300	2.110	2.102	2.262	2.133	2.107
$d(\text{Zn-O}^{\text{CPh}_2})$	[Å]	2.056	1.887	1.898	2.099	1.906	1.883
$d(\text{Zn-O}^{\text{C}_3\text{H}_6})$	[Å]	1.957 & 2.035 [‡]	1.963	1.974	2.059 [†]	1.951	1.932

[‡] due to symmetry Zn1 coordinates two O1; [†] alcoholate coordinating three zinc.

while the central ones have a coordination number of five, resulting in the observable trends within the data of Table 3. The terminal zinc ions (Zn2 from Figure 14 and Zn1, Zn4 from Figure 16) show larger values for the angles within the five-membered ring $\angle \text{O}^{\text{CPh}_2}\text{-Zn-N}$. For the angle $\angle \text{O}^{\text{C}_3\text{H}_6}\text{-Zn-N}$ of the six-membered ring this trend can only be observed for the structure motif **A**. The Zn-N and Zn-O^{CPh₂} distances in the terminal $[\text{LZn}]$ units are shorter than in the central ones. For the Zn-O^{C₃H₆} distance this trend is not pronounced. The Zn-Zn distances found in coordination motif **B** are comparable to the ones in motif **A**. The terminal Zn-Zn distances measure $d(\text{Zn1-Zn2}) = 2.975 \text{ \AA}$ and $d(\text{Zn3-Zn4}) = 2.978 \text{ \AA}$, while the central distance measures $d(\text{Zn2-Zn3}) = 3.184 \text{ \AA}$. Both distances are longer than in **A** ($d(\text{Zn1-Zn2}) = 2.911 \text{ \AA}$ and $d(\text{Zn1-Zn1}) = 3.086 \text{ \AA}$), due to the different bridging mode in **B**. The performance of $[\text{L}^{\text{ProOH}}\text{Zn}]_2$ for CO₂/epoxide copolymerization is discussed in section 2.4.2 and the influence of the Zn-Zn distance and flexibility of the ligand on the activity of the catalyst is also

explored further.

Overall, five different coordination motifs were observed in the solid state (see color coding in Figure 17). Therefore, it seems likely that various coordination motifs can be expected in solution. In fact, a complex ¹H-NMR spectrum of crystalline material of [L^{ProOH}Zn]₂ with broad signals was observed at RT. Upon cooling to 238 K the signals sharpened. The resulting ¹H-NMR spectrum is depicted in Figure 108 in the Appendix A.2.1. Nevertheless, the spectrum remains very complex. To determine the number of distinct coordination environments in solution, a ¹³C-NMR experiment was performed. For the C₁-symmetric ligand two signals were observed for the *ipso*-carbon atoms of the phenyl substituent (see Figure 12). Hence, for every [L^{ProOH}Zn] coordination environment two signals should likewise be observable. From the signals assigned to the quaternary carbons of the phenyl substituents of the ¹³C-NMR spectrum in THF, five major species can be observed, as depicted in figure Figure 18. The full ¹³C-NMR spectrum can be found in Figure 109 in the Appendix A.2.1. Furthermore, in CDCl₃ the same observation can be made in the range of 154–148 ppm (see Figure 110 in Appendix A.2.1). In Figure 18 it can be observed that one pair of signals has a lower abundance than the other pairs.

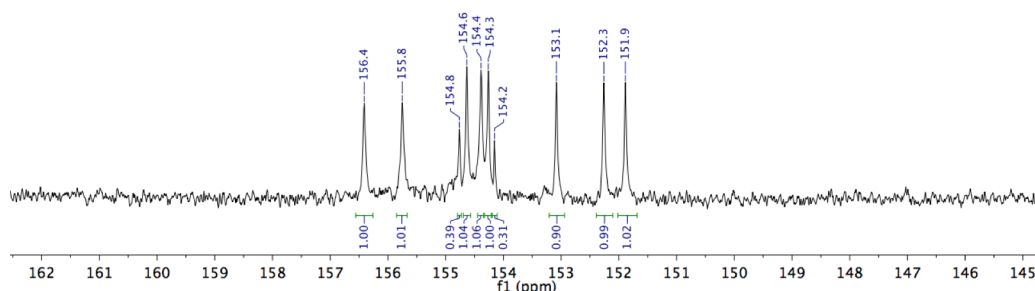


Figure 18: Section of ¹³C-NMR spectrum of [L^{ProOH}Zn]₂ corresponding to the *ipso*-carbon atom of the phenyl substituents in THF at 239 K.

For the polymerization experiments, structural information in solution, especially regarding the nuclearity of the complex, is of high interest. This is essential for evaluating whether the self-assembly strategy to form a dinuclear complex, following the polymerization mechanism depicted in Scheme 3, was successful. Therefore, DOSY-NMR experiments of complex [L^{ProOH}Zn]₂, with the addition of Si(TMS)₄ as internal standard, were performed to determine the molar mass of the complex in solution.^{143–145} The addition of the internal standard allow to neglect the corrections, which are otherwise mandatory concerning the influence of the hydrodynamic radius by temperature due to changes of solvent viscosity. This is possible since the internal standard (applying calibration curves from literature) is affected by the mentioned factors to a same extent as the compound of interest.^{143,144} The obtained values for the molecular mass depend on

the assumed shape of the complex in solution; the values for an ellipsoid shape (DSE) and the *merge* shape are given. The *merge* shape combines the calibration curves for various geometries using all references.^{143,144} Both shapes are considered most representative for this case, especially the DSE geometry (see Figure 14 and Figure 16). A disc shape appears non-suitable.

The DOSY-NMR experiments were performed at 50 °C, -34 °C and -50 °C in CDCl₃, with Si(TMS)₄ as internal standard. At 50 °C, a single species with a diffusion coefficient of $D = 7.446 \times 10^{-10} \text{ m}^2/\text{s}$ was observed for the complex, while the internal standard Si(TMS)₄ gave $D = 1.389 \times 10^{-9} \text{ m}^2/\text{s}$ (see Figure 19).

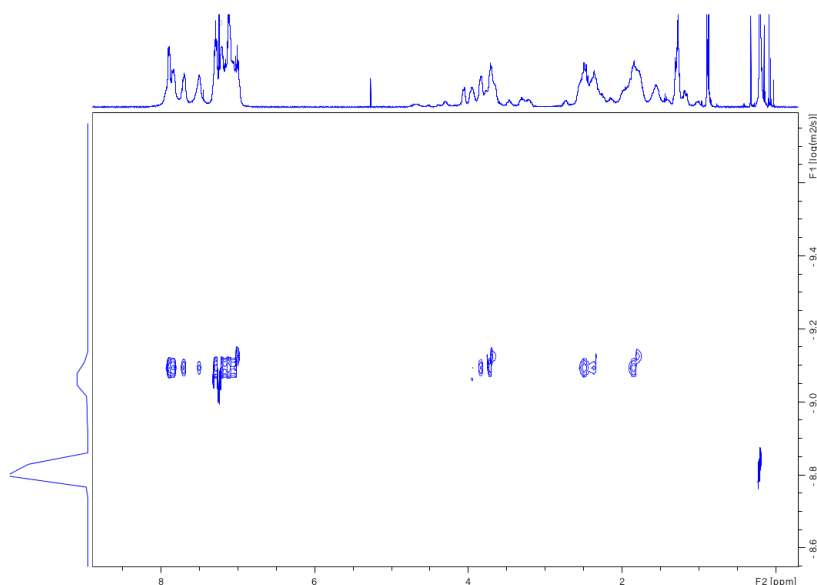


Figure 19: DOSY-NMR spectrum of [L^{ProOH}Zn]₂ in CDCl₃ at 323 K. Si(TMS)₄ as internal standard. Processing was performed with TopSpin NMR software from Bruker.

The calculation of the approximate molecular mass through determination of the T_1/T_2 relaxation times,^{143–145} resulted in $M_{\text{DSE}} = 766 \text{ g/mol}$ and $M_{\text{merge}} = 892 \text{ g/mol}$. Both correspond to a [LZn]₂ species ($M = 749.6 \text{ g/mol}$) with a deviation of 2% for the DSE and 16% for the *merge* geometry. At -34 °C two species could be observed, the major one corresponding to $D = 2.127 \times 10^{-10} \text{ m}^2/\text{s}$, and a minor species with $D = 1.879 \times 10^{-10} \text{ m}^2/\text{s}$ ($D = 3.893 \times 10^{-10} \text{ m}^2/\text{s}$ for Si(TMS)₄, see Figure 112 in Appendix A.2.1). The approximated molecular mass of the major species was calculated to be $M_{\text{DSE}} = 741 \text{ g/mol}$ and $M_{\text{merge}} = 861 \text{ g/mol}$, showing a deviation from the expected values for the dinuclear L₂Zn₂ species of 1% for the DSE and 13% for the *merge* geometry. The minor species has an estimated molecular mass of $M_{\text{DSE}} = 920 \text{ g/mol}$ and $M_{\text{merge}} = 1087 \text{ g/mol}$, corresponding to a higher aggregation. The calibration curves for this method do not reach 1000 g/mol. Therefore, only speculations

can be made if the higher aggregate that was found at low temperatures is of trimeric or tetrameric nature. The determined molecular mass points towards a trimeric L₃Zn₃ species ($M = 1124.4$ g/mol). However, since the only observed species at elevated temperatures is dimeric, it seems plausible that two of such units aggregate, forming a tetrameric L₄Zn₄ species, as it was observed in the molecular structures from X-ray diffraction (Figure 14 and Figure 16). Such a dimerization of two L₂Zn₂ species would cause a drastic change in geometry, possibly towards a more spherical shape (CS). Therefore, the molecular mass for $D = 1.879 \times 10^{-10}$ m²/s ($D = 3.893 \times 10^{-10}$ m²/s for Si(TMS)₄) was determined assuming a spherical shape, resulting in $M_{CS} = 1454$ g/mol and showing a deviation of 3 % from the calculated value of a tetranuclear L₄Zn₄ species ($M = 1499$ g/mol).^{143–145}

Cooling down even lower for the DOSY-NMR experiment (-50 °C) only allowed the observation of a greater abundance of the higher aggregate. No additional species with even higher molecular weight were identified (see Figure 114 in Appendix A.2.1). If the found species with $D = 1.879 \times 10^{-10}$ m²/s (at -35 °C) would be a L₃Zn₃, a tetranuclear L₄Zn₄ equivalent would be expected to be found upon decreasing the temperature further. Since this was not observed, it could be interpreted as further support for the assumption that the complex at low temperatures is a tetranuclear L₄Zn₄ species with a spherical shape.

Nevertheless, a monomeric species ($M = 374.8$ g/mol) was not observed, even in a coordinating solvent such as THF (see Figure 113 in Appendix A.2.1). In THF-d₈ only two slightly different sets of signals were observed for the complex (see Figure 113 in Appendix A.2.3). The major species corresponds to a diffusion coefficient of $D = 5.261 \times 10^{-10}$ m²/s and a small fraction to a slightly bigger species with $D = 5.233 \times 10^{-10}$ m²/s, resulting from the coordination of THF or a different bridging mode between two [LZn] units. It should be noted that the shape of the observed L₂Zn₂ species can differ depending on the coordination motif between two [LZn] units (compare Figure 21), thus giving a possible explanation for the broadened signals observed in the DOSY-NMR spectra. However, the fittings that were performed to obtain the diffusion coefficients from a T_1/T_2 relaxation experiments were of satisfying quality, indicating the reliability of the determined diffusion coefficients. The comparison of the NMR measurements in CDCl₃ and THF allows the assumption that there is no (or a negligible) solvent dependence between the two solvents. Furthermore, it can be speculated that the solvent environment of the cyclic ether THF is comparable to that of the cyclic ether CHO, which will be applied for catalysis (see section 2.4.2).

So far, we can conclude that only dinuclear [L^{ProOH}Zn]₂ complexes are present in solution at temperatures convenient for catalysis. For further support of this assumption and due to the neutral charge of the complex, a LIFDI-MS measurement was performed

from a toluene solution, showing one species at $m/z = 747$ which, according to its mass and isotopic pattern, corresponds to a dinuclear $[L_2Zn_2+H]^+$ species (see Figure 107 in Appendix A.1.1). The elemental stoichiometry and composition determined by elemental analysis is in good agreement with the calculated values. Finally, it should be mentioned that the use of different zinc sources ($Zn(HMDS)_2$ or $ZnEt_2$) or solvents for the synthesis yield the same $[L^{ProOH}Zn]_2$ complex. No difference was observed in the analytic data of different batches.

All in all, the complex $[L^{ProOH}Zn]_2$ was isolated successfully and its dinuclear nature at ambient or elevated temperatures in solution could be determined.

DFT calculations for estimation of the absolute configuration of the $[L^{ProOH}Zn]_2$ species in solution

In order to estimate which dinuclear species are present in solution that cause the five sets of signals for the quaternary carbons of the phenyl substituents in the ¹³C-NMR spectrum (ten signals in the range of 156–151 ppm (THF-d₈), see Figure 109 in Appendix A.2.1) DFT calculations for the dinuclear $[L^{ProOH}Zn]_2$ complex were performed. More detailed information regarding these species is crucial because of their influence on the stereoinformation within a formed polymer, when they are applied as catalysts.

The first step was the modeling of the possible configuration of the complex and the geometry optimization using the universal force-field assumption (performed by the software Avogadro V.1.1.1). Then, the spin-restricted Kohn-Sham procedure with the generalized gradient approximation (GGA) with the functional BP86, the basis set def2-tzvp, the auxiliary basis set def2-tzvp/j and the RI approximation were used for the geometric optimization performed by Orca Version 3.0.3. The summary of the modeled structures and the resulting relative single-point energies of the calculation can be found in Table 4.

An exemplary determination of configuration for entry 9 from Table 4 can be found in Figure 20. The O-atoms that bridge two $[LZn]$ units are either described as “O” referring to the propanolyl moiety, or as “OPh” referring to the diphenylmethanolyl moiety within the ligand. These oxygen atoms coordinate two zinc ions. The relative configuration of the nitrogen atoms (N–Zn bond) towards the Zn_2O_2 plane (gray plane in Figure 20) is expressed with *cis* or *trans*, depending on their relative positioning to the Zn_2O_2 plane.

2.4 COMPLEX DESIGN OF ONO PINCER TYPE LIGANDS FOR THE COPOLYMERIZATION OF CO₂ AND EPOXIDES

Table 4: Results of the DFT calculations on the configurations of [L^{ProOH}Zn]₂.

Entry	bridge*	rel.conf.†	N‡	Zn‡	transf.‡	ΔSP§	order		
1	2 O	<i>cis</i>	<i>RR</i>	<i>RR</i>	2O- <i>trans-RR-RS</i>	4.3	3		
2			<i>SS</i>	<i>SS</i>					
3			<i>RR</i>	<i>RR</i>	2O- <i>cis-SS-SS</i>				
4			<i>SS</i>	<i>SS</i>	10			7	
5			<i>RS</i>	<i>RR</i>	2O- <i>trans-RS-RS</i>				
6		<i>SS</i>	<i>SS</i>	2O- <i>trans-RS-RS</i>					
7		<i>trans</i>	<i>RR</i>	<i>RS</i>		7.1	4		
8			<i>SS</i>	<i>RS</i>				2O- <i>cis-SS-SS</i>	
9			<i>RS</i>	<i>RS</i>	2O- <i>trans-RS-RS</i>			0.0	1
10			<i>SR</i>	<i>SR</i>					
11	2 OPh		<i>cis</i>	<i>RR</i>	<i>RR</i>				
12		<i>SS</i>		<i>SS</i>					
13		<i>RR</i>		<i>RR</i>	decoordination [⊠]	20	14		
14		<i>SS</i>		<i>SS</i>					
15		<i>RS</i>		<i>RR</i>	OPhO- <i>cis-SR-SS</i>			24	16
16		<i>SS</i>	<i>SS</i>						
17		<i>trans</i>	<i>RR</i>	<i>RS</i>					
18			<i>SS</i>	<i>RS</i>		decoordination [⊠]			
19			<i>RS</i>	<i>SR</i>	2OPh- <i>trans-RS-SR</i>	7.5	5		
20			<i>RS</i>	<i>RS</i>					
21	OPhO		<i>cis</i>	<i>RR</i>	<i>SS</i>			OPhO- <i>trans-RR-RS</i>	17
22		<i>RR</i>		<i>RR</i>	OPhO- <i>trans-RR-RS</i>				
23		<i>SS</i>		<i>RR</i>	OPhO- <i>trans-SS-SR</i>				
24		<i>SS</i>		<i>SS</i>	2O- <i>trans-RS-RS</i>	20	15		
25		<i>RS</i>		<i>SS</i>					
26		<i>RR</i>	<i>RR</i>	<i>trans-SR-SR</i>	7.7			6	
27		<i>SR</i>	<i>SS</i>						
28		<i>RR</i>	<i>RR</i>						
29		<i>trans</i>	<i>RR</i>	<i>RS</i>			2.0		2
30			<i>SR</i>	<i>SR</i>					
31	<i>SS</i>		<i>RS</i>	decoordination [⊠]	17	12			
32	<i>SR</i>		<i>SR</i>						
33	<i>RS</i>		<i>RS</i>	decoordination [⊠]					
34	<i>SR</i>	<i>SR</i>	16	10					
35	<i>SR</i>	<i>SR</i>							
36	<i>RS</i>	<i>RS</i>	<i>cis-SR-SS</i>	20	14				

*: moieties of the ligands that bridge two [LZn] units. O referring to the propanolyl moiety and OPh to the diphenylmethanolyl moiety. †: relative positioning of the N atoms towards the Zn₂O₂ plane between two [LZn] units. ‡: configuration at the N or Zn atoms. In case of an OPhO bridge does the first initial indicate the configuration at the OPh bridging [LZn] unit. §: ΔSP = SP – SP_{2O-trans-RS-RS} in kcal/mol. ⊠: decoordination of a ligand moiety as result of the DFT optimization.

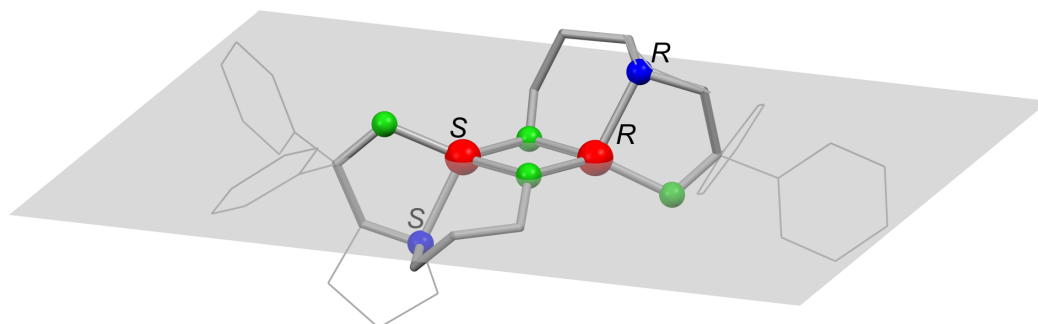


Figure 20: Exemplary determination of the complex configuration after the DFT calculation for entry 9 from Table 4. Displayed here is the modeled and optimized configuration for 2O-*trans-RS-RS*. Blue: nitrogen atom, green: oxygen atom, red: zinc atom.

In some cases, the stereoconfiguration within the modeled complex changed to a different one through geometry optimization. The configuration found after the DFT calculation is given in the column “transf.” within Table 4. Such a transformation gives a first hint towards an unfavorable thermodynamically state of the configuration. In some cases, the decooordination of a ligand moiety was observed after the DFT optimization, implying a thermodynamic unfavorable configuration. However, the relative single-point energies (ΔSP , relative to entry 9) allow for an estimation of the thermodynamic most stable configurations of the complex. From the performed calculations in Table 4, the three energetically most favorable configurations are 2O-*trans-RS-RS*, OPhO-*trans-RR-RS* and 2O-*cis-RR-RR* (entries 9, 29 and 1), in order of increasing single-point energy, within a reasonable 5 kcal/mol window. These three configurations are displayed in Figure 21.

The energetically subsequent configuration motif, fourth in order of energy, is at 7.1 kcal/mol relative to the lowest (*trans-RS-RS* with C_1 -symmetry). This corresponds to 2.8 kcal/mol difference to the *cis-RR-RR* configuration (entry 1). Due to this small energetic difference and an estimated error of the method of approximately ± 3 kcal/mol, the energetically closest configurations to entry 1 (being entries 7, 19, 26 and possibly 4) are evaluated against experimental evidence and discussed in the following. Considering the symmetry of the three energetically lowest species (*trans-RS-RS* is C_1 , OPhO-*trans-RR-RS* is C_1 and 2O-*cis-RR-RR* is C_2 symmetric) five different sets of signals for the quaternary carbon atoms of the phenyl substituents in the ¹³C-NMR spectrum can be expected, two from the C_1 and one from the C_2 symmetric compounds. Reflecting on the measured ¹³C-NMR spectrum (ten signals in the range

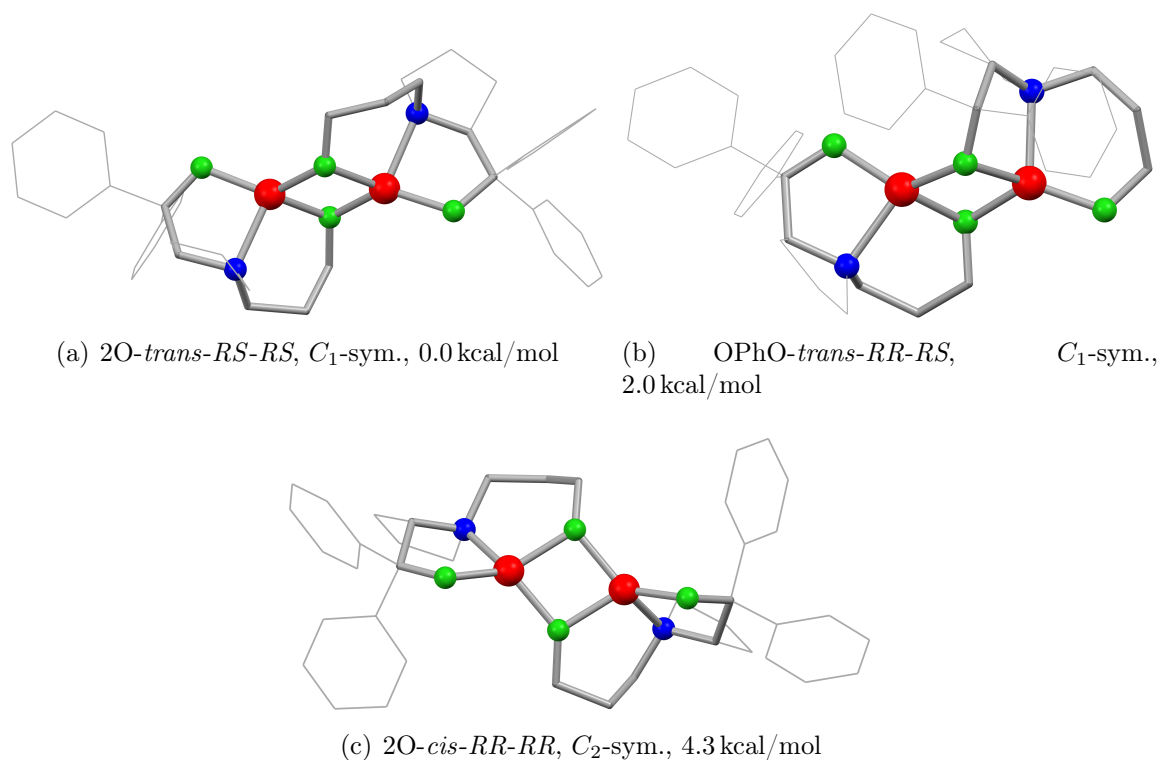


Figure 21: Visualization of the three lowest configurations of [L^{ProOH}Zn]₂ found by DFT calculations. The absolute configuration (according to the described nomenclature), its symmetry and the relative single-point energies ΔSP are given. H atoms are omitted for clarity. Blue: nitrogen atom, green: oxygen atom, red: zinc atom.

of 156–151 ppm see Figure 18) five coordination environments were observed, agreeing with the result of the DFT calculation. Furthermore, in the ¹³C-NMR spectrum, four of the five species occur with the same abundance, while one is only present with ca. 30% relative intensity. The latter is, therefore, most likely independent of the other four signals and of higher symmetry, e.g. from the C₂ symmetric compound. To go further into detail and to differentiate entries 1 from entries 4, 7, 19, and 27 (closest in energy), the symmetry of the configurations needs to be considered. For each of the configurations around 7–8 kcal/mol (entries 7, 19, 27) two sets of signals can be expected. In order to obtain five sets of signals one configuration of higher symmetry (C₂ symmetric) needs to be present, thus excluding the OPhO-bridged species, *trans* configurations and *RS*-heterogeneous configuration at the nitrogen atoms. Thus, only entries 1 and 4 remain to be considered. With a difference of 5.7 kcal/mol between these entries, the thermodynamics are in favor of entry 1. Furthermore, taking into account the configurations in the molecular structures from X-ray diffraction where all nitrogen atoms were found in a *R*-configuration (see Figure 14 and Figure 16), it further supports a *cis-RR* over a *cis-SS* configuration. Therefore, species (c) of Figure 21 is the most likely configuration. Last but not least, the molecular structure that was obtained for the equivalent nickel complex shows a dimeric species in the solid state with the same C₂ symmetric *cis-RR-RR* configuration (see Figure 40) as species (c), thus supporting the accuracy of the third species found by the DFT calculations.

Even though the applied annotation for determining the absolute configuration of the L₂Zn₂ units is not fully applicable to the molecular structures from X-ray diffraction due to higher coordination numbers, an acceptable estimate can be achieved excluding the stereo determination at the Zn atoms. In Figure 14, the asymmetric unit would correspond to an OPhO-*trans-RR* and the central L₂Zn₂ unit to a 2O-*cis-RR* configuration. Comparing these configurations with the ones from the three species of lowest energy found in the DFT calculations allow to observe similarities: entry 29 possibly corresponding to OPhO-*trans-RR* and entry 1 corresponding to 2O-*cis-RR*. This match further supports the obtained results from the DFT calculations and, therefore, their accuracy for the newly identified species (c) in Figure 21.

All in all, the DFT calculations with RKS BP86 def2-tzvp def2-tzvp/j RI found three thermodynamic minima. It could be shown that the theoretical calculations meet the experimental evidence surprisingly well, allowing insights into the absolute configuration of the [L^{ProOH}Zn]₂ species in solution. This information is crucial for understanding the stereoinformation in the polymeric product when [L^{ProOH}Zn]₂ is applied for catalysis (see section 2.4.2).

2.4.2. Copolymerization experiments applying [L^{ProOH}Zn]₂

In this section the polymerization experiments and polymer analysis that were performed applying catalyst [L^{ProOH}Zn]₂ are presented and discussed.

The investigation of [L^{ProOH}Zn]₂ as catalyst for the copolymerization of cyclohexene oxide and CO₂ started with initial testing of its activity at high CO₂ pressures (>10 bar). These tests proved to be successful, yielding an almost solid block of PCHC, due to a high conversion.

Consequently, the pressure was lowered successively, reaching the remarkably low pressure of 1 bar in CO₂, which is desirable from a process technical point of view. The catalytic activity of the complex was tested at 80 °C and with catalyst loadings of 0.05–0.10 mol%. In detail this corresponds to catalyst to monomer ratios of [CHO]:[cat] = 1000, 1500 and 2000, calculated for a dimeric catalyst species L₂Zn₂, as it was found in solution (see section 2.4.1). Table 5 summarizes the results of the copolymerization experiments. The polymerizations were carried out in Schlenk tubes in neat CHO under 1 bar of CO₂ pressure and the reactions were allowed to run for 24 h. During the polymerizations, samples were taken from the reaction solution after 1, 3, 5, 8 and 24 h. Selected reactions were followed by an *in situ* IR dip probe monitoring the carbonyl stretch vibration band (at 1750 cm⁻¹), to observe the product formation. The obtained IR spectra were correlated to the reaction progress determined by the samples. The reaction progress determined by the samples and the IR measurements can be found in the Appendix (Appendix A in Figure 128 and Figure 129). The results of catalysis from Table 5 are discussed more thoroughly below.

An important criterion for the quality of a catalyst is the chemoselectivity for the desired product. As mentioned in the introduction (see section 2.2) several reaction pathways and products are possible when performing CO₂/epoxide copolymerizations. The tested catalyst provided a chemoselectivity in carbonates of >99 % and, more importantly, for the desired PCHC up to 99 %. Furthermore, this chemoselectivity in PCHC was not observed to go below 97 %. Thus, the product formation by catalyst [L^{ProOH}Zn]₂ is highly selective and negligible amount of the undesired product poly(cyclohexene oxide) is formed (<1 %). The chemoselectivity was determined by ¹H-NMR measurements of the polymer in CDCl₃ from the relative integrals of the signals at δ = 4.61 ppm (PCHC), δ = 4.36, 3.53 ppm (end-groups of PCHC), δ = 3.98 ppm (cyclic carbonate) and δ = 3.32 ppm (homopolymer). An exemplary integration can be found in Figure 22. The full ¹H-NMR spectra of the obtained polymers can be found in the Appendix in Figure 127.

Table 5: Polymerization experiments performed with [L^{ProoH}Zn]₂.*

Entry	[CHO]:[cat.] [†]	carb. [§]	p.c. [§]	M _N ^p / kg/mol	D ^D	P _r [#]	TON [£]	TOF ₂₄ ^f / h ⁻¹	TOF _{max} (hours) [‡] / h ⁻¹	H ₂ O [§] / ppm
1	1022	98%	97%	2.67	1.52	35%	145	6	40 (0-1)	13.7
2	1006	98%	97%	4.06	1.43	40%	194	8	31 (0-1)	19.8
3	1007	99%	98%	2.85	1.30	36%	519	22	48 (1-8)	15.4 ∞
4	1010	99%	98%	2.60	1.25	36%	457	19	54 (1-8)	13.5 ∞
5	1510	99%	99%	4.16	1.38	35%	321	13	92 (0-1)	13.7
6	1497	99%	98%	4.20	1.52	38%	251	10	69 (0-1)	19.8
7	1511	99%	98%	2.34	1.24	33%	609	25	44 (1-8)	13.5 ∞
8	1510	99%	98%	2.54	1.20	38%	610	25	48 (1-8)	15.4 ∞
9	2016	>99%	99%	1.65	1.33	35%	566	24	51 (1-8)	13.5 ∞
10	2021	98%	98%	1.20	1.24	35%	450	19	41 (1-8)	15.4 ∞

*: polymerizations were carried out in neat CHO and 1 bar of CO₂ at 80 °C over 24 h of reaction time. Reactions were performed in Schlenk tubes. During the polymerizations samples were taken from the reaction solution after 1, 3, 5, 8 and 24 h. Reactions of the entries 1, 2, 5, 6, 7 and 8 were equipped with an *in situ* IR dip probe to monitor product formation which was referenced to the product in the samples.

†: assuming a dimeric species.

§: % carbonate (carb.), % polycarbonate (p.c.), determined by ¹H-NMR of the polymer in CDCl₃ from the relative integrals of the signals at δ = 3.32 (homopolymer), δ = 3.98 (cyclic carbonate) and δ = 4.61 ppm (copolymer).

b: determined by GPC in THF with toluene as internal standard calibrated with polystyrene.

D: dispersity D = M_w/M_n.

#: probability of a racemo diad P_r determined from the relative tetrad concentration by ¹³C-NMR of the carbonyl region.¹⁰³

£: determined by number of monomer units consumed divided by the number of catalysts, assuming an active L₂Zn₂ unit.

TON = (m_{PM}/M_{carbonate unit})/([cat.] × V_{CHO}). M_{carbonate unit} = 142 g/mol. m_{PM}: mass of polymer obtained from sample. [cat.]: concentration of catalyst. V_{CHO}: Volume of CHO of the sample.

f: TOF referring to the entire reaction time of 24 h. TOF = TON / t.

‡: TOF_{max} calculated for the period of time with maximal activity of the catalyst. In parentheses is the period of time at which the maximal activity was found. e.g. (3 – 8) meaning from the third hour until the eighth hour of reaction time.

§: water content of the CHO determined by *Karl-Fischer* titration.

∞: the used glassware was slanzized by vapor deposition of TMS-Cl.

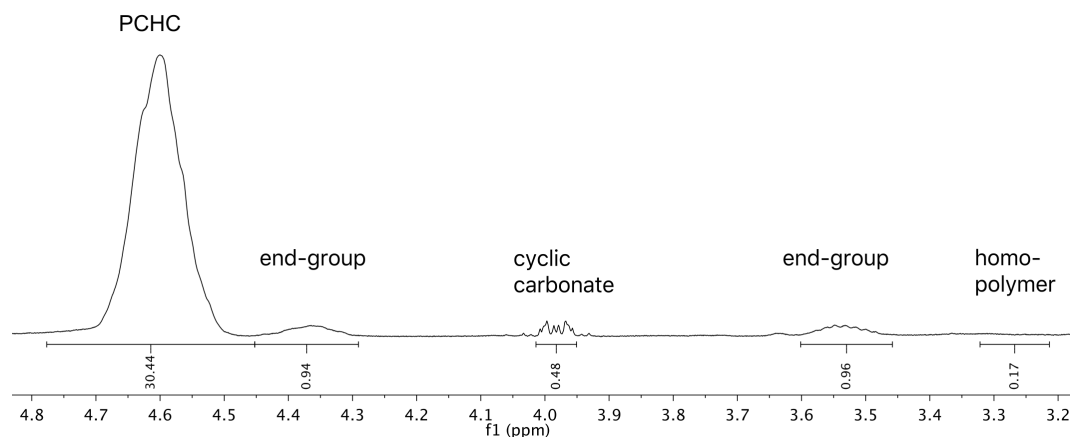


Figure 22: Section of the ¹H-NMR spectrum in CDCl₃ of the polymer obtained from entry 4 in Table 5.

The formed polymers were found to have an average molecular weight M_N of 1.20 up to 4.20 kg/mol with dispersities in the range of $\bar{D} = 1.20 - 1.52$ (exact Mark-Houwink parameters of PCHC are not known). In comparison to other CO₂/epoxide copolymerization catalysts working at higher pressures, these values are low.^{124,146} However, for a suitable comparison between catalysts, the reaction conditions need to be considered. The most prominent catalysts that are active at at 1 bar of CO₂ are the ones from Sugimoto *et al.*¹¹⁴ ($M_N = 5.4$ kg/mol with $\bar{D} = 4.15$ without co-catalyst and $M_N = 2.9 - 15$ kg/mol with $\bar{D} = 1.13-3.44$ with co-catalyst), Williams *et al.*¹¹⁸ ($M_N = 5.1 - 11$ kg/mol with $\bar{D} = 1.03-1.26$), Nozaki *et al.*¹³¹ ($M_N = 1.6$ kg/mol with $\bar{D} = 1.22$) and Xiao *et al.*⁸⁷ ($M_N = 20 - 43$ kg/mol with $\bar{D} = 1.22$). For all of them, except for the latter, the molecular masses of the formed polycarbonates are in the same order of magnitude as found for [L^{ProOH}Zn]₂. Moreover, the system of Xiao *et al.* (magnesium-based), which provides higher molecular masses, shows only 66% selectivity for carbonates.⁸⁷

Comparing the M_N and \bar{D} values (Table 5) of entries 1, 2, 5 and 6 (untreated glassware, $M_N = 2.56 - 4.20$ kg/mol and $\bar{D} = 1.38-1.52$) with the other entries of the table ($M_N = 1.20 - 2.85$ kg/mol and $\bar{D} = 1.20-1.32$) where silanized glassware was used, a trend to higher M_N values and broader polydispersities is observed for the runs with untreated glassware. This is probably due to a higher content of water. The broader polydispersities can be explained by a deactivation mechanism due to sensitivity of the catalyst towards water (see section 2.4.2 and especially Figure 38 and Scheme 13, as well as Figure 26). This might imply that in presence of water (and CO₂) a different catalytically active species forms. The higher M_N values in presence of water, however, cannot be explained that easily. At this point, the question remains open but is

discussed later in this section, where mechanistic insights are developed.

To determine the influence of the catalyst on the secondary structure of the polymer, the carbonyl region from ¹³C-NMR measurements of the PCHC was fitted by *MestReNova* to determine its tacticity.^{102,103} The relative abundance of the assigned tetrad sequences was derived from the fit. This was done by applying the Bovey formalism of the Bernoullian method.^{104,105} The probability for the formation of a racemo diad is represented by the statistic value P_r , which can be found in Table 5. In the case of PCHC the carbonyl region represents tetrad sequences for which the following statistical expressions^{103,104} apply:

$$\begin{aligned} [rrr] &= P_r^3; \\ [rrm] &= 2(P_r^2(1 - P_r)); \\ [rmr] &= P_r^2(1 - P_r); \\ [mrm] &= P_r(1 - P_r)^2; \\ [mmr] &= 2((1 - P_r)^2 P_r); \\ [mmm] &= (1 - P_r)^3. \end{aligned}$$

The assignment of the tetrad sequences was done according to literature¹⁰³ and is exemplarily depicted in Figure 23. In the Appendix in Figure 130 further ¹³C-NMR spectra with the performed fits and corresponding surface areas, which were used to determine the tacticity, can be found. The evaluation of the obtained relative surface areas of the

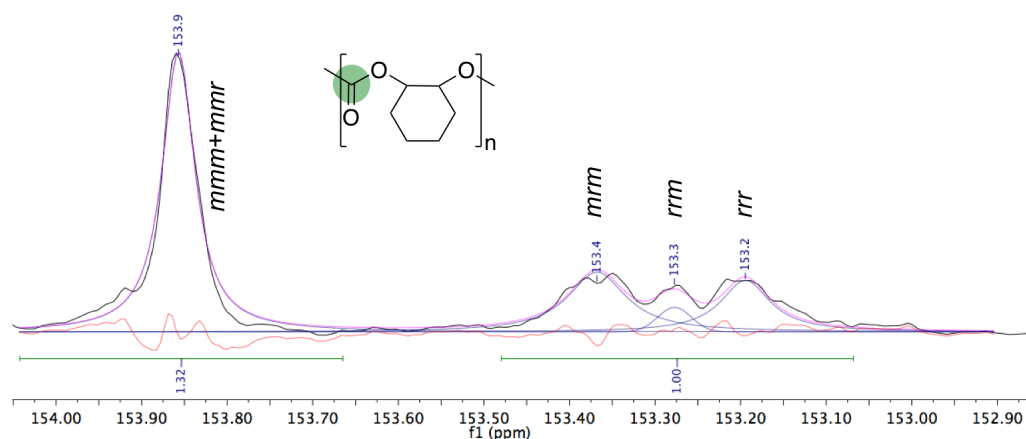
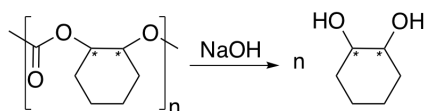


Figure 23: Carbonyl section of the ¹³C-NMR spectrum in CDCl₃. The fit (purple line) of the region and assignment of the tetrad sequences are displayed.¹⁰³ Black line: experimental data, blue line: fit of the according peak, red line: visualization of error.

assigned tetrads showed the formation of a polymer with enriched isotacticity deriving from the observed values for P_r in the range of 33 – 40%. The structurally related

complex by Nozaki *et al.* (Complex **7** in Figure 8) forms PCHC with P_r values down to 15%.¹⁰⁶ This value was estimated from the obtained ¹³C-NMR spectrum in Figure 2 of the publication (83/17 ratio of *m/r*-centered tetrads with 70% *ee*),¹⁰⁶ applying updated procedures for determining the tacticity of PCHC.¹⁴⁷ For detailed information on data analysis and how to obtain the P_r values see Appendix A.3.4.

After these insights into the tacticity of the polymer, demonstrating an enrichment of *m*-diads, the question arises whether these diads also allow for the observation of an enantioenrichment. To test this, the PCHC product was hydrolyzed with a NaOH solution in a 1:1 mixture of water and methanol to obtain the corresponding *trans*-cyclohexan-1,2-diol, preserving the absolute stereoconfiguration (see Scheme 9). The



Scheme 9: Hydrolysis of PCHC with a NaOH solution in a 1:1 mixture of water and methanol to obtain the corresponding *trans*-cyclohexan-1,2-diol for chiral-CG analysis.

obtained diol was analyzed by chiral GC. However, the hydrolyzed polymer did not show any enantiomeric excess within the diol. Racemic cyclohexan-1,2-diol and enantiomerically pure cyclohexan-1,2-diol was used for calibrating the GC, concluding that the catalyst $[L^{ProOH}Zn]_2$ does not distinguish between the enantiomers during polymerization under the given polymerization conditions. For a more detailed interpretation, the enantiomeric-site control or chain-end control mechanism need to be considered. In the site controlled mechanism the stereoinformation in the polymer originates from the catalyst, while in the chain-end control mechanism the configuration of the last incorporated monomeric unit determines the subsequent one. It cannot be unambiguously established which stereoisomers of the catalyst are responsible for the catalysis but, considering the findings and DFT calculations from section 2.4.1, it is most likely more than one. The presence of different stereoisomers should influence the formed PCHC in a site-controlled mechanism, which could explain why only an isoenriched PCHC was formed. However, it can only be speculated by these observations that no enantioselective PCHC was formed. In Figure 24, hypothetical products corresponding to the two different control mechanisms are shown. Both scenarios, (a) and (b), could explain the observed tacticity and stereoinformation that were formed. In (a) a chain-end controlled PCHC forming an isoenriched polymer is suggested. Checking this hypothesis against literature renders this scenario unlikely. The proposed chain-end controlled mechanism published in 2006 by Coates *et al.* showed the formation of a syndiospecific CO₂/CHO copolymer.¹⁰³ A chain-end control mechanism is not known to form isoselective PCHC. The remaining scenario (b) in Figure 24 proposes that both

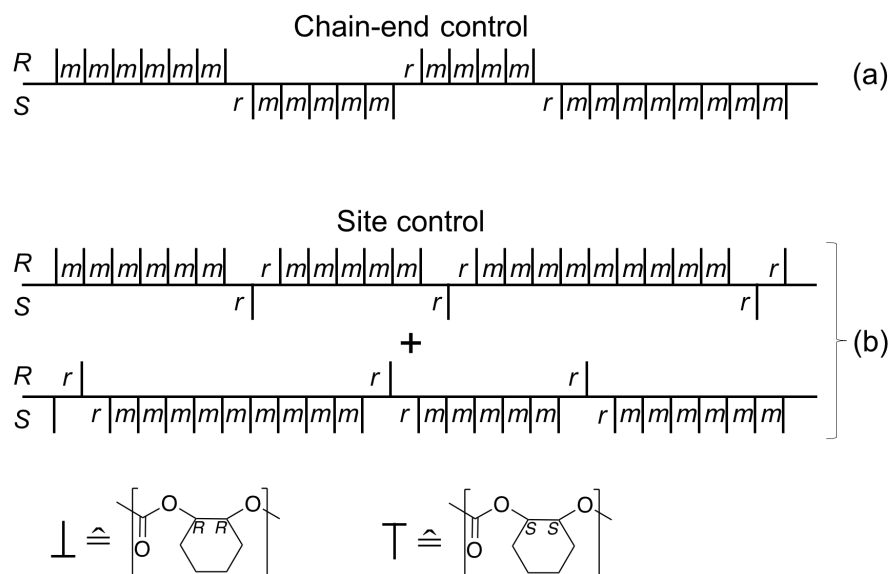


Figure 24: Display of PCHC products by different control mechanisms explaining the observable tacticity and stereoinformation (a) PCHC obtained by the chain-end control mechanism. (b) PCHC obtained by the site control mechanism with selectivity for *R/S* enriched PCHC.

enantiomers of the formed isotactic polymer are produced in a racemic fashion. Given the obtained analytic data of the polymer and considering the catalyst behavior in solution, scenario (b) seems to be the more likely explanation for the findings in tacticity and stereoinformation within the PCHC.

It seems plausible that the symmetry of the active species has a strong influence on the tacticity. The complex here studied was found to occur as C_2 -symmetric and C_1 -symmetric species (Figure 21). An active species deriving from a C_2 -symmetric precatalyst could produce a different product than one deriving from a C_1 -symmetric precatalyst, one possibly directing a syndio- and the other an isotactic PCHC. These questions, however, are difficult to answer without the challenging task of separating the stereoisomers of the catalyst, with a remaining possibility that they interconvert. The most challenging circumstances for a mechanistic study would be a combination of both mechanisms, the chain-end-controlled and the site-controlled, each one for each of the different species.

It can be assumed that the proposed scenario (b) in Figure 24, implying a site control without enantioselectivity, is the more probable mechanism of control during the polymerization.

The next column of Table 5 shows the turnover numbers (TON). They were determined to be in the range of 145 – 321, applying untreated glass. The TON could be increased to values of 457 – 610, depending on the catalyst loading, by the use of

silanized glassware. For a diluted reaction with a 2000:1 ratio of CHO to catalyst the TON was found to be between 450 – 566, and for a 1500:1 ratio the TON was observed to be as high as 610. The TON was determined by equation 2.

$$TON = \frac{n_{\text{rep.unit}}}{n_{\text{cat.}}} = \frac{m_{\text{polymer}}/M_{\text{rep.unit}}}{m_{\text{cat.}}/M_{\text{cat.}} \cdot (V_{\text{CHO}}^{\text{sample}}/V_{\text{CHO}}^0)} \quad (2)$$

Here the approximation was made that $M_{\text{rep.unit}} = M_{\text{C}_7\text{H}_{10}\text{O}_3} = 142 \text{ g/mol}$, with abbreviation ‘‘Rep.unit’’ referring to the repeating cyclohexene carbonate unit. It was assumed that all obtained repeating units consist of cyclohexene carbonate, which is justifiable due to the high selectivity of the catalyst for carbonates of >99%. $m_{\text{cat.}}$ is the mass of the catalyst applied for the polymerization experiment, while the term $V_{\text{CHO}}^{\text{sample}}/V_{\text{CHO}}^0$ represents the fraction of catalyst that was taken as a sample from the reaction solution. $V_{\text{CHO}}^{\text{sample}}$ represents the volume of the sample and V_{CHO}^0 the injected volume of CHO at $t = 0$.

From the TON values the corresponding TOF₂₄ (turnover frequency) was calculated, here after 24 h (Table 5). The obtained TOF₂₄ values are in the range of 6 – 13 h⁻¹ for the untreated glassware and in the range of 19 – 25 h⁻¹ for the polymerizations performed with silanized glassware. Batches of catalyst formed by using Zn(HMDS)₂ or ZnEt₂, in DCM or THF, crystalline or bulk material showed no observable difference in their catalytic activity. The subsequent column of Table 5 shows the TOF_{max} value. These values describe the catalyst at its highest activity. The values after 24 h (average over 24 h) do not represent the activity accurately since, for example, an initiation phase and the increase of viscosity at high conversions are not accounted for.

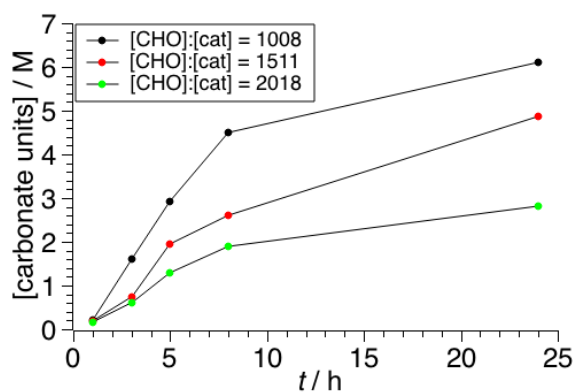


Figure 25: Product formation against time. The depicted concentration of carbonate units are the average values for the corresponding entries from Table 5 (entries 3, 4; 7, 8 and 9, 10). The copolymerizations of CHO and CO₂ (1 bar) were performed at 80°C applying [L^{ProOH}Zn]₂. The [carbonate units] correlates to [1 - [CHO]]. Samples were taken from the reaction solution to determine [carbonate units].

The numbers in parenthesis behind the TOF_{max} values given in this column refer to the time frame at which the highest activity was observed. This time frame was determined from the plot of [carbonate unit] against time. This product formation against time for different catalyst loading can be found in Figure 25. The points represent the average values from two independent runs with equal catalyst loading and reaction conditions. This plot illustrates why the lower (1 h) and upper time limit (8 h) for the calculation of the TOF_{max} were applied. Within the first hour the polymerization has not initiated yet, and after 8 h the decrease of activity due to limited diffusion becomes dominant. Thus, a seven hour window was chosen to determine the TOF_{max} for runs with silanized glassware. Without silanized glassware the highest activity was determined within the first hour of the reaction, showing no or a very short initiation period as observable in Figure 28.

Comparing the obtained TON and TOF values with the ones from prominent CO₂/CHO copolymerization catalysts allows these values to be put in perspective (also see section 2.2.3). For a first comparison, the structurally similar complex reported by Nozaki *et al.*¹³¹ should be considered (in Figure 8 complex **7**). This zinc-based catalyst shows a TOF of 2 h⁻¹ (19 h reaction time, TON = 40 performed in toluene at 40 °C). The observed catalytic activity of [L^{ProOH}Zn]₂ is far greater, which is surprising considering that the ligand derives from this system. Another catalyst with structural similarity to [L^{ProOH}Zn]₂, published by Ding *et al.*¹³², is listed among other state-of-the-art catalysts in Table 6 (complex **8** in Figure 8). The table is sorted chronologically but does not represent all catalysts that are active at 1 bar, although the best performing ones are listed. The TON and TOF values given in Table 6 represent the highest reported activity of the corresponding catalyst at 1 bar of CO₂. The catalysts developed over the years and, as mentioned in the introduction (section 2.2.3), the system of Rieger *et al.*¹¹⁶ holds the record in activity at elevated pressures and even at 1 bar of CO₂ (complex **5** in Figure 7). Furthermore, it is a zinc-based catalyst, which is of advantage due to a low toxicity and colorless nature of the metal. However, the applicability is also the limiting factor of this system. On the one hand, the yield of its ligand is as low as 3% in the last step alone and, on the other hand, the chemoselectivity of the catalysts for PCHC at 1 bar CO₂ pressure is only 47%. Nevertheless, the catalyst is proof of principle for very high activities (entry 9, Table 6). The complexes by Williams *et al.*, all based on the same macrocyclic ligand, show TON values up to 527 and TOF values up to 500 h⁻¹ with various metals (Table 6), while even demonstrating a good tolerance to water (the zinc complex **6** is displayed in Figure 7). The salen-type complexes, in this table represented by Lu *et al.*¹⁴⁸ (entry 6, Table 6), show remarkable catalytic activities: here TOF values up to 263 h⁻¹ were found. However, toxic metals are usually required for these catalysts to show high activities (Table 6).

The obtained TON for [L^{ProOH}Zn]₂ (Table 5) are very good, when comparing them to the catalysts from literature. These values, however, have to be put in relation to the duration of the experiment and, thus, only become conclusive when the time factor is considered. For that reason, the TOF is a better value for the purpose of comparison. For [L^{ProOH}Zn]₂ the highest TOF observed was 25 h⁻¹ over 24 h, which is as high as that of the benchmark zinc catalyst by Williams *et al.* (entry 5, Table 6), calculated for a 24 h reaction period. However, an initial TOF values of 92 h⁻¹ have been observed for [L^{ProOH}Zn]₂, when untreated glass was applied. Under these reaction conditions the catalyst loses the high activity fast (see Figure 26). The highly modified and optimized cobalt-based systems by Williams *et al.* and by Lu *et al.* show higher activities than the corresponding zinc systems.^{103,149–157} The only zinc-based system that has a higher activity is the macrocycle from Rieger *et al.*, which comes along with the previously mentioned deficits in chemoselectivity and accessibility of the complex. It should be emphasized that such comparisons in general are difficult due to manifold

Table 6: Selection of literature-known catalysts for the CO₂/CHO copolymerization and their corresponding activity at 1 bar of CO₂ pressure. Sorted chronologically by year of publication.

Entry	Author	Metal	TON [†]	TOF [†] / h ⁻¹	Conditions
1	Inoue <i>et al.</i> ¹²¹	Mn	70	3 (24 h)	neat CHO, 80 °C
2	Ding <i>et al.</i> ¹³²	Zn	>20	>3 (6 h)	in toluene, 60 °C
3	Ding <i>et al.</i> ⁸⁷	Mg	86	43 (2 h)	in toluene, 60 °C
4	Sugimoto <i>et al.</i> ¹¹⁴	Co	75	3(24 h)	neat CHO, 25 °C
5	Williams <i>et al.</i> ¹¹⁸	Zn	527	25 (24 h)	neat CHO, 100 °C
6	Lu <i>et al.</i> ¹⁴⁸	Co	1315	263 (5 h)	neat CHO, 50 °C
7	Williams <i>et al.</i> ¹²⁹	Co	250	500 (0.5 h)	neat CHO, 80 °C
8	Williams <i>et al.</i> ¹²⁸	Fe	290	6 (48 h)	neat CHO, 80 °C
9	Rieger <i>et al.</i> ¹¹⁶	Zn	939 [§]	939 [§] (1 h)	neat CHO, 100 °C
10 [‡]	Le Roux <i>et al.</i> ¹⁵⁸	Zr	888	37 (24 h)	neat CHO, 60 °C

†: Number in parenthesis represents the time at highest activity or the duration of the experiment. The values from the publication: Lit.:¹²¹ Calc. from Tab. 1 (11), Lit.:¹³² Calc. from Tab. 1 (4), Lit.:⁸⁷ Tab. 4 (5), Lit.:¹¹⁴ Calc. from Tab. 3 (4), Lit.:¹¹⁸ Tab. 1 (3), Lit.:¹⁴⁸ Tab. 1 (6), Lit.:¹²⁹ Tab. 5 (3), Lit.:¹²⁸ Tab. 1 (1), Lit.:¹¹⁶ Tab. S2 (2), Lit.:¹⁵⁸ Tab. 2 (7). Calc.: calculated from the given data, Tab.: Table (entry or run) within the publication.

‡: performed at 0.5 bar CO₂. §: 47% selectivity for PCHC. Similar complex shows 85% selectivity for PCHC with 409 h⁻¹.

conditions of optimal efficiency, the influence of co-catalysts and other factors influencing each catalytic system differently. Furthermore, for a novel catalyst there is always the pending possibility that the optimal conditions for the catalyst were not yet found. For [L^{ProOH}Zn]₂ only the activity at 80 °C with a profoundly simple stirring equipment

has been explored. At this point it should be mentioned that the activity of catalysts applied for polymerization reaction in general is, among other factors, strongly dependent on the stirring equipment. In the experiments performed herein no impeller was used and instead only a 0.5 cm stirring bar, showing very low vortex formation, was applied. This implies that in a potential optimization or up-scaling of the reaction with a more suitable impeller the catalyst activity can be increased by at least one order of magnitude. Another essential factor that will need to be determined is the optimal reaction temperature for the ONO-pincer catalyst.

All in all, the [L^{ProOH}Zn]₂ complex shows outstanding activities at low pressures while controlling the tacticity of the formed PCHC. The observed high activities of the here presented zinc complexes with ONO-pincer ligand L^{ProOH} indicate that a new class of promising catalysts for the field of CO₂/epoxide copolymerization has been developed.

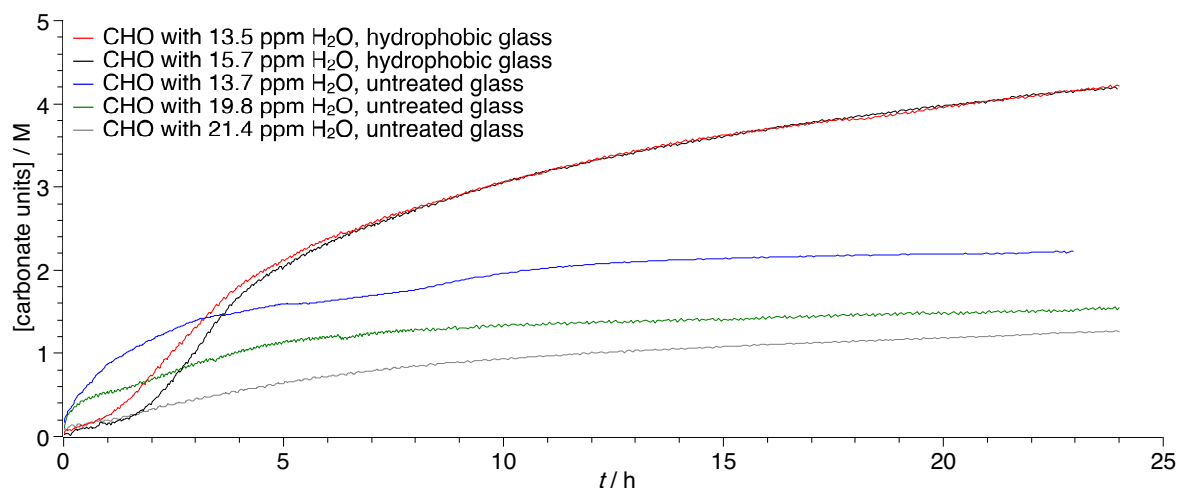


Figure 26: PCHC formation monitored by *in situ* IR measurements *via* the increase of the band at 1750 cm⁻¹ and correlated to the samples taken from the reaction solution to determine [carbonate units]. [CHO]:[cat] = 1500, 1 bar CO₂, 80 °C. Reactions with different content of water.

In the last column of Table 5, the water content of the corresponding polymerization experiments, determined by *Karl-Fischer* titration (with membrane from Mettler Toledo), is shown. Furthermore, the use of silanized glassware is indicated. In Figure 26 and Figure 28 the influence of water (in the CHO and on the glass surface) on the product formation is shown. In previous paragraphs references to these Figures have been made, to demonstrate that the initiation phase and activity are strongly influenced. In this paragraph, these two Figures will be discussed more thoroughly. The PCHC formation was recorded by *in situ* IR monitoring of the increase of the band at 1750 cm⁻¹ and correlated to the samples taken from the reaction solution. The band at

1750 cm⁻¹ corresponds to the C=O-stretching vibration within the PCHC. Thus, the band correlates with [carbonate units] (or with consumed CHO). To convert the rising IR band to a concentration in carbonate units the samples taken from the reaction solution were evaluated and used to determine the factor to obtain [carbonate units]. The correlations can be found in the Appendix in Figure 128. The reactions that are illustrated in Figure 26 and Figure 28 have been performed with a [CHO]:[cat] ratio of 1500, at 1 bar CO₂ and 80 °C. The determined water content within the CHO, as well as whether silanized glassware was used, are indicated in the legend. Figure 28 shows the initiation phase during the first 5 h of the same reactions as depicted in Figure 26. From Figure 26 an impression of the catalyst's water sensitivity over longer reaction periods can be obtained, illustrating that double the amount of PCHC was formed (red and black vs. blue line) by removal of physisorbed water and elimination of active sites on the borosilicate glass (TMS-Cl vapor deposition to silanize the glassware). The amount of formed PCHC will decrease by another approximately 50 % when the applied CHO has ca. 10 ppm more water (grey vs. blue line). This observation might raise the question of why CHO with an even lower water content (<13.5 ppm) was not used. CHO is a very challenging substance to dry and to keep dry. Besides the demanding drying process in comparison to standard solvents, the contact to many Lewis acids (e.g. molecular sieves, Dow silicon grease (contains thickeners)) leads to the formation of the homopolymer. Further details on the drying and purification process of the CHO can be found in the experimental section (section 6.2.16). For polymerization attempts with >30 ppm of water and untreated glassware no catalytic activity was observed. One possible explanation of this sensitivity was obtained from a crystallization attempt under non-inert conditions. In Figure 27, a picture of a cubic tetranuclear zinc complex is given. The oxygen atom O5 likely originates from water.

Table 7: Selected bond lengths [Å] within the molecular structure in Figure 27 of the crystallization attempt of [L^{ProOH}Zn]₂ under non-inert conditions. The atom distances were obtained from a measurement where rest-electron-density could not be assigned, therefore the values are not as accurate.

Atoms	Bond lengths
Zn51–O144	2.290
Zn51–O97	1.994
Zn51–O5	2.043
Zn98–O144	1.994
Zn98–N100	2.157
Zn98–O99	1.889

The formation of this cubic structure, which can be considered very stable, could explain why the formed complex cannot be activated for the CO₂/epoxide copolymer-

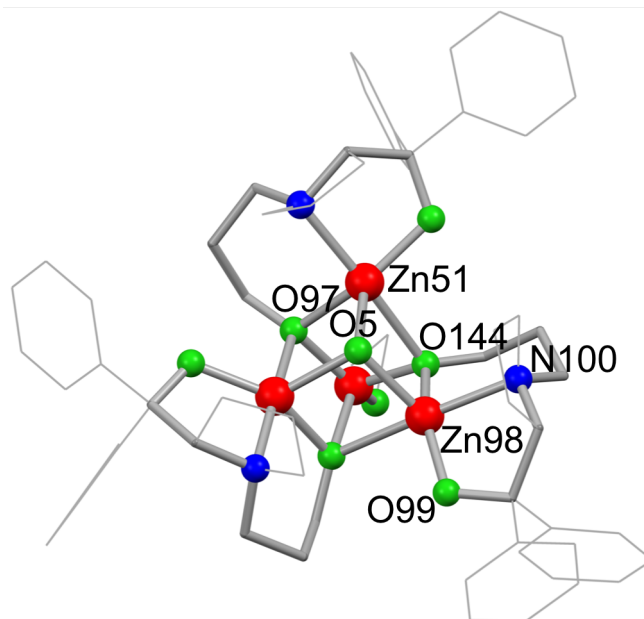


Figure 27: Picture obtained from a crystallization attempt of $[L^{\text{ProOH}}\text{Zn}]_2$ under non-inert conditions. Hydrogen atoms were omitted for clarity. Atom O5 likely originates from water.

ization. The water likely saturates the coordination environment of the zinc atoms. For the obtained picture selected atom distances are given in Table 7, yet, in this measurement rest-electron-density could not be assigned, therefore the values are not as accurate. The picture was obtained in a crystallization attempt without CO₂ being present. A discussion of the water sensitivity under conditions that are closer to the catalytic ones can be found below in the next subparagraph. There, the reaction of the complex with CO₂ is presented and a possible explanation regarding the water sensitivity, including the found initiation phase (Figure 28), will be given.

After the catalytic performance of $[L^{\text{ProOH}}\text{Zn}]_2$ has been discussed, the nature of the active species and the order in catalyst within the rate law was the object of investigation. For this purpose a Jordi Burés plot of the performed polymerizations was prepared, which can be found in Figure 29.¹⁵⁹ The product formation as [carbonate units] against $t \cdot [\text{cat.}]^n$ with $n = 0 - 4$ at different catalyst loadings is shown. The variable n represents the order in catalyst of the rate law and is varied from 0 – 4 (here in steps of 1). With this method/plot the product formation becomes independent of the catalyst concentration (the lines overlap) when the correct order in catalyst (n) is selected. From Figure 29 the highest overlay was found for $n = 1$, implying that the catalytically active species remains dinuclear in nature, as it was found in section 2.4.1.

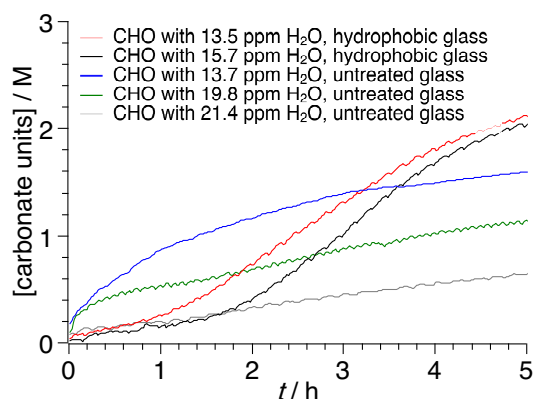


Figure 28: PCHC formation monitored by *in situ* IR measurement at the increase of the band at 1750 cm^{-1} and correlated to the samples taken from the reaction solution to determine [carbonate units]. $[\text{CHO}]:[\text{cat}] = 1500$, 1 bar CO₂, 80 °C. Reactions with different content of water. Display of the reaction's initiation phase and highest activity between the first 5 h from Figure 26.

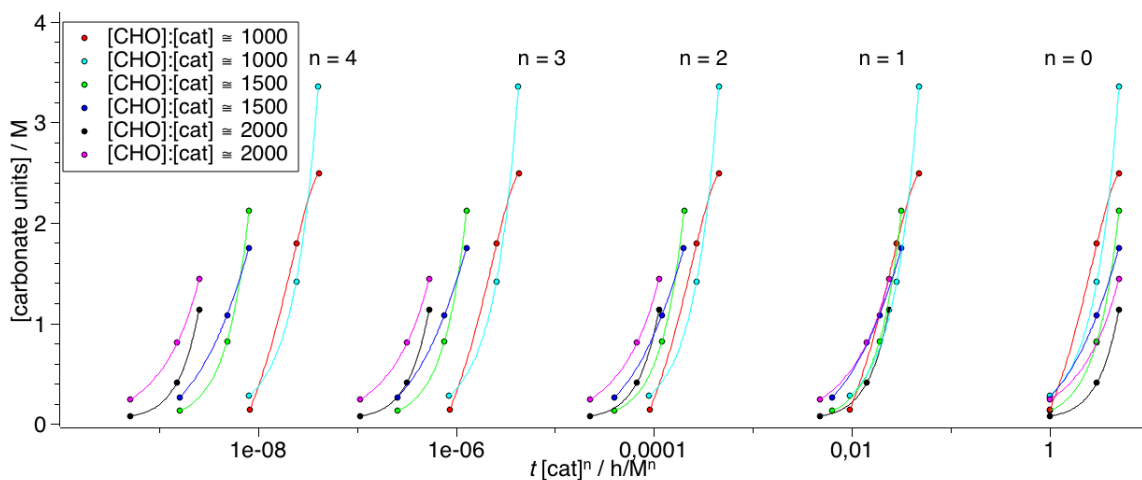


Figure 29: Jordi Burés plot of the performed polymerizations.¹⁵⁹ The product formation against $t \cdot [\text{cat}]^n$ is plotted with $n = 0 - 4$, representing the order in catalyst of the rate law. The calculation of [cat.] was done for a dinuclear complex, as it was found in section 2.4.1.

In order to exclude that other species with a higher order in catalyst (referring to the rate law) are present yielding in an overall non-natural number for n , a refined Jordi Burés plot can be found in Figure 30. Here, the variable n was altered in steps of 0.25 in the range of 0.5 – 1.5. Again, from this plot the highest overlay seems to be at $n = 1.0$, in this case it is not as certain though. However, it can be assumed that the order in catalyst is close to 1, with respect to the accuracy of this method.

Concluding, further support was found, that even during the catalysis the complex does not deaggregate to a mononuclear species or aggregate to a species of higher nuclearity. The tendency of the complex for autoaggregation seems to be a successful strategy for forming a dinuclear species for the polymerization catalysis.

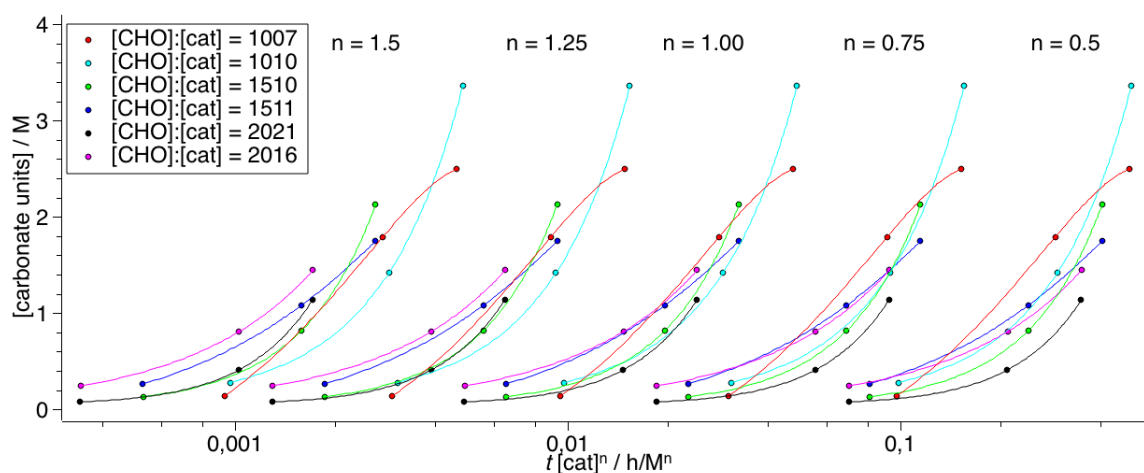


Figure 30: Refined Jordi Burés plot of the performed polymerizations to exclude rational numbers for n .¹⁵⁹ The product formation against $t \cdot [\text{cat}]^n$ is plotted with $n = 0.5 - 1.5$, representing the order in catalyst of the rate law. The calculation of $[\text{cat}]$ was done for a dinuclear complex, as it was found in section 2.4.1.

To determine the initial temperature needed for the catalyst to be active, an experiment was performed where the temperature of a reaction solution of the catalyst in CHO under 1 bar of CO₂ was slowly increased until product formation was observed (see Figure 30). The product formation, as performed previously, was monitored by *in situ* IR spectroscopy. As the oil bath of the reaction mixture reached 50 °C, an increase of the C=O-stretch vibration band at 1750 cm⁻¹, together with a decrease of the CO₂ band at 2350 cm⁻¹, was observed. Thus, the catalyst requires at least 50 °C for the formation of polycarbonate, or at least for the initiation. It is not clear from this experiment if only the initiation or also the propagation requires 50 °C. Most likely, the initiation has a higher energy barrier and therefore requires the elevated temperature. Further discussion on the initiation step can be found in the following paragraph. To

perform this experiment, reaction conditions had to be used that show no or only a short initiation phase. For that reason, untreated glassware had to be used in this experiment (compare Figure 28). The obtained polymer from this experiment was analyzed for its tacticity. Surprisingly, no higher stereocontrol was observed than in runs at 80 °C.

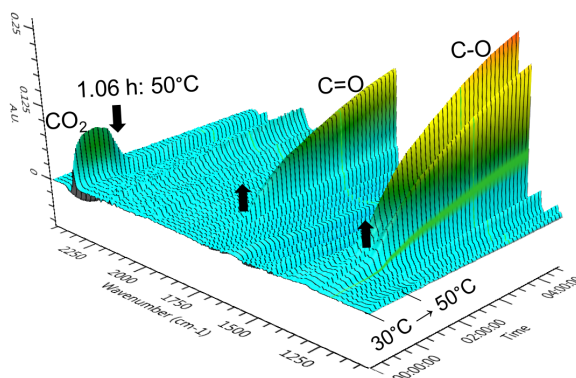


Figure 31: 3D-plot of the *in situ* IR measurement. The experiment was started at 30 °C and the temperature was slowly increased. At 50 °C (at 1 h 6 min of the reaction progress) an increase of the C=O-stretch vibration band at 1750 cm⁻¹ can be observed together with a decrease of the CO₂ band at 2350 cm⁻¹.

End-group analysis: towards the initiation mechanism

To determine the end-groups of the obtained polymers, NMR and MS experiments were performed. In the ¹H-NMR spectrum of the obtained polymers (see Figure 32) possible end-groups can be identified. The signals at 3.54 and 4.36 ppm belong to hydroxyl end-groups. These signals are the most common end-groups from the CO₂/CHO copolymerization and can be found with an estimated 75 % probability.^{118,129,132}

Besides the hydroxyl end-group, the signals at 5.92, 5.71, and 5.06 ppm reflect the formation of olefinic cyclohex-2-en-1-olate end-groups which occur with roughly 25 % probability. 2D-NMR spectroscopy and mass spectrometry confirmed these findings. This type of end-group is less common and might originate from an elimination of a carbonato unit as it is depicted in Scheme 10. Such an elimination reaction could either occur during polymerization or during the removal of the CHO under vacuum and heat. In the case of a post-synthetic elimination, also the elimination of water from a hydroxyl end-group needs to be considered.

In the case that such an elimination occurs during polymerization it would mean that the so-formed olefinic end-groups cannot be reincorporated through a chain-transfer reaction, terminating propagation at this end of the polymer chain. The formation of

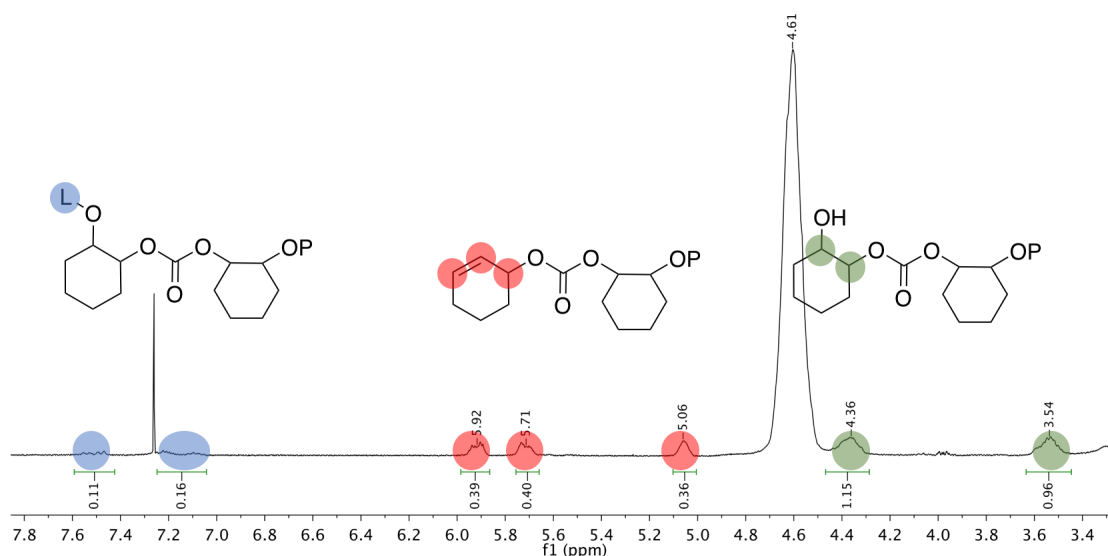
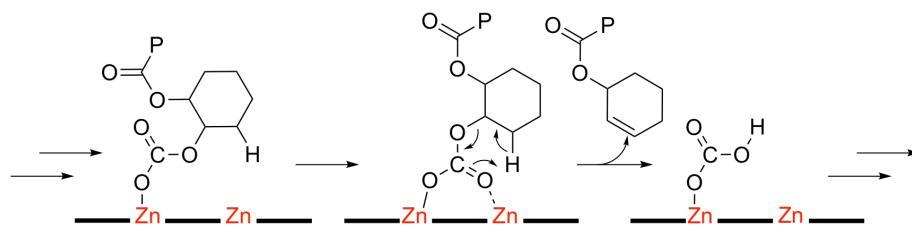


Figure 32: End-group section of ¹H-NMR spectrum in CDCl₃ of the PCHC obtained using [L^{ProOH}Zn]₂ with assignment of the end-groups. -OP represents the polymer chain.



Scheme 10: Proposed mechanism for the elimination of a carbonato species that would form a cyclohex-2-en-1-olate end-group. P representing the polymer chain.

cyclohex-2-en-1-olate end-groups could, however, explain the relatively broad dispersity (see Table 5) considering a living polymerization.¹⁶⁰ In fact, the term living polymerization would not apply in this case. To test whether the proposed elimination reaction occurs during polymerization or during the removal of the CHO, the molecular mass distribution at different times of the polymerization were plotted in Figure 33. Here it can be observed that the molecular mass increases with continuously narrower molecular mass distribution (\mathcal{D}). This criterion of a living polymerization points toward a post-synthetic elimination, leading to the follow-up question whether a mechanism, similar to the one shown in Scheme 10, or a simple elimination of water occurs. To test this, a polymer sample with a beforehand determined ratio of olefinic to hydroxyl end-groups (by NMR) was heated under vacuum to the previously applied temperatures. In the case that an elimination of water is the cause of the olefin end-groups, this event should only be weakly associated to the remaining catalyst in the polymer ($c_{\text{hydroxyl end-group}} > c_{\text{cat.}}$) and should continue to increase over time until only olefinic end-groups remain

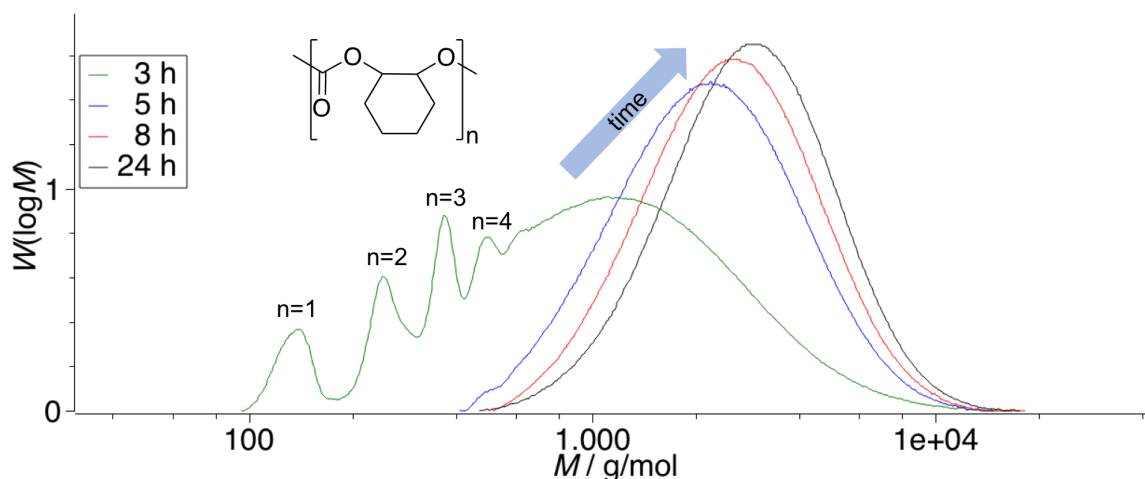


Figure 33: Molecular mass distribution from samples taken after 3 ($\bar{D} = 2.28$), 5 ($\bar{D} = 1.42$), 8 ($\bar{D} = 1.36$), 24 h ($\bar{D} = 1.34$) of reaction progress determined by GPC analysis. GPC analysis was performed in THF, calibrated with polystyrene, and toluene was added as internal standard. The M_N values were found to be after 24 h: 2432 g/mol, 8 h: 2144 g/mol, 5 h: 1794 g/mol, 3 h: NA.

(assuming exclusively the modification of the chain ends). If the opposite is the case and the formation of olefinic end-groups is associated to the catalyst, the concentration of olefinic end-groups should remain steady since diffusion of the catalyst within the polymer is strongly hindered even at elevated temperature. Thus, a polymer sample was heated repeatedly for longer periods of time to ca. 150 °C. No further formation of olefinic end-groups was observed by NMR spectroscopy. This result points to the formation of olefinic end-groups associated to the catalyst. Nonetheless, considering the number of polymer end-groups per catalyst (see section 2.4.2), the relative amount of olefinic end-groups should not exceed the amount of catalyst within the polymer, if diffusion of the catalyst within the polymer above the glass temperature is neglected. Yet, the olefinic end-groups were observed to increase up to 25 % (by NMR). For the sake of completeness, the mechanism of depolymerization⁹⁵ should be mentioned in this respect, since it can alter the end-groups of the polycarbonate. However, this mechanism cannot be evaluated, since the thermal treatment of PCHC (in presence of the catalyst) was not subject of this work. Furthermore, a base-induced rearrangement of CHO, which would yield in an allylic alcohols, needs to be considered.¹⁶¹ The integration of such an allylic alcohol would terminate the growing polymer chain. The base required for such an rearrangement could origin form the catalyst, possibly through hydrolysis or release of the ligand.

To this point the origin of the olefinic groups remains open. However, the relatively high content of olefinic end-groups that have been found in the polymer (see Figure 32), possibly gives some unique opportunities for post-synthetic modifications. The

polymer could, for example, be interconnected by an olefinic polymerization to form comb polymers providing altered material properties. Polymerization through a ROMP mechanism is not possible with cyclohexene moieties, even though oligomers from cyclohexene could be produced.¹⁶² However, if cyclopentene oxide is used as monomer for the CO₂/epoxide copolymerization, ROMP becomes accessible for this type of post-synthetic modification. To explore these options, the scope of epoxides that can be copolymerized with [L^{ProOH}Zn]₂ needs to be investigated further.

For future works and depending on the desired end-groups, it would be recommended to precipitate the polymer with methanol from a solution in DCM to avoid the formation of the olefinic end-groups. ToF-ESI-MS analysis of the PCHC product in a 1:1 mixture

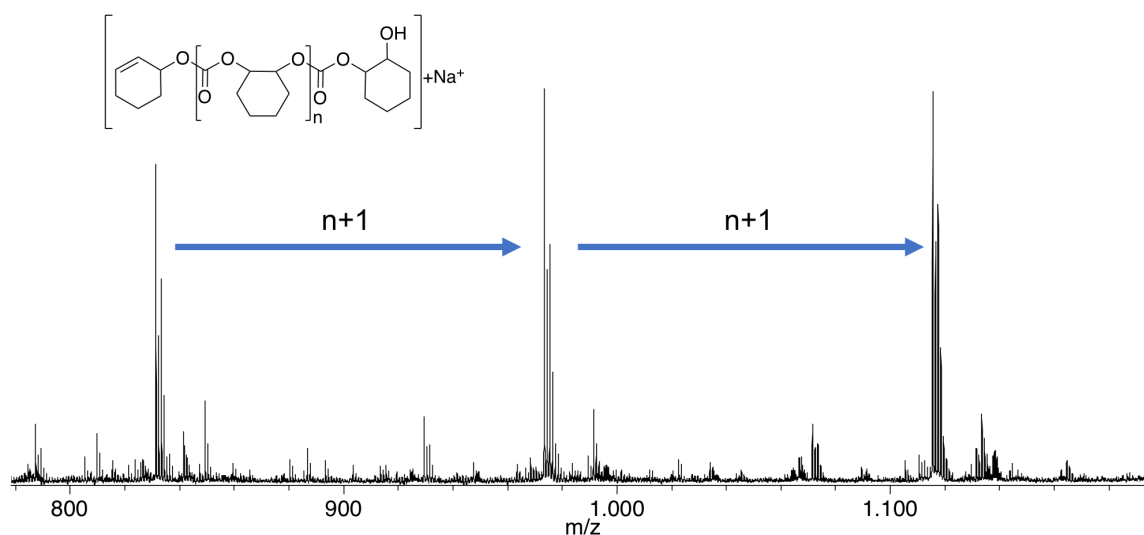


Figure 34: ToF-ESI-MS of the obtained PCHC in a 1:1 mixture of THF/methanol with assignment of the main ion peaks to an olefin and an alcoholate end-group.

of THF/methanol supports the observation that was made by NMR spectroscopy (see Figure 34). The main ion peaks could be assigned to PCHC with one olefinic and one alcohol end-group. For the repeating units with a lower signal intensity in the spectrum shown in Figure 34, no matching end-group could be assigned and thus, a different workup of the polymer was performed and the ToF-ESI-MS measurement was repeated. For this purpose the same batch of polymer was precipitated from a DCM solution with methanol. The obtained high resolution mass spectrum is depicted in Figure 35, allowing the observation of higher charged polycarbonates. The assignment of mono- and di-cationic species (the two left ones in Figure 35) is in good agreement with the calculated m/z values and corresponds to the same end-groups as found in Figure 34. The proposed tri-cationic species, however, does not match well to the

experimentally found m/z values. The suggested species on the right was found to be the closest in its monoisotopic mass value to the experimentally observed mass ion peak.

To obtain further insight, MALDI-MS experiments of the PCHC were performed.

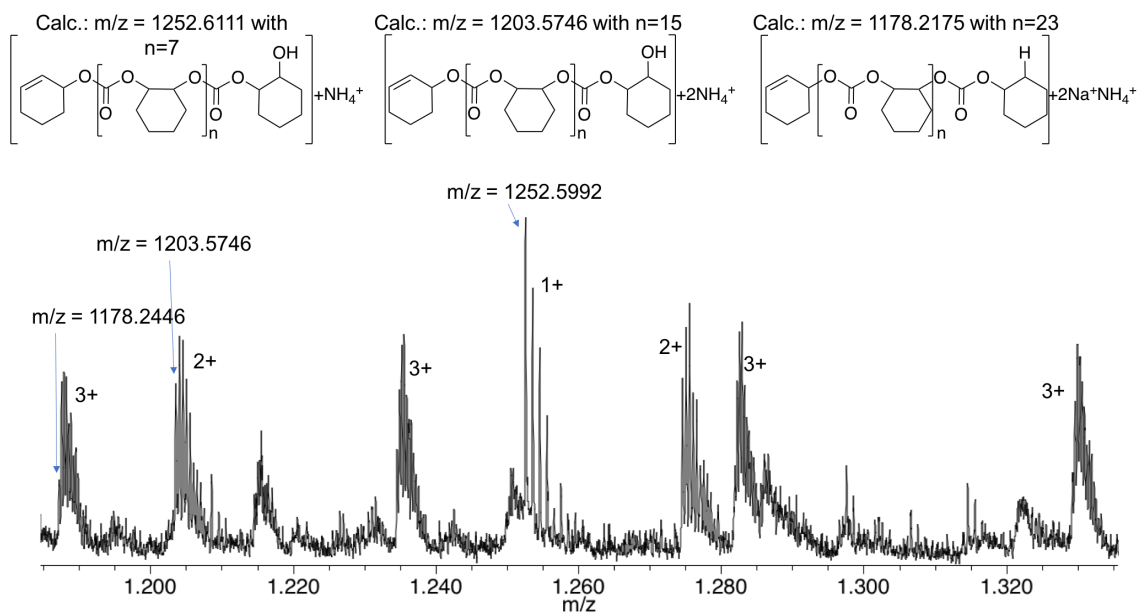


Figure 35: ToF-ESI-MS of the obtained PCHC in a 1:1 mixture of THF/methanol with assignment of the main ion peaks.

The observed pattern of the repeating carbonate units differs from the one observed by ToF-ESI-MS (see Figure 36). Plausible end-groups of the signals are assigned in Figure 36. At this point it should be emphasized that because of the low signal-to-noise ratio and the error margin of the measurement, the assignment is not as certain as for the ToF-ESI-MS measurements. Nevertheless, MALDI-MS at this point seems to be the only mass spectrometric method that allows to obtain further insights regarding the end-groups associated with the initiation mechanism, since different species can be observed.

The pattern of the repeating carbonate units found by MALDI-MS in between different entries of Table 5 does not differ. Neither is the pattern influenced by the amount of water that is present during the polymerization.

Some vague insights into the polymerization mechanism can be drawn from the MALDI-MS experiments. The assigned end-groups for A, B, and E are similar to the ones observed in the ToF-ESI-MS and NMR spectrum (Figure 32). However, the assigned end-groups of species C and D point to a PCHC unit holding the catalyst's ligand as end-group. In Figure 32 (in blue) such an end-group was previously proposed. Yet, the NMR spectrum in Figure 32 and the MALDI-MS alone do not provide sufficient sup-

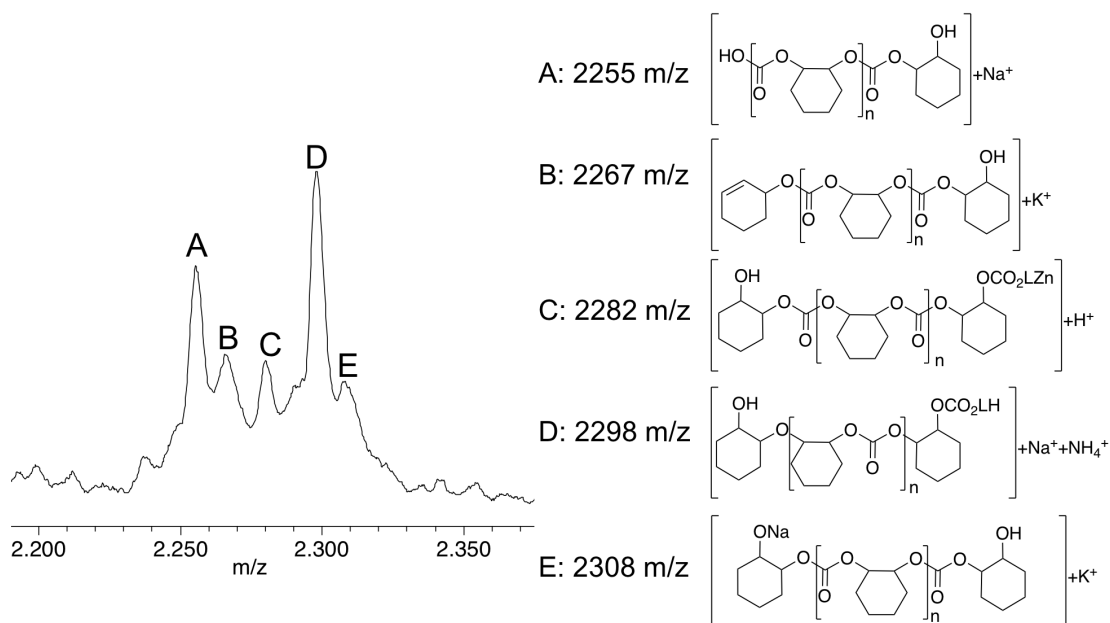


Figure 36: Signal pattern obtained by MALDI-MS (linear-modus) of the PCHC with plausible assignment of the ion peaks. Only with the Linear-Modus of the Autoflex Speed from *Bruker* a signal was observed. In the reflectron-modus no signal was observed, thus no HR-MALDI-MS was obtained.

port for the claim that the ligand is actually incorporated into the polymer, especially since the sample for which the NMR spectrum was recorded had been taken directly from a polymerization reaction without further purification. Thus, the catalyst/ligand must have remained in the sample. To clarify if the ligand actually was incorporated into the PCHC, the polymer was dissolved in DCM and precipitated with methanol. By this, the ligand, which is soluble in this mixture, should be separated from the precipitated polymer. ¹H-NMR measurements of the precipitant should no longer allow the observation of aromatic signals from the ligand. However, the aromatic signals remain observable after repeated precipitation, supporting the assumption that a small portion of the ligand is found as end-group in the obtained PCHC. The involvement of the ligand in the initiation mechanism was also proposed for the structurally similar complex by Nozaki *et al.*^{131,147}

However, taking all these observations into account, especially the apparent initiation dependence on water (Figure 28) and the observed end-groups, allows to derive a hypothesis about the initiating step of this polymerization. Either

- the first epoxide opening occurs through the attack of an external nucleophile/co-catalyst as known to occur for some catalysts^{96,97,153,163}

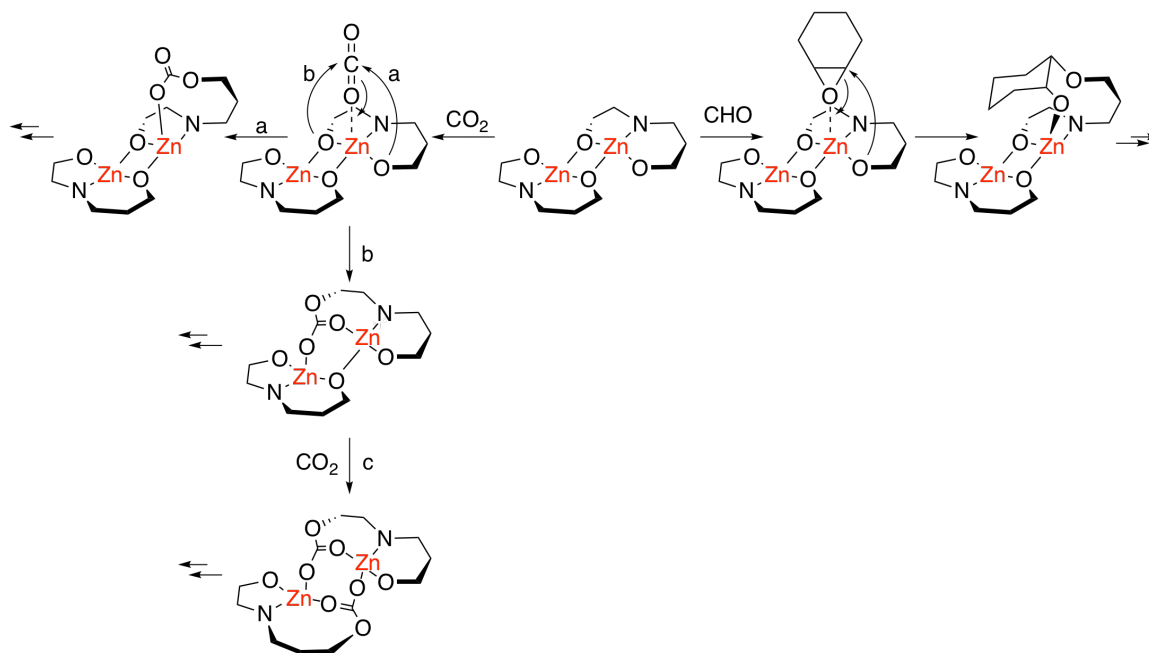
or

- one of the ligand arms initiates the first epoxide opening as alcoholate/carbonato species.^{96,132}

The first case seems unlikely, since no nucleophiles were added to the reaction solution. However, traces of water remaining in the CHO could be involved. Evidence for an initiation associated with water might be the different initiation times that were observed when using hydrophobic or untreated glassware, as displayed in Figure 26. For untreated glassware a higher amount of residual water on its surface can be expected.^{164,165} Nevertheless, if the determined contents of water in the CHO, obtained by a *Karl-Fischer* titration (with membrane), are accurate, then the water amount within the CHO is approximately two orders of magnitude smaller than the amount of catalyst. The residual water within the CO₂ (after drying over P₂O₅), however, was not determined and can therefore not be evaluated. Nonetheless, the bottle of CO₂ gas was used for all experiments within this work, without and with observed initiation phase (see Figure 28). Thus, the first case of an external nucleophile/co-catalyst seems unlikely. Nevertheless, to further test this hypothesis an experiment was performed, during which 1 eq. of chloride ions (as NBu₄Cl in CHO) was injected into a reaction with silanized glassware during the initiation phase.¹²⁸ The Cl⁻, which serves as good nucleophile (in apolar solvents), could open the first epoxide and possibly initiate the polymerization. However, no initiation was observed. For all of the given reasons, the first case of an external nucleophile/co-catalyst is therefore dismissed.

Considering the second case, it is known from literature that acetate, alcoholate or other ligands/co-catalysts may be responsible for the initiation step.^{88,109,129,132} In the polymerization experiments performed herein no nucleophile or co-catalyst was added, nor does the complex coordinate an additional ligand. Consequently, the ligand's side arms need to be considered. From the findings of the end-group analysis (Figure 32 and Figure 36) it is plausible that the ligand is partially present as end-groups, and thus likely involved in the initiation process. One plausible mechanism would be the decoordination and nucleophilic attack of the flexible⁸³ (and longer) propanolate side arm on the first epoxide or CO₂ unit, as depicted in Scheme 11. The first step could either be the opening of a CHO unit, forming another alcoholate species (right pathway), or the activation of CO₂ and formation of a carbonato complex (left pathway). The latter pathway could either form a terminal (a), a mono- μ -carbonato (b) or a di- μ -carbonato complex (c).

To differentiate if the first step is the reaction with CHO or CO₂ the complex [L^{ProOH}Zn]₂ was mixed with either of them separately. For the mixture of the complex with CHO no reaction was observed. However, the addition of CO₂ to a solution of the complex in THF formed a colorless precipitate at 50 °C, pointing to the left reaction pathway of



Scheme 11: Proposed mechanism for the nucleophilic attack of the propanolate side arm on a coordinating CO₂ (left) or CHO (right) to initiate the polymerization. The left pathway is split in two: (a) formation of a non-bridging carbonato complex and (b) the formation of a bridging mono- or di-carbonato complex. The ligand is depicted in a simplistic fashion for clarity. The double arrow refers to the nucleophilic attack of the carbonato moiety onto the first CHO, entering the mechanism in Scheme 3.

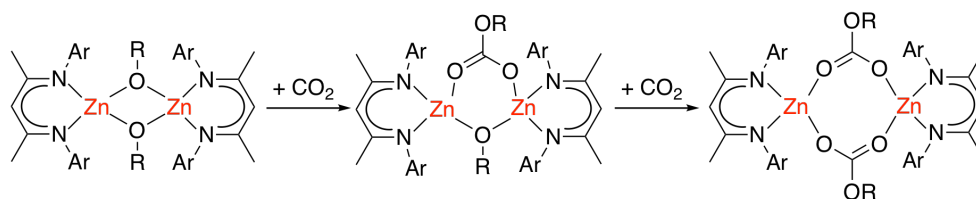
Scheme 11. In literature similar conversions with CO₂ have been observed. Coates *et al.* found that their μ -alcoholate-bridged dizinc complexes form a mono-/di- μ -carbonato-bridged species under CO₂, see Scheme 12.⁸⁶ Furthermore, also for the complex from Williams *et al.* the formation of a dicarbonato species was proposed (not bridging and different coordination motif).⁹⁸

To further analyze the formed complexes, an IR spectrum of the obtained solid was measured and is shown in Figure 37 (bottom).

Additionally, the IR spectrum of the free ligand (top) and the complex [L^{ProOH}Zn]₂ (middle) are shown. The complex, after treatment with CO₂, seems to be intact and still coordinating the ligand. The two bands that are observable in the IR spectrum at 1492 and 1419 cm⁻¹ (assignment was not possible) might be associated to the active carbonate species of under catalytic conditions. A purely inorganic salt can be excluded.

Due to poor solubility of the obtained precipitate in either polar (DMSO-d₆, CD₃OD) or apolar (CDCl₃, THF-d₈, toluene-d₈) standard NMR solvents, NMR experiments gave no conclusive data. This behavior and the sensitivity of similar CO₂-activating compounds has been reported before.¹⁶⁶

2.4 COMPLEX DESIGN OF ONO PINCER TYPE LIGANDS FOR THE COPOLYMERIZATION OF CO₂ AND EPOXIDES



Scheme 12: Proposed insertion by Coates *et al.* of CO₂ into the μ -alkoholate-bridged dizinc β -diiminate complexes forming a mono- or di- μ -carbonato-bridged species, depending on the substituent R.⁸⁶

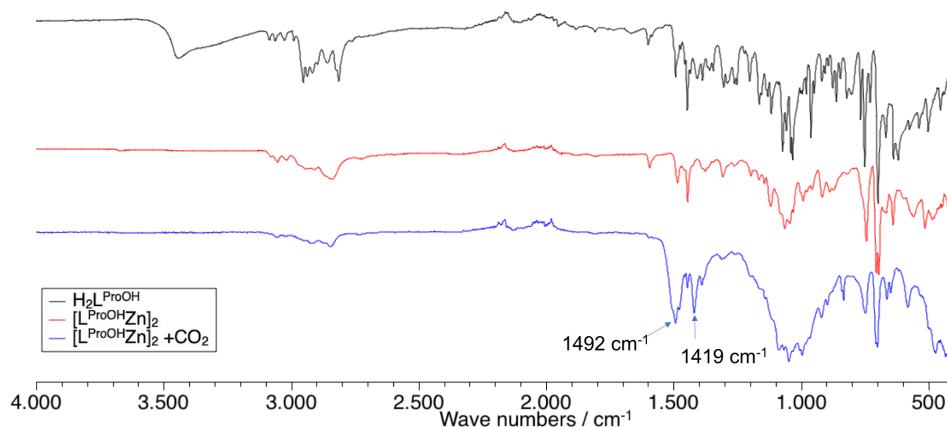


Figure 37: ATR-IR spectrum of the ligand H₂L^{ProOH} (top/black), the complex [L^{ProOH}Zn]₂ (middle/red) and product of the complex [L^{ProOH}Zn]₂ with CO₂ (bottom/blue).

For a successful initiation, the consecutive step onto the second monomer needs to be considered for the left pathway of Scheme 11. Three possible carbonate species are depicted and in the following paragraph their potential of initiating the polymerization, thus the opening of the first CHO, is discussed shortly.

For a terminal carbonate species (path (a)) the nucleophilic attack onto a CHO coordinating to the neighboring zinc would probably be associated with a high energetic barrier due to the rearrangement of the complex for the terminal carbonate to reach the coordinating monomer. However, since this species is still alcoholate-bridged, the Zn–Zn distance is shorter than for the mono- or di- μ -carbonato-bridged species (path (b)). This possibly makes up for the rearrangement energy needed. The proposed mono- and di- μ -carbonato-bridged species formed *via* pathway (b) would show a greater Zn–Zn distance, resulting in a possible increase in energetic barrier. Yet, a carbonato bridge would also grant more flexibility to go through the transition states of the catalytic cycle. To this point no accurate statement can be made regarding the coordination mode of the carbonato species. With high certainty, however, the formation of an *in situ* generated carbonato-zinc species initiates the polymerization by opening the first epoxide. Furthermore, the poor solubility might explain the initiation phase that was observed.

Attempts to crystallize one of the carbonato complexes shown in Scheme 11 (path left) yielded in a few small single crystals, suitable for X-ray diffraction experiments. The molecular structure is shown in Figure 38. The single crystals were observed to crystallize in space group $P1_13$, resulting in an asymmetric unit of its molecular structure (displayed on the right) with a C_3 -axis going through the carbon atoms of the central carbonato ligands (top view in the middle in Figure 38). The top as well as the bottom plane (left depiction) of the molecular structure are composed of three $[L^{\text{ProOH}}\text{Zn}]$ units connected by a central carbonato ligand. The central plane of three Zn holds no additional L^{ProOH} ligand and is, instead, coordinated by the ligand moieties of the top and bottom $[L^{\text{ProOH}}\text{Zn}]$ units and another central carbonato ligand. Selected atom distances found within the molecular structure in Figure 38 are given in Table 8. The corresponding bond angles are given in the appendix. The Zn–O distances of the zinc to the L^{ProOH} ligand in the bridging and non bridging coordination motifs are similar to the ones found within $[L^{\text{ProOH}}\text{Zn}]_2$. The Zn–Zn distances within the molecular structure in Figure 38 are larger in comparison within $[L^{\text{ProOH}}\text{Zn}]_2$ (compare Table 8 with Table 3).

Table 8: Selected atom distances [\AA] within the molecular structure of $[(L^{\text{ProOH}}\text{Zn})_3\text{CO}_3]_2(\text{Zn}_3\text{CO}_3)$ in Figure 38.

Atoms	Atom distance	Atoms	Atom distance
Zn1–O1	1.892(3)	Zn2–N11	2.091(3)
Zn3–O12	1.919(3)	Zn1–N1	2.137(4)
Zn3–O2	1.933(3)	Zn2–O21'	2.306(3)
Zn1–O3	1.942(3)	Zn1–Zn1'	4.834
Zn3–O11''	1.952(3)	Zn2–Zn2'	4.457
Zn1–O2	1.965(3)	Zn3–Zn3'	4.963
Zn2–O13	1.966(3)	Zn1–Zn3	3.421
Zn2–O12	1.969(3)	Zn2–Zn3	3.161
Zn2–O11	2.008(3)	Zn2–Zn3'	3.216
Zn3–O21	2.015(3)		

The formation of the complex $[(L^{\text{ProOH}}\text{Zn})_3\text{CO}_3]_2(\text{Zn}_3\text{CO}_3)$ (Figure 38) can be explained by the balanced equation found in Scheme 13. Water seems to be responsible for its formation. Thus, the $[(L^{\text{ProOH}}\text{Zn})_3\text{CO}_3]_2(\text{Zn}_3\text{CO}_3)$ complex could explain the catalyst's sensitivity towards water under catalytic conditions.



Scheme 13: Reaction scheme leading to the formation of $[(L^{\text{ProOH}}\text{Zn})_3\text{CO}_3]_2(\text{Zn}_3\text{CO}_3)$ depicted in Figure 38.

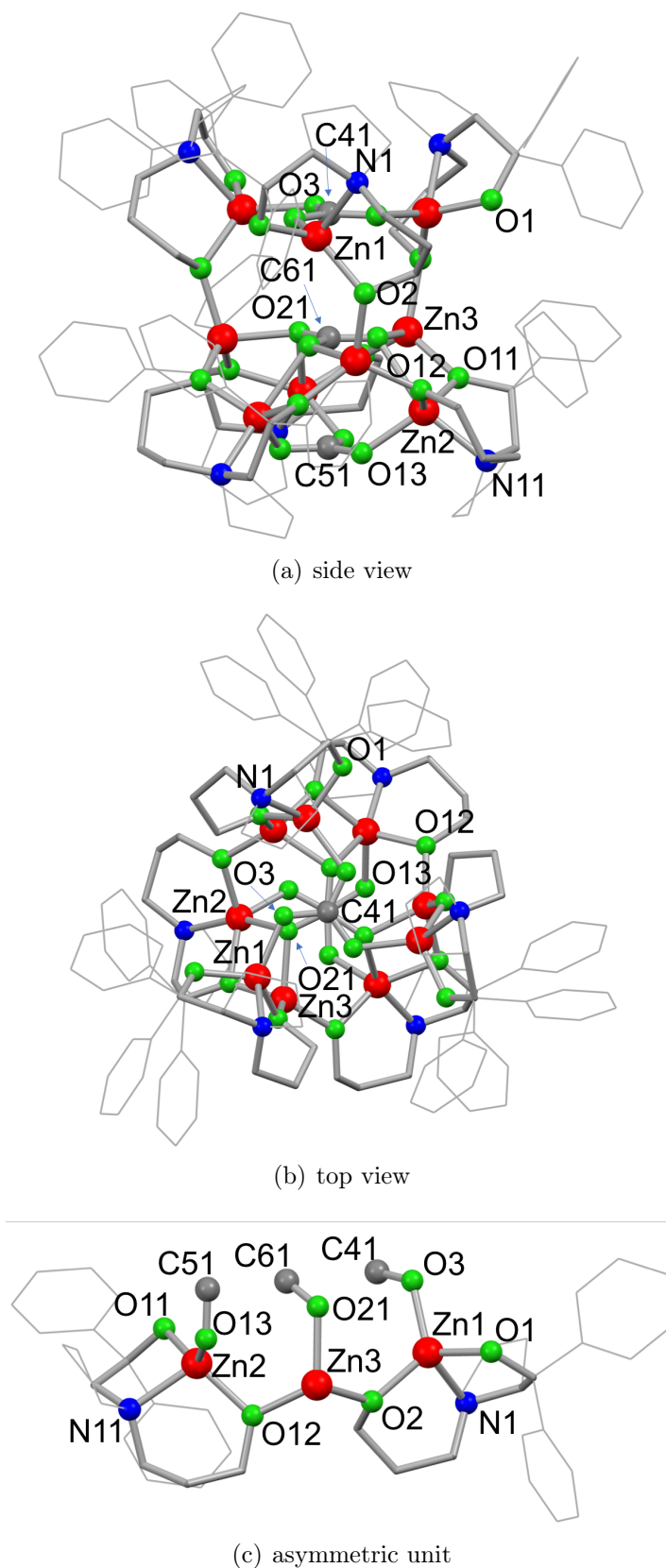


Figure 38: Molecular structure of the reaction product of $[L^{\text{ProOH}}\text{Zn}]_2$ with CO_2 and water in THF. Left: side view with three LZn-units bridged by a CO_3 -unit on the top on and on the bottom, while the plane in the middle is formed by three CO_3 -bridged Zn. Middle: top view, showing the C_3 -axis. Right: asymmetric unit consisting of two LZn-OC(O₂) units and one bridging Zn-OC(O₂) unit. Hydrogen atoms were omitted for clarity.

The discussion of the previous section, which dealt with the trend that higher M_N values and broader polydispersity at lower catalytic activities are observed for the runs with untreated glassware, can be continued. The untreated glassware is likely the reason for a higher water content in the polymerization reactions, forming complex $[\text{L}_3\text{Zn}_3\text{CO}_3-\text{Zn}_3\text{CO}_3-\text{L}_3\text{Zn}_3\text{CO}_3]$. This species or a different carbonato complex might be the active species. The presence of two different active species would explain the broad dispersity for the PCHC. In Figure 39 a GPC analysis of a polymerization with untreated glassware is shown, indicating a bimodal molecular mass distribution. This supports the assumption of two active species present during catalysis when untreated glassware is used. Such bimodal molecular mass distribution is not observed when silanized glassware was applied.

Furthermore, species $[\text{L}_3\text{Zn}_3\text{CO}_3-\text{Zn}_3\text{CO}_3-\text{L}_3\text{Zn}_3\text{CO}_3]$ can explain why the catalyst

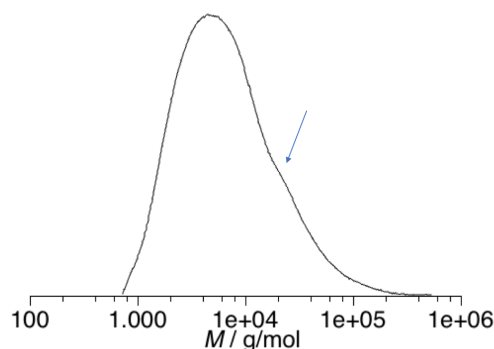
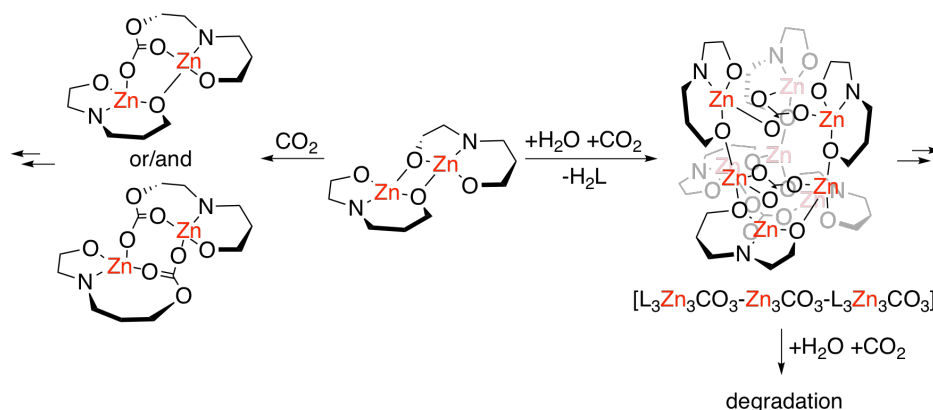


Figure 39: Molecular mass distribution of a PCHC sample of a polymerization that was performed in untreated glassware with a water content of ca. 13.4 ppm, determined by *Karl-Fischer* titration. A shoulder is observed at ca. 2000 g/mol, indicated by the arrow. GPC analysis was performed in THF, calibrated with polystyrene, and toluene was added as internal standard. $M_N = 4.2$ kg/mol.

shows no activity at high water contents (untreated glassware and >30 ppm of water in the CHO). Further addition of water and CO₂ leads to continuous release of free ligand $\text{H}_2\text{L}^{\text{ProOH}}$, and degradation of the catalyst. In Scheme 14 a summary of the proposed catalytic species without (left) and with water (right) is given.

If the assumed initiation mechanism in Scheme 11 (left) is operative, this would imply that $[\text{L}^{\text{ProOH}}\text{Zn}]_2$ forms cyclic PCHC. This topology would be preserved until the first chain-transfer takes place, opening the ring. In this scenario, the first and last incorporated carbonate unit are in close proximity. If back-biting of the polymer chain onto the first carbonate would occur, this cyclic topology would even be preserved, which would be highly interesting. The obtained mass spectra were analyzed, but no such cyclic product was observed. Therefore a back-biting seems not to occur.



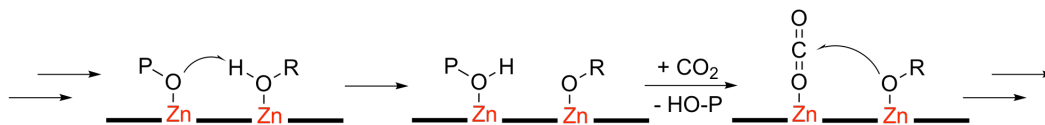
Scheme 14: Summary of the proposed catalytic species without (left) and in the presence of water (right). Right: Proposed reaction scheme leading to the formation of $[L_3Zn_3CO_3-Zn_3CO_3-L_3Zn_3CO_3]$ depicted in Figure 38. Further degradation is depicted. Stoichiometry is not considered in this scheme and the ligand is depicted in a simplistic fashion for clarity.

All in all, it can be said that the end-group analysis allowed to make some assumptions regarding the initiation step of the polymerization. Furthermore, $[L^{ProOH}Zn]_2$ forms a PCHC that features, besides the common hydroxyl end-groups, a relatively high abundance of olefinic end-groups, which may give the opportunity for post-synthetic modification. The obtained knowledge of the catalyst's initiation mechanism might enable the development of an even more active catalyst in future works. It might even direct to the development of a water stable and stereoselective ONO-pincer catalyst.

Chain-transfer of the polymerization reaction.

In 2016, the group of Darensbourg *et al.* published a paper which gave insights into the influence of water in the CO₂/epoxide copolymerization.⁵⁰ They could demonstrate that the presence of water effects chain-transfer, because it first leads to the hydrolysis of the epoxide, forming the corresponding diol, which then is responsible for the chain-transfer during the polymerization reaction (salen-Co system). They observed that during the initial stages all water was consumed for the hydrolysis reaction, before the actual polymerization took place. These conclusions were drawn from observing the IR region at 3000–3800 cm⁻¹. In the polymerization experiments of this work, where *in situ* IR measurements were performed, such observations could not be made, since the applied dip probe only measures in a spectral window of 650–2800 cm⁻¹. Nevertheless, a transfer agent is likely present during the polymerization, since only relatively low M_N values were obtained. From the obtained data it cannot be said if water is directly responsible for the transfer or if cyclohexane-1,2-diol is formed from it, causing the

transfer. In any case, one cyclohexane-1,2-diol would be formed out of one molecule of water, so that the number of chains formed from one catalyst molecule should translate into the amount of water present. The proposed reaction mechanism for a dinuclear system is shown in Scheme 15.



Scheme 15: Proposed mechanism for the chain-transfer reaction. P representing the polycarbonate chain and R = H or cyclohexan-2-yl. The chelating ligand is only schematically depicted.

In order to quantify the chain-transfers during the polymerization, the average number of chains produced by one catalyst molecule were calculated and is given in Table 9, together with the corresponding M_N values and averaged number of carbonate units per chain. The Table refers to the polymerizations found in Table 5 and the values that are average were reactions performed at comparable conditions. The last two entries in Table 9 (averaged entries of (1&2) and (5&6)) refer to polymerizations where non-modified glassware was applied and all others to entries with silanized glassware. Even though only few data points are available, contradicting trends are formed for the reactions with non-modified and silanized glassware, which is developed in the following paragraph.

For the experiments with silanized glassware the number of PCHC chains produced

Table 9: Averaged number of carbonate units per PCHC-chain and number of PCHC-chains produced by one catalyst unit. Averaged entries of (1&2) and (5&6) were performed with non-modified glassware, the others with silanized glassware.

averaged entries*	[CHO]:[cat.]	M_N / kg/mol	# carb. per chain [†]	$n_{\text{chains}}/n_{\text{cat.}}$ [‡]
3 & 4 [⊗]	1008	2.72	19	89
7 & 8 [⊗]	1511	2.44	17	85
9 & 10 [⊗]	2018	1.42	10	80
1 & 2	1014	3.37	24	10
5 & 6	1504	4.18	29	14

*: referring to Table 5. †: averaged number of carbonate units per PCHC-chain. $M_N/M_{\text{carbonate unit}}$ with $M_{\text{carbonate unit}} = 142$ g/mol. ‡: averaged number of PCHC-chains in the samples produced by one catalyst unit. ⊗: the used glassware was treated with TMS-Cl.

by a catalyst seem to increase at higher catalyst loading. This might imply that the catalyst is associated to the transfer reaction. Furthermore, the average molecular

weight of the polymer, correlating with the number of carbonate units per chain, was observed to decrease with the catalyst loading. For the experiments with non-modified glassware these trends seem to be inverted. With higher catalyst loading a smaller number of chains per catalyst and lower M_N values were observed. Furthermore, when comparing the experiments where non-modified glassware was used to the ones with silanized glassware, the supposedly dryer reaction with silanized glassware shows more chain-transfers and lower M_N values than the experiments with non-modified glassware. If the water or the diol are acting as transfer agent, the conditions with a higher water content should result in lower M_N values and a higher number of chains per catalyst.⁵⁰ However, the observed contradictory trends cannot be explained on the basis.

Concluding remarks

The catalyst $[L^{\text{ProOH}}\text{Zn}]_2$ can easily be synthesized in very high yields and is able to copolymerize CO₂ and CHO chemoselectively (>98 % in PCHC), forming an isotactic-enriched PCHC ($P_r \cong 35\%$). Moreover, it is able to do so with high activity even at pressures as low as 1 bar in CO₂. It could be shown that the complex in solution is likely of dinuclear nature even under polymerization conditions, thus demonstrating that auto-assembly is a suitable approach for ONO-pincer type zinc complexes for the CO₂/epoxide copolymerization. Finally, the initiation temperature, a degradation product in the presence of water, the polymer end-groups, and strong indicators for the initiation mechanism, occurring *via* CO₂ insertion as the first step, could be collected.

2.4.3. Metal variations of $[L^{\text{ProOH}}\text{Zn}]_2$ and their activity: Ni, Co and Mg complexes

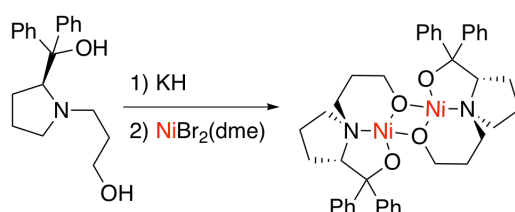
In this section, derivatives and complexes similar to the obtained complex $[L^{\text{ProOH}}\text{Zn}]_2$, their synthesis and their catalytic activity are presented. However, the compound characteristics and catalytic activities have not been investigated as detailed as for $[L^{\text{ProOH}}\text{Zn}]_2$. Even though some of the compounds that are presented here showed activity for the CO₂/epoxide copolymerization, none of them reached the activities of $[L^{\text{ProOH}}\text{Zn}]_2$. To pursue the purpose of this work, viz. to find new catalysts with high activity, some of the complexes have not been fully characterized, when their catalytic activity was low or the product properties were insufficient. However, it should be kept in mind that the ONO-pincer type catalysts are sensitive towards water. The specific water sensitivity has not been investigated for the derivatives in this section, which could have led to false negatives in cases of extreme water sensitivity. Initial testing at elevated pressures, which was used to decide if a further investigation of catalytic activity should be pursued, was performed at similar water contents (± 15 ppm) for

all catalysts including [L^{ProOH}Zn]₂. It can be assumed that, as far as it is justifiable, acceptable conditions were tested. Nevertheless, it needs to be pointed out that the positive effect of using silanized glassware on the activity was found out after the testings of some of the potential catalysts had been performed.

However, from the gather experience it appears, that at higher CO₂ pressures the catalysts are less inhibited by water. Thus, it seems reasonable to further assume that the results from the initial testings of the catalysts are valid and allow a qualitative statement of their activity.

Synthesis and application of the [L^{ProOH}Ni]₂ complex

In Scheme 16 the synthetic route to the nickel complex [L^{ProOH}Ni]₂ is depicted. Two



Scheme 16: Synthesis of [L^{ProOH}Ni]₂ performed in THF. A stoichiometry is not displayed in this Scheme.

equivalents of KH were used for deprotonation, forming the corresponding dialcoholate. The complex was formed by addition (dme)NiBr₂, driven by the salt elimination of KBr. The complex [L^{ProOH}Ni]₂ has a deep purple color and was crystallized by layering of a THF solution with pentanes. The obtained single crystals were suited for X-ray diffraction and the obtained molecular structure is depicted in Figure 40.

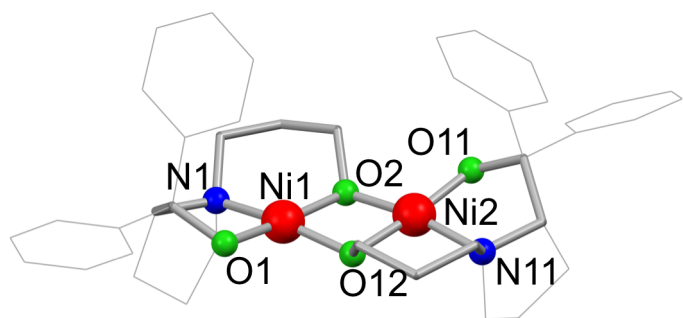


Figure 40: Molecular structure of [L^{ProOH}Ni]₂. Hydrogen atoms omitted for clarity.

[L^{ProOH}Ni]₂ was found to crystallize in the *P*2₁ space group. In fact, it showed in the solid state the same configuration as found by the DFT calculations for the *C*₂ symmetric species of [L^{ProOH}Zn]₂. This is under the premise that nickel prefers a square

planar coordination environment. Nevertheless, in the solid state, the geometry of the nickel ions is slightly distorted (11.7° torsion angle), allowing the application of the nomenclature that was applied in section 2.4.1 for the DFT calculations. Thus, [L^{ProOH}Ni]₂ shows a 2O-*cis-RR-RR* configuration. In Table 10 selected atom distances within the molecular structure of Figure 40 are given. The corresponding bond angles can be found in the appendix. The Ni – Ni distance measures 2.83 Å, which is shorter than the distances found in [L^{ProOH}Zn]₂ (range of 2.911 – 3.184 Å, depending on the bridging mode).

Table 10: Selected atom distances [Å] within the molecular structure displayed in Figure 40 of [L^{ProOH}Ni]₂.

Atoms	Distances	Atoms	Distances
Ni1–O1	1.838(2)	Ni2–O12	1.876(2)
Ni1–O2	1.878(2)	Ni2–O2	1.878(2)
Ni1–O12	1.890(2)	Ni2–N11	1.923(3)
Ni1–N1	1.927(2)	Ni1–Ni2	2.8302(5)
Ni2–O11	1.830(2)		

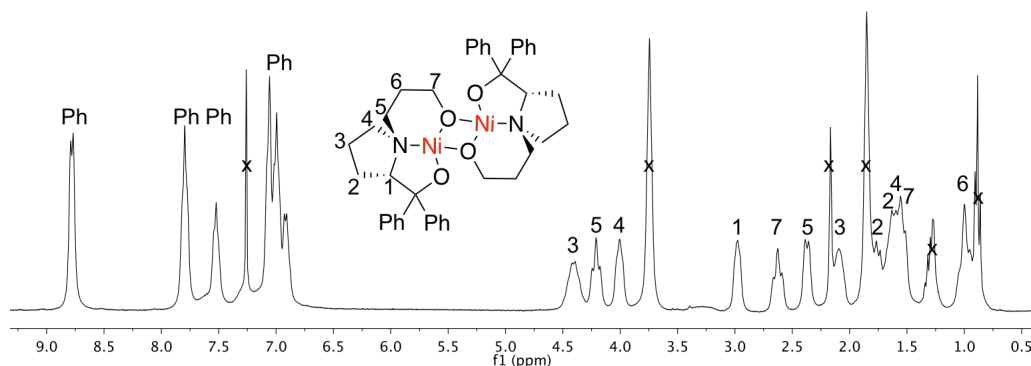


Figure 41: ¹H-NMR spectrum of crystalline material of [L^{ProOH}Ni]₂ in CDCl₃. Assignment of the signals was done using 2D-NMR experiments.

Crystalline material of [L^{ProOH}Ni]₂ was dissolved in CDCl₃ and 1D- and 2D-NMR experiments were performed to analyze the complex in solution. The ¹H- and ¹³C-NMR spectra are depicted in Figure 41 and Figure 42, respectively. The number of signals in both spectra point towards the persistence of the C₂ symmetry even in solution (two signals in the range of 147–154 ppm in Figure 42). Furthermore, there is even evidence that the complex is quite rigid in solution. The strong low field shift of signal 3 in Figure 41, which originates from one of the aliphatic protons, points to its proximity to the nickel atom, even on the NMR time scale. The indicated interaction

is visualized within the molecular structure in Figure 43.

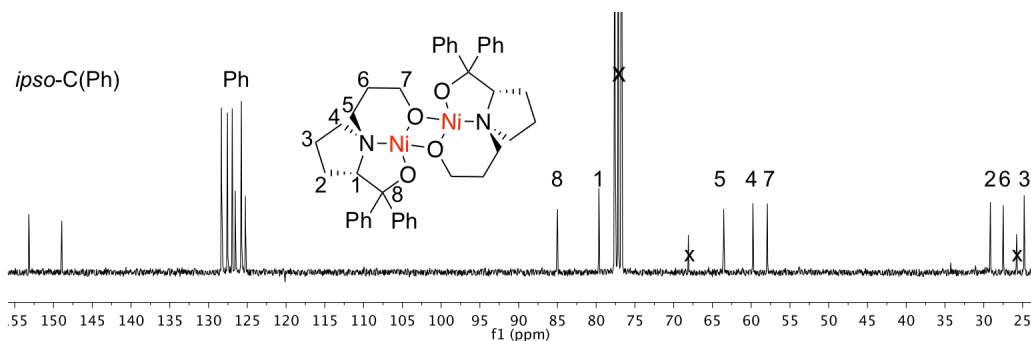


Figure 42: ¹³C-NMR spectrum of crystalline material of [L^{ProOH}Ni]₂ in CDCl₃. Assignment of the signals was done using 2D-NMR experiments.

The signals in the ¹H-NMR spectrum are relatively broad and, in fact, the compound becomes paramagnetic when left to stand in solution, likely due to the coordination of an additional ligand moiety (e.g. water, since the NMR spectrum was measured in non-dried solvents).

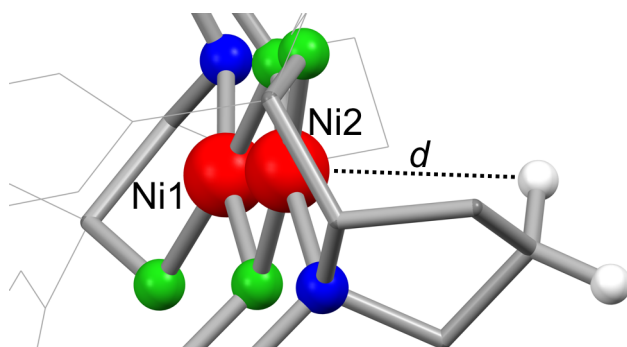


Figure 43: Side view of the molecular structure of [L^{ProOH}Ni]₂ illustrating the proximity of the hydrogen atom (3 in Figure 41) and Ni2 of $d(\text{Ni-H}) = 2.949 \text{ \AA}$. Most hydrogen atoms were omitted for clarity.

The MALDI-MS experiment in a DCTB A 4-5 matrix showed the molecular ion peak at $735.6 m/z$ corresponding to the $[\text{L}_2\text{Ni}_2+\text{H}]^+$ species.

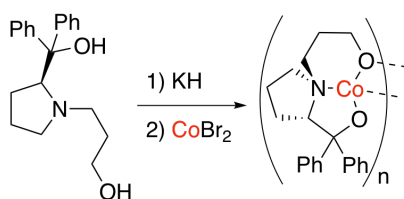
It could be shown that [L^{ProOH}Ni]₂ was isolated successfully and thus, it was applied for the copolymerization experiments. Despite applying crystalline material at 50 bar of CO₂ pressure and 80 °C, [L^{ProOH}Ni]₂ showed no activity for the CO₂/CHO copolymerization, not even forming the homopolymer. A plausible reason is that the corresponding carbonato species cannot form. This is possibly due to the favored coordination number of four for Ni(II) ions in a square planar geometry. Therefore resulting in the

rigidity of the complex and conceivably being linked to the complexes inability insert CO₂ into the Ni–O bond.

All in all, even though [L^{ProOH}Ni]₂ is not active for the desired catalysis, the isolation of [L^{ProOH}Ni]₂ further supports the coordination motif that was found by the DFT calculation for the corresponding zinc complex.

Synthesis and application of the [L^{ProOH}Co]_n complex

In Scheme 17 the synthetic route to the cobalt complex [L^{ProOH}Co]₂ is depicted. How-

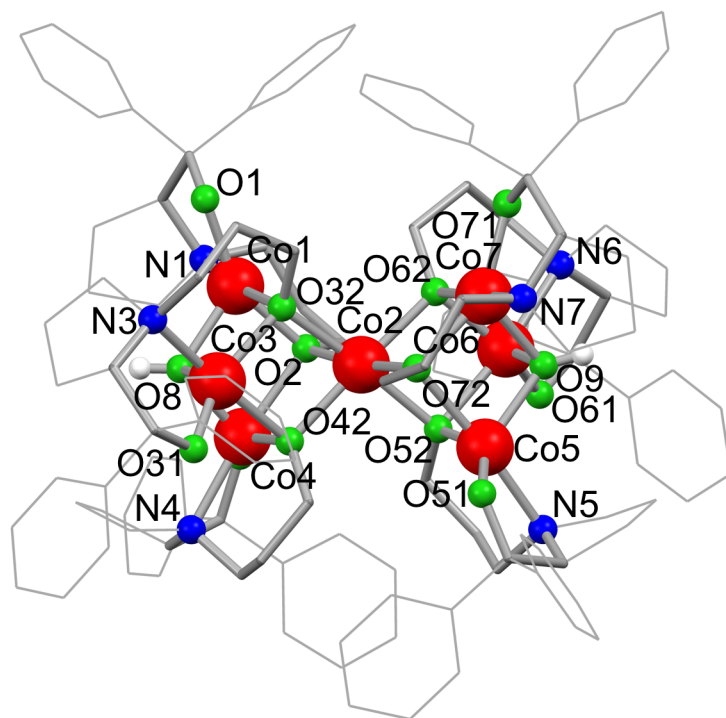


Scheme 17: Synthesis of [L^{ProOH}Co]_n performed in THF. The corresponding stoichiometry is not displayed in this Scheme.

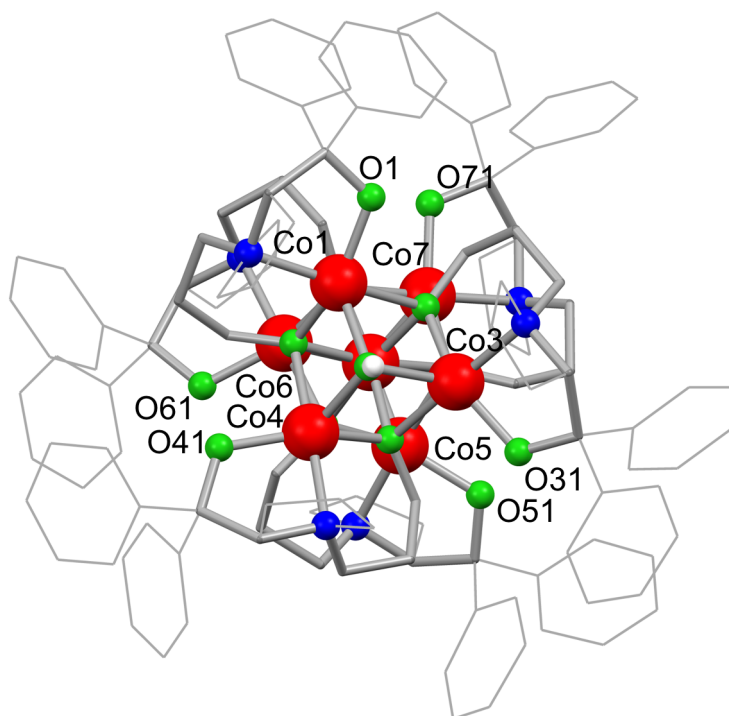
ever, since Co(II) has a tendency to higher coordination numbers than Ni(II) and Zn(II), the tridentate ligand can be expected to form higher aggregates with Co(II) than it was observed for the zinc and nickel complexes. Nevertheless, the synthetic route chosen is equivalent to that of the previously discussed nickel complex. Thus, the deprotonation was done by two equivalents KH forming the corresponding dialcoholate compound, and the complexation by addition of CoBr₂.

From a batch of the complex that had been exposed to air it was possible to obtain crystals and x-ray diffraction revealed the molecular structure which is displayed in Figure 44. It consists of two cubes with the Co and O atoms positioned at its corners, and one Co atom forming one corner of both cubes, connecting them. The corner opposite to this Co atom is formed by an O atom from a hydroxo moiety. From the structure, the expected higher coordination number of the cobalt complex can be observed. However, the formation of the depicted structure likely involved the presence of water, as it can be concluded from the end-capped hydroxo groups. Selected bond lengths within the molecular structure displayed in Figure 44 of [(HO(L^{ProOH}₃Co₃)₂Co)] are given in Table 11. The associated bond angles can be found in the appendix.

It was not possible to obtain single crystals from material under water-free conditions, nor was an assignable signal found in MS experiments. This leaves open the question of the aggregation and structure of [L^{ProOH}Co]_n under water-free conditions. However,



(a) side view



(b) top view

Figure 44: Obtained molecular structure of $[(\text{HO}(\text{L}^{\text{ProOH}}_3\text{Co}_3)_2\text{Co})]$, from a batch which was exposed to air. Hydrogen atoms were omitted for clarity.

Table 11: Selected bond lengths [Å] within the molecular structure displayed in Figure 44 of [(HO(L^{ProOH}₃Co₃)₂Co)].

Atoms	Bond lengths	Atoms	Bond lengths
Co4–O41	1.900(5)	Co2–O72	2.104(5)
Co5–O51	1.907(5)	Co2–O2	2.114(5)
Co6–O61	1.911(5)	Co2–O42	2.119(5)
Co7–O71	1.914(5)	Co2–O52	2.119(5)
Co3–O31	1.917(5)	Co5–N5	2.123(6)
Co1–O1	1.918(5)	Co2–O62	2.133(5)
Co5–O52	1.997(5)	Co1–N1	2.134(6)
Co7–O72	2.002(5)	Co2–O32	2.136(5)
Co1–O2	2.003(5)	Co3–N3	2.139(6)
Co4–O42	2.014(5)	Co4–N4	2.142(6)
Co3–O32	2.023(5)	Co6–N6	2.145(6)
Co6–O62	2.023(5)	Co7–N7	2.151(6)
Co1–O8	2.059(5)	Co7–O62	2.174(5)
Co7–O9	2.059(5)	Co3–O42	2.175(5)
Co6–O9	2.060(5)	Co4–O2	2.197(5)
Co3–O8	2.072(5)	Co1–O32	2.198(5)
Co4–O8	2.072(5)	Co6–O52	2.207(5)
Co5–O9	2.086(5)	Co5–O72	2.223(5)

inspired by the obtained crystal structure shown in Figure 44, a structure was modeled of how the complex might look like in water-free conditions. It is depicted in Figure 45. For this example, a tetranuclear cubic-shaped molecular structure with the propanolyl moiety as bridging units within the cube was assumed, as found in Figure 44. The bridging propanolyl moiety allows the sterically more demanding phenyl substituent moieties to be in a terminal position. However, the suggested cubic coordination motif, combined with the sterically demanding groups facing outwards as suggested in Figure 45, might render the insertion of CO₂ into the Co–O-bonds difficult.

Testing of the obtained powder material for the CO₂/CHO copolymerization with a CHO to complex ratio of 500:1 at 50 bar pressure and 80 °C showed poor activity with a TOF of 0.8 h⁻¹ and a TON of 15. The GPC analysis of the obtained polymer showed an average molecular mass of $M_N = 3.431 \times 10^4$ g/mol with three maxima (see Appendix A.3.2 in Figure 131). The obtained M_N values are not impressive, considering the applied pressures¹¹⁶ and, furthermore, three maxima point to three different species that are active.

All in all, the complex [L^{ProOH}Co]_n was isolated, even though its exact nuclearity

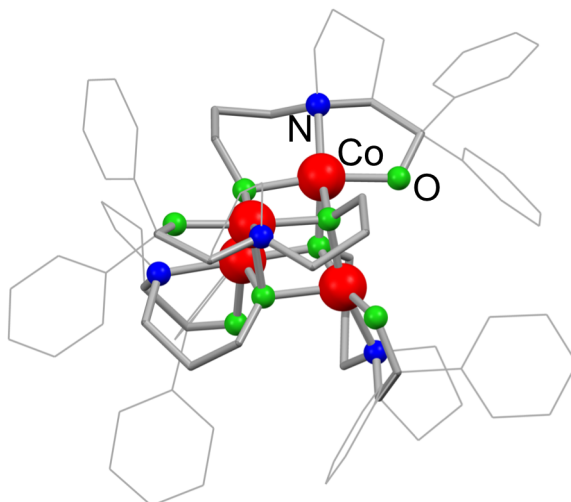


Figure 45: Possible structure of $[\text{L}^{\text{ProOH}}\text{Co}]_n$, with $n = 4$. The structure was modeled following the structure given in Figure 44. Geometry optimization was done applying UFF. Hydrogen atoms were omitted for clarity.

remains open to investigation, and a crystal structure of the adduct with water was obtained. The complex shows activity for the CO₂/epoxide polymerization. However, the activity of the complex is so low, even at 50 bar pressure, that a further characterization was not pursued.

Synthesis and application of the $[\text{L}^{\text{ProOH}}\text{Mg}]_2$ complex

For testing if the corresponding magnesium complex with L^{ProOH} is active for the CO₂/CHO copolymerization, the complex was synthesized similar to the synthesis of the zinc species described in section 2.4.1, but instead of ZnEt₂ the magnesium precursor MgBu₂ was used. After removal of all volatile compounds, the obtained colorless solid was applied for the catalysis but no activity could be observed. Characterization of the compound was therefore not further pursued.

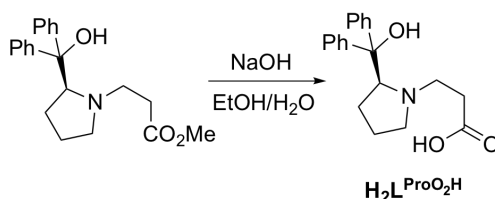
However, a reason might have been the use of MgBu₂ as metal source for the complexation. In an oral exchange with Charlotte Williams it was pointed out to me that copolymerization attempts, where MgBu₂ was used as a metal source, also in the working group of Williams *et al.*, were not successful. It might be an impurity in this precursor that inhibits the catalysis. For that reason in future works it is recommended to use a different magnesium source instead.¹³⁰

2.4.4. Closely-related ligand variations of L^{ProOH}, their synthesis, complexation and initial testing for copolymerization

In this section, alterations of the ligand scaffold are presented, discussed and applied for the copolymerization after complexation with a zinc precursor.

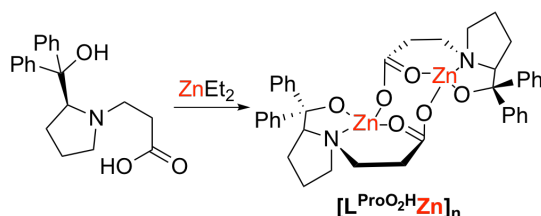
Synthesis and application of L^{ProO₂H}

The first modification was the saponification of the methyl ester, which was used



Scheme 18: Synthesis of [L^{ProO₂H}Zn]_n performed in THF. The corresponding stoichiometry is not displayed in this Scheme.

for the isolation of H₂L^{ProOH}, in order to obtain the carboxylic acid. The idea behind this modification is to mimic an acetate ligand which is commonly found in precatalysts for the CO₂/epoxide copolymerization.⁷⁰ The reaction is displayed in Scheme 18 and the obtained ¹H- and ¹³C-NMR spectra are shown in Figure 46. The proton signal of the carboxylic acid was not observed in the ¹H-NMR spectrum, but in the ¹³C-NMR spectrum the corresponding carbon atom of this moiety can be found. All signals of the NMR spectra could be assigned using 2D-NMR experiments. Together with the measured mass spectrum, showing the molecular ion peak, it can be concluded that the saponification yielded the target compound after *aquous* workup.



Scheme 19: Synthetic path and proposed structure for complex [L^{ProO₂H}Zn]_n, with n = 2. The structure is derived from Scheme 12. The associated literature⁸⁶ in the discussion can be found in section 2.4.2.

In Scheme 19 the complexation reaction is illustrated with a proposed structure, based on literature^{86,90} and the findings for [L^{ProOH}Zn]₂ (section 2.4.2). The ¹³C-NMR mea-

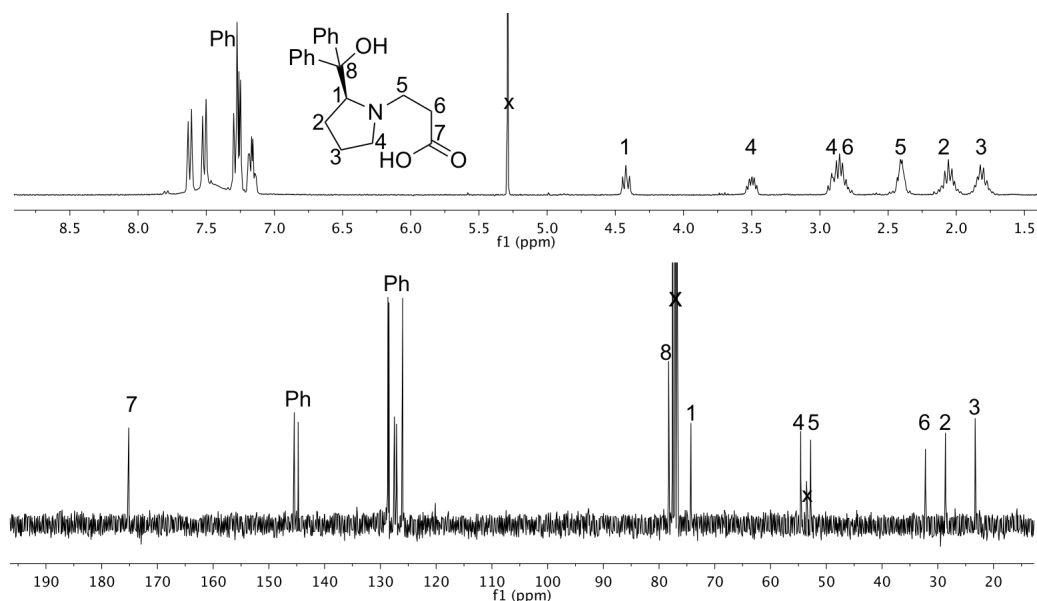


Figure 46: ¹H- (top) and ¹³C-NMR spectrum (bottom) of H₂L^{ProO₂H} in CDCl₃ with assignment of the signals.

measurements of the complex in CDCl₃ (Figure 47) showed at least 10 signals in the region of the *ipso*-carbon of the phenyl groups (corresponding to ca. 5 [LZn] environments), but only 4 main signals from the carboxylate (corresponding to 4 [LZn] environments). The full spectrum can be found in Appendix A.2.2 in Figure 115. In Figure 47 also the ¹³C-NMR spectrum of [L^{ProOH}Zn]₂ is given for a better comparison. Performed LIFDI-MS measurements gave no result.

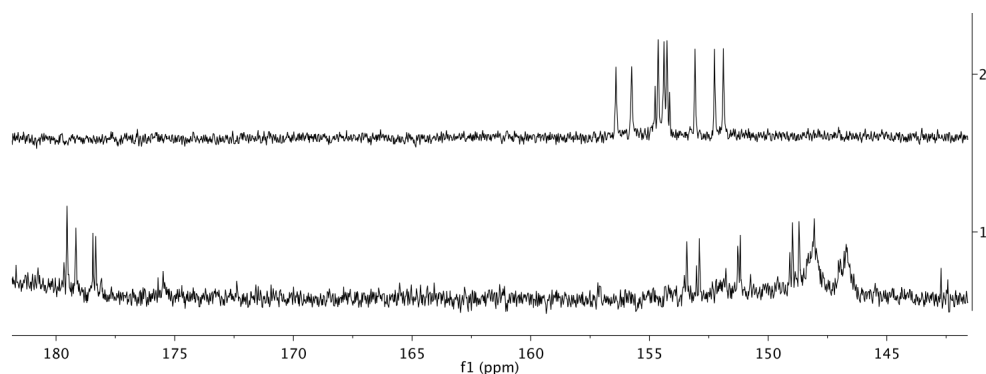


Figure 47: Section of the ¹³C-NMR spectrum of [L^{ProO₂H}Zn]₂ (bottom) and [L^{ProOH}Zn]₂ (top) in CDCl₃.

The bridging of the two zinc centers was assumed to occur by the carboxylate moieties which are unsubstituted, therefore decrease sterical pressure by placing the phenyl substituent alcoholate moieties at the terminal positions. From the proposed structure in Scheme 19 several different configurations are conceivable. For a better illustration two

stereoisomers are depicted in Figure 48 as 3D-models. These two isomers were modeled, by taking the results of the DFT calculations under account for [L^{ProOH}Zn]₂ (Figure 21). From the DFT calculation the C₂-symmetric *cis*-RR-configuration seems to be energetically unfavorable over the C₁-symmetric *trans*-RR-configuration. However, for a conclusive picture all configurations would need to be calculated and compared.

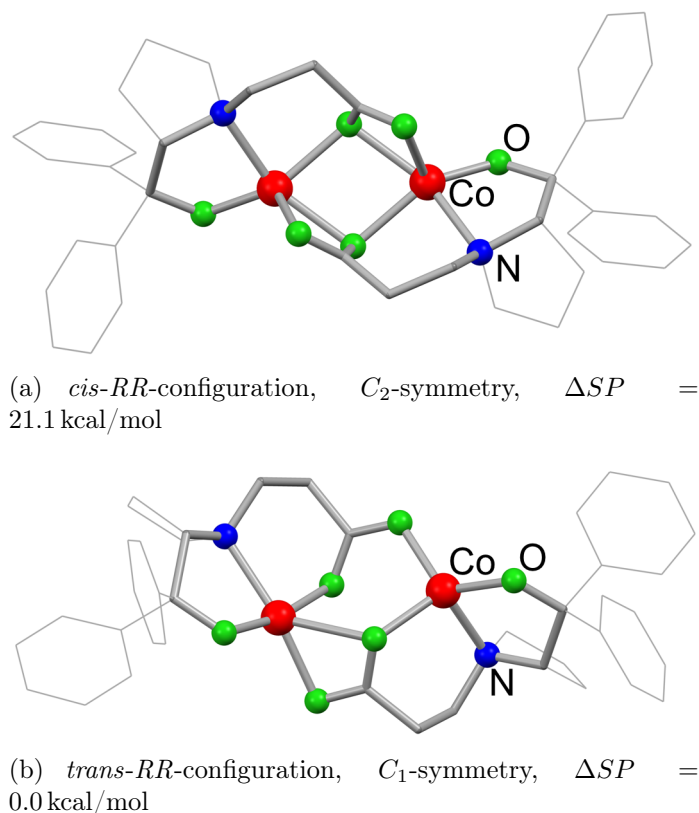


Figure 48: Possible structure of [L^{ProO₂H}Zn]_n, with n = 2. The structure was modeled following the results of the DFT calculations for [L^{ProOH}Zn]₂ in Figure 21. The model was designed and optimized applying UFF (Avogadro 1.1.1) and the spin-restricted Kohn-Sham program with the generalized gradient approximation (GGA) with the functional BP86, the base set def2-tzvp, the auxiliary basis sets def2-tzvp/j and the RI approximation were used for the geometry optimization performed by Orca Version 3.0.3. Hydrogen atoms were omitted for clarity.

The complex was tested for its capability for the CO₂/CHO copolymerization as part of a screening experiment applying a Carousel 12 reactor (multi-reactor, allowing to run 12 reactions parallel). Four reactions were performed with this complex with a [CHO]:[cat] ratio of 1000:1 at 80 °C and various reaction times. After the reaction time, the polymerizations were quenched by exposure to air and removal of CHO. [L^{ProO₂H}Zn]_n was found to be active even at 1 bar of CO₂, as it was found for [L^{ProOH}Zn]₂. The TON after 8 h of reaction time reached 20, corresponding to a TOF of 2.4 h⁻¹. The product

formation against time is given in Figure 49. Short oligomers of the desired cyclohexene carbonate were observed by ¹H-NMR spectroscopy. It was estimated that an average of ca. 3–4 units were connected during the catalysis, thus no further determination of M_N by GPC or determination of tacticity was pursued. The polymerization was performed in untreated glassware, although the previously discussed catalyst [L^{ProOH}Zn]₂ showed, as a reference experiment (under the same conditions, in a different vial of the multi-reactor), a TON of 131 (after 5 h) and a TOF of 26 h⁻¹. Thus, roughly 1/6 of the activity of [L^{ProOH}Zn]₂ was observed for [L^{ProO₂H}Zn]_n in the initial testing. As a consequence, the investigation of [L^{ProOH}Zn]₂ was pursued more thoroughly. Nevertheless, if the proposed structure for [L^{ProO₂H}Zn]_n in Figure 48 is accurate, the initial step could differ from the one observed for [L^{ProOH}Zn]₂ (first CO₂ insertion). The opening of a CHO unit could occur first, since it holds a carboxylate moiety. For future studies, a comparison of the different initiation mechanisms of [L^{ProOH}Zn]₂ and [L^{ProO₂H}Zn]_n could be interesting.

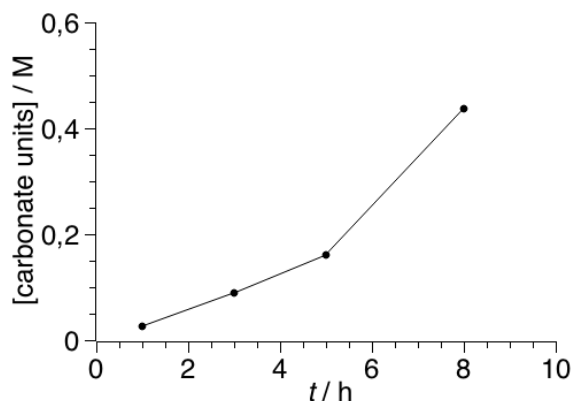


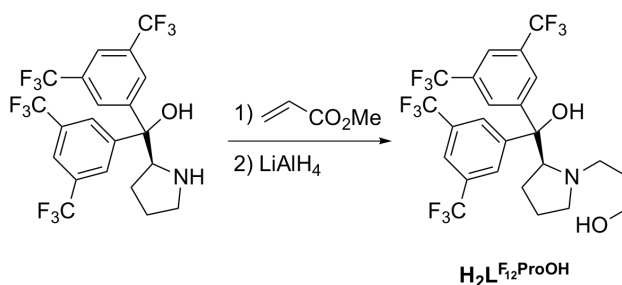
Figure 49: PCHC formation over a reaction time of 8 h applying [L^{ProO₂H}Zn]₂. The copolymerization of CHO and CO₂ (1 bar) was performed at 80°C. [carbonate units] correlates to [1-[CHO]]. Each point represents a reaction vial from the multi-reactor. Each was quenched by removal of CHO at the corresponding time. [carbonate units] was corrected for the content of catalyst and is under the assumption of 100 % selectivity for carbonate.

All in all, a closely-related ligand variation of L^{ProOH} was isolated, characterized, and used for complexation of zinc(II). The complex was found to be active for the CO₂/epoxide copolymerization. Even though the structure of the complex was not determined experimentally, a suggestion of possible structures could be made. The altered ligand scaffold might allow a possible contrast to the initiation mechanism of [L^{ProOH}Zn]₂, since the carboxylate moiety could first react with an epoxide monomer

to initiate the polymerization.

Synthesis and application of L^{F₁₂ProOH}

In this section, the effect of altering the electron-donating properties of the ligand L^{ProOH} by introducing -CF₃ groups is studied. Similar alterations have proved to be beneficial for catalytic activity in catalyst systems known from literature.^{111,167,168} The synthetic route that was followed to isolate the ligand H₂L^{F₁₂ProOH} is similar to the one for the isolation of H₂L^{ProOH}, except starting from the commercially available tetrakis(trifluoromethyl) substituted precursor (see Scheme 20). Furthermore, the formation of the aza-Michael coupled product required an extended time of heating, due to the reduced nucleophilicity.



Scheme 20: Synthetic path for the isolation of H₂L^{F₁₂ProOH}.

In Figure 50 the obtained ¹H- (top) and ¹³C-NMR spectrum (bottom) of H₂L^{F₁₂ProOH} are displayed. In the ¹⁹F-NMR spectrum one signal at δ = -62.9 ppm was observed.

After treating H₂L^{F₁₂ProOH} with ZnEt₂, the obtained complex was applied for CO₂/CHO copolymerization experiments. However, only the homopolymer poly(cyclohexene oxide) (PCO) was obtained. Thus, the investigation of this complex was stopped.

Synthesis and application of L^{ProOHMe}

After the modification of the phenyl moiety by introducing electron-withdrawing groups was not successful, it was attempted to alter the unsubstituted propanolyl moiety by introducing an electron-donating methyl group. For that purpose the synthetic route to H₂L^{ProOH} (Scheme 7) was altered by replacing the methyl acrylate by but-3-en-2-one (see Scheme 21).

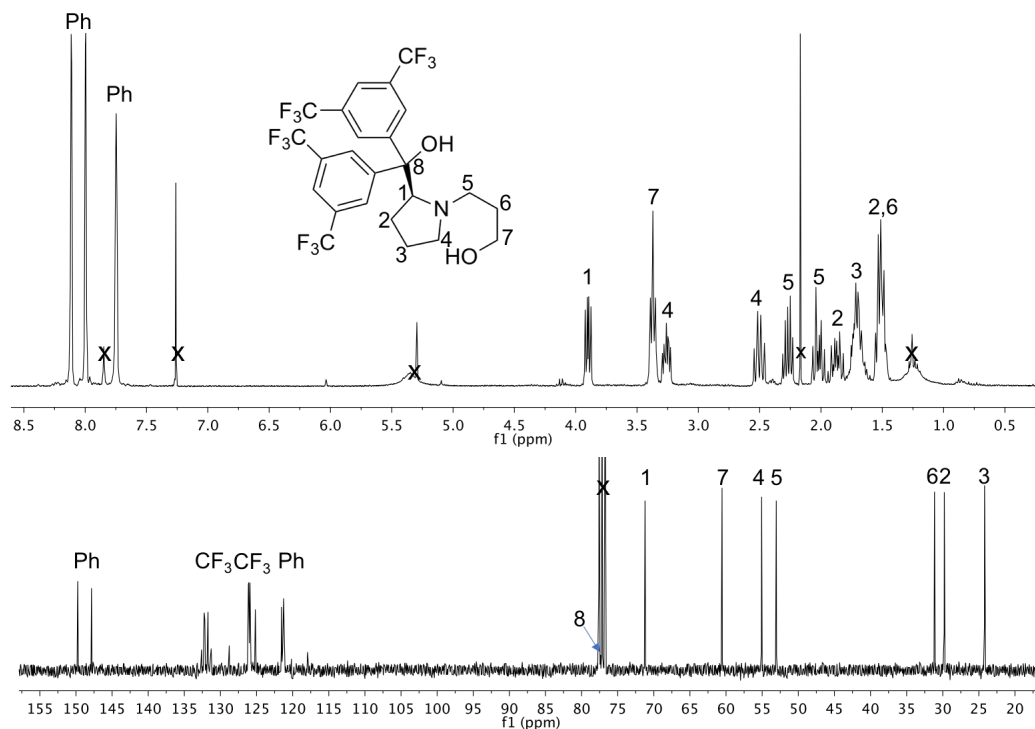
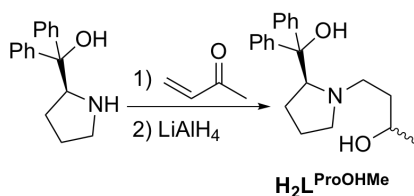


Figure 50: ¹H- (top) and ¹³C-NMR spectrum (bottom) of H₂L^{F12}ProOH in CDCl₃ with assignment of the signals.



Scheme 21: Synthetic path for the isolation of H₂L^{Pro}OHMe.

By this synthetic route a new chiral center was created and thus, two stereoisomers of the compound formed. Separation of the isomers was not successful by column chromatography. In Figure 51 the obtained ¹H-NMR spectrum of the diastereomeric mixture is given. The presence of two diastereomers made the assignment of some of the NMR signals challenging, due to very similar chemical shifts. The assigned signals for the protons 2, 3, 5 and 6 (in Figure 51) is therefore not certain. However, from the two doublets at 0.95 and 0.93 ppm a ratio 1.7:1 for the diastereomers could be determined.

After coordinating the ligand with Et₂Zn, as previously described, the obtained complex was tested under 1 bar CO₂ and 80 °C for its applicability for the copolymerization with CHO. However, only traces of the desired carbonate were observed.

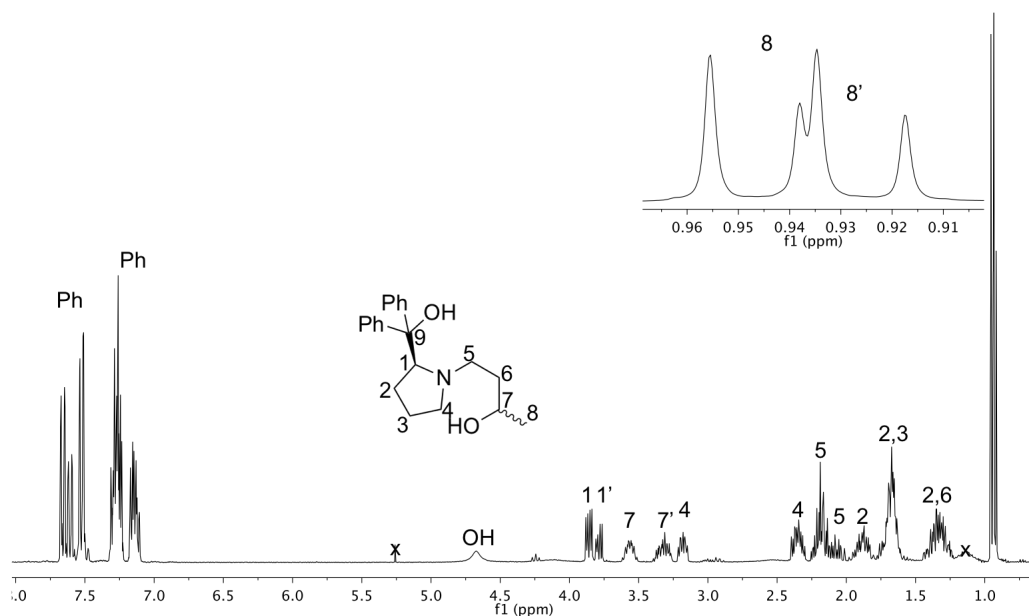


Figure 51: ¹H-NMR spectrum of H₂L^{ProOHMe} in CDCl₃ with assignment of the signals. Assignments for the protons 2, 3, 5 and 6 are not certain due to signal overlay of the isomers.

Ligand variation for future works

In this subsection some ligand variations will be suggested that could be of interest for

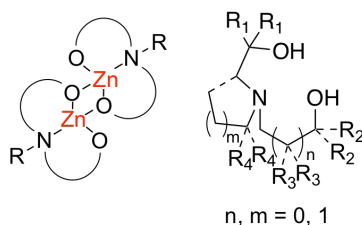


Figure 52: General ONO-type complex design and a generalized ligand design. Possible substituents could be: R = alkyl (has to be long enough for reasons of solubility); R₁ = Ph, aryl, alkyl, CF₃; R₂ = Ph, aryl (involving R₃), alkyl, CF₃; R₃ = olefin (involving R₂), aryl, alkyl; R₄ = aryl, alkyl, CF₃; dashed bond = opened or closed, m = 0, 1, 2, 3 etc.

future works towards the discovery of new ONO-type catalysts for the CO₂/epoxide copolymerization. The generalized ligand design and a general coordination motif are depicted in Figure 52. The given variations are very general, representing only the basic idea for optimizing the catalyst. In Figure 53 specific derivatives are provided, with a suggested synthetic route to obtain them.

Furthermore, the propanolyl side arm could be altered by using different aza-Michael acceptors¹⁴², as depicted in Scheme 22. This was already indicated in Figure 53, but beyond this, the pathway allows the modification of the substituents R and R'.^{169,170}

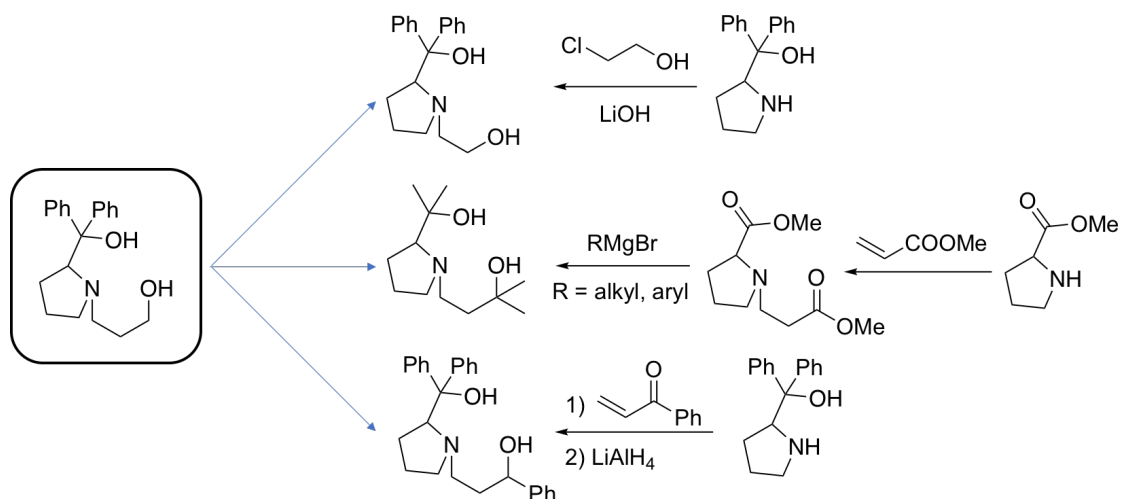
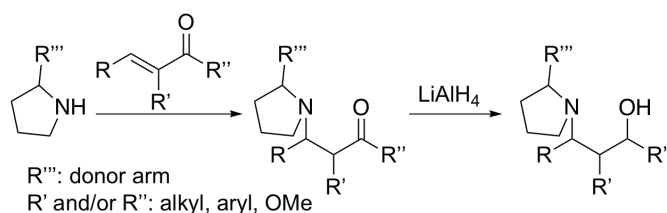


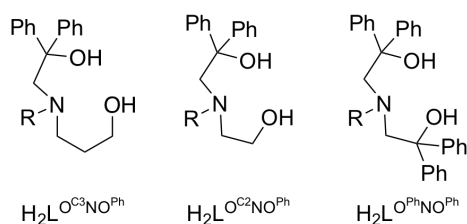
Figure 53: Specific derivatives of the ligand with a suggested synthetic route to obtain them.
R = Me.

However, the formed isomers from the reduction would need to be separated or a stereoselective reduction performed.



Scheme 22: Possible synthetic path for altering the propanolyl moiety of the ONO-pincer type ligands.

Going one step further, there are many more proline (and piperidine) derivatives commercially available, that allow the easy modification of the pyrrolidine moiety on the 2-, 3- and 4-position, by starting with the corresponding derivative.

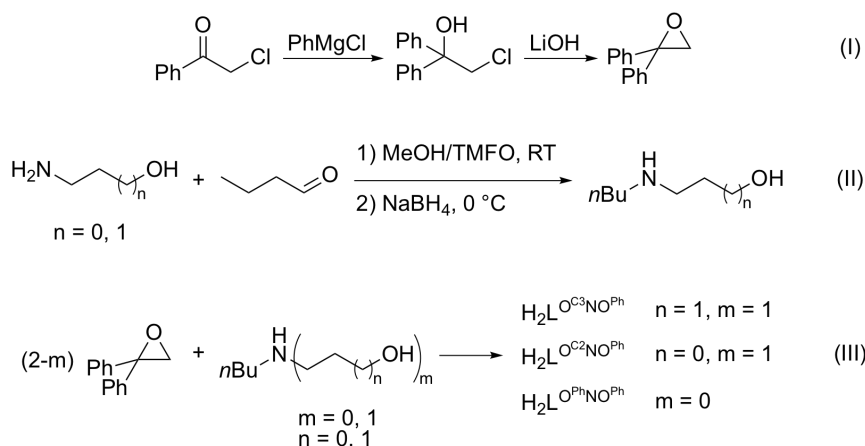


Scheme 23: ONO-pincer ligands $H_2L^{O^{C3}NO^{Ph}}$, $H_2L^{O^{C2}NO^{Ph}}$ and $H_2L^{O^{Ph}NO^{Ph}}$. R = *n*Bu

For mechanistic investigations or for optimizing the catalyst's activity exclusively, the

stereocenter can be neglected. By *opening* the pyrrolidine ring (dashed bond in Figure 52) a new range of synthetically easily accessible ligands can be obtained. This was, in fact, the approach pursued at the end of this work and the ligands H₂L^{OC³NO^{Ph}}, H₂L^{OC²NO^{Ph}} and H₂L^{O^{Ph}NO^{Ph}} were synthesized (see Scheme 23). Due to time restrictions only the route to the ligands could be explored, but their application was not investigated. Scheme 24 shows the synthetic route with the substituent R chosen to be *n*-butyl, due to its low price. Important is that the alkyl chain is long enough to ensure solubility of the resulting complex in CHO (R = ethyl will not suffice).

The products of reactions (I) and (II) in Scheme 24 are commercially available, although their price is rather high. These synthetic route allows an easy and fast protocol for isolating the target compounds, which can be run in >50 g batches. The route *via* the 2,2-diphenyloxirane was chosen since the direct reaction of 2-chloro-1,1-diphenylethan-1-ol with the amine gave several side products. The reaction (III) was performed without solvent and yet takes weeks for a high yielding product formation. The formation of H₂L^{OC²NO^{Ph}} was the fastest and cleanest, while H₂L^{OC³NO^{Ph}} had formed ca. 5 % of a side product, and H₂L^{O^{Ph}NO^{Ph}} was not completed (ca. 52 %) even after 17 days of reaction time (at increasing temperatures). The latter showed after 5 days at 120 °C a more pronounced formation of side products than the other two ligands.



Scheme 24: Synthetic route to obtain the ONO-pincer ligands H₂L^{OC³NO^{Ph}}, H₂L^{OC²NO^{Ph}} and H₂L^{O^{Ph}NO^{Ph}}. 171–174

The ligands were characterized by NMR spectroscopy and the ¹H-NMR spectra of H₂L^{OC³NO^{Ph}} and H₂L^{OC²NO^{Ph}} are depicted in Figure 54 and Figure 55, respectively. The spectrum of H₂L^{O^{Ph}NO^{Ph}} is not depicted since the reaction was not complete (ca. 52 %) yet. However, the product signals were assigned and can be found in the experimental section (section 6.2.11).

The purity of the ligands H₂L^{OC³NO^{Ph}}, H₂L^{OC²NO^{Ph}} and H₂L^{O^{Ph}NO^{Ph}} is not yet satisfying for a complexation reaction and subsequent catalytic application, especially for the

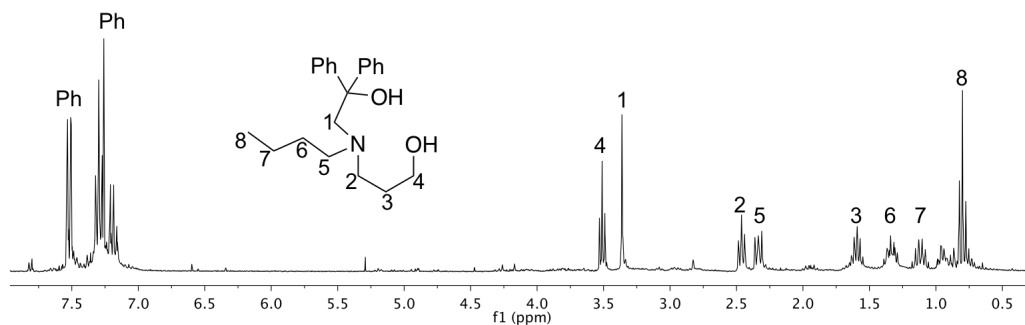


Figure 54: $^1\text{H-NMR}$ spectrum of $\text{H}_2\text{L}^{\text{OC}^3\text{NO}^{\text{Ph}}}$ in CDCl_3 with assignment of the signals.

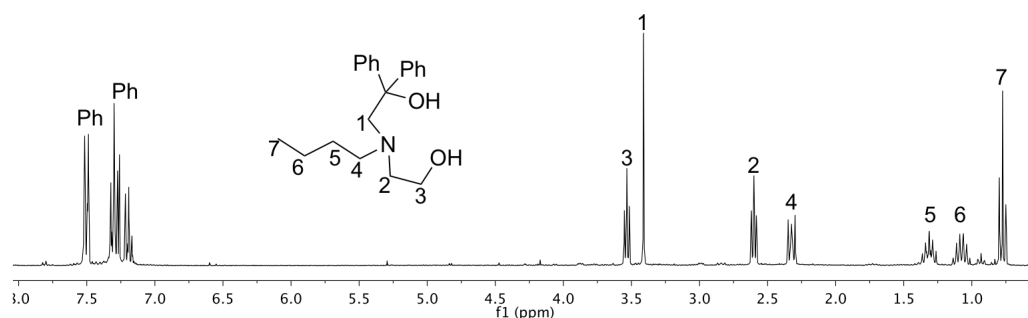
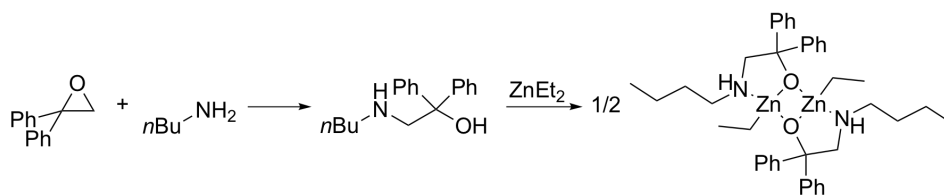


Figure 55: $^1\text{H-NMR}$ spectrum of $\text{H}_2\text{L}^{\text{OC}^2\text{NO}^{\text{Ph}}}$ in CDCl_3 with assignment of the signals.

latter. It is recommended to further purify the ligand systems in future works, e.g. by distillation on a high vacuum line. Furthermore, it should be noted that in the reaction (III) to yield $\text{H}_2\text{L}^{\text{O}^{\text{Ph}}\text{NO}^{\text{Ph}}}$ the single converted intermediate $\text{HL}^{\text{O}^{\text{Ph}}\text{NH}^{\text{H}}}$ can be obtained cleanly after 7 day of stirring at 60°C . It was even possible to form a complex of this intermediate with Et_2Zn (see Scheme 25).



Scheme 25: Synthetic route to obtain the ONO-pincer complex $[\text{L}^{\text{O}^{\text{Ph}}\text{NH}^{\text{H}}}\text{ZnEt}]_2$ shown in Figure 56.

Single crystals of the complex could be obtained from layering a solution of the complex with hexanes, which were suited for X-ray diffraction experiments. The obtained molecular structure can be found in Figure 56 and selected atom distances are given in Table 12. The Zn–Zn distance was determined to be 2.967 \AA , with is larger than in complex $[\text{L}^{\text{ProOH}}\text{Zn}]_2$.

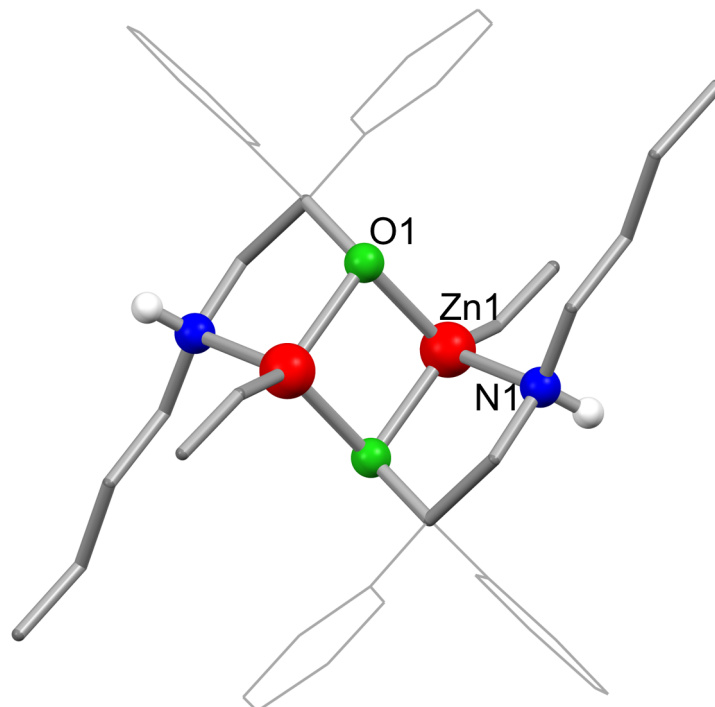


Figure 56: Obtained molecular structure of $[L^{O^{PhNH}}ZnEt]_2$. Most hydrogen atoms were omitted for clarity.

Table 12: Selected atom distances [\AA] (sorted) of $[L^{O^{PhNH}}ZnEt]_2$ (see Figure 56). The corresponding bond angles can be found in the Appendix.

Atoms	Distance
Zn1–O1	2.0307(11)
Zn1–O1'	2.0591(11)
Zn1–N1'	2.1355(14)
Zn1–Zn1'	2.9673(4)

This intermediate could potentially be used for further modifications of ONO-pincer ligands. Beyond this, further potential ligands for future investigations are depicted in Figure 57.

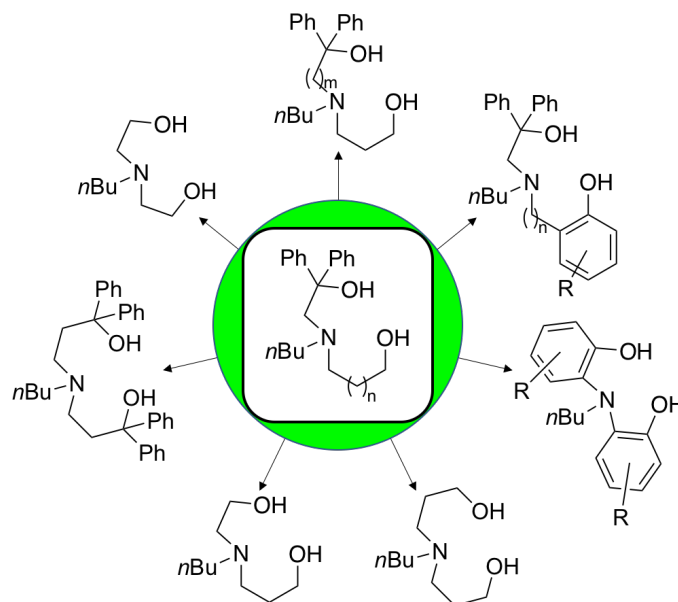
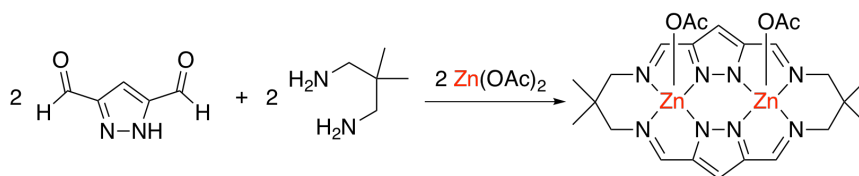


Figure 57: Possible derivatives of the open ONO-pincer ligand. $n = 0, 1$; $m = 1, 2$.

2.5. Synthesis and application of macrocyclic pyrazole-based complexes for the CO₂/epoxide copolymerization

In this section, a possible replacement of the phenolate moiety of the Williams catalyst¹¹⁸ by a pyrazolyl moiety is explored (see complex **6** in Figure 7). This would increase the Zn–Zn distance and might prove beneficial for the catalyst’s activity. Furthermore, the catalyst of the Williams group showed a good tolerance to water, in comparison to the tested ONO-pincer complexes described in section 2.4.2.

2.5.1. Synthesis and characterization of [L^{CPI}(Zn-OAc)₂]



Scheme 26: Synthesis of [L^{CPI}(Zn-OAc)₂] performed in THF.¹⁷⁵

The given synthetic strategy by Williams *et al.* was adapted in the attempt to form the Schiff base product. However, this strategy was not successful and therefore, the

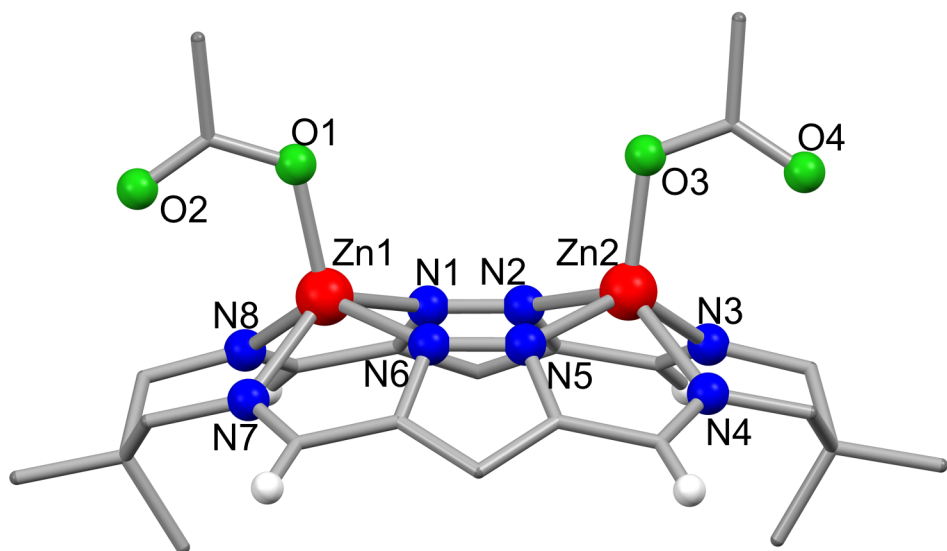
synthetic route established by the group of Brooker *et al.* for a similar copper complex was used to prepare and isolate the Cyclic-Pyrazole-Imine (CPI) complex [L^{CPI}(Zn-OAc)₂] (see Scheme 26).¹⁷⁵ To form the macrocyclic ligand, a metal-template synthesis has to be used, else a polymeric product is obtained. The group of Williams *et al.* protonated the ligand to close the macrocycle, which was not successful with this ligand holding a pyrazole moiety.¹¹⁸

The crystal structure of the target compound [L^{CPI}(Zn-OAc)₂] was obtained. The molecular structure within the crystal is displayed in Figure 58 and selected atom distances are given in Table 13.

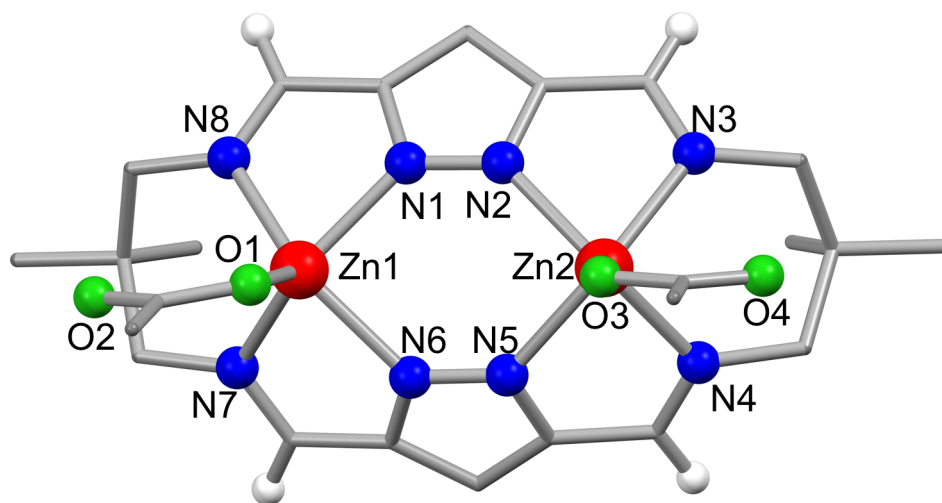
Table 13: Selected atom distances [Å] (sorted) of [L^{CPI}(Zn-OAc)₂] (see Figure 58). The corresponding bond angles can be found in the Appendix.

Atoms	Distance	Atoms	Distance
Zn1–O1	1.9344(18)	Zn2–N5	2.1078(19)
Zn2–O3	1.9434(17)	Zn2–N4	2.1108(19)
Zn1–N1	2.0708(19)	Zn1–N6	2.1237(19)
Zn2–N2	2.096(2)	Zn1–N8	2.140(2)
Zn1–N7	2.1054(19)	Zn2–N3	2.147(2)

The [L^{CPI}(Zn-OAc)₂] complex was found to crystallize in the space group $P2_1/n$. The zinc atoms are located above the plane formed by the four nitrogen atoms of each ligand pocket. The two planes that are formed by the four nitrogen atoms of one ligand pocket meet at an angle of ca. 34°. Therefore, the complex forms a bowl shape which might be maintained in solution. The Zn–Zn distance in the molecular structure is $d = 4.223$ Å. The ¹H- and ¹³C-NMR spectra with assignment of the signals for the obtained complex are shown in Figure 60 and Figure 59, respectively. The bowl shape of the complex, which was found within the crystal structure, is in agreement with the recorded NMR spectra. However, a different coordination motif of the complex would also explain the observed NMR spectra. In this motif the zinc ions are located on opposite sides of the ligand plane, each coordinating one acetate ligand, and forming an inversion center in the middle of the complex. NMR spectroscopy does not allow to differentiate between these two coordination motifs. Therefore, either could be present in solution, even though the preservation of the coordination motive found in Figure 58 is considered more likely. The NOESY-NMR spectrum (see Figure 61) provides indicators of a rigid nature of the complex. The missing NOE signal in the marked circle A in comparison to B as well as the missing NOE signal in D in comparison to C (Figure 61) allow the assumption that the complex does not interconvert between coordination motives in solution at 301 K.



(a) side view



(b) top view

Figure 58: Obtained molecular structure of $[L^{CPI}(Zn-OAc)_2]$. Most hydrogen atoms were omitted for clarity.

2.5 SYNTHESIS AND APPLICATION OF MACROCYCLIC PYRAZOLE-BASED COMPLEXES FOR THE CO₂/EPOXIDE COPOLYMERIZATION

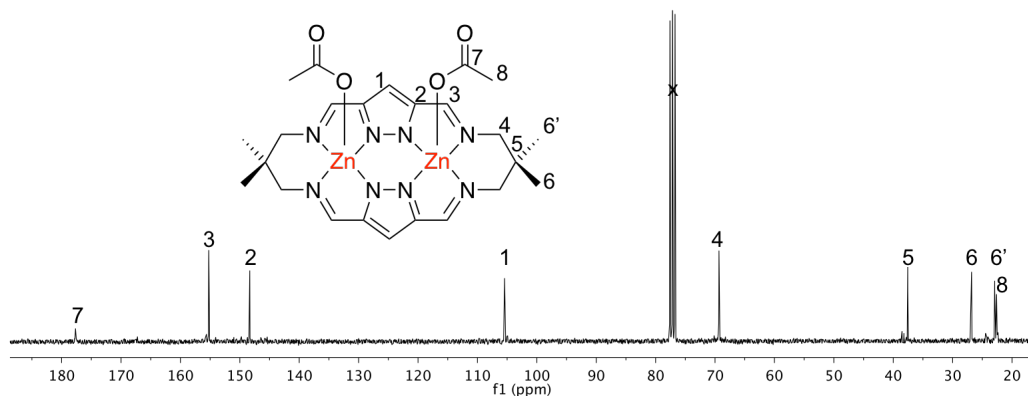


Figure 59: ¹³C-NMR spectrum of [L^{CPI}(Zn-OAc)₂] in CDCl₃. Assignment of the signals was done using 2D-NMR spectroscopy.

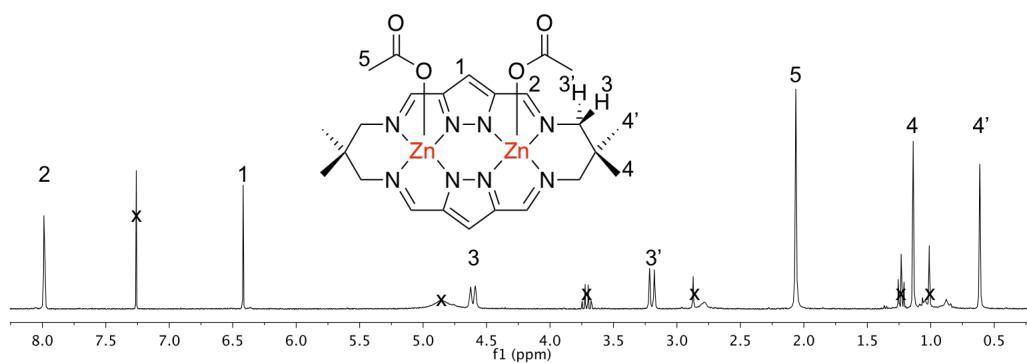


Figure 60: ¹H-NMR spectrum of [L^{CPI}(Zn-OAc)₂] in CDCl₃. Assignment of the signals was done using 2D-NMR spectroscopy.

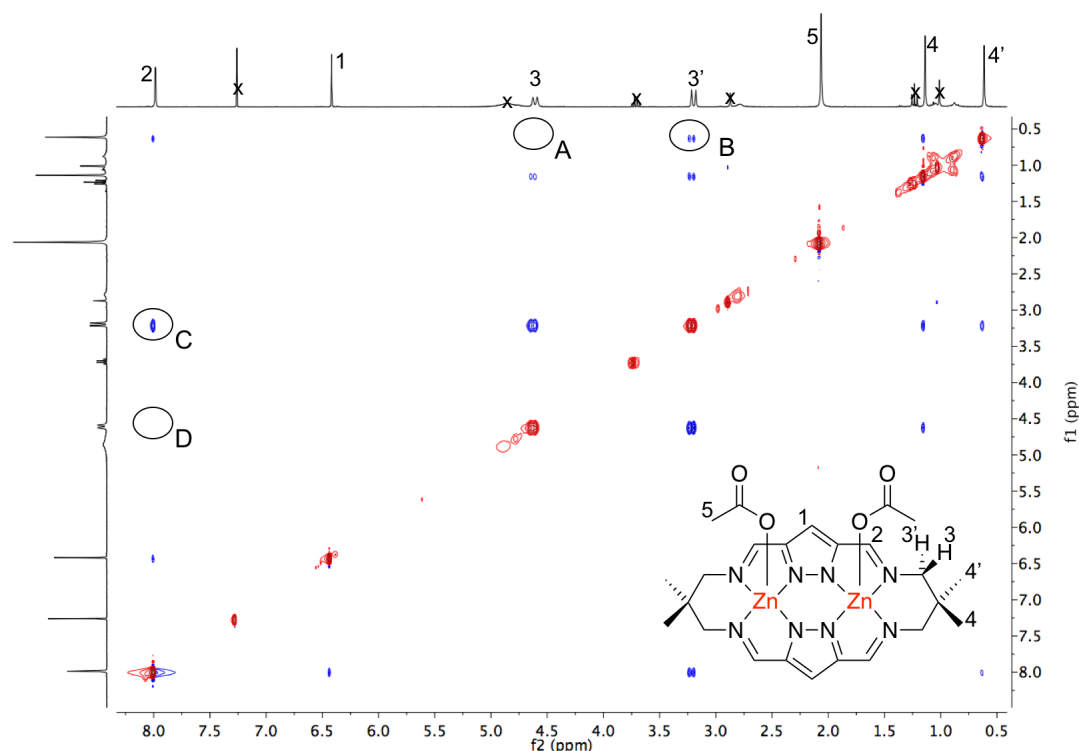
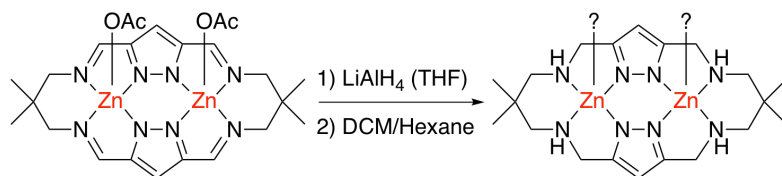


Figure 61: NOESY-NMR spectrum of $[L^{CPI}(Zn-OAc)_2]$ in $CDCl_3$ at 301 K.

2.5.2. Synthesis and characterization of $[L^{CPA}(Zn-Cl)_2]$ complex

In order to isolate the reduced species of the ligand different reducing agents were investigated. For this purpose, the complex $[L^{CPI}(Zn-OAc)_2]$ was treated with reducing agents without prior removal of the metal ions. The standard reducing agent $NaBH_4$ did not suffice and stronger ones were applied. $LiAlH_4$ (in THF) was, according to 1H -NMR spectroscopy, sufficient (see Scheme 27) and the proton signal of the imine moiety at $\delta = 7.99$ ppm disappeared (see Figure 62). However, so did the signals for the acetate at $\delta = 2.06$ ppm.



Scheme 27: Synthesis of Cyclic-Pyrazole-Amine (CPA) complex $[L^{CPA}(Zn-X)_2]$ performed in THF and crystallized from a DCM solution.

Initially it was thought that the acetate had been reduced to ethanolate. However, in the 1H -NMR no signals corresponding to an ethanolate ligand are visible. The question of the coordinating ligand was left open until single crystals suited for X-ray diffraction were obtained. The crystal structure was obtained and the molecular structure of

[L^{CPA}(Zn-X)₂] showed that X = Cl. It seems that the complex in presence of LiAlH₄ forms a species able to activate DCM (used for the crystallization) and CDCl₃ (from the NMR measurements). The chlorido ligands may also originate from trace amounts of chloride in these solvents, even though the amount of obtained crystalline material which was analyzed by NMR spectroscopy speaks against this option.

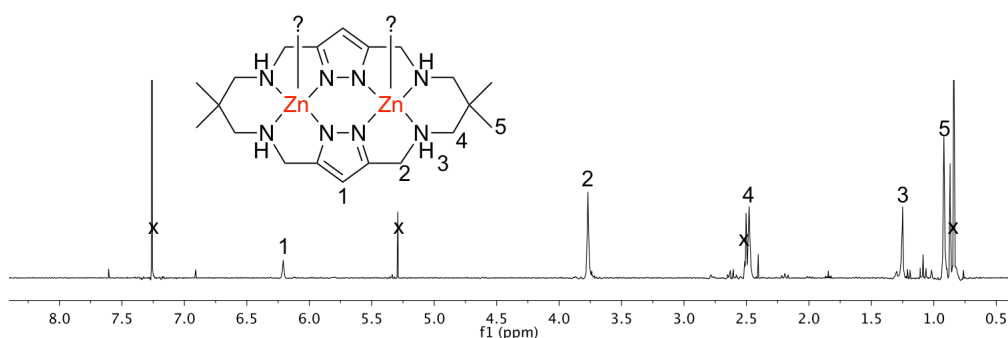


Figure 62: ¹H-NMR spectrum of [L^{CPA}(Zn-X)₂] in CD₂Cl₂. Assignment of the signals was done *via* 2D-NMR spectroscopy.

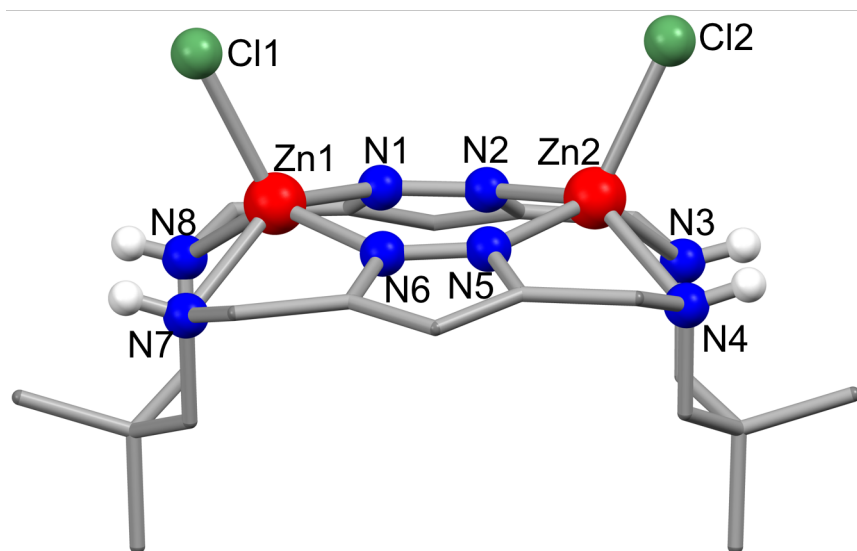
[L^{CPA}(Zn-Cl)₂] was found to crystallize also in the space group $P2_1/n$. The zinc atoms are above the plane formed by the four nitrogen atoms of one ligand pocket, similar to [L^{CPI}(Zn-OAc)₂]. The two plains that are formed by the four nitrogen atoms of one ligand pocket meet at an angle of ca. 37°. The complex forms a bowl shape with the methylene groups (CH₂-N) all pointing in one direction. Between the zinc atoms a distance of $d = 4.107 \text{ \AA}$ was measured, which is shorter than the 4.223 Å that were measured for [L^{CPI}(Zn-OAc)₂]. Selected atom distances can be found in Table 14. The corresponding bond angles can be found in the Appendix.

Table 14: Selected atom distances [Å] (sorted) of [L^{CPA}(Zn-Cl)₂] (see Figure 63). The corresponding bond angles can be found in the Appendix.

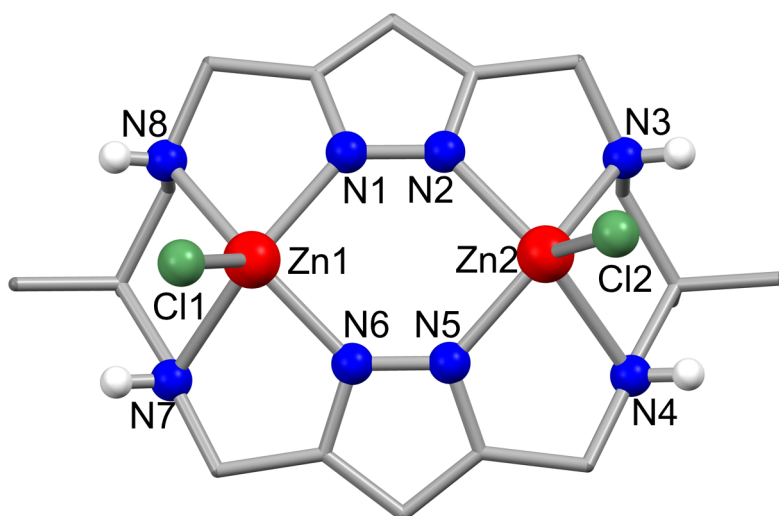
Atoms	Distance	Atoms	Distance
Zn1-N1	2.025(3)	Zn1-N8	2.184(3)
Zn1-N6	2.031(3)	Zn1-N7	2.234(3)
Zn2-N5	2.033(3)	Zn2-N4	2.258(3)
Zn2-N2	2.045(3)	Zn2-Cl2	2.2718(8)
Zn2-N3	2.174(3)	Zn1-Cl1	2.2777(8)

2.5.3. Application of macrocyclic complexes for the CO₂/epoxide copolymerization

The complexes [L^{CPI}(Zn-OAc)₂] and [L^{CPA}(Zn-Cl)₂] were tested as catalysts for the CO₂/CHO copolymerization. Both were tested at 50 bar of pressure at 80 °C, however,



(a) side view



(b) top view

Figure 63: Obtained molecular structure of $[L^{\text{CPA}}(\text{Zn-X})_2]$ with $\text{X} = \text{Cl}$. Most hydrogen atoms were omitted for clarity.

no PCHC formation was observed in the polymerization experiments. It could be argued that within the [L^{CPA}(Zn-Cl)₂] complex the Zn-Cl bond is too strong for allowing the initiation. However, for the [L^{CPI}(Zn-OAc)₂] complex the PCHC formation should have been observed. The most likely reason seems that the Zn-Zn separation is too wide and the complex too rigid to act as a catalyst for the CO₂/CHO copolymerization.

Concluding, the synthesis and characterization of [L^{CPI}(Zn-OAc)₂] and [L^{CPA}(Zn-Cl)₂] was successful. However, neither of the complexes is active for the catalysis. Beyond this, possibly the activation of DCM and CDCl₃ took place by a species that formed from [L^{CPI}(Zn-OAc)₂] with LiAlH₄. This would make these type of ligand interesting for future investigations, maybe even with other metals such as iron to target iron(IV)-oxo complexes.

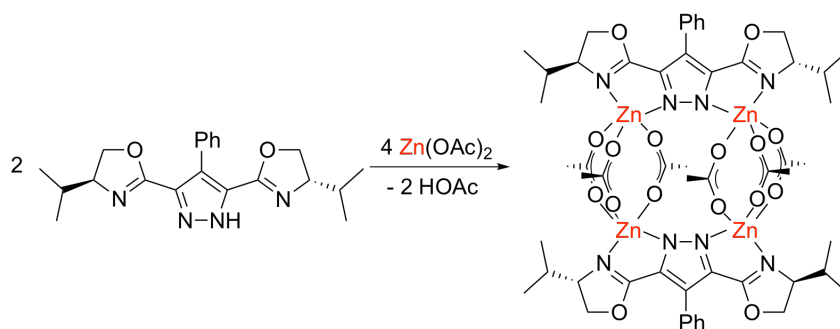
2.6. Synthesis and application of bis(oxazoline)-pyrazole (BOX) complexes for the CO₂/epoxide copolymerization

In this last section on CO₂/epoxide copolymerization, bis(oxazoline)-pyrazole (BOX) complexes are discussed and the results of their polymerization activity are presented. Mononuclear oxazoline complexes have been presented in the introduction (section 2.2.3, Figure 8, complex **9**). They showed good stereocontrol and yet, due to the mononuclearity, they cannot benefit from the cooperative effect present in a dinuclear catalyst.

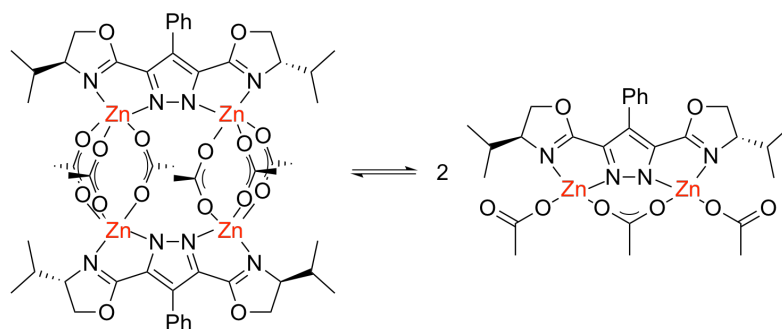
Pyrazole-bridged BOX complexes have been developed by the group of Meyer *et al.*, however, they have never been tested successfully for the CO₂/epoxide copolymerization.¹⁷⁶⁻¹⁷⁸ Zinc and cobalt complexes were generated and characterized as part of this work. In section 2.6.3 the performance of these complexes as catalysts for the CO₂/epoxide copolymers will be discussed.

2.6.1. Synthesis and characterization of the [L^{BOX}Zn₂(OAc)₃]₂ complex

The synthesis of the complex was performed according to Scheme 28. For the deprotonation of the pyrazol moiety (pK_a (N-H) of 19.8 in dmsO) the acetate from the Zn(OAc)₂ sufficed.^{179,180} The formed acetic acid was removed under vacuum, yielding the desired complex. Its ¹H-NMR spectrum, with assignment of the signals using 2D-NMR spectroscopy, is depicted in Figure 64. The corresponding ¹³C-NMR spectrum can be found in the Appendix in Figure 117. More relevant is, however, the aggregation of the complex in solution. The proposed structure could be split in two and even an equilibrium in solution is plausible between the dimeric (tetrazinc) and monomeric

Scheme 28: Synthesis of [L^{BOX}Zn₂(OAc)₃]₂.

(dizinc) species as depicted in Scheme 29.

Scheme 29: Proposed equilibrium between the monomeric [L^{BOX}Zn₂(OAc)₃] and the dimeric [L^{BOX}Zn₂(OAc)₃]₂ complex.

In order to identify the aggregation in solution DOSY-NMR experiments were performed. The obtained spectrum can be found in the Appendix in Figure 116. Two species can be observed with diffusion coefficients of $D = 6.737 \times 10^{-10} \text{ m}^2/\text{s}$ (major species) for the larger and $D = 9.455 \times 10^{-10} \text{ m}^2/\text{s}$ for the smaller species. For the determination of these coefficients the TopSpin software from Bruker was used for a more reliable processing of the spectra, as it was previously described in section 2.4.1. In the DOSY-NMR measurement no internal standard was added. Nevertheless, a determination of the molecular weight in solution was still possible using the residual proton signal of the solvent CD₂Cl₂^{143,144}, since at this chemical shift there is no overlay of signals. The diffusion coefficient of the solvent was determined to be $D = 3.339 \times 10^{-9} \text{ m}^2/\text{s}$. Using these three diffusion coefficient values allow for an estimation of the molecular masses in solution.

For $D = 6.737 \times 10^{-10} \text{ m}^2/\text{s}$ a molecular mass value of $M_{\text{CS}} = 1528 \text{ g/mol}$ for a spherical shape, and $M_{\text{merge}} = 1178 \text{ g/mol}$ for a *merged* geometry, were obtained. These

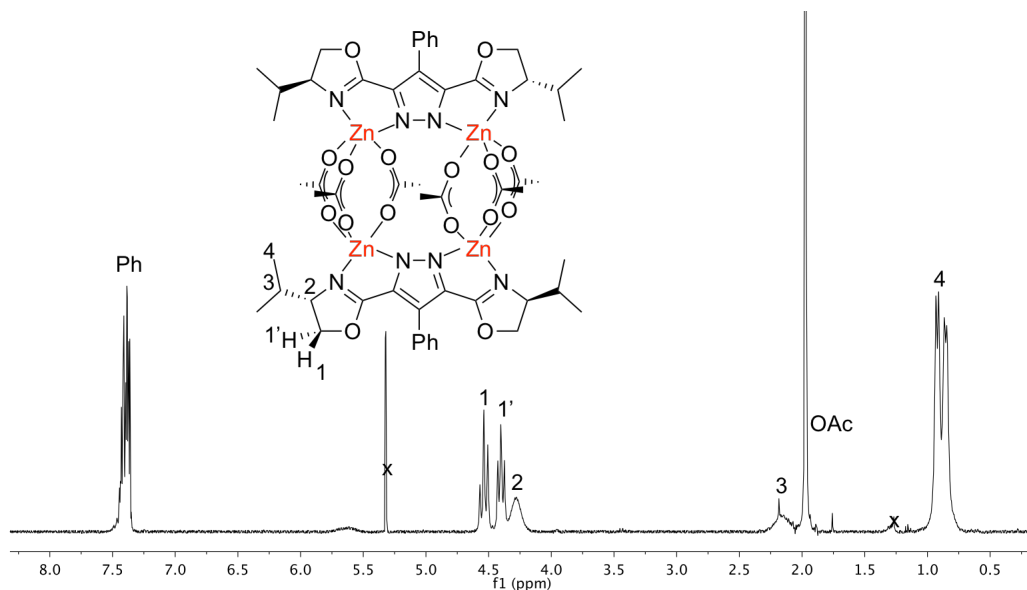


Figure 64: ¹H-NMR spectrum of [L^{BOX}Zn₂(OAc)₃]₂ in CD₂Cl₂. Assignment of the signals was done using 2D-NMR spectroscopy.

correspond with an error of -12% and 14% to the tetranuclear zinc complex ($M = 1347$ g/mol), respectively (Scheme 29 left). The species with a diffusion coefficient of $D = 9.455 \times 10^{-10}$ m²/s calculates to a M_{CS} value of 742 g/mol (-9% error to the dinuclear zinc complex), and a M_{merge} value of 626 g/mol (8% error to the dinuclear zinc complex). Concluding from these findings an equilibrium as proposed in Scheme 29 seems plausible.

In Figure 65 the ESI mass spectrum is depicted. However, it was not possible to assign the ion peaks with the high intensity between 1110–1190 m/z . From the isotopic pattern of the signals in the range of 1200–1290 m/z a tetranuclear zinc species can be derived.

The third experimental evidence pointing strongly to a tetranuclear zinc complex as depicted in Scheme 28, is the crystal structure of [L^{BOX}Zn₂(OAc)₃]₂. The molecular structure is shown in Figure 66 and selected atom distances are given in Table 15. The two L^{BOX} ligands hold each two zinc atoms and the two {L^{BOX}Zn₂} subunits are bridged by the acetate groups between pairs of zinc ions. The two ligands within the structure are tilted towards each other (Pz–Pz plain) by 37° and therefore, the four zinc atoms are not located in one plain. Between the zinc ions of each {L^{BOX}Zn₂} subunit an average distance of 4.476 Å was measured. Between the zinc atoms bridged by the acetate ligands, a shorter distance of 3.307 Å was determined. This difference might point towards a cooperativity between the latter pair of zinc atoms when the complex is applied for the CO₂/epoxide copolymerization reaction.

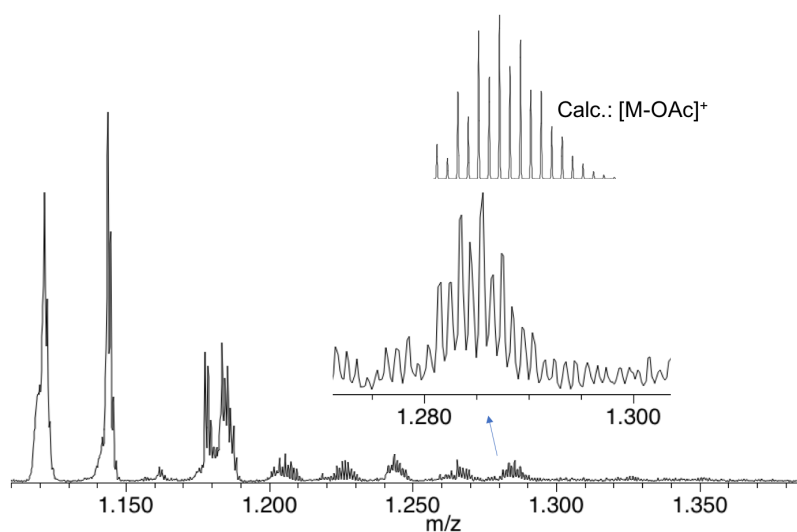


Figure 65: Section of the ESI mass spectrum of $[L^{\text{BOX}}\text{Zn}_2(\text{OAc})_3]_2$ in THF.

Table 15: Selected atom distances [Å] (sorted) of $[L^{\text{BOX}}\text{Zn}_2(\text{OAc})_3]_2$ (see Figure 66). The corresponding bond angles can be found in the Appendix.

Atoms	Distance	Atoms	Distance	Atoms	Distance
Zn1–O21	1.958(3)	Zn2–O27	2.058(3)	Zn3–O30	2.109(3)
Zn2–O31	1.958(3)	Zn1–O25	2.062(3)	Zn4–N12	2.119(3)
Zn1–O23	2.019(3)	Zn4–O24	2.074(3)	Zn2–N4	2.146(3)
Zn3–O32	2.021(3)	Zn3–N13	2.078(3)	Zn2–N2	2.146(3)
Zn2–O29	2.030(3)	Zn4–O25	2.078(3)	Zn3–N11	2.167(3)
Zn4–O22	2.038(3)	Zn4–N14	2.078(3)	Zn1–N3	2.171(3)
Zn3–O27	2.041(3)	Zn1–N1	2.102(3)	Zn4–O26	2.479(3)

All in all, the isolation and characterization of $[L^{\text{BOX}}\text{Zn}_2(\text{OAc})_3]_2$ was successful and the complex was found to be primarily tetranuclear in solution, as well as tetranuclear in the solid state. The complex was tested for its catalytic activity (section 2.6.3).

2.6.2. Synthesis and characterization of the $[L^{\text{BOX}}\text{Co}_2(\text{OAc})_3]_2$ complex

In order to form the corresponding cobalt complex $[L^{\text{BOX}}\text{Co}_2(\text{OAc})_3]_2$, the same synthetic approach was followed applying $\text{Co}(\text{OAc})_2$ instead of $\text{Zn}(\text{OAc})_2$; the synthetic route is shown in Scheme 30. To characterize the complex, a paramagnetic ^1H -NMR spectrum was recorded, showing five major signals which agrees well with the expected number of signals for the proposed structure in Scheme 30 (see Appendix A.2.4 in Figure 118). However, the integration of these signals does differ.

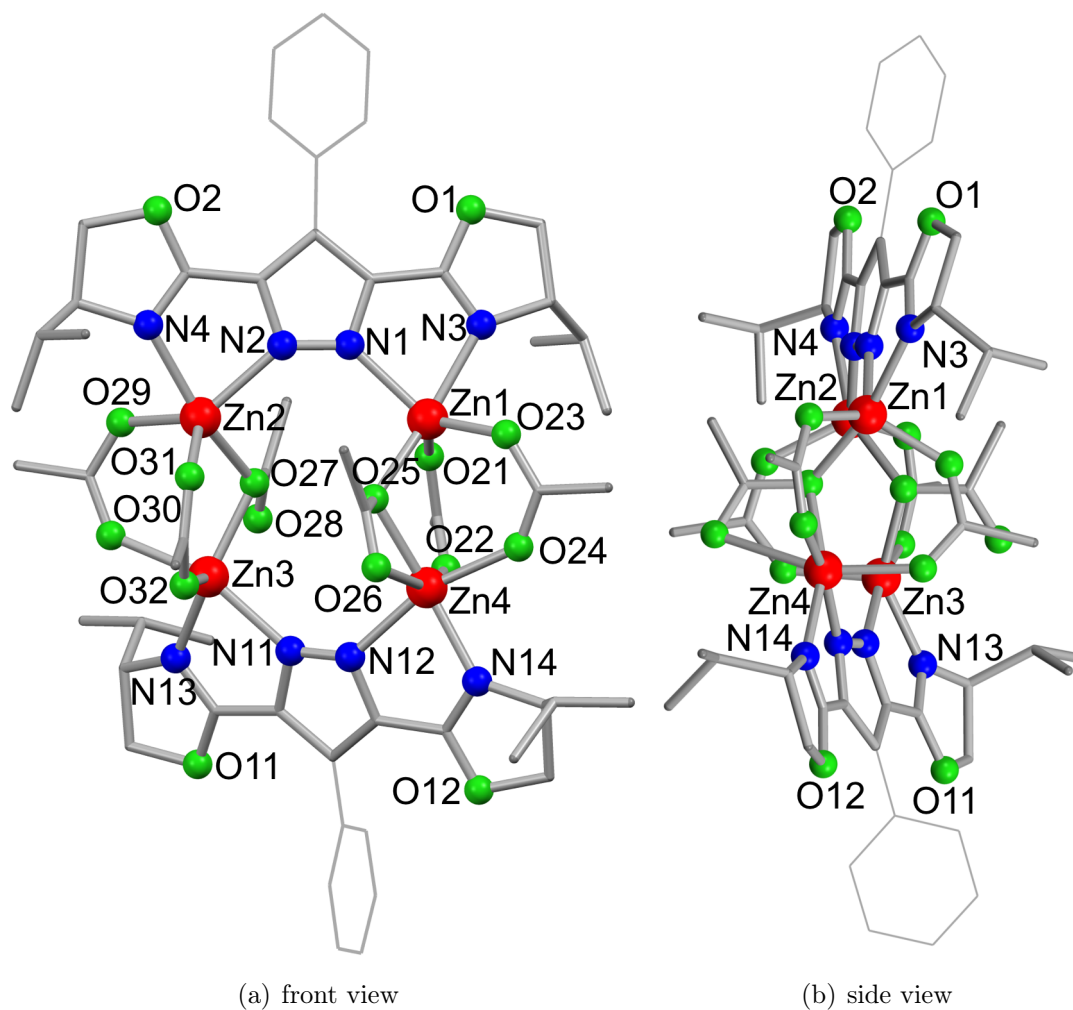
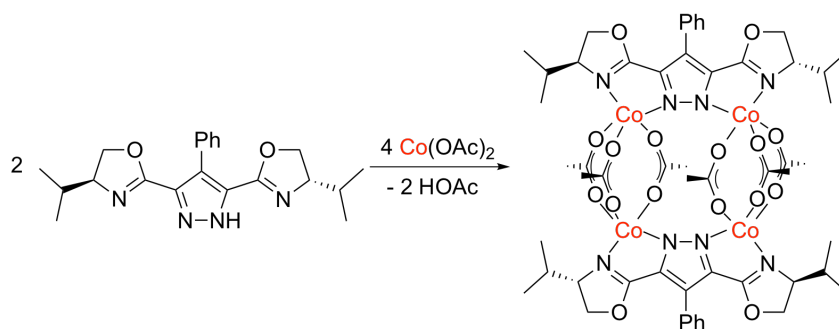


Figure 66: Molecular structure of $[L^{BOX}Zn_2(OAc)_3]_2$. Hydrogen atoms were omitted for clarity.

Scheme 30: Synthesis of $[L^{\text{BOX}}\text{Co}_2(\text{OAc})_3]_2$.

Due to the observed paramagnetism, an EPR spectrum in frozen DCM solution was measured, giving the g -values $g_1 = 2.124$, $g_2 = 2.060$ and $g_3 = 2.024$. The spectrum together with a simulation is depicted in Figure 67.

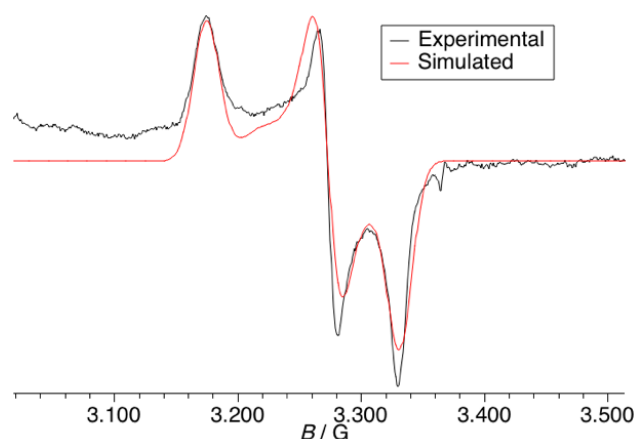


Figure 67: EPR spectrum of $[L^{\text{BOX}}\text{Co}_2(\text{OAc})_3]_2$ in a frozen DCM solution at 160 K. Obtained g -values: $g_1 = 2.124$, $g_2 = 2.060$ and $g_3 = 2.024$.

Neither of the latter two spectroscopic methods allowed to draw firm conclusions regarding the structure of the complex. ESI-MS experiments neither allowed the assignment of the molecular ion peak expected for $[L^{\text{BOX}}\text{Co}_2(\text{OAc})_3]_2$. The only structural evidence that was obtained is shown in Figure 68. It shows the molecular structure of complex $[L^{\text{PzBOX}+\text{H}_2\text{O}}\text{CoOAc}]_4$ where one oxazoline moiety of the ligand is hydrolyzed and a cobalt:pyrazole-ligand ratio of 1:1 is present. Furthermore, four acetate ligands can be found in the structure. The atom distances and bond angles for this structure can be found in the Appendix. This complex is assumed to be the degradation product of $[L^{\text{BOX}}\text{Co}_2(\text{OAc})_3]_2$.

Despite a multitude of crystallization attempts, only purple powder of the complex was

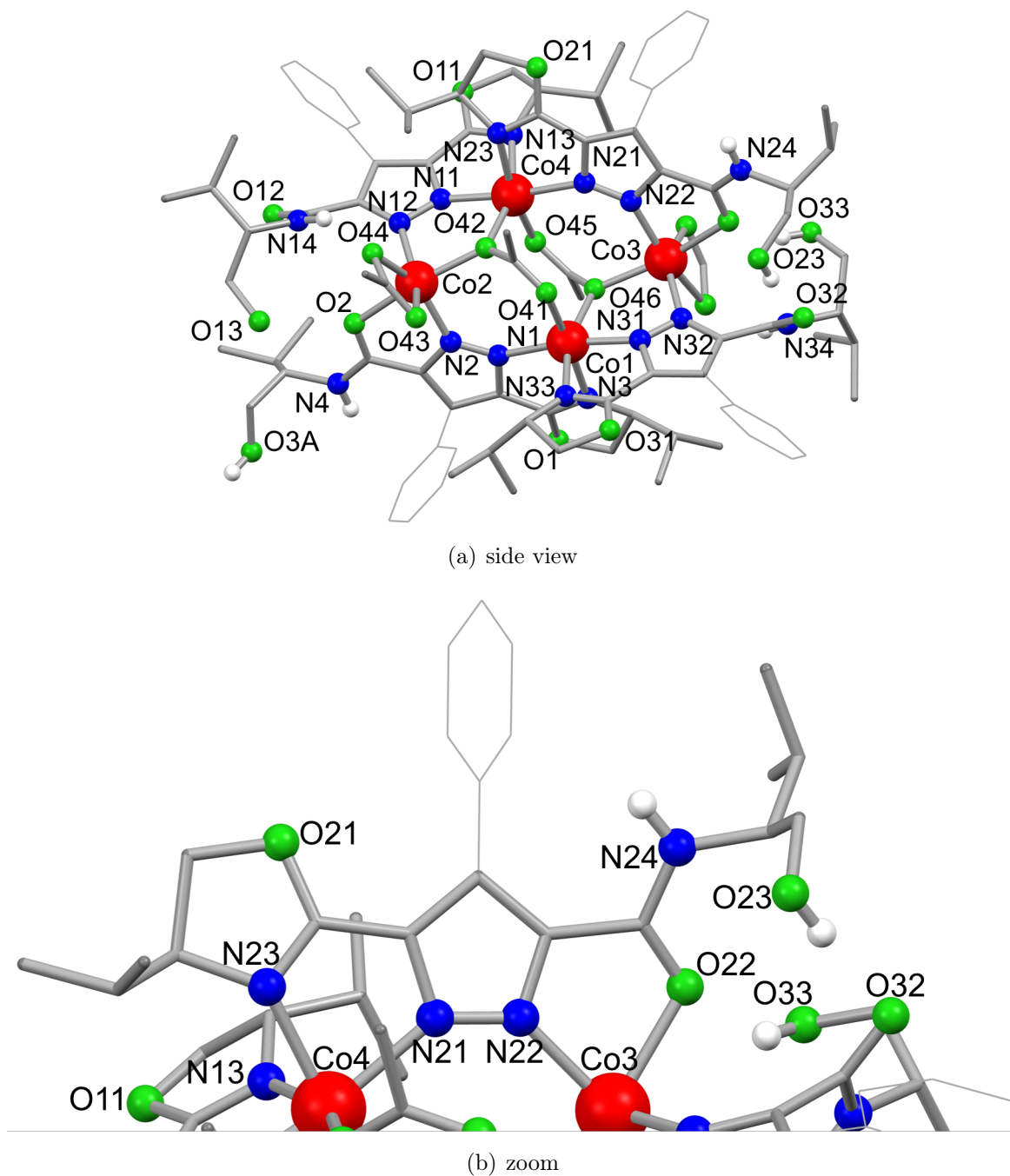


Figure 68: Molecular structure of the degradation product obtained from an attempt to crystallize $[L^{\text{BOX}}\text{Co}_2(\text{OAc})_3]_2$. Most hydrogen atoms omitted for clarity.

obtained. To be able to make a supported statement of the cobalt complex's structural motif, a similar ligand with a lower tendency to hydrolyze was used (see Figure 69).

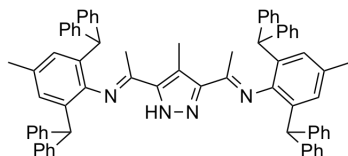


Figure 69: Ligand HL^{PI^{Ph}}.

This ligand system which seems suited was first described within my master thesis¹⁸¹ and is also used within this work (see section 3). It holds a pyrazole and two imine moieties allowing it to coordinate two metals, just as it is the case for L^{BOX}. Thus, the imine in L^{PI^{Ph}} should hereby mimic the oxazoline moiety. For that reason, HL^{PI^{Ph}} and two equivalents of Co(OAc)₂ were used to form a complex. Indeed, it was possible to crystallize the compound and the structural motif similar to the one in Figure 66 was observed (see Figure 70). Selected atom distances for [L^{PI^{Ph}}Co₂(OAc)₃(OH)_{0.5}]₂ can be found in Table 16 and the corresponding bond angles are given in the Appendix. The two L^{PI^{Ph}} ligands hold each two cobalt atoms and two times three acetate ligands bridge the cobalt atoms of two [L^{PI^{Ph}}Co₂] units. Additionally, one molecule of water (O7) originating from the solvents was found bridging two of the cobalt atoms (reaction was not performed under the exclusion of water). The two L^{PI^{Ph}} ligands within the structure are tilted towards each other (Pz–Pz plain) by 33° (37° in [L^{BOX}Zn₂(OAc)₃]₂) and, again, the four metal atoms are not in one plane. Between the cobalt atoms coordinating to the same pyrazol ligand, an average distance of 4.316 Å was measured (4.476 Å in [L^{BOX}Zn₂(OAc)₃]₂). Between the cobalt atoms that are bridged by the acetate and hydroxo ligands, a shorter distance of 3.526 Å (3.307 Å in [L^{BOX}Zn₂(OAc)₃]₂) was measured. It can, with caution, be assumed that the most probable structure of the intact [L^{BOX}Co₂(OAc)₃]₂ complex is similar to the one depicted in Scheme 30.

Concluding, the synthesis and characterization of [L^{BOX}Co₂(OAc)₃]₂ allowed an educated guess of the most likely structure of the compound. Especially considering the findings for the corresponding zinc complex [L^{BOX}Zn₂(OAc)₃]₂, a similar structure for the here described cobalt complex seems the most probable. Both complexes, the one with zinc and the one with cobalt, were tested for their catalytic activity (section 2.6.3).

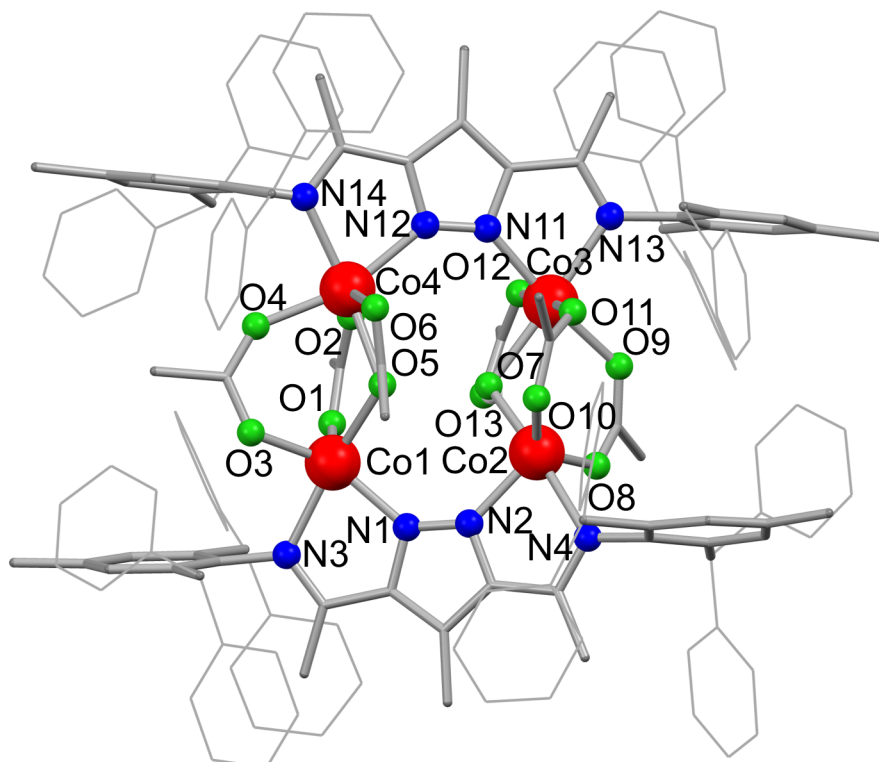


Figure 70: Molecular structure obtained for $[L^{\text{PIPh}}\text{Co}_2(\text{OAc})_3(\text{OH})_{0.5}]_2$. Most hydrogen atoms were omitted for clarity.

Table 16: Selected atom distances [\AA] (sorted) of $[L^{\text{PIPh}}\text{Co}_2(\text{OAc})_3(\text{OH})_{0.5}]_2$ (see Figure 70). The corresponding bond angles can be found in the Appendix.

Atoms	Distance	Atoms	Distance
Co2–O8	1.956(3)	Co3–O12	2.084(3)
Co1–O1	1.972(3)	Co2–O7	2.103(3)
Co2–O10	1.977(3)	Co4–N12	2.113(4)
Co1–O3	1.999(3)	Co1–O5	2.116(3)
Co4–O2	2.024(3)	Co4–N14	2.122(4)
Co2–N2	2.029(3)	Co3–O7	2.162(3)
Co1–N1	2.048(3)	Co1–N3	2.170(4)
Co4–O4	2.057(3)	Co3–N13	2.170(4)
Co3–N11	2.071(4)	Co4–O5	2.200(3)
Co3–O11	2.074(3)	Co4–O6	2.237(3)
Co3–O9	2.077(3)	Co2–N4	2.267(3)

2.6.3. Application of the [L^{BOX}Zn₂(OAc)₃]₂ and [L^{BOX}Co₂(OAc)₃]₂ complexes for the CO₂/epoxide copolymerization.

The bis(oxazoline)-pyrazole complexes [L^{BOX}Zn₂(OAc)₃]₂ and [L^{BOX}Co₂(OAc)₃]₂ were applied for the CO₂/CHO copolymerization.

The complexes proved to be active for the desired copolymerization and the obtained results can be found in Table 17. The tested [CHO]:[cat] ratio was 2000:1 (assuming a tetranuclear species), and between 3–6 mL of CHO at a reaction temperature of 80 °C were applied. Reactions with $p(\text{CO}_2) > 1$ bar were performed in a Büchi Picoclave reactor depicted in Figure 105; the ones with $p(\text{CO}_2) = 1$ bar in Schlenk tubes. The tested pressures were in the range of 1 – 50 bars with either 18 or 24 h of reaction time. The conversions go up to 16 % for the cobalt complex at 50 bar, but are very low especially at pressures < 50 bar. The TON values, again, for the cobalt complex at 50 bar reach 327, corresponding to a TOF of 18 h⁻¹. These values are acceptable but, considering the reaction conditions and compared to literature, low. At these reaction conditions TOF values 3–4 orders of magnitude greater have been reported.^{91,110,116} Among the catalysts, the cobalt complex shows a higher activity and a better selectivity for PCHC at almost all pressures. At lower pressures the fraction of formed polyether increases. It should be emphasized that for both catalysts the PCHC formed at low pressures consists of only a few repeating units and is better described as oligomer. This is represented in the given M_N . Standing out, however, is entry 10, where $M_N = 1003$ g/mol was determined. A possible explanation could be the different polymerization setup. Nevertheless, it is remarkable that the complex does show activity even at 1 bar of CO₂. The values of M_N in Table 17 were determined by ¹H-NMR spectroscopy, due to the relative high content of PCO which cannot be differentiated from the PCHC by the detector of the GPC setup available. This is nicely illustrated in Figure 133 (Appendix A.3.3), where at ca. 4×10^4 g/mol the GPC detector shows a polymer signal, while in the NMR the end-group integration only allows for the observation of the oligomer (see Figure 133 and Figure 134 in Appendix A.3.3).

For the entries 1 and 6 a GPC was run and the obtained PDI values are 7.6 and 1.16, respectively (see section A.3.3 in Figure 132). The latter points towards a living polymerization, while the very broad value of 7.6 might originate from several active species, and/or the continuous deactivation of the catalyst and/or the equilibrium in Scheme 29. The average molecular weight was 6189 g/mol, determined by the GPC measurements for entry 6 (calibrated against polystyrene). The accurate molecular mass likely lies in between the two obtained values. The hydrodynamic volume of PCHC in a GPC measurement is different from the polystyrene used for the calibration (Mark-Houwink parameter unknown). Furthermore, in the NMR measurement,

molecules with high molecular masses relax slower¹⁸², influencing the integration values that were used to determine the molecular masses listed in Table 17.

Besides the data that is represented in Table 17, the stereocontrol the complexes exert on the PCHC was investigated. In Figure 71 the ¹³C-NMR spectra of two polymer samples are shown with assignment of the triad and tetrad sequences.¹⁰³ Considering the remarks in Appendix A.3.4, up to 66% *m*-centered tetrads were determined. An isoenriched polymer was hence generated. The analysis of the hydrolyzed PCHC did not show any enantiomeric excess (value within the error of the measurement).

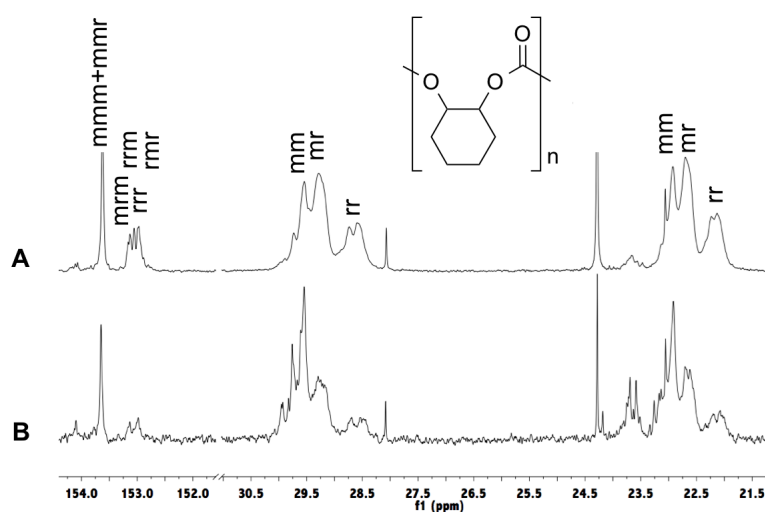


Figure 71: ¹³C-NMR spectrum in CDCl₃ with assignment of the triad and tetrad sequences of the polymer obtained by the BOX complexes.¹⁰³ A: [L^{BOX}Co₂(OAc)₃]₂, B: [L^{BOX}Zn₂(OAc)₃]₂. Up to 66% *m*-centered tetrads were determined.

From the observation that the macrocyclic complexes (section 2.5) are not active for the catalysis (too long Zn–Zn distance: $d = 4.223 \text{ \AA}$ for [L^{CPI}(Zn–OAc)₂] and $d = 4.107 \text{ \AA}$ for [L^{CPA}(Zn–Cl)₂]), it can be hypothesized that the two metals that perform the catalysis are not held by the same BOX-ligand (average Zn–Zn distance: $d = 4.476 \text{ \AA}$), but are the ones that are bridged by the acetate ligands (average Zn–Zn distance: $d = 3.307 \text{ \AA}$). This implies a tetranuclear catalyst system. The order in catalyst in the rate law would need to be determined in order to allow a supported statement on the nuclearity of the active species. Independent of the nuclearity, it can safely be assumed that one of the acetates of the precatalyst initiates the polymerization by opening the first epoxide.

It was not possible to take samples from the reaction solution during polymerization with $p(\text{CO}_2) > 1 \text{ bar}$, nor was the measurement of *in situ* IR under high pressures available with this specific setup of the reactor. Kinetic studies were therefore not

Table 17: Obtained results for applying [L^{BOX}Zr₂(OAc)₃]₂ (top) and [L^{BOX}Co₂(OAc)₃]₂ (bottom) for the CO₂/CHO copolymerization at different pressures.[†]

entry	$p(\text{CO}_2)$ / bar	t / h	conversion / %	TON ^f	TOF ^f / h ⁻¹	p.c.* / %	cyclic* / %	PCO* / %	M_N^* / g/mol	PDI ^g
1	50	18	8	168	9.3	91	5	4	1802	7.6
2	35	18	4	55	3.1	89	6	5	664	-
3	20	18	2	33	1.8	74	7	19	962	-
4	5	24	3	65	2.8	71	12	17	598	-
5	1	24	1	4	0.2	70	10	20	658	-
6	50	18	16	327	18	99	1	<0.5	9003	1.16
7	35	18	4	89	5.0	94	3	3	774	-
8	20	18	3	60	3.3	85	3.5	11.6	1051	-
9	5	24	3	64	2.7	75	15	10	630	-
10	1	24	2	37	1.5	84	8.5	8	1003	-

[†]: [CHO]:[cat] = 2000:1 (assuming a tetranuclear species), between 3–6 mL of CHO, $T = 80^\circ\text{C}$, reactions with $p(\text{CO}_2) > 1$ bar were performed in the reactor depicted in Figure 105, the ones with $p(\text{CO}_2) = 1$ bar in Schlenk tubes.

*: % polycarbonate (p.c.), % cyclic carbonate, % PCO and M_N were determined by ¹H-NMR of the polymer in CDCl₃ from the relative integrals of the signals at $\delta = 3.32$ ppm (homopolymer), $\delta = 3.98$ ppm (cyclic carbonate), $\delta = 4.34$ ppm (end-group of PCHC) and $\delta = 4.61$ ppm (copolymer).

D: dispersity = M_w/M_n . Determined by GPC in THF with toluene as internal standard calibrated with polystyrene.

^f: TOF referring to the entire reaction time t . TOF = TON / t .

pursued for these two complexes. Regarding the relatively low activities of the BOX complexes in comparison to the complex of section 2.4.2, the future investigation of the ONO-pincer type systems appears more promising.

Concluding, the two isolated bis(oxazoline)-pyrazole complexes [L^{BOX}Zn₂(OAc)₃]₂ and [L^{BOX}Co₂(OAc)₃]₂ are suited catalysts for the CO₂/epoxide copolymerization, albeit with relatively low activities. The cobalt complex demonstrated a slightly higher activity than the zinc compound, showing a TOF of 18 h⁻¹ at 50 bar and 80 °C, producing an isoenriched PCHC with good chemoselectivity.

2.7. Summary of results of the CO₂/epoxide copolymerizations

Several promising novel catalysts to the field of CO₂/epoxide copolymerization were discovered, combining extraordinary design, activity and/or stereoselectivity.

Two new pyrazol-bridged BOX catalysts were found that produce isotactic enriched PCHC. They are again depicted in Figure 72.

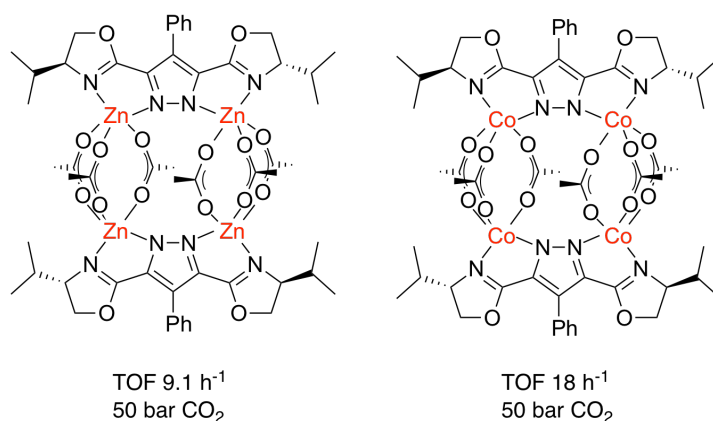


Figure 72: Newly discovered [L^{BOX}Zn₂(OAc)₃]₂ and [L^{BOX}Co₂(OAc)₃]₂ complexes for the CO₂/epoxide copolymerization.

The highlight of this chapter, and possibly this thesis are the ONO-pincer type catalysts, their synthesized and characterization in section 2.4.1, and their application described in section 2.4.2 (see Figure 73).

The structure in the solid state and in solution of the [L^{ProOH}Zn]₂ complex and its derivatives was thoroughly explored. The self-assembly strategy for these new ONO-pincer type complexes for the CO₂/epoxide copolymerization opens a new field of complex design for future investigations, with great potential and possible industrial applicability.

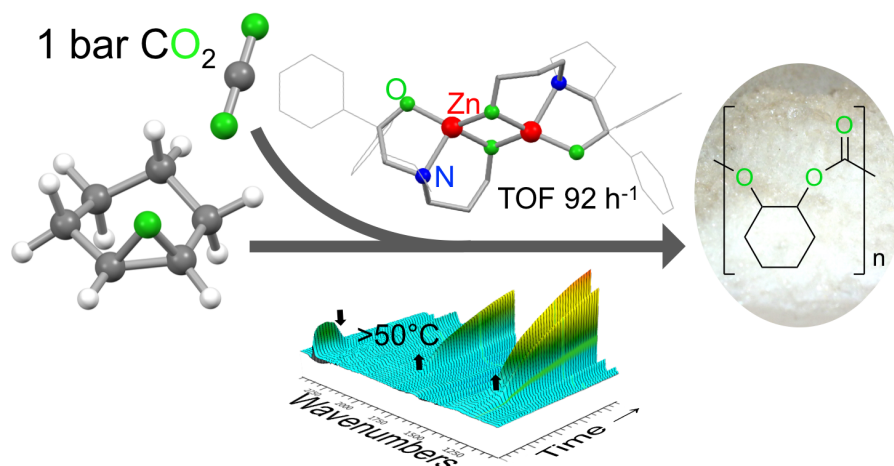


Figure 73: A novel chiral zinc catalyst that can be isolated in 97% yield from commercial sources, and that produces polycarbonates selectively from neat cyclohexene oxide under 1 bar of CO₂ at temperatures above 50 °C. At 80 °C reaction temperature, average TON values up to 610 and TOF values up to 92 h⁻¹ were measured, producing an isotactic-enriched polycarbonate with a probability P_m of 65% for the formation of a *meso* diad. Some mechanistic insight as well as structural characterization of the precatalyst have been obtained.

2.8. Outlook for the CO₂/epoxide copolymerization

As first point, further mechanistic studies should be performed on the [L^{ProOH}Zn]₂ complex. For this purpose but also to optimize the catalyst, the derivatives, especially with ligands suggested in Figure 57, should be further investigated. A great step forward would be the discovery of a less water-sensitive ONO-pincer system, providing great potential for the CCU.

Last but not least, in future works the potential versatility in different epoxides that can be copolymerized by the [L^{ProOH}Zn]₂ complex and its derivatives should be explored, especially focusing on sustainable epoxide monomers (Figure 4). Also, the field of synthesizing block copolymers to modify material properties should be addressed, since it has become increasingly popular in recent years.

3. Chapter 2: Study on the Cooperative Effects within a Dinuclear Palladium Complex through the Investigation of the Allyl Exchange

3.1. Introduction

The first chapter of this thesis exploits cooperativity within dinuclear complexes for a catalytic application. In this chapter a model complex will be described that allows the observation of interactions within a dinuclear complex, seeing to obtain some fundamental understanding of such cooperative effects. Residues within the complex will be altered to understand their influence on the neighboring moieties.

The model complexes under investigation feature allyl moieties. Therefore, the relevance of allyl complexes in catalysis will be briefly reflected.

3.1.1. The cooperative effects that are subject of this investigation

In the last decades, complexes that hold two metal centers in close proximity gained attention for catalytic applications. Such catalysts can be superior over their single-metal-center equivalents.¹⁸³ The gain in catalytic activity by dinuclear complexes can exceed the expected value from a simple increase in catalyst concentration of a mononuclear system, due to cooperative effects between the metals.^{110,183–188} These cooperative effects are not fully understood yet. A rigid model complex chelating two metal centers (in this study two palladium ions) at a fixed distance was the object of investigation (see Figure 1), to gain further insights into some of the associated cooperative effects. The cooperativity will be resembled by the interactions between the palladium centers, which is communicated through the coordinating ligands at each site. By exchanging the coordinating moieties (A and B in Figure 1) the resulting change in interaction will allow a relative evaluation of cooperativity. In order to observe the interactions, one of the palladium centers should be coordinated with an allyl moiety. These are known for their fluxional behavior which can be monitored by NMR spectroscopy. The interactions within the model complex will be derived from the behavior of the allyl moiety, which will serve as a spectator-ligand. The second palladium was coordinated by two halides, which can be easily varied among halides with different size (in this study Cl and Br). The halides are meant to resemble a coordinating substrate to the catalyst (here palladium). The differently sized halides should change the interaction in between the metal centers by influencing the fluxional behavior of the allyl moieties at the neighboring metal. Allyl moieties usually coordinate in a η^3 -fashion to a palladium center. They undergo different exchange mechanisms, which will be further developed

in section 3.1.2.

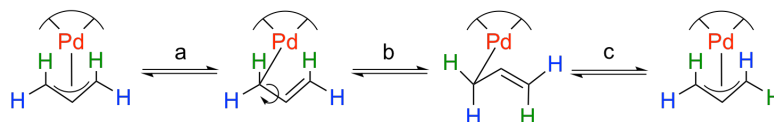
Allyl complexes in catalysis:

Allyl-metal complexes can be found in many catalytic reactions. Especially, but not only, allyl-palladium complexes have received a lot of attention. They occur as intermediates in various catalytic reactions.^{189–199}

Some prominent allyl-palladium reactions are *e.g.* the Tsuji-Trost reaction and its asymmetric variants^{184,200–212}, the Carroll rearrangement^{213–215} and the Saegusa-Ito oxidation (the oxo variation).^{216–218} Even though, other metals form allyl species in prominent catalytic reactions,^{201,219–222} palladium is one of the most prominent, thus this work will focus on allyl palladium complexes exclusively.

3.1.2. Fluxional behavior of allyl moieties: the exchange mechanisms

The exchange of the *syn*- with the *anti*-positioned proton is assumed to take place *via* a $\eta^3 - \eta^1 - \eta^3$ sequence.^{223,224}

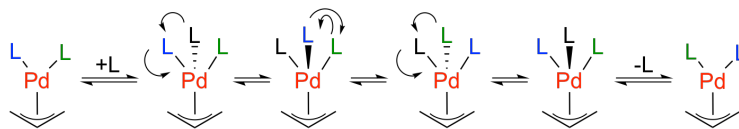


Scheme 31: *syn/anti* Exchange mechanism of an η^3 -allyl-palladium complex. The hydrogen atoms in *anti* position are marked in green and the ones in *syn* position in blue (left structure). a: Transition from η^3 - to η^1 -coordination, forming a single bond between the α -C and β -C atom. b: Rotation around the α -C- β -C-bond. c: Transition from an η^1 - to an η^3 -coordination.^{225–227}

Besides the *syn/anti* exchange, allyl complexes also perform a *syn/syn* exchange *via* processes named apparent-allyl-rotation. The simple axial rotation around the Pd-allyl-bond is unlikely, since a tetrahedral transition state is unfavorable for palladium complexes (geometry of orbitals). The suggested mechanism therefore avoids a tetrahedral coordination at the palladium. For the *syn/syn* exchange, which is equal to the *anti/anti* exchange, two different mechanisms are proposed. The first one is associative (see Scheme 32) and the second one is dissociative (see Scheme 33).

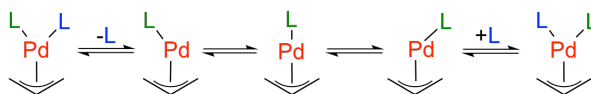
The associative mechanism is assumed to take place *via* the coordination of a solvent molecule or other coordination substrate, forming a five-coordinate intermediate which undergoes a Berry-pseudo-rotation and subsequent decoordination, leading to

the apparent-allyl-rotation.^{223,228–231} Such a process is associated with a negative entropy of activation.



Scheme 32: Associative *syn/syn*-exchange mechanism proposed to occur within a η^3 -allyl-palladium complex. An additional ligand L initiates the exchange. The trigonal-bipyramidal coordination environment allows a *Berry pseudorotation*. In the last step is the dissociation of the initiating ligand L.^{228,232–234}

The dissociative mechanism (see Scheme 33) assumes that a non-allyl ligand detaches from the metal, forming a T-shaped tricoordinated intermediate. This allows rotation around the remaining Pd–L-bond of the second non-allyl ligands. Recoordination of the non-allyl ligand is the last step of this dissociative apparent-allyl-rotation.^{228,232,233,235}



Scheme 33: Dissociative *syn/syn*-exchange mechanism proposed to occur within η^3 -allyl-palladium complexes. The coordinating ligand can be bidentate, implying a partial dissociation.^{228,230,231}

The *syn/syn* mechanism for the presented bimetallic complexes is depicted in a simplified fashion in Figure 74 (a). This symbol will be used from now on to refer to these exchanges. It needs to be stressed that the symbol is not referring to a transition state with the palladium in a tetrahedral coordination environment. For the *syn/anti* exchange the symbol b) in Figure 74 will be used.

The synthesis, characterization and first kinetic studies for the complexes $[\text{L}^{\text{PI}^{\text{iPr}}}\text{PdBr}_2\text{-Pd}(\text{C}_3\text{H}_5)]$ and $[\text{L}^{\text{PI}^{\text{Ph}}}\text{PdBr}_2\text{Pd}(\text{C}_3\text{H}_5)]$ have been performed during the preceding Master Thesis. The obtained results will be reflected and again presented within this work, contrasting them with to the new kinetic studies on the corresponding chloro complexes $[\text{L}^{\text{PI}^{\text{iPr}}}\text{PdCl}_2\text{Pd}(\text{C}_3\text{H}_5)]$ and $[\text{L}^{\text{PI}^{\text{Ph}}}\text{PdCl}_2\text{Pd}(\text{C}_3\text{H}_5)]$. The contents of this chapter will be published under the title: “Allyl Dynamics at Unsymmetric Dinuclear Palladium Complexes” by Mike Schütze, Michael John, Sebastian Dechert and Franc Meyer*.

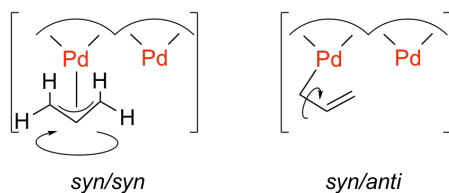
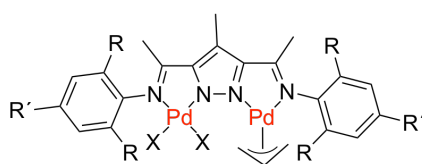


Figure 74: Sketch representative for the allyl exchange mechanisms. a) *syn/syn* Exchange referring to the mechanisms in Scheme 33 or Scheme 32. b) The *syn/anti* referring to the mechanism in Scheme 31.

3.2. Synthesis and characterization of the Pyrazole-bridged-Imine complexes $[L^{PI}PdX_2Pd(C_3H_5)]$



- 1: R = *i*Pr, R' = H, X = Cl
 2: R = *i*Pr, R' = H, X = Br
 3: R = CHPh₂, R' = Me, X = Cl
 4: R = CHPh₂, R' = Me, X = Br

Within this chapter the following nomenclature for the four complexes will apply: $[L^{PI^{iPr}}PdCl_2Pd(C_3H_5)]$ is **1**, $[L^{PI^{iPr}}PdBr_2Pd(C_3H_5)]$ is **2**, $[L^{PI^{Ph}}PdCl_2Pd(C_3H_5)]$ is **3** and $[L^{PI^{Ph}}PdBr_2Pd(C_3H_5)]$ is **4**.

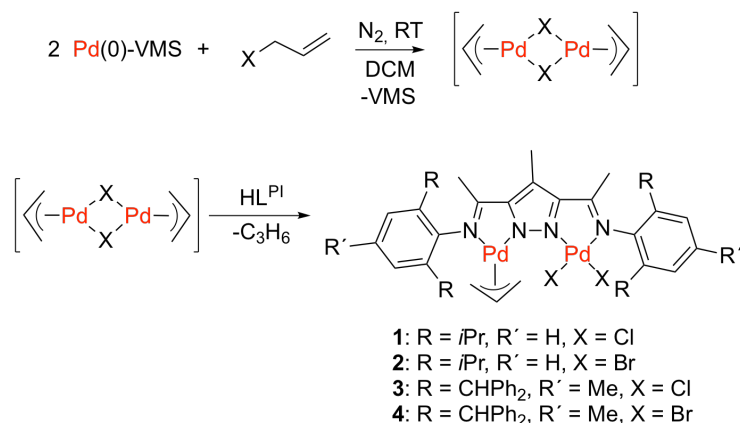
3.2.1. Synthesis of the η^3 -allyl complexes $[L^{PI^{iPr}}PdCl_2Pd(C_3H_5)]$ and $[L^{PI^{Ph}}PdCl_2Pd(C_3H_5)]$

Complexes **1** and **3** were synthesized by adapting protocols developed during the preceding master thesis.¹⁸¹

The yellow precursor complexes $[(C_3H_5)PdX]_2$ were generated *in situ* from the oxidative addition of the allyl halide on 1,3-divinyl-1,1,3,3-tetramethyldisiloxane palladium(0) (see Scheme 34). The reaction of the ligands $L^{PI^{Ph}}$ and $L^{PI^{iPr}}$ with $[(C_3H_5)PdX]_2$ led to the formation of the target complexes under release of propene (see Scheme 34). It can be assumed that the ligand was deprotonated by one of the allyl moieties, since no base was added.

Besides the crystal structures of the two bromo complexes the structure of $[L^{PI^{iPr}}PdCl_2Pd(C_3H_5)]$ (**1**) was obtained (see Figure 77). For an easier description and discussion of the complexes, the nomenclature in Figure 75 is introduced. Complex **1** (see Figure 77) was found to crystallize in a monoclinic crystal system with four molecules in the unit cell. The plane of the aniline π -system is almost orthogonal to the plane of the

3.2 SYNTHESIS AND CHARACTERIZATION OF THE PYRAZOLE-BRIDGED-IMINE COMPLEXES $[L^{PI}PdX_2Pd(C_3H_5)]$



Scheme 34: Synthetic route to the complexes $[L^{PI}PdCl_2Pd(C_3H_5)]$.¹⁸¹ R = *i*Pr, R' = H for $[L^{PI^{iPr}}PdCl_2Pd(C_3H_5)]$ (**1**) and R = CPh₂, R' = Me for $[L^{PI^{Ph}}PdCl_2Pd(C_3H_5)]$ (**3**).

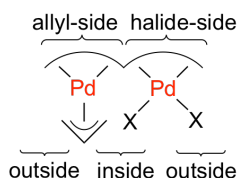


Figure 75: Nomenclature within the allyl-complexes that will be applied in this chapter.

backbone. The N1–Pd1–N3 bite angle on the allyl-side is 77.0° (for comparison: 76.6° in **2** and 78.1° in **4**). On the halide-side the N2–Pd2–N4 bite angles are slightly larger at 78.9° (78.3° in **2** and 79.8° in **4**). The Pd–Pd distance measures 4.350 \AA in **2** and 4.353 \AA in **1**, which is 0.16 \AA shorter than in **4** (4.513 \AA), resulting from the greater bulkiness of the CPh₂ substituents in $L^{PI^{Ph}}$. Furthermore, the complexes are strongly distorted with a Pd–N–N–Pd torsion angle of 31.3° in **1**, 42.8° in **2**, and 49.9° in **4** (see Figure 76).

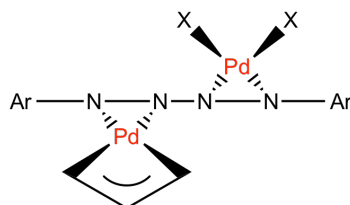


Figure 76: Side view on the complexes for better visualization of the distortion.

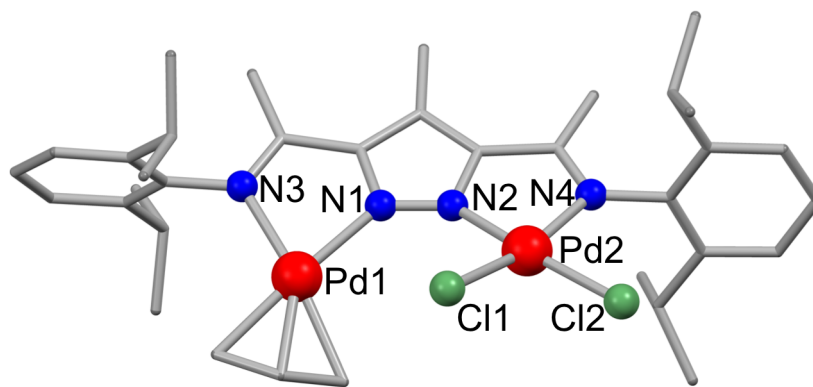
This distortion is quite remarkable since the palladium atoms are in-plane with the ligand in complexes of the type $[L^{PI}Pd_2Cl_3]$.²³⁶ Thus, it can be assumed that the complexes are under inner tension due to the steric repulsion of the allyl and the halide moieties, relative to the $[L^{PI}Pd_2Cl_3]$ complexes.^{181,236}

Table 18: Selected atom distances determined from the molecular structure of the complexes in Figure 77. The corresponding bond angles can be found in the Appendix.

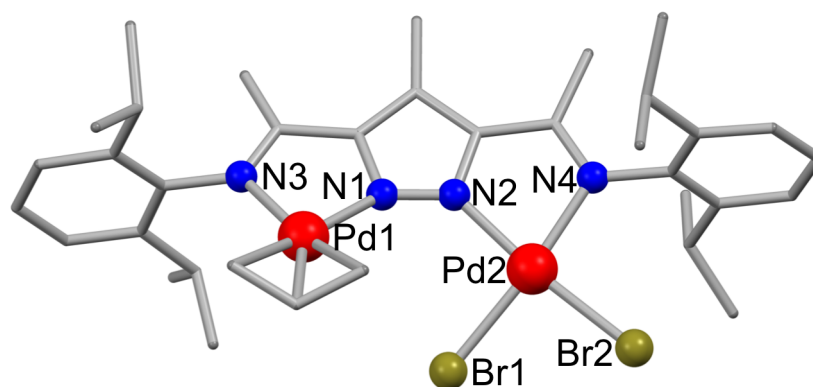
Bond	$[\text{L}^{\text{Pr}^{\text{tr}}}\text{PdCl}_2\text{Pd}(\text{C}_3\text{H}_5)]$ Length / Å	$[\text{L}^{\text{Pr}^{\text{tr}}}\text{PdBr}_2\text{Pd}(\text{C}_3\text{H}_5)]$ Length / Å	$\text{HL}^{\text{Pr}^{\text{tr}}}$ Length / Å	$[\text{L}^{\text{Pr}^{\text{tr}}}\text{PdBr}_2\text{Pd}(\text{C}_3\text{H}_5)]$ Length / Å
Pd2-X2 _{outside}	2.2994(7)	2.423(1)	-	2.4173(6)
Pd2-X1 _{inside}	2.2837(8)	2.416(1)	-	2.4026(5)
Pd2-N2	2.008(2)	1.997(6)	-	2.019(3)
Pd2-N4	2.044(2)	2.063(6)	-	2.065(3)
Pd1-N1	2.086(2)	2.084(7)	-	2.132(3)
Pd1-N3	2.105(2)	2.113(8)	-	2.104(3)
Pd1-C _{allyl} ¹ _{outside}	2.113(3)	2.12(8)*	-	2.102(5)
Pd1-C _{allyl} ¹	2.118(3)	2.12(7)*	-	2.119(4)
Pd1-C _{allyl} ¹ _{inside}	2.146(3)	2.16(8)*	-	2.147(4)
N1-N2	1.327(3)	1.322(8)	1.334(4)	1.337(4)
N3=C allyl-side	1.295(4)	1.29(1)	1.277(5)	1.303(4)
N4=C halide-side	1.300(4)	1.32(1)	1.275(6)	1.312(5)
N3-C _{allyl} ¹ _{allyl-side}	1.436(3)	1.459(9)	1.408(5)	1.434(5)
N4-C _{allyl} ¹ _{halide-side}	1.446(3)	1.458(9)	1.443(4)	1.425(5)

*. For evaluating the *trans*-influence at the palladium, the average of the measured Pd1-C_{allyl}¹ distances in $[\text{L}^{\text{Pr}^{\text{tr}}}\text{PdBr}_2\text{Pd}(\text{C}_3\text{H}_5)]$ was used, since the allyl group is disordered in the molecular structure.

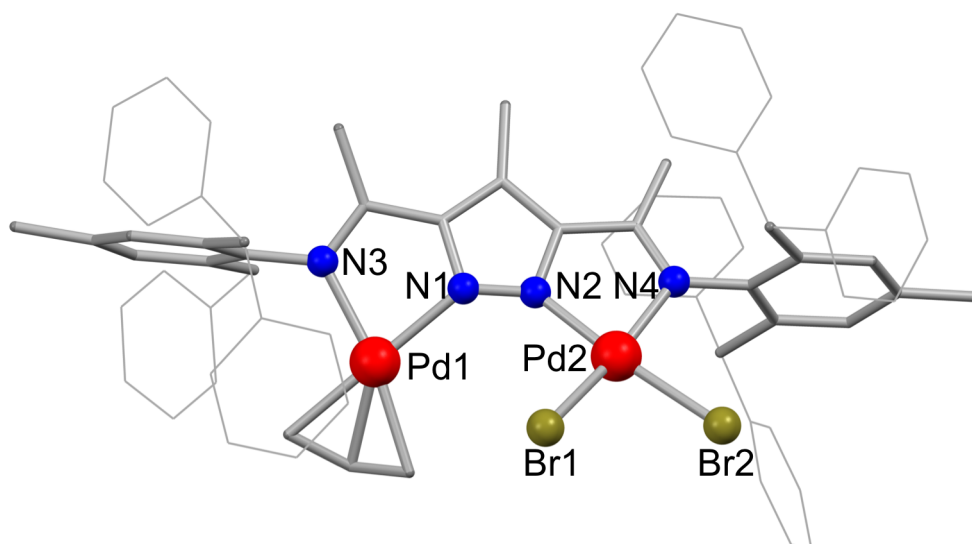
3.2 SYNTHESIS AND CHARACTERIZATION OF THE PYRAZOLE-BRIDGED-IMINE COMPLEXES $[L^{PI}PdX_2Pd(C_3H_5)]$



(a) 1: $n = iPr$, $X = Cl$



(b) 2: $n = iPr$, $X = Br$



(c) 4: $n = Ph$, $X = Br$

Figure 77: Molecular structure of the allyl $[L^{PI}PdX_2Pd(C_3H_5)]$ complexes.¹⁸¹ Hydrogen atoms were omitted for clarity.

A selection of atom distances, determined from the molecular structures of the corresponding complexes, is listed in Table 18. Comparing the Pd2–X bond lengths allows

to hypothesize about the strength of the ligands' thermodynamic *trans*-influence. In all three complexes the Pd–X bond *trans* to the imine donor is slightly longer than the one *trans* to the pyrazolate (pz). This could indicate that the *trans*-influence of the imine donor is greater than that of the pyrazolate group. The Pd1–CH₂^{allyl} distances on the inside are longer in comparison to the carbons on the outside. Inside refers to the CH₂-group of the allyl moiety that is in *trans*-position to the imine donor and outside to the one in *trans*-position to the pyrazolate. This is in agreement with the trend observed for the Pd2–X bond lengths, supporting the hypothesis that the *trans*-influence of the imine donor is larger than of the pyrazolate-N.

The C=N-stretch vibrational bands from the IR spectra can be found in Table 19 together with the C=N-stretch vibrational bands of the corresponding free ligands.

Table 19: Comparison of the C=N-stretch vibrational bands of the free ligands HL^{PIⁱPr} and HL^{PI^{Ph}} as well as the complexes [L^{PIⁱPr}PdCl₂Pd(C₃H₅)] (**1**), [L^{PIⁱPr}PdBr₂Pd(C₃H₅)] (**2**), [L^{PI^{Ph}}PdCl₂Pd(C₃H₅)] (**3**) and [L^{PI^{Ph}}PdBr₂Pd(C₃H₅)] (**4**).^{181,236}

Compound	$\tilde{\nu}_{\text{C=N}}$ [cm ⁻¹]	
HL ^{PIⁱPr}	1630	
1	1592	1570
2	1573	1541
HL ^{PI^{Ph}}	1630	
3	1599	1571
4	1569	1540

Evidence was collected that the structures in solution and solid state are similar. Characterization by 1D/2D-NMR spectroscopy was performed in CD₂Cl₂ and the compounds showed some remarkable chemical shifts. A summary of selected ¹H- and ¹³C-NMR chemical shifts can be found in Table 20. The CH₃–CN groups are high-field-shifted in HL^{PI^{Ph}} and its complexes. This results from the aromatic ring current present in the phenyl groups of the HCPPh₂ substitutes, which lead to an electromagnetic anisotropy at the close-by CH₃–CN groups (NH tautomerism present). In the free ligand HL^{PI^{Ph}} different conformations with different relative positions of the methyl group towards the phenyl rings are accessible leading to a broad signal at 1.04 ppm. In the palladium complexes this rotational freedom is no longer given, leading to a rigid positioning of the CH₃–CN moiety orthogonal to the phenyl plain of the CHPh₂ groups (see dashed lines at atom C42 in Figure 78). On the halide-side the CH₃–CN moiety is positioned above the π -system of two phenyl groups, shifting it to a sharp signal at –0.48 ppm (protons at C42 in Figure 78). While on the allyl-side only one of the phenyl-planes faces the CH₃–CN group, shifting it to 1.55 ppm (protons at C6 in Figure 78). The CPh₂ moiety attached to the 6-position of the aniline faces the *anti*-positioned proton (H81A in Figure 78) situated at the outside of the allyl moiety. This

3.2 SYNTHESIS AND CHARACTERIZATION OF THE PYRAZOLE-BRIDGED-IMINE COMPLEXES $[L^{PI}PdX_2Pd(C_3H_5)]$

Table 20: Selection of characteristic 1H -NMR (top) and ^{13}C -NMR (bottom) signals of the compounds in ppm $HL^{PI^{iPr}}$, $[L^{PI^{iPr}}PdCl_2Pd(C_3H_5)]$ (**1**), $[L^{PI^{iPr}}PdBr_2Pd(C_3H_5)]$ (**2**), $HL^{PI^{Ph}}$, $[L^{PI^{Ph}}PdCl_2Pd(C_3H_5)]$ (**3**) and $[L^{PI^{Ph}}PdBr_2Pd(C_3H_5)]$ (**4**); NMR spectra recorded in CD_2Cl_2 .

1H -NMR signals						
moiety	$HL^{PI^{iPr}}$	1	2	$HL^{PI^{Ph}}$	3	4
CH_3 -Pz	2.81	2.53	2.53	2.01	1.55	1.54
CH_3 -CN _{halide-side}	2.17	2.17	2.17	1.04	-0.44	-0.48
CH_3 -CN _{allyl-side}		2.20	2.21		1.03	1.05
CHR_2 _{allyl-side}	2.85	2.82	2.84	5.31	5.33	5.35
CHR_2 _{allyl-side}		3.11	3.09		5.48	5.55
CHR_2 _{halide-side}		3.14	3.11		6.18	6.09
CHR_2 _{halide-side}		3.18	3.21		6.22	6.24
allyl- $H_{anti, outside}$		2.71	2.66		1.61	1.73
allyl- $H_{syn, outside}$		2.82	2.83		2.53	2.49
allyl- $H_{anti, inside}$		3.52	3.50		3.23	3.27
allyl- $H_{syn, inside}$		5.06	5.08		4.99	5.05

^{13}C -NMR signals						
moiety	$HL^{PI^{iPr}}$	1	2	$HL^{PI^{Ph}}$	3	4
allyl- CH_2 _{outside}		62.0	60.6		60.7	59.2
allyl- CH_2 _{inside}		69.1	70.90		68.6	70.3
allyl-CH		116.4	116.3		115.7	115.8
CN _{halide-side}	160.5	169.8	170.1	144.30	172.7	172.7
CN _{allyl-side}		171.1	171.1		175.0	175.2

also leads to a high field shift for the allyl- $H_{anti, outside}$ proton from 2.71 to 1.61 ppm for the chloro complexes, comparing **1** with **3**, and from 2.66 to 1.73 ppm for the bromo complexes, comparing **2** with **4**. This observation implies that the observed solid-state structures are similar to the ones in DCM solution. Another influence of the phenyl substituents is the observed low-field shift of the proton signal in the CHR_2 -group, when comparing **1** and **2** with **3** and **4**.

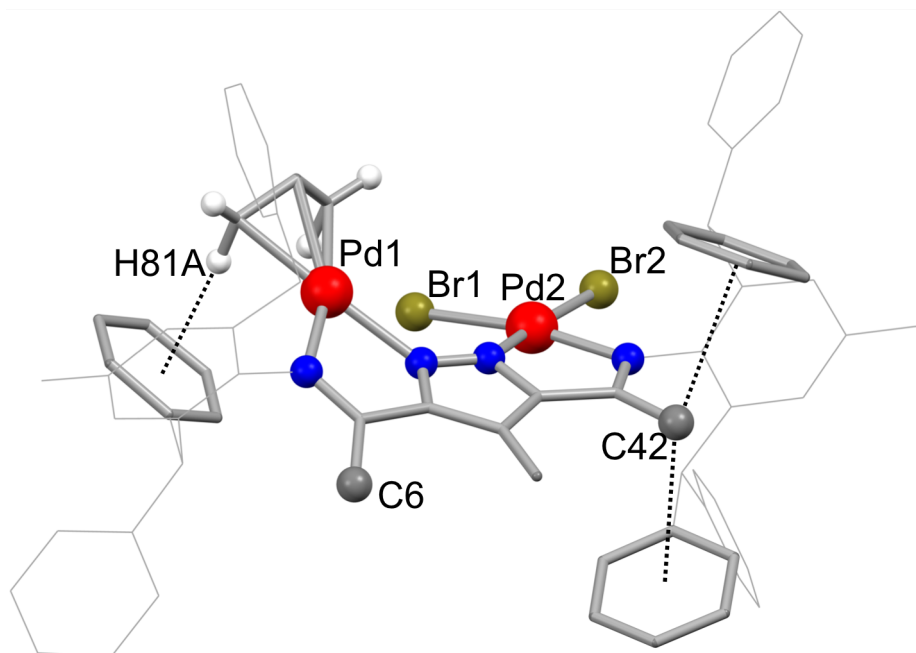


Figure 78: Molecular structure of the allyl $[L^{P^Ph} PdBr_2 Pd(C_3H_5)]$ (**4**) complex with the correlated interactions from NMR spectroscopy highlighted.¹⁸¹ Most hydrogen atoms were omitted for clarity.

The complexes **1** and **2** were observed to be thermally unstable in solution, if stored for several hours at temperatures $> -30^\circ C$. A signal at ca. 4 ppm in the 1H -NMR spectrum is the indicator of its decomposition. After longer periods of time in solution Pd(0) forms. The reductive elimination of allyl halide could be the cause. However, there was no allyl halide observed by 1H -NMR spectroscopy of the reaction mixture.

3.3. Kinetic measurements through EXSY experiments

To determine the exchange rates and the exchange constants of the allyl moiety in the complexes, EXSY-NMR experiments at different temperatures were performed to obtain a better understanding of the cooperative interactions between the metals. The diagonal and the cross signals in the EXSY-NMR spectra assigned to the allyl ligand were integrated and the absolute values of the integrated area were used to calculate

the exchange rates with EXSYCalc.²³⁷ In Figure 79 an example assignment of the allyl signals and the associated exchange within the EXSY experiment is depicted. Further details on the evaluation of the EXSY-NMR spectra can be found in Appendix A.2.6.

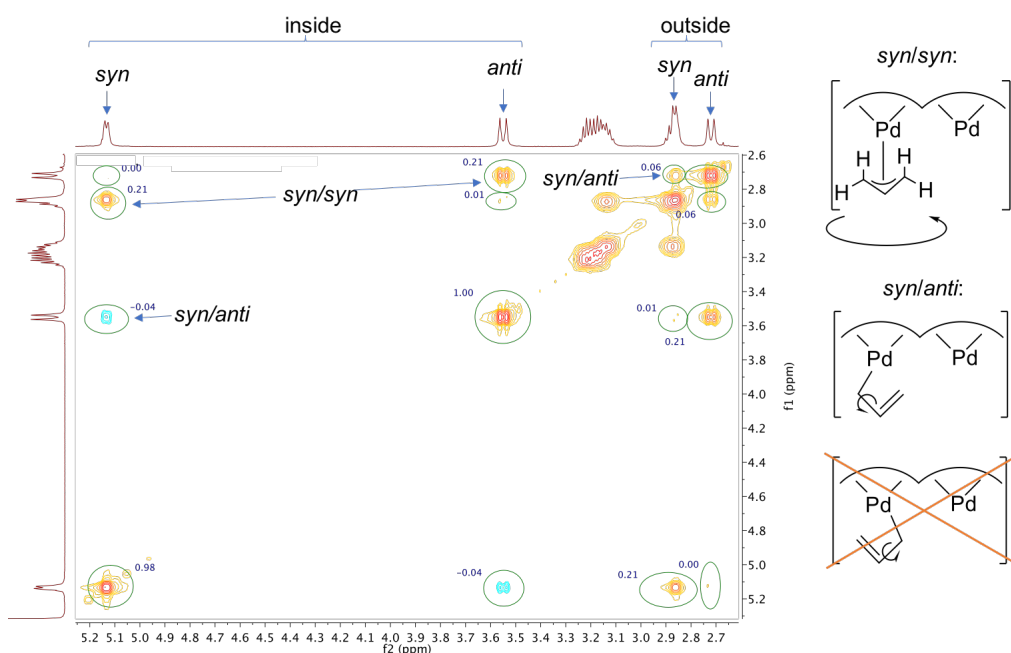


Figure 79: Allyl-section of the ^1H -ESXY-NMR spectrum in CD_2Cl_2 with assignment of the relevant signals.

In complex **4**, the heaviest of the four complexes, a NOE-dominated positive cross-peak signal can be observed, which decreases upon raising the temperature. The cross-peak signal of the *syn/anti* exchange on the inside of the complex are increasingly positive at decreasing temperatures. In complexes **1**, **2** and **3**, for all temperatures, a negative cross peak signal was observed with increasing intensity from **1** over **2** to **3** (at the same temperature). This does not exclude, but it is a strong indication that no *syn/anti* exchange on the inside of the complexes is occurring. However, on the outside of the allyl moiety a *syn/anti* exchange is occurring in all four complexes.

Nevertheless, the same influence of the NOE that is seen for the allyl protons on the inside should equally influence the allyl protons on the outside, due to equal distances. Thus, resulting in the necessity to correct the determined *syn/anti* exchange constants. This was done by subtraction of the determined exchange value (negative or positive) for the *syn/anti* exchange occurring on the inside, from the exchange value (positive) on the outside. The correction of the *syn/syn* exchange, due to the overlay with the NOE, was not necessary as ^{13}C -EXSY experiments showed (see Appendix A.2.5, Table 32 (top), Entries 10 and 12). These experiments allow the determination of the *syn/syn*

exchange with the NOE reduced by a factor of $4.4 \cdot 10^{-5}$.²³⁸ This explains the slightly higher values for the *syn/syn* exchange obtained by the two ¹³C-EXSY experiments. However, the *syn/anti* exchange cannot be observed in a ¹³C-EXSY experiment and the influence of the NOE cannot be avoided when measuring the *syn/anti* exchange. Furthermore, the theoretical relative value of the NOE, regarding the difference in distance between the *syn* ($\bar{d} = 4.061 \text{ \AA}$) and the *anti* positioned protons ($\bar{d} = 2.368 \text{ \AA}$) is only 4.2%.²³⁸

The exchange rates k determined for the complexes can be found in Table 21 for **1**, in Table 22 for **2**, in Table 23 for **3** and in Table 24 for **4**. Furthermore, the Gibbs free energy of activation was calculated from the exchange constants using eq. 3.²³⁹ The obtained values can be found in the previously mentioned tables, together with the exchange constants.

$$\Delta G^\ddagger = -\ln\left(\frac{kh}{k_B T}\right) \cdot RT \quad (3)$$

Table 21: Exchange rates determined for the *syn/anti* and the *syn/syn* exchange and the calculated Gibbs free energies of activation in complex **1**.

Entry	$T /$ °C	$d\delta /$ s	$k_{syn/anti}^{outside} /$ s ⁻¹	$k_{syn/syn} /$ s ⁻¹	$\Delta G^\ddagger_{syn/anti} /$ kJ/mol	$\Delta G^\ddagger_{syn/syn} /$ kJ/mol
1	-30	0.2	0.08±0.1	0.29±0.03	64±2	61.6±0.2
2	-25	0.1	0.07±0.1	0.45±0.04	66±3	62.0±0.2
3	-20	0.1	0.12±0.1	0.63±0.03	66±2	62.6±0.1
4	0	0.1	1.2±0.1	2.5±0.4	66.3±0.2	64.5±0.3
5	5	0.1	1.9±0.1	3.2±0.5	66.4±0.1	65.3±0.4
6	10	0.1	3.2±0.1	4.9±0.5	66.4±0.1	65.4±0.2
7	15	0.1	5.0±0.4	6.9±0.5	66.6±0.2	65.8±0.2
8	20	0.1	6.4±0.2	8.2±1	67.2±0.1	66.6±0.4

Table 22: Exchange rates determined for the *syn/anti* and the *syn/syn* exchange and the calculated Gibbs free energies of activation in complex **2**.

Entry	$T /$ °C	$d\delta /$ s	$k_{syn/anti}^{outside} /$ s ⁻¹	$k_{syn/syn} /$ s ⁻¹	$\Delta G^\ddagger_{syn/anti} /$ kJ/mol	$\Delta G^\ddagger_{syn/syn} /$ kJ/mol
1	-37	0.5	1.7±0.2	0.40±0.1	56.3±0.3	59.1±0.5
2	-30	0.2	4.3±0.4	0.46±0.1	56.1±0.2	60.7±0.3
3	-25	0.1	7.6±0.8	0.65±0.1	56.2±0.2	61.2±0.3
4	-20	0.1	11±1	1.6±0.6	56.6±0.2	60.6±0.8

Table 23: Exchange rates determined for the *syn/anti* and the *syn/syn* exchange and the calculated Gibbs free energies of activation in complex **3**.

Entry	$T /$ °C	$d\delta /$ s	$k_{syn/anti}^{outside} /$ s ⁻¹	$k_{syn/syn} /$ s ⁻¹	$\Delta G_{syn/anti}^{\ddagger} /$ kJ/mol	$\Delta G_{syn/syn}^{\ddagger} /$ kJ/mol
1	-37	0.5	0	0.10±0.05		62±1
2	-30	0.2	0.03±0.03	0.13±0.04		63.2±0.6
3	-25	0.1	0.06±0.09	0.19±0.04		63.8±0.4
4	-20	0.1	0.01±0.03	0.41±0.1		63.5±0.6
5	0	0.1	0.23±0.02	3.1±0.2	70.0±0.2	64.1±0.1
6	5	0.1	0.42±0.04	4.3±0.2	69.9±0.2	64.5±0.1
7	10	0.1	0.67±0.07	6.1±0.2	70.1±0.2	64.9±0.1
8	15	0.1	1.0±0.1	8.8±0.2	70.3±0.2	65.3±0.1

Table 24: Exchange rates determined for the *syn/anti* and the *syn/syn* exchange and the calculated Gibbs free energies of activation in complex **4**.

Entry	$T /$ °C	$d\delta /$ s	$k_{syn/anti}^{outside} /$ s ⁻¹	$k_{syn/syn} /$ s ⁻¹	$\Delta G_{syn/anti}^{\ddagger} /$ kJ/mol	$\Delta G_{syn/syn}^{\ddagger} /$ kJ/mol
1	-30	0.2	0.65±0.2	0.18±0.01	60.0±0.1	62.6±0.1
2	-25	0.1	1.3±0.2	0.23±0.01	59.8±0.1	63.4±0.1
3	-20	0.1	2.5±0.2	0.34±0.03	59.7±0.1	63.9±0.2
4	-15	0.05	4.5±0.5	0.29±0.05	59.6±0.2	65.5±0.4
5	-10	0.05	7.6±0.8	0.51±0.07	59.7±0.2	65.6±0.3
6	-5	0.02	13±1	0.80±0.1	59.7±0.2	65.9±0.4
7	0	0.02	20±2	1.3±0.1	59.8±0.2	66.1±0.1

The sterically more demanding ligand (in **3** and **4**) decreases the exchange rate for both exchange modes. This can be concluded by comparing the exchange rates of complexes **1** with **3** and the ones of **2** with **4**. The *syn/anti* exchange rates decrease by an average factor of 4.8 for the chloro complexes, comparing **1** with **3** (temperature range from 0 to 15 °C) and by a factor of 5.5 for the bromo complexes, comparing **2** with **4** (temperature range from -30 to -20 °C). For the *syn/syn* exchange the average factors are 1.3 for the chloro (**1** vs. **3**) and 3.4 for the bromo complexes (**2** vs. **4**). Comparison of the exchange rates between **1** and **2** as well as between **3** and **4** shows that the *syn/anti* exchange in the bromo species for both ligands ($L^{PI^{iPr}}$ and $L^{PI^{Ph}}$) is faster and the dominant exchange mechanism. Even more notable is the fact that the *syn/anti* exchange of the bromo complexes can be observed at temperatures as low as -37 °C, while for the chloro complexes, taking into account the error of the measurements, the *syn/anti* exchange slowly becomes observable at temperatures around 0 °C. At temperatures higher than 0 °C, where the data for the chloro complexes were recorded, the 1H -EXSY spectra of the bromo complexes are no longer reasonably evaluable.

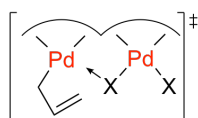


Figure 80: Proposed intermediate for the *syn/anti* exchange of the allyl moiety.

To explain this observation the intermediate species shown in Figure 80 is proposed. Such a species is reasonable since similar bridging μ -halide ligands are found in complexes such as $[L^{PI}Pd_2Cl_3]$, and thus the intermediate of the allyl moiety in a η^1 -coordinative fashion would be stabilized.²³⁶ In the solid-state structures the palladium ions are not in one plain with the ligand, forcing the rigid ligand to twist. This twist, represented by the Pd-N-N-Pd torsion angle, is stronger in the bromo complexes relative to the equivalent chloro complex, again due to the larger radius of the bromo moiety. Thus, this inner “tension” further decreases the ΔG^\ddagger values for the *syn/anti* exchange of the bromo moieties and increases the exchange rates. Such an intermediate could explain the influence of the metal-metal distance on the *syn/anti* exchange rates, with respect to the sterical difference between $L^{PI^{iPr}}$ and $L^{PI^{Ph}}$. The Pd-Pd distance of 4.35 Å of the $L^{PI^{iPr}}$ complexes is smaller in comparison to the 4.51 Å of the complex with $L^{PI^{Ph}}$. For this reason, it seems reasonable to assume the formation of the bridging intermediate (Figure 80) is energetically more favorable when the metals are in close proximity. Implying, that for the larger bromo moiety, the bridged intermediate will be more favorable than for the smaller chloro moiety. As a consequence, there is a *syn/anti* exchange of up to $k = 11 \text{ s}^{-1}$ ($T = -20 \text{ °C}$) observable for complex **2**, while

4, at the same temperature, only undergoes 2.5 exchanges per second. The same trend is obvious when comparing **1** and **3**. Finally, another possible consequence of the intermediate is the exclusive occurrence of the *syn/anti* exchanges on the outside of the allyl moiety, in addition to the previously discussed *trans*-influence. The η^1 -allyl state, which could theoretically occur on both sides, possibly is directed by the influence of the nearby halide ligand and its tendency to adopt a bridging position to only occur on the inside of the complexes, as shown in Figure 80.

The determined ΔG^\ddagger values for the three complexes (Table 21 to Table 24) are in good agreement with literature values of related complexes.^{176,224,229–232,235,240,241} However, most of the complexes from literature do not share high structural similarity, especially regarding the second metal in close proximity, coordinating a non-allyl moiety.¹⁷⁶ In order to determine the kinetic parameters ΔH^\ddagger for the allyl exchanges, Eyring plots, according to eq. 4, were examined. The ΔS^\ddagger values were determined from a plot of ΔG^\ddagger against T . Both plots can be found in Appendix A.2.7, the Eyring plot in Figure 119 and the plot of ΔG^\ddagger against T in Figure 120.

$$\ln\left(\frac{k}{T}\right) = -\frac{\Delta H^\ddagger}{RT} + \ln\left(\frac{k_B}{h}\right) + \frac{\Delta S^\ddagger}{R} \quad (4)$$

Table 25: Determined values for ΔH^\ddagger (in kJ/mol) and ΔS^\ddagger (in J mol⁻¹ K⁻¹) from the Eyring plots.

complex	$\Delta H^\ddagger_{syn/anti}$	$\Delta H^\ddagger_{syn/syn}$	$\Delta S^\ddagger_{syn/anti}$	$\Delta S^\ddagger_{syn/syn}$
1	53±3	38±0.5	-47±9	-96±2
2	51±5	29±13	-17±18	-125±57
3	63±3	44±0.9	-27±10	-58±7
4	62±1	35±2	-2±2	-72±5

The slope in the Eyring plots of the linear fit multiplied by $-R$ (R being the universal gas constant) resulted in the values for ΔH^\ddagger . The ΔS^\ddagger values are the slope of the linear fits of the plot of ΔG^\ddagger against T in Figure 120 (Appendix A.2.7) multiplied by -1 (see Table 25). The trends that are observable for the obtained values will be discussed in this paragraph. The enthalpy ΔH^\ddagger is smaller for the bromo complexes in comparison to their equivalent chloro species. This applies for *syn/syn* as well as the *syn/anti* exchange rates. The $\Delta H^\ddagger_{syn/anti}$ values are positive in a range of 51–63 kJ/mol. The $\Delta H^\ddagger_{syn/syn}$ values (range of 29–44 kJ/mol) are in average 22 kJ/mol smaller than the $\Delta H^\ddagger_{syn/anti}$ values, which is expected since the *syn/syn* exchange occurs for all complexes down to temperatures as low as -30°C . The ΔS^\ddagger values obtained for the *syn/syn* exchange are in a range of -58 down to -125 J mol⁻¹ K⁻¹, indicating that the associa-

tive mechanism for this process is the more probable one. The obtained ΔH^\ddagger and ΔS^\ddagger values for complexes **1**–**4** are similar to values in literature for other allyl-palladium complexes.^{176,224,229–232,235,240,241} However, the ΔH^\ddagger values in literature are in many cases smaller by a factor of two, probably due to the sterically higher demand of the ligands $L^{\text{PI}^i\text{Pr}}$ and $L^{\text{PI}^{\text{Ph}}}$ in comparison to the ones in literature.

The next step was to determine if the concentration of the complex in CD_2Cl_2 solution influences the *syn/syn* and the *syn/anti* exchange rates of the allyl moiety. For that purpose ^1H -EXSY experiments at constant temperature and mixing time, but different concentrations of the complexes **1** and **2**, were performed (see Table 26 and Table 27). From these experiments the following conclusions can be drawn: The *syn/anti* exchange rates have a very low concentration dependence, while the *syn/syn* exchange rates are strongly dependent on the concentration.

Table 26: Allyl exchange rate constants of the concentration-dependent measurements at 5 °C (mixing time $d\delta = 0.1$ s) for **1**.

Entry	c / mmol/l	$k_{\text{syn/anti}}$ / s^{-1}	$k_{\text{syn/syn}}$ / s^{-1}
1	20	1.9 ± 0.05	3.8
2	15	1.9 ± 0.05	3.4
3	10	1.9 ± 0.05	3.0
4	5	1.8 ± 0.05	2.4

Table 27: Allyl exchange rate constants of the concentration-dependent measurements at -20 °C ($d\delta = 0.1$ s) for **2**.

Entry	c / mmol/l	$k_{\text{syn/anti}}$ / s^{-1}	$k_{\text{syn/syn}}$ / s^{-1}
1	20	11 ± 0.4	2.5
2	19	11 ± 0.4	2.3
3	10^*	9.9 ± 0.4	1.5
4	5	9.5 ± 0.4	1.1

*: values resulting from an average of two measurements. Entries 1 and 2–4 were two different samples of complex **2**.

One hypothesis, explaining this phenomenon is the auto-dissociation of the halide ligands from the palladium, generating free halide ions. Such a dissociative equilibrium should shift towards dissociated species with a decrease of concentration. In an associative *syn/syn* exchange mechanism, this would lead to an increase of the exchange rate, as it was observed. A plot of $k_{\text{syn/syn}}$ vs. $c_0^{1/2}$ (assuming from the law of mass action:

$[\text{PdCl}_2] \gg [\text{Cl}] = [\text{PdCl}]$) results in a linear dependency (see Figure 81) supporting this hypothesis.

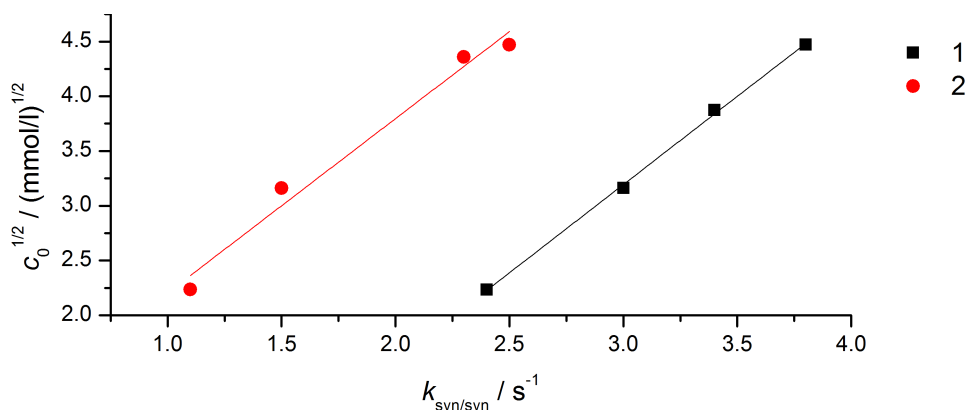


Figure 81: Plots of $c_0^{1/2}$ vs. $k_{syn/syn}$ of **1** and **2**.

3.3.1. Reversible complex exchange initiated by the presence of halide ions

To confirm the hypothesis that an associative *syn/syn* exchange mechanism takes place, an additional experiment was performed in which the influence of added halide ions was tested. To a solution of **1** in CD_2Cl_2 , 0.5 eq. of Bu_4NCl was added and temperature-dependent ^1H -EXSY experiments were performed. One of these spectra is displayed in Figure 82 and the determined exchange rate constants, together with the values for the Gibbs free energy, are listed in Table 28.

Table 28: Determined exchange constants k (in s^{-1}) for the *syn/anti*, the *syn/syn* and the complex-complex exchanges as well as the calculated Gibbs free energy ΔG^\ddagger (in kJ/mol) for the corresponding exchanges of the complex **1** with 0.5 eq. of Bu_4NCl .

$T / ^\circ\text{C}$	$d\delta / \text{s}$	$k_{syn/anti}$	$k_{syn/syn}$	$k_{c.e.}$	$\Delta G^\ddagger_{syn/anti}$	$\Delta G^\ddagger_{syn/syn}$	$\Delta G^\ddagger_{c.e.}$
-20	0.1	0.29 ± 0.1	10 ± 1	0.08 ± 0.08	64.3 ± 0.7	56.7 ± 0.2	66.9 ± 0.2
-10	0.1	0.68 ± 0.1	12 ± 1	0.28 ± 0.06	65.0 ± 0.3	58.7 ± 0.2	66.9 ± 0.2
0	0.1	1.3 ± 0.1	16 ± 2	0.59 ± 0.06	66.1 ± 0.2	60.4 ± 0.2	67.9 ± 0.2
10	0.05	3.5 ± 0.4	32 ± 3	1.6 ± 0.1	66.2 ± 0.2	61.0 ± 0.2	68.7 ± 0.2

c.e.: complex exchange.

The *syn/syn* exchange mechanism becomes strongly dominant over the *syn/anti* exchange, by the addition of chloride ions. This points towards an associative mechanism. The values for the *syn/anti* exchange remain similar to the ones determined for complex **1** without additional chloride ions. The kinetic parameters for ΔH^\ddagger and ΔS^\ddagger were

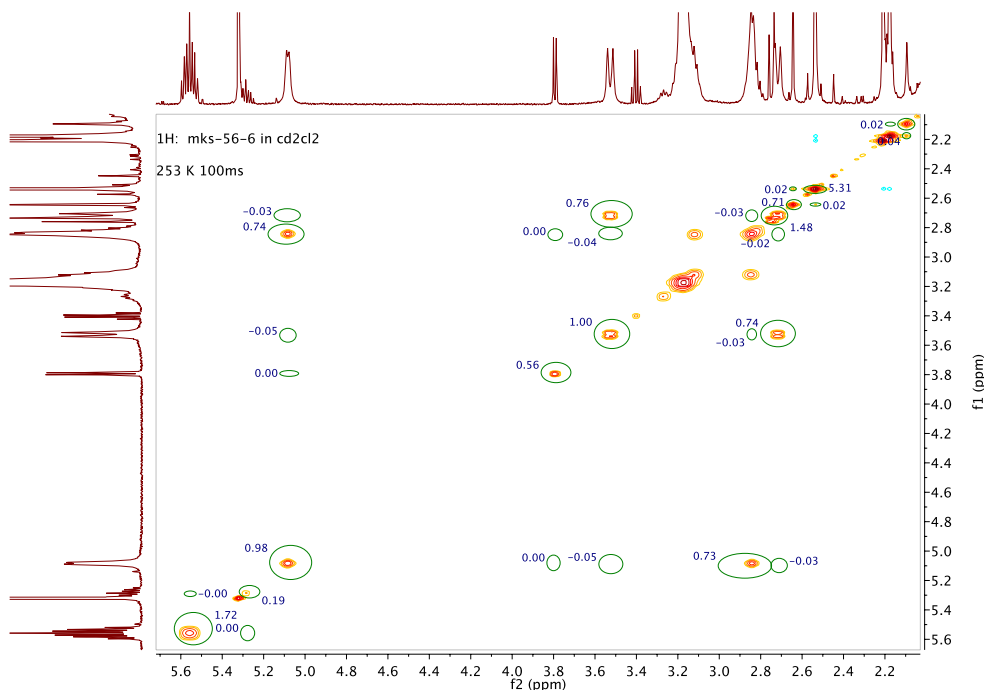
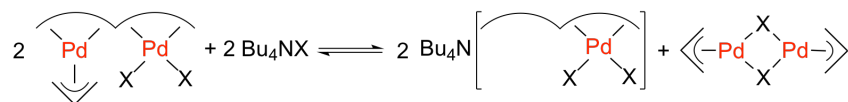


Figure 82: Part of the ^1H -EXSY spectrum at $-20\text{ }^\circ\text{C}$ of **1** with 0.5 eq. Bu_4NCl added.

obtained as previously described (see Appendix A.2.7 in Figure 121 and Figure 123), resulting in $\Delta H^\ddagger_{syn/anti} = 49 \pm 6 \text{ kJ/mol}$, $\Delta H^\ddagger_{syn/syn} = 19 \pm 6 \text{ kJ/mol}$, $\Delta S^\ddagger_{syn/anti} = -60 \pm 21 \text{ J mol}^{-1} \text{ K}^{-1}$ and $\Delta S^\ddagger_{syn/syn} = -149 \pm 21 \text{ J mol}^{-1} \text{ K}^{-1}$. Regarding the *syn/anti* exchange, the values for ΔH^\ddagger and ΔS^\ddagger decrease by $\Delta\Delta H^\ddagger = 4 \text{ kJ/mol}$ and $\Delta\Delta S^\ddagger = 13 \text{ J mol}^{-1} \text{ K}^{-1}$, while the values for the *syn/syn* exchange decrease by $\Delta\Delta H^\ddagger = 19 \text{ kJ/mol}$ and $\Delta\Delta S^\ddagger = 53 \text{ J mol}^{-1} \text{ K}^{-1}$, through the addition of chloride ions.

Interestingly, in addition to a strong increase in the *syn/syn* exchange rate, the formation of allyl-palladium(II)-chloride dimer can be observed (triplet of triplets at 5.29 ppm, doublet with 6.7 Hz coupling at 3.79 ppm and a doublet with 12 Hz coupling at 2.75 ppm, Figure 83 (middle)). Since the diagonal *anti*-positioned proton signal of the allylpalladium(II)-chloride dimer is overlaid with the allyl- $\text{H}_{anti, outside}$ signal of **1**, the integrated area of the diagonal signal was subtracted from the diagonal signal of the *syn* positioned proton signal of allylpalladium(II)-chloride dimer. Doing so, it was possible to determine the exchange constants and the Gibbs free energy for the complex/complex exchange between **1** and the allylpalladium(II)-chloride dimer. Using the previously performed ^1H -EXSY experiments enabled the access to the allyl exchange constants (see Table 28). From an Eyring plot (Appendix A.2.7 in Figure 122), the following kinetic values for the complex exchange were determined: $\Delta H^\ddagger_{c.e.} = 51 \pm 4 \text{ kJ/mol}$, $\Delta S^\ddagger_{c.e.} = -60 \pm 15 \text{ J mol}^{-1} \text{ K}^{-1}$. Resulting from the formation

of the allylpalladium(II)-chloride dimer a complex exchange as displayed in Scheme 35 can be proposed.



Scheme 35: Proposed complex exchange between the allyl complex and the allylpalladium(II)-chloride dimer.

In regards to the allyl exchange, the formation of the allylpalladium(II)-chloride dimer implies that a part of the observed *syn/syn* exchanges originate from the complex/complex exchange. The formation of the allylpalladium(II)-chloride dimer through the addition of chloride ions could also be observed for complex **3**. Furthermore, it could be shown that the formation of the allylpalladium(II)-chloride dimer is fully reversible. In Figure 83 a ^1H -NMR spectrum of **3** is displayed (bottom) to which 1 eq. of Bu_4NCl (middle) was added, leading to the formation of allylpalladium(II)-chloride dimer, effecting the allyl signals of **3** (see signals at 5.13, 4.99, 3.23, 2.53 and 1.61 ppm). Furthermore, the ligand-backbone signals are influenced by this equilibrium. The substituents at the aniline sidearms become homotop, which can be interpreted as the decoordination of an allyl moiety. This observation further supports the proposed equilibrium in Scheme 35. The addition of water, as a potential ligand, to a DCM solutions of the complexes did not have any impact on the exchange rates.

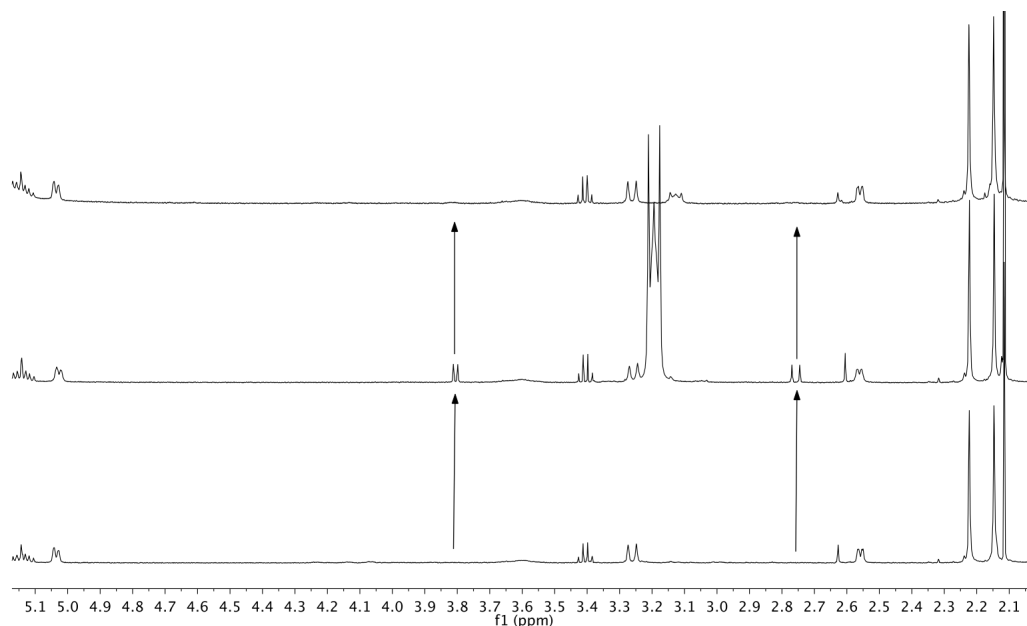


Figure 83: Section of the $^1\text{H-NMR}$ spectra (300 MHz) of **3** in CD_2Cl_2 (bottom). Addition of 1 eq. of Bu_4NCl (middle). After aqueous extraction of the Bu_4NCl and subsequent drying with MgSO_4 (top).

3.4. Summary and Outlook

In Summary, a new pyrazolate-based compartmental ligand with sterically very demanding side arms was synthesized and characterized. The new ligand $\text{L}^{\text{PI}^{\text{Ph}}}$ and the previously known $\text{L}^{\text{PI}^{\text{iPr}}}$ were used to prepare four new dipalladium complexes. Each complex features an allylpalladium unit next to a palladium dihalide unit. The allyl moiety was found to undergo both *syn/syn* and *syn/anti* exchanges. This enables the four complexes to be models for investigation cooperativity. The fluxual behavior of the allyl moieties can be interpreted as representative for the cooperative interactions (e.g. sterical interactions) within this type dinuclear complexes.

To further describe the cooperativity, the exchange rate constants as well as the activation parameters describing the allyl exchange were determined. It was found that the *syn/anti* exchange occurs exclusively on the outside of the complex. By comparing the exchange constants it could be shown that the sterical demand of the ligand scaffold and the metal–metal distance influence the allyl exchange rates. Most importantly, it could be shown that cooperative effects, mediated by the halide ligand, between the two metals take place, which strongly influence the allyl exchange. The intermediate (Figure 80) was proposed to explain the observed phenomena. Furthermore, it was possible to demonstrate that an associative *syn/syn* exchange takes place and that, the addition of halide ions triggers complete dissociation of the allylpalladium unit and a reversible formation of the allylpalladium(II)-halide dimer. A visual summary

is given in Figure 84. For future investigations the exchange of the palladium ions for other metal, e.g. nickel, could be investigated, to extend our understanding on cooperativity.

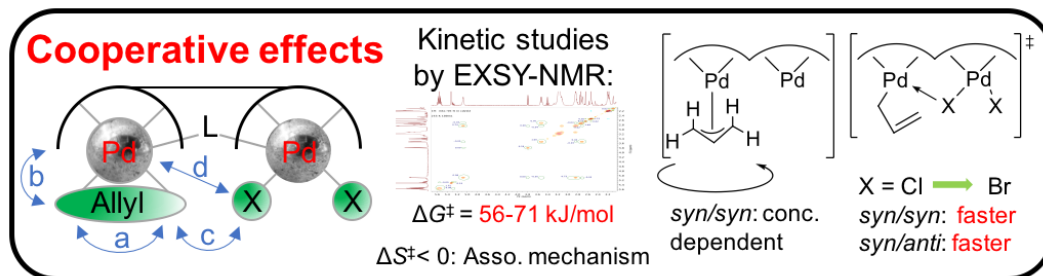


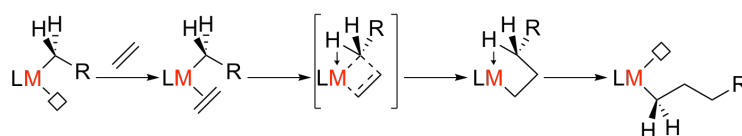
Figure 84: Summary of this chapter.

4. Chapter 3: Copolymerization Experiments of Ethylene and MMA Through a Nickel Complex

4.1. Introduction

4.1.1. Introduction to olefin polymerization

Polyolefins are the most produced plastic within the 300 million tonnes polymer industry. Europe is the second biggest producer of these materials, after China (thermoplastics and polyurethanes). Within Europe, Germany is by far the country with the highest demand in polymers of ca. 24.6% of the produced thermoplastics and polyurethanes (in 2015).⁸ Besides the step-growth approach, the chain-growth mechanism is used for the production of polymers.²⁴² The most prominent polymerizations that use the chain-growth mechanism are: the cationic and anionic polymerizations²⁴³, the radical polymerizations^{244–248} and the metal-site catalyzed polymerizations^{249–256}. The latter two are prominent in industry for polyolefin production (e.g. PE-LD, PE-LLD, PE-HD, PP, etc.). While in the radical approach high pressure and temperature are applied, the metal catalyzed polymerizations use e.g. the Ziegler-Natta or Phillips catalysts. Each approach yields polymers with different material properties and applications, depending on e.g. the micro-structure, crystallinity, molecular weight and/or molecular weight distribution. Highly branched polyethylene is obtained through free radical polymerization, while the metal-catalyzed polyethylene synthesis has a wider portfolio of products including PE-HD, PE-MD and PE-LLD. This illustrates a higher level of control *via* the catalytic approach under milder reaction conditions.²⁵⁷



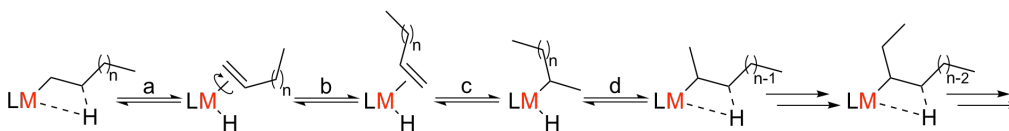
Scheme 36: Proposed Cossee-Arlman mechanism for the α -olefin polymerization.²⁵⁸

The Cossee-Arlman mechanism (see Scheme 36) is the consensus mechanism for the propagation of the olefin polymerization, e.g., found for the Ziegler-Natta or Phillips catalysts.^{259,260}

Industrially applied catalysts for the olefin polymerization are based on early- or mid-transition metals, rendering them oxophilic. The resistance of late transition metals towards polar moieties can be beneficial, not only, in respect of tolerance to impurities, but also making them potential candidates for the copolymerization with polar

monomers.²⁵³ Many comprehensive books, reviews and publications have been written on the topic of olefin polymerization^{261–263} and also on the application of late transition metals.^{263–267}

Another mechanism that is known to occur in the olefin polymerization with late transition metals is the so called “chain walking”. In Scheme 37 the proposed mechanism is depicted. The result of its occurrence are short branches within the polymer. However, there are also examples where the chain walking mechanism was used to form linear PE *via* ω ,1-enchainment from higher α -olefins.²⁶⁷ Long branches can form, when a π -bound olefin (e.g. see Scheme 37) decoordinates and is incorporated into another growing polymer chain.



Scheme 37: The proposed mechanism of the chain walking.^{268–270} a: β -hydride elimination, b: rotation, c: hydride retransfer, d: rotation.

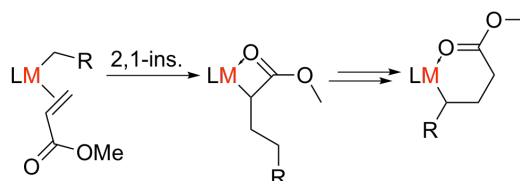
The concept of cooperativity has also been applied for olefin polymerization. The works of Marks *et al.* should be mentioned in this context, due to their great contributions to this field and the understanding of cooperativity in general.^{185,271–275}

4.1.2. Copolymerization of ethylene with polar monomers

Polyethylene is utilized in a broad variety of applications, however, to even further extend this scope the controlled copolymerization with polar monomers (e.g. methyl methacrylate) is desirable. Currently the free-radical copolymerization is used, lacking a control over the formation of the product. In the catalytic approach the oxophilic nature of early transition metals directs research towards the application of late transition metals, avoiding the need of introducing protecting groups for polar functionalities prior to conversion.^{276–278} A controlled incorporation of polar monomers into polyethylene would allow a fine-tuning of material properties such as adhesion, robustness, permeability, crystallinity as well as surface-related characteristics.

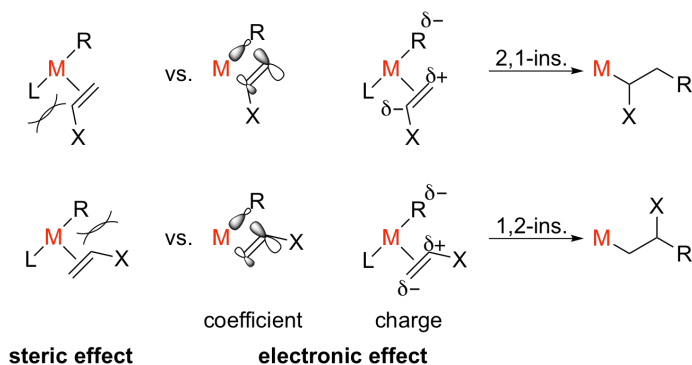
The endeavor for a coordination-metal-catalyzed incorporation of polar monomers, e.g. acrylates, gave rise to some challenges that need to be faced. Brookhart *et al.* demonstrated that back biting of the polar moiety onto the catalytic center hinders the coordination of a subsequent monomer unit (see Scheme 38).^{265,279} After the coordination and 2,1-insertion of the acrylate monomer, the formed four-membered ring was

found to rearrange to a six-membered one.²⁸⁰ Either of these cyclic intermediates interfere with the propagation reaction. As a consequence, a strong retardation of the rate or even suppression of activity has been observed, due to the presence of polar monomers.^{281–290}



Scheme 38: Backbiting illustrated with MA. MA performs a 2,1-insertion yielding a chelating ligand that blocks the free coordination site.^{265,279} The displayed four-membered species rearranges to a six-membered one, both preventing the coordination of the subsequent olefin unit.²⁹¹

Another challenge associated with the preferential 2,1-insertion of acrylates into the metal-carbon bond is caused by their electronic effects (see Scheme 39).^{291,292} As a general rule, electron-deficient monomers undergo a 2,1-insertion while electron-rich ones prefer a 1,2-insertion. However, on account of steric effects, a 2,1-insertion of single substituted ether units was observed.^{292,293} A 1,2-insertion of MA can be favored with bulky ligands, while electronically the 2,1-insertion is preferred.²⁹⁴



Scheme 39: Origin of the regioselectivity for the insertion of vinyl monomers into metal-alkyl bonds.²⁹² X = polar group.

The factors that influence the insertion are: the monomer distortion in the transition state (directing to 2,1-ins.), steric effects between ligand and monomer^{295,296}, interaction of the LUMO orbital at the metal with the sp^2 hybridized carbon atoms of the monomer²⁹³, and the overall polar momentum during the transition state. The dominating factor will direct the insertion mechanism. For example in propylene and vinyl ether the different electronic configuration at the sp^2 carbon atoms cause a 1,2-insertion.²⁹³ Comparable orbital coefficients yield in a 2,1-insertion in electron-density

poor monomer (see Scheme 39).²⁹³ For the latter, the 2,1-insertion yields a newly formed α -carbon which is electron deficient.²⁹² This is a disadvantage, because an intramolecular nucleophilic attack mechanism of the polymer chain leads to the insertion of the subsequent olefin unit, which occurs better with an electronic rich α -carbon atom.²⁹⁷ Therefore, the catalyst is further deactivated. An electron rich neutral catalyst can be used to counteract on this effect. However, an anionic complex can also be counterproductive, as it might impede the initial coordination of the monomers. An different strategy is the introduction of sterically demanding groups at the ligand to circumvent a 2,1-insertion.^{292,297,298}

The mechanism of olefin polymerization (Scheme 36), chain walking (Scheme 37), backbiting of polar monomers (Scheme 38) as well as their cause of regioselectivity (Scheme 39) have been illustrated. All of the above need to be considered for the development of efficient copolymerization catalysts. Some breakthroughs have been made in the field of olefin polymerization and their copolymerizing with polar monomers within the last decades. Selected examples will be presented in the next section to give an impression of the state-of-the-art catalysts. It has to be kept in mind that an activation with MAO or MMAO is necessary for some complexes to be transformed into the active species.²⁹⁹⁻³⁰⁵

4.1.3. Prominent late transition metal catalysts for the polymerization of olefins and their copolymerization with polar monomers

In this section a small selection of catalysts will be presented from the vast variety of catalysts that have been investigated in the field of olefin polymerization and olefin copolymerization. Mononuclear systems will be presented first and then systems with more than one active center will be presented.

Many outstanding catalyst systems are known to literature and only a small fraction can be presented in this chapter. For more in-depth discussion one should go through the comprehensive books and reviews published on this topic^{253,262,263,302,306-308} and the references within. The selection of mononuclear (pre)catalysts that will be briefly presented in this work is depicted in Figure 85.

A very prominent catalyst which is able to copolymerize methyl acrylate (MA) with ethylene was published by Brookhart *et al.*^{264,280,309-312} It was demonstrated that MA is predominantly found as terminal unit of branches within the PE and not as part of the backbone. This implies that after the incorporation of a MA unit the active center needs to move away from the polar functionality *via* chain-walking for the chain-growth

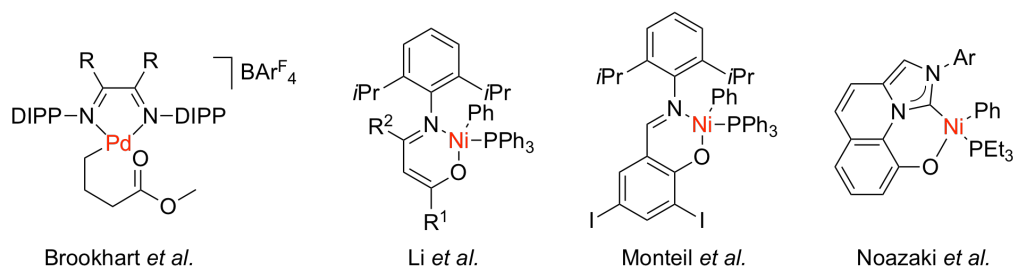


Figure 85: Selection of mononuclear (pre)catalysts that are known to literature for the olefin polymerization and their copolymerization with polar monomers.

to continue. The depicted α -diimine catalyst (Figure 85, left) and similar systems have been investigated intensively and it was found that the copolymerization properties depend strongly on the backbone substituents R.^{294,311–313} A broad range of monomers could be copolymerized with ethylene, and just recently the copolymerization of ethylene and vinylalkoxysilanes was discovered with α -diimine catalysts (Pd and Ni).^{314,315} The second complex on the left in Figure 85 features a ketone-imine ligand. This family of complexes are also able to copolymerize acrylates with olefines. The complex in Figure 85 was investigated for its copolymerization activity by Li *et al.*³¹⁶ After its activation with MMAO it provides an activity of $0.12\text{--}2.65\text{ g mmol}^{-1}\text{ h}^{-1}\text{ bar}^{-1}$ while incorporating 1–17% MMA into the PE.

The catalyst reported by Monteil *et al.* (second from the right in Figure 85), represents the class of phenoxy-imine catalysts. It is able to copolymerize ethylene with MMA.³¹⁷ However, in the publication a radical mechanism is suggested. This is in contrast to the expected coordination-insertion mechanism, which is common for most nickel systems. The radical species is assumed to originate from a homolytic Ni–C bond cleavage. This example is illustrated in order to emphasize that the reaction mechanism needs to be evaluated carefully. This not only applies for nickel but also for other metals such as palladium, where radical mechanisms were found to be active and the origin of catalytic activity in homo- and copolymerizations.^{307,318,319}

The last catalyst that is shown in Figure 85 was published by Nozaki *et al.* in 2016.²⁸² It is part of a series of Ni/IzQO complexes that are able to copolymerize a range of polar monomers. However, it was not able to do so with MA, emphasizing that until today the incorporation of acrylates remains a challenge.

There have been many approaches to solve the problems associated with these polar monomer. Marks *et al.* demonstrated that a SO_2 -groups in close proximity to the metal center is beneficial for the olefin polymerization, due to a stabilizing effect (interaction b/d in Figure 1).³²⁵ In 2017 it could be demonstrated that even the copolymerization

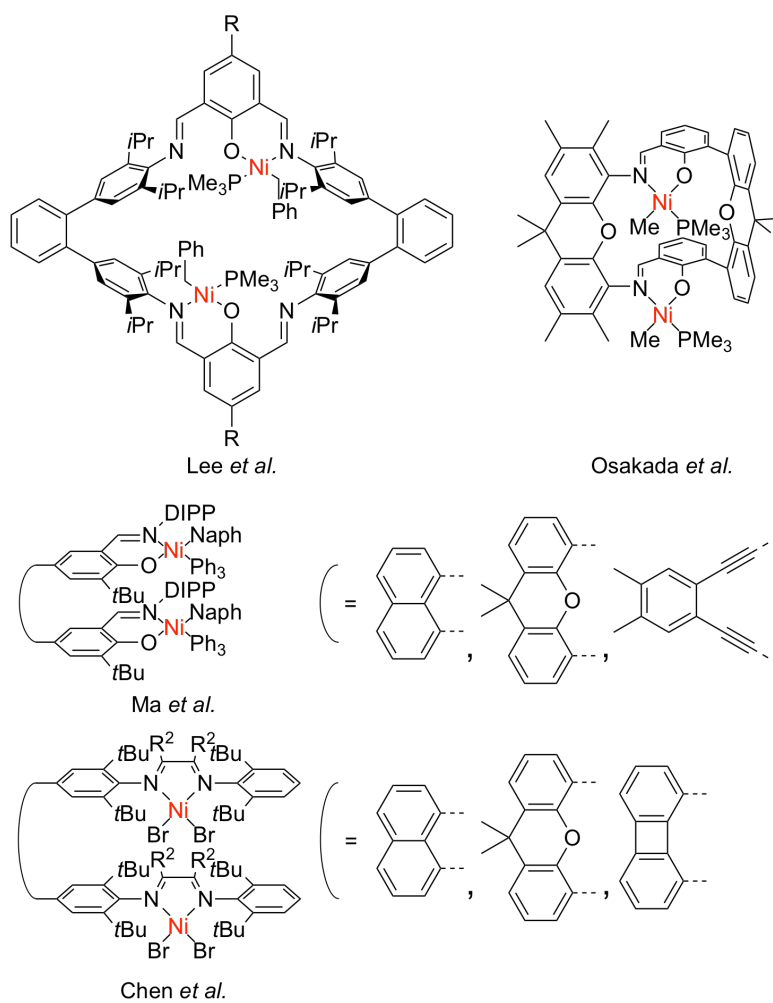


Figure 86: Selection of dinuclear (pre)catalysts from literature for the olefin polymerization and its copolymerization with polar monomers.^{320–324} Complex by Lee *et al.* with $R = \text{H}, \text{Me}, \text{F}$.³²⁰ Complex by Chen *et al.* with $R^2 = \text{Me}, \text{Naph}$.³²³

of ethylene and MA was possible through this strategy.³²⁶

A different strategic approach involved the formation of a H-bond with the acrylate substrate, in proximity to the active site.^{327,328} By this H-bonding interaction the tendency of back biting from the polar monomers is supposed to decrease, resulting in an increased copolymerization capability (interaction b in Figure 1).

Chen *et al.* addressed the associated challenge in regard of polar monomers with a second-coordination-sphere strategy.²⁹⁰ They developed different α -diimine catalysts that copolymerize, among other polar monomers, MA and ethylene.

As last strategy presented, takes advantage of a small M–M distance, increasing bimetallic effects and leading to a slower β -H elimination as well as a higher tolerance for polar monomers.³²² Guided by this benefit, the development of dinuclear catalysts has become a center of interest to various research groups. In this work the focus will be on the latter strategy. Therefore, in Figure 86 a selection of recently published dinuclear catalysts is given.

The first catalyst depicted (Figure 86, top left) was published by Lee *et al.* It can be interpreted as a dinuclear version of the phenoxy-imine systems. The catalyst was found to produce PE with M_w values up to 38000 g/mol, dispersity values in the range of 5.1–9.4 and activities up to 620 kg/molNi/h have been measured.³²⁰ The salicylaldimine nickel catalyst developed by Osakada *et al.* shares structural similarities with Lee’s catalyst. It demonstrated activities of 2.1 kg/molNi/h for PE. This catalysts was tested for copolymerization experiments with various monomers and incorporation into PE was found for the monomers: 1,6-heptadiene (3.6 mol %), 1,7-octadiene (2.0 mol %), 2,2-diallyl-5,5-dimethyl-1,3-dioxane (1.8 mol %), tert-butyl butenoate (1.4 mol %), ethyl pentenoate (0.4 mol %) and 5-norbornene-2-carboxylic acid methyl ester (4.1 mol %).^{321,329} However, the catalyst was not able to incorporate MA.

In 2016, Ma *et al.* published a series of complexes that are able to copolymerize ethylene with vinyl acetate, allyl acetate and vinyl pivalate; all three substrates are considered challenging to copolymerize.^{322,330} Nevertheless, none of these dinuclear approaches reported a successful copolymerization of MA or MMA. The mononuclear system of Bookhart *et al.* (see Figure 85) was reported to be successful in copolymerizing acrylates. Therefore, the idea of generating a dinuclear system based on the α -diimine catalyst seems appealing. Chen *et al.* pursuit this idea and designed a new catalyst depicted on the bottom of Figure 85.^{323,324} These catalysts showed a high

4.2 OBJECTIVE OF THIS WORK ON THE COPOLYMERIZATION OF ETHYLENE WITH METHYL METHACRYLATE

activity for the homopolymerization of ethylene with up to 500 kg/molNi/h at 80 °C. The cooperative effects between the nickel atoms were suggested to be the cause for a slow β -H elimination and chain walking. Additionally, this cooperativity yielded in a low branching density for the resulting PE.³²³ The complexes were tested for copolymerizing ethylene and MA.³²⁴ The corresponding palladium complexes were found to maintain activity for the homopolymerization in the presence of MA. Surprisingly, none of the MA was found to be incorporated. However, they could confirmed the successful incorporation of MA into PE by the system of Brookhart.³²⁴

The dinuclear examples in Figure 86 have in common, that they form two parallel plains by each metal and its coordinating atoms. A different topology, with both metals and the ligand backbone in one plain, was published in 2006 by Meyer *et al.*²³⁶ The metals were bridged by a pyrazolate ligand and the complex was found to be active for the ethylene polymerization, after activation with MAO. However, its applicability for the copolymerization with polar monomers has not been investigated yet. This is not the first system, were this type of topology was tested³³¹, however, there are very few pyrazolate bridged systems that have been applied for copolymerizations of polar monomers.³³²

4.2. Objective of this Work on the Copolymerization of Ethylene with Methyl Methacrylate

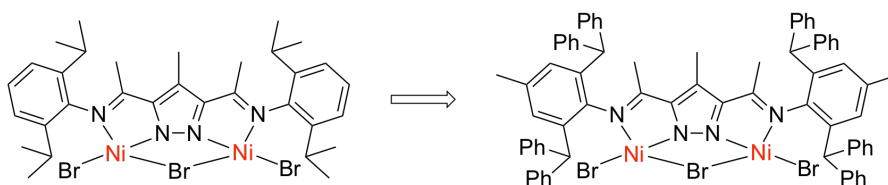
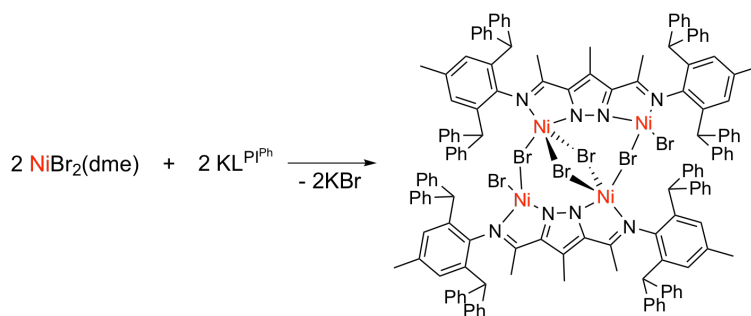


Figure 87: Complex published by Meyer *et al.* (left) and the complex isolated during my master thesis (right).¹⁸¹ The structures depicted are only a suggestion at this point.

The objective of this chapter is to explore the potential of pyrazolate bridged bimetallic complexes, that was isolated during my master thesis, for olefin polymerization and copolymerization.¹⁸¹ The system is inspired by, and closely related to, the complex that was published in 2006 by Meyer *et al.*²³⁶ and that is suggested to be a dinuclear mimic of the Brookhart system with the metals and the ligand backbone in one plain. The new complex features very bulky aryl moieties to shield the upper and lower sphere of the complex (Figure 87). This new nickel complex will be further analyzed and then

tested for its applicability for the polymerization of ethylene and MMA as well as for the copolymerization of both monomers.

4.3. Synthesis and characterization of the $[L^{PI^{Ph}}Ni_2Br_3]_2$ complex



Scheme 40: Synthesis of $[L^{PI^{Ph}}Ni_2Br_3]_2$.

In order to isolate the target nickel complex the synthetic route shown in Scheme 40 was followed. The reaction was performed in DCM and the deprotonation of the ligand was done by $KOtBu$. This synthesis of the corresponding chloro complex was first described during my master thesis.¹⁸¹ However, very limited structural information for the complexes was described within that work. In this work the characterization of the complex will be continued.

The first new structural information, that will be discussed, has been shown in Figure 88. The displayed molecular structure was obtained from crystallization attempts. However, residual electron density could not be assigned when the crystal structure was solved, however, a vast structural idea of $[L^{PI^{Ph}}Ni_2Br_3]_2$ can be obtained.

The numerous attempts, to obtain better crystals of $[L^{PI^{Ph}}Ni_2Br_3]_2$, failed. In order to further support the tetranuclearity of the complex in the solid state, crystallization attempts of the corresponding copper complexes were performed. Copper can be assumed to coordinate in a similar fashion. The crystallization of the copper complex was successful and yielded in the molecular structure shown in Figure 89. Selected atom distances can be found in Table 29 and the corresponding bond angles are given in the Appendix. In Table 29 also the atom distanced from the molecular structure of $[L^{PI^{Ph}}Ni_2Br_3]_2$ in Figure 88 are given. However, the obtained atom distances within $[L^{PI^{Ph}}Ni_2Br_3]_2$ should only be assumed as an estimation. The corresponding bond lengths within the copper and nickel complex are similar, however, the ones within the nickel complex show a trend to slightly larger values (see Table 29). Furthermore, the

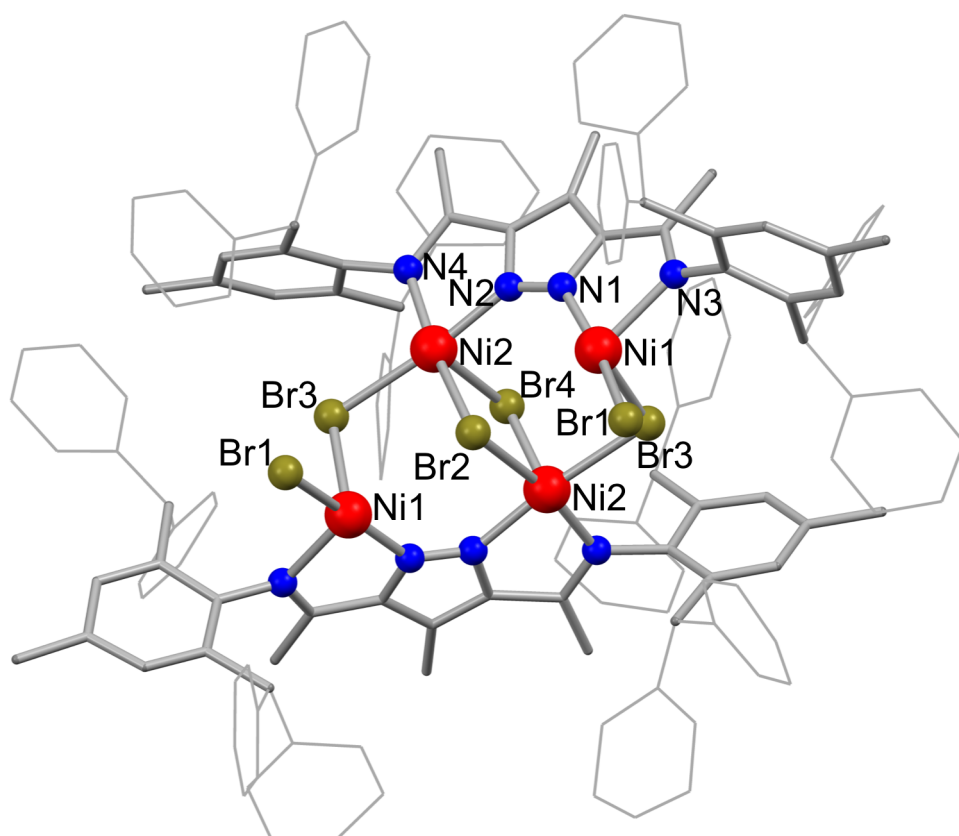


Figure 88: Picture of $[L^{PI^h}Ni_2Br_3]_2$ obtained from a crystallization attempt. Hydrogen atoms were omitted for clarity.

copper and the nickel complex show a highly similar structural motif (see Figure 88, Figure 89 and Table 29). Such a tetranuclear structure can therefore be assumed to be the most likely for the nickel complex in the solid state. The structural motif suggested in Figure 87 can also be found within the two molecular structures of Figure 88 and Figure 89. For a better illustration the asymmetric unit of the copper complex is displayed in Figure 90. Without the Cl4 atom the structure highly resembles the one suggested in Figure 87. This substructure can also be found within the nickel complex. None of the Ni(II) ions in Figure 88 show the preferred squared planar coordination environment, therefore the complex should be paramagnetic. The metal–metal distance of two pyrazolate-bridged metals found within the complexes is 4.105 Å for the nickel complex (Figure 88) and 4.015 Å for the copper complex (Figure 89).

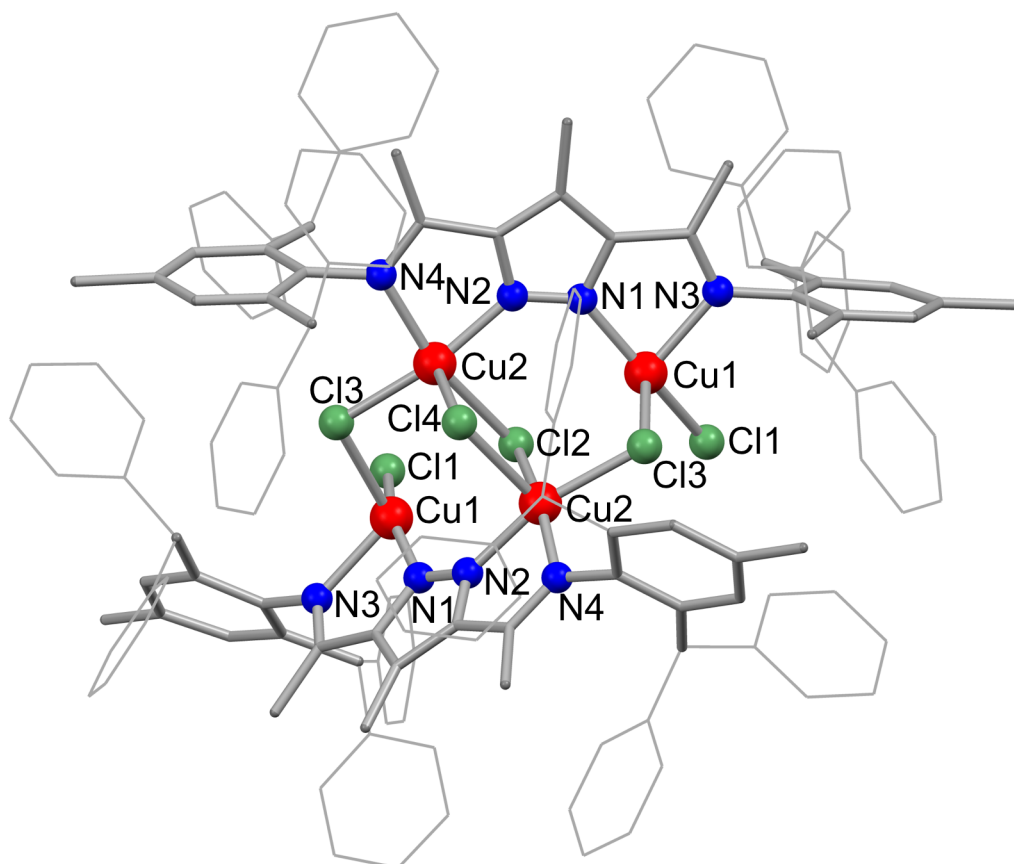


Figure 89: Molecular structure of $[L^{\text{PIPh}}\text{Cu}_2\text{Cl}_3]_2$. The synthesis was performed corresponding to complex $[L^{\text{PIPh}}\text{Ni}_2\text{Br}_3]_2$ using CuCl_2 instead of NiBr_2 . Hydrogen atoms were omitted for clarity.

For the application in homogeneous catalysis, the aggregation of the complex in solution is, however, of higher importance. NMR experiments of the paramagnetic nickel

Table 29: Selected atom distances [\AA] (sorted) of $[\text{L}^{\text{PI}^{\text{Ph}}}\text{Cu}_2\text{Cl}_3]_2$ (see Figure 89). The corresponding bond angles can be found in the Appendix. For comparison the atom distances from the molecular structure of $[\text{L}^{\text{PI}^{\text{Ph}}}\text{Ni}_2\text{Br}_3]_2$ in Figure 88 are given (estimations).

Atoms	Distance	Atoms	Distance
Cu2–N2	1.931(5)	Ni2–N2	1.985
Cu1–N1	1.933(5)	Ni1–N1	1.956
Cu2–N4	2.054(5)	Ni2–N4	2.021
Cu1–N3	2.062(6)	Ni1–N3	2.136
Cu1–Cl1	2.1670(19)	Ni1–Br1	2.344
Cu2–Cl3	2.2394(17)	Ni2–Br3	2.493
Cu1–Cl3'	2.4237(18)	Ni1–Br3	2.502
Cl4–Cu2'	2.4317(17)	Br4–Ni2	2.496
Cu2–Cl4	2.4319(17)	Ni2–Br4	2.496
Cl2–Cu2'	2.4402(18)	Br2–Ni2	2.547
Cu2–Cl2	2.4403(18)	Ni2–Br2	2.547

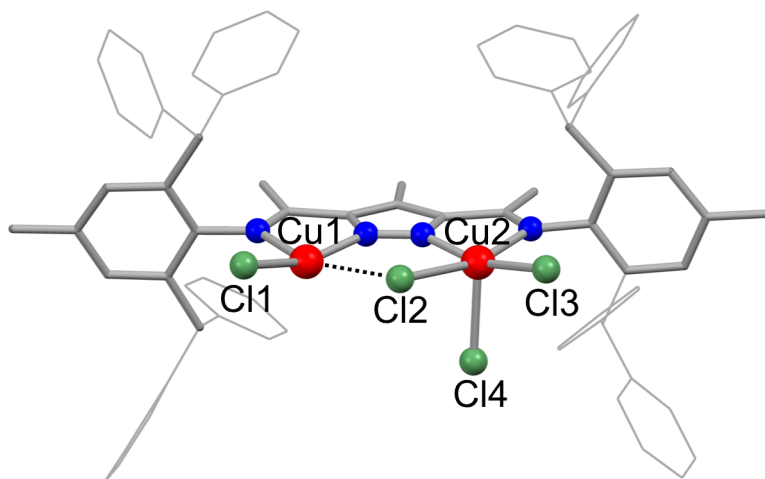


Figure 90: Asymmetric unit of the molecular structure of $[\text{L}^{\text{PI}^{\text{Ph}}}\text{Cu}_2\text{Cl}_3]_2$. Hydrogen atoms were omitted for clarity.

compound were performed and in Appendix A.2.8 in Figure 125 the paramagnetic $^1\text{H-NMR}$ spectrum of $[\text{L}^{\text{PI}^{\text{Ph}}}\text{Ni}_2\text{Br}_3]_2$ in CD_3CN is depicted. However, no structural information can be obtained from this spectrum. To identify the aggregation of the complex in solution a paramagnetic DOSY-NMR experiment was performed (Appendix A.2.8 in Figure 126). From this experiment, using the T_1/T_2 relaxation of the complex signals, the diffusion coefficient of the major species was obtained using the TopSpin software from Bruker and by averaging the diffusion coefficients determined at several different chemical shifts of the species. This method was also used and described in sections 2.4.1 and 2.6.1. A diffusion coefficient value of $D = 7.133 \times 10^{-10} \text{ m}^2/\text{s}$ was determined. In the DOSY-NMR measurement no internal standard was added, however, a determination of the molecular weight in solution was possible by using the residual proton signal of the solvent CD_3CN .^{143,144} This residual proton signal was sufficiently separated from the complex signals and its diffusion coefficient was determined to be $D = 3.932 \times 10^{-9} \text{ m}^2/\text{s}$. Comparing these two diffusion coefficients a molecular mass value of $M_{\text{Merge}} = 1400 \text{ g/mol}$ was estimated for the nickel complex of $[\text{L}^{\text{PI}^{\text{Ph}}}]^-$ in CD_3CN solution, for a merged geometry. This corresponds to the dinuclear nickel complex ($M = 1365 \text{ g/mol}$ for $\text{C}_{74}\text{H}_{63}\text{Br}_3\text{N}_4\text{Ni}_2$), with an error of -2% .

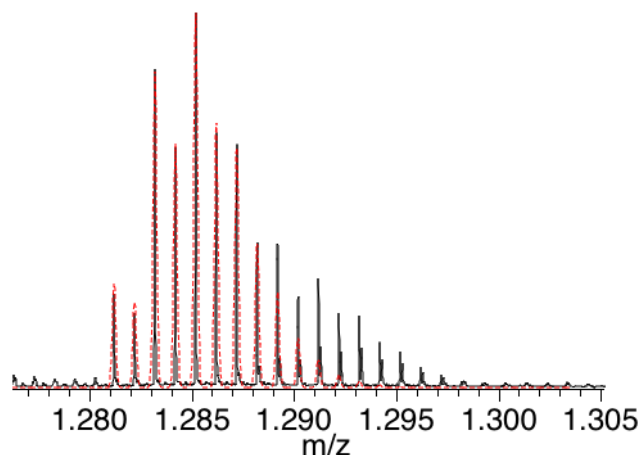


Figure 91: ESI-MS (positive mode) of $[\text{L}^{\text{PI}^{\text{Ph}}}\text{Ni}_2\text{Br}_3]_2$ in MeOH. Signal assigned to the $[\text{M}-\text{Br}]^+$ species, with M describing a $[\text{LNi}_2\text{Br}_3]$ species. Black line: experimental data. Red line: simulated spectrum for $\text{C}_{74}\text{H}_{63}\text{Br}_2\text{N}_4\text{Ni}_2$.

In order to further support the monomeric (dinuclear) aggregation in solution, mass spectrometric experiments were performed. In ESI-MS experiments the $[\text{M}-\text{Br}]^+$ species, with M being a monomeric form $[\text{LNi}_2\text{Br}_3]$, was observed (see Figure 91). The expected isotopic pattern for such a species (shown in red) is in good agreement with the experimental data (black line). The corresponding dimeric (tetranuclear) species

4.4 APPLICATION OF THE $[L^{PI^{Ph}}Ni_2Br_3]_2$ COMPLEX FOR THE OLEFIN POLYMERIZATION AND COPOLYMERIZATION

of $[M-Br]^+$ with $M = [LNi_2Br_3]_2$ was not observed.

Finally it is worth mentioning, that the nickel complex shows a solvatochromic effect (see Figure 92), which is a well known phenomena for nickel complexes.³³³



Figure 92: The complex $[L^{PI^{Ph}}Ni_2Br_3]_2$ in a crystallization attempt in toluene (left) and in the coordinating solvent MeCN (right).

To sum up, even though no high resolution crystal structure of the complex was obtained, structural information could be gathered. Experimental evidence suggests the presence of a dinuclear nickel complex in MeCN solution, supported by MS- and DOSY-NMR experiments, and a tetranuclear species in the solid state, supported by a low resolution crystal structure of the complex and a crystal structure of the corresponding copper complex.

In the next section the potential of the complex for the homopolymerization of ethylene and MMA as well as for the copolymerization of both will be explored.

4.4. Application of the $[L^{PI^{Ph}}Ni_2Br_3]_2$ complex for the olefin polymerization and copolymerization

A catalyst that is supposed to copolymerize ethylene and MMA needs to be able to perform the homopolymerization of each monomer separately as well. For that reason, the activity for the polymerization of ethylene and MMA were tested first, and then the copolymerization was attempted.

The polymerization of ethylene was performed in a BüchiGlasUster glass pressure vessel holding 200 mL. Toluene (ca. 70 mL) was used as solvent for the reaction and either 5 or 10 bar of ethylene were applied at either 5 °C or at room temperature. The reactions were allowed to run for 1 h and ca. 1000 eq. of MAO as co-catalyst were added to form the active species from the precatalyst. The results of the polymerization experiments with ethylene are summarized in Table 30 (top). The *TOF* values observed for the catalyst are in a range of 5878–19015 h⁻¹.

Table 30: Obtained results for applying $[L^{P^{Ph}}Ni_2Br_3]_2$ for the homopolymerization of ethylene[†] (top) and methyl methacrylate (middle) and the copolymerization[†] of both monomers (bottom).

Entry	$p_{C_2H_4}$ / bar	T / °C	t / h	[cat.] [‡] / mM	[MAO]:[cat.] [‡]	[MMA]:[cat.] [‡]	m (PE) / mg	$TON^{\ddagger\text{E}}$	TOF^f / h ⁻¹
1	10	25	1	$8.8 \cdot 10^{-2}$	1014	-	2500	19015	19015
2	10	5	1	$6.6 \cdot 10^{-2}$	1008	-	1490	15432	15432
3	5	23	1	$7.8 \cdot 10^{-2}$	1343	-	1111	5878	5878

Entry	$p_{C_2H_4}$ / bar	T / °C	t / h	[cat.] [‡] / mM	[MAO]:[cat.] [‡]	[MMA]:[cat.] [‡]	m (PMMA) / mg	$TON^{\ddagger\text{E}}$	TOF^f / h ⁻¹
4*	-	23	44.5	$8.1 \cdot 10^{-1}$	936	5827	714	1475	33

Entry	$p_{C_2H_4}$ / bar	T / °C	t / h	[cat.] / mM	[MAO]:[cat.]	[MMA]:[cat.]	m (polymer) / mg	$TON^{\ddagger\text{E}}$	TOF^f / h ⁻¹
5	5	23	18.7	$2.8 \cdot 10^{-2}$	1297	1662	737	13288	712
6	10	25	20	$6.4 \cdot 10^{-2}$	1075	948	3200	33864	1693
7	10	5	16	$6.4 \cdot 10^{-2}$	1030	8361	959	10148	634

†: Performed in a BüchiGlasUster glass pressure vessel and toluene as solvent.

*: Reaction was performed in a Schlenk tube with DCM as solvent and the stabilizer present.

‡: assuming a dinuclear species.

§: assuming the formation of PE.

E: $TON = (m_{PM}/M_{repeating\ unit})/(n(cat.))$.

f: TOF referring to the entire reaction time. $TOF = TON / t$.

The sample from Entry 1 could be dissolved after the drying process and its $^{13}C\{^1H\}$ -NMR spectrum is depicted in Figure 93, with assignment of the branches. The degree of branching, in comparison to the one found for (mononuclear) nickel catalysts from literature, is quite similar and unremarkable.³³⁴ The chain-walking mechanism can be considered responsible for the observed short-chain-branching. The nomenclature of the branches, which is depicted within the spectrum, was taken from literature.^{334,335}

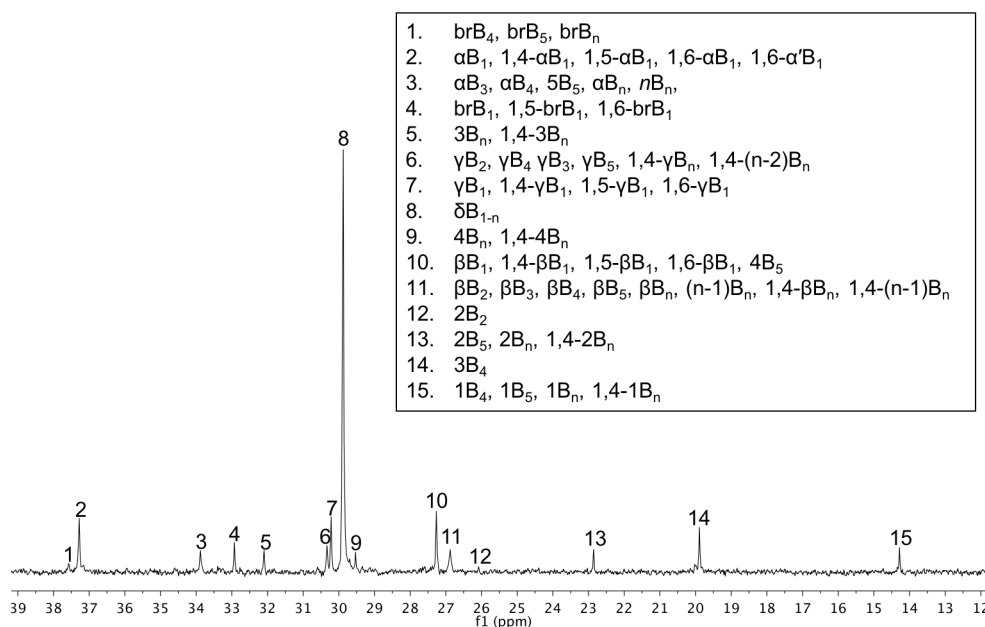


Figure 93: $^{13}C\{^1H\}$ -NMR spectrum of the obtained PE with assignment of the branches.³³⁵

The nomenclature referring with xB_n to: n : length of the branch; x : number of carbon atoms with the CH_3 group assigned as starting point 1; Greek letters: refer to the backbone position relative to the branching points (tertiary carbon atoms). The tertiary carbon atoms of the branching point are addressed with “br”; $1,m$: refers to paired branches with m being the number of carbon atoms in between two branches. The tertiary carbon atoms of the branching point are included in this counting.³³⁴

Further characterization of the synthesized PE was done by HT-GPC measurements in trichlorobenzene. The obtained broad molecular mass distribution is displayed in Figure 94. The observable shoulder of the mass distribution pattern and the PDI of 6.2 indicates more than one active species during the reaction or the gradual degradation of the catalyst during catalysis.

A mechanistic investigation that gave cause of the shoulder in the GPC measurement was not carried out. Nevertheless, Meyer *et al.* published a similar palladium complex in 2010.³³⁶ This complex formed of a tetranuclear platform with CH_3 and a $\mu-CH_2$ group, in the presence of a methylating agent. The formation of a related nickel

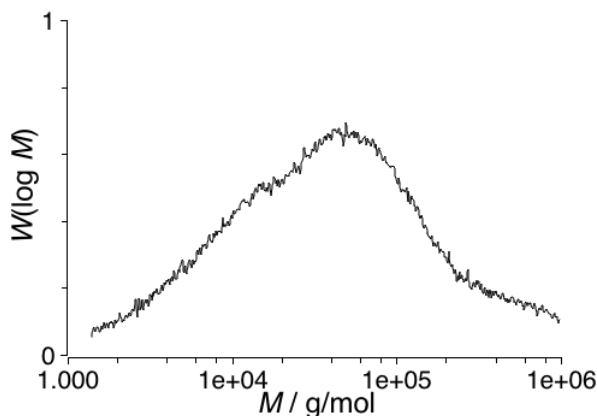


Figure 94: Molecular mass distribution determined by HT-GPC analysis of a PE sample. The distribution has its maximum at approximately $5 \cdot 10^4$ g/mol. GPC analysis was performed in 1,2,4-TCB and calibration was done with PE standards.

species from $[L^{PI^{Ph}}Ni_2Br_3]_2$ seems plausible, generated by the MAO during catalysis. This was, however not further investigated, since the potential of the complex for the copolymerization was not known yet. Consequently, the testing of the catalyst for the polymerization of MMA was performed. Entry 4 in Table 30 illustrates, that the catalyst is also capable of forming the homopolymer PMMA. The formed PMMA was found to be atactic, as it can be observed from the 1H -NMR spectrum in Figure 95 and from its comparison to literature.³³⁷

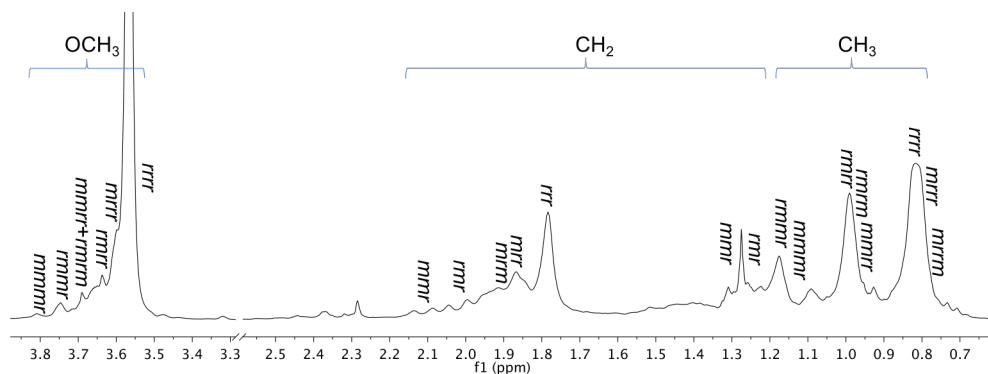


Figure 95: Section of the 1H -NMR spectrum of the obtained PMMA with attempted assignment of tetrads and pentads.³³⁷

The PE and PMMA polymer samples (Entries 1 and 4) were analyzed by ATR-IR spectroscopy. The obtained spectra, with assignment of selected IR-bands, can be found in Figure 96. IR experiments were also used for the copolymerization experiments in order to determine if the MMA was successfully incorporated. The obtained homopolymers are shown in Figure 97.

4.4 APPLICATION OF THE $[L^{PI^{Ph}}Ni_2Br_3]_2$ COMPLEX FOR THE OLEFIN POLYMERIZATION AND COPOLYMERIZATION

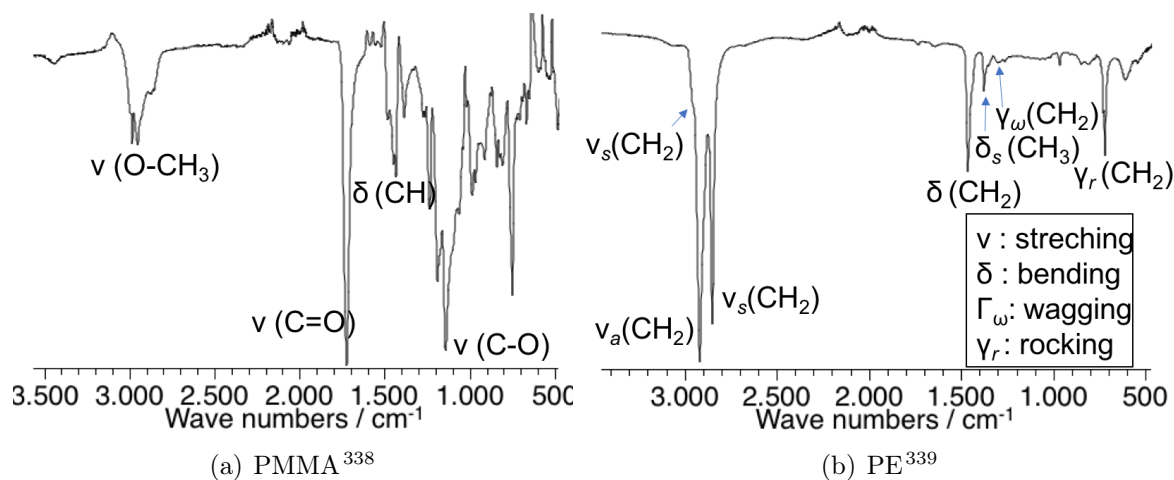


Figure 96: ATR-IR measurement of the obtained PMMA (a) and PE (b) with assignment of selected IR-bands.

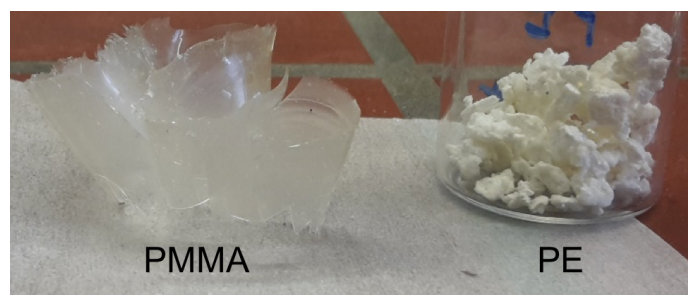


Figure 97: Photo of the obtained polymeric products, catalyzed by $[L^{PI^{Ph}}Ni_2Br_3]_2$. On the left the PMMA and on the right the PE is placed.

The catalyst was thus shown to fulfill the required activity in homopolymerization of both monomers separately. Therefore, copolymerization attempts were performed. The last three Entries 5–7 in Table 30 summarize these polymerization results and *TOF* values for the reactions. The *TOF* values were calculated under the approximation of exclusive polyethylene formation. As expected, the presence of the polar monomer led to a retardation of the reaction, so that the activities are lower than the ones found for the homopolymerization of ethylene. To determine if any MMA was incorporated into the PE (back bone or chain-end positions) an ATR-IR measurement of the obtained polymer was performed. It can be found in Figure 98 together with the IR-spectra of the obtained homopolymer samples.

The absence of the C=O stretch vibrational band in sample **C** is a strong indicator that the MMA was not incorporated. However, since the polymer sample was precipitated from the reaction solution, the possibility remains that the copolymer remained

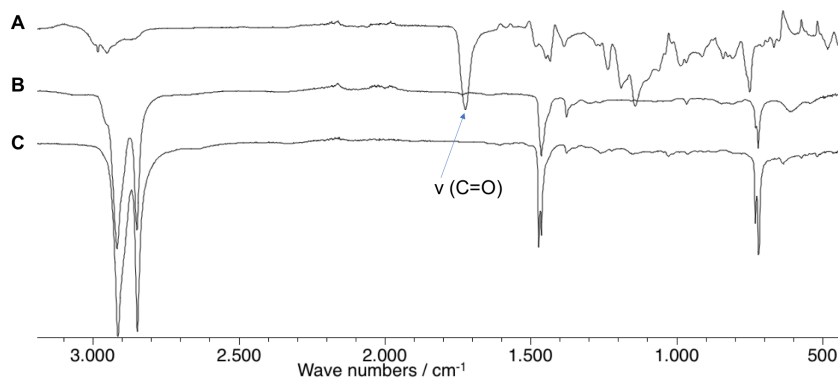


Figure 98: ATR-IR measurement of the obtained PMMA (A), PE (B) and the polymer from the copolymerization attempt (C).

in solution due to its better solubility. This scenario is unlikely, since the activity of the complex for ethylene is higher than for MMA, which should result in a higher fraction of ethylene in the product. Thus, a polymer with solubility properties similar to those of PE, rather than PMMA, can be expected. Nevertheless, to exclude this possibility, the solvent of a copolymerization sample was removed and the obtained polymeric product analyzed by HT-GPC. In Figure 99 the molecular mass distribution is shown, together with the ones from the obtained PMMA sample (red line) and a PE sample (green line). The bimodal distribution, with similar maxima to the samples from the homopolymers, again points strongly to unsuccessful results of the copolymerization. The catalyst seems not to be able to incorporate MMA into the backbone or the chain-ends of PE. However, the catalyst is not deactivated by the presence of the acrylate and forms the homopolymers.

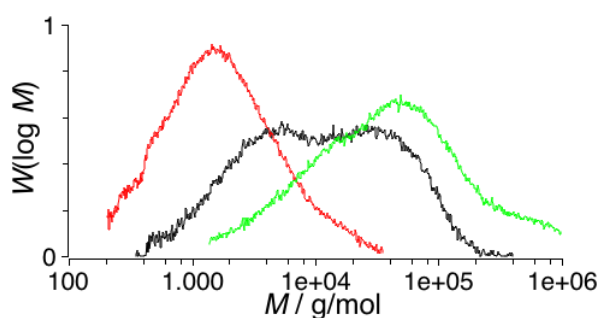


Figure 99: Molecular mass distribution determined by HT-GPC analysis. Black line: Bimodal distribution with maxima at approximately $5 \cdot 10^3$ and $3 \cdot 10^4$ g/mol obtained from a copolymerization attempt. Red line: PMMA sample. Green line: PE sample. GPC analysis was performed in TCB and calibration was done with PE standards.

4.5. Summary and conclusion

A dinuclear nickel complex, which was first isolated during my master thesis, was thoroughly characterized. Experimental evidence suggested that the complex form a tetranuclear molecular structure in the solid state, bridged by the halide ligands. In MeCN solution, however, a dinuclear complex was evidenced by mass spectrometry and DOSY-NMR spectroscopy. The complex, after activation with MAO, proved to be active for the formation of PE, providing a TOF of up to 19000 h^{-1} at 10 bar ethylene pressure and $25\text{ }^{\circ}\text{C}$. It also allows to catalyze the formation of PMMA with a TOF of 33 h^{-1} at $23\text{ }^{\circ}\text{C}$. For the formation of the copolymer the complex appears to be not suited. A visual summary is given in Figure 100.

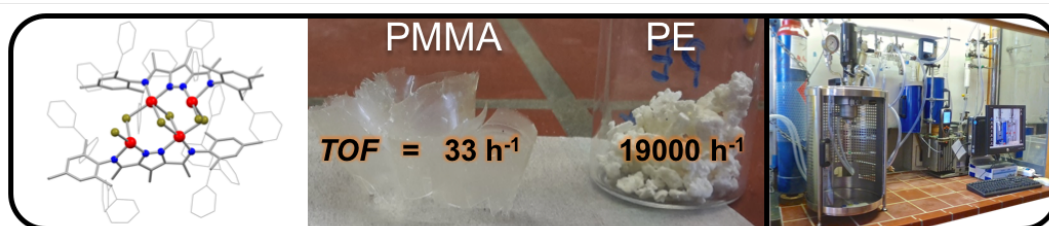


Figure 100: Visual summary of this chapter.

5. Summary and Conclusion

This work contributed to the understanding of cooperativity in bi- and oligometallic complexes (see Figure 1) through three chapters.

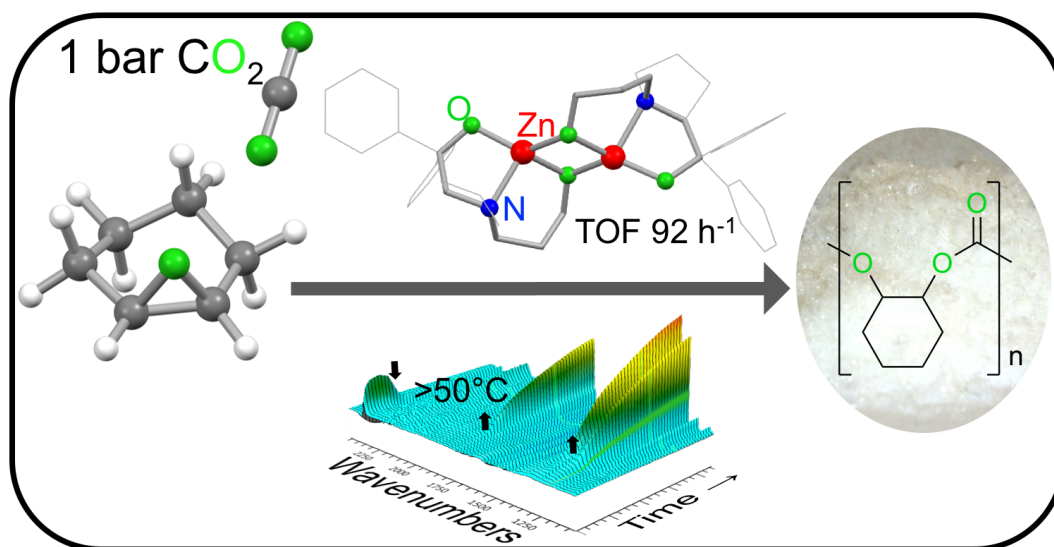


Figure 101: Novel readily accessible chiral zinc catalyst producing polycarbonates selectively under 1 bar of CO_2 . Average TON values of 610 and TOF values up to 92 h^{-1} were measured, producing an isotactic-enriched polycarbonate.

The first chapter on CO_2 /epoxide copolymerization led to the discovery of several promising novel catalysts to the field. One in particular, with an ONO-pincer ligand, provided high polymerizations activity and stereoselectivity. The self-assembled ONO-pincer type catalysts proved to be highly active. They serve as proof of concept to the field of CO_2 /epoxide copolymerization with their new design, coming along with a great potential for future applications, continuing several beneficial features of previously reported catalysts (see Figure 101).

In the second chapter, the interactions and mutual effects within a dinuclear complex holding an allylpalladium unit and a palladium dihalide unit in close proximity were investigated. New valuable insights into the interactions between the two fragments were gained by changing the substituents and ligands within the complex. The extent of interaction was represented by the allyl exchanges, investigated by kinetic studies through EXSY-NMR spectroscopy. Four model complexes were used for the investigations and to understand the cooperative effects of interest. A visual summary is given in Figure 102.

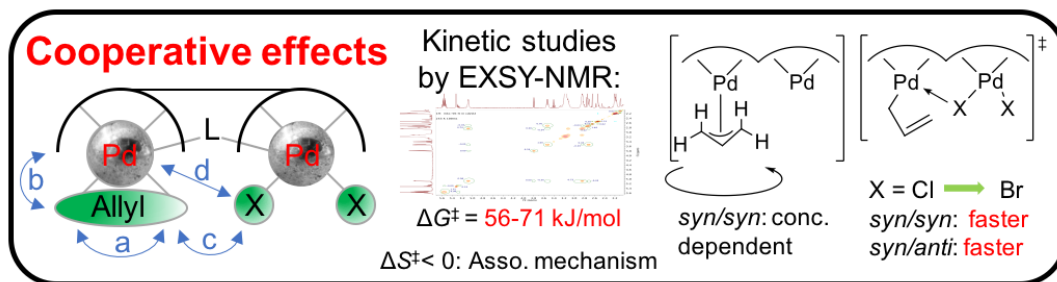


Figure 102: Visual summary of the investigation on the cooperative effects within a dinuclear complex, describing the interactions a–d of Figure 1.

In the last chapter, a dinuclear nickel complex was investigated for its applicability for the copolymerization of ethylene and MMA. Even though the complex was not found to be active for forming the copolymer, it was able to form the homopolymers PMMA and PE. The complex, after activation with MAO, catalyzes the formation of PMMA with a TOF of 33 h^{-1} (at 23°C) and provided a TOF of up to 19000 h^{-1} (at 25°C and 10 bar ethylene pressure) for PE (see Figure 103).

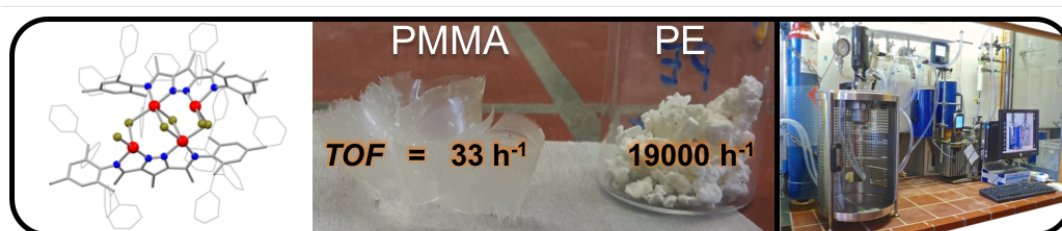


Figure 103: Polymerization results applying a dinuclear nickel catalyst for the formation of PMMA and PE.

6. Experimental Section

6.1. General Considerations

All air and/or water sensitive manipulations were carried out under an anaerobic and anhydrous atmosphere of dry dinitrogen or argon by using standard Schlenk techniques or a glovebox, unless mentioned otherwise. Filtrations and extractions under inert conditions were performed with a glass microfiber filter WHATMAN *GF/B* (25 mm) punched out by a syringe and connected to a Teflon tube. Solvents and other liquid reactants/solutions were transferred with *Norm-Ject* syringes through septa. Diethyl ether and pentane were dried over sodium benzophenone ketyl; THF, benzene, toluene and hexanes over potassium benzophenone ketyl; CHO, MeCN over CaH₂; CH₂Cl₂ and CHCl₃ over P₂O₅; MeOH and EtOH over Mg; and distilled prior to use. Deuterated solvents were dried and distilled according to the undeuterated analogues. Carbon dioxide (Airgas, 99.999% purity, with 120 bar of Helium) was dried over phosphorus pentoxide. Glassware was dried prior to use at 140 °C overnight in a heating oven and then repeatedly heated by an industrial heat gun under vacuum and set under inert gas in an alternating fashion.

NMR spectra were measured on an Avance III 300, HD 400 or HD 500 spectrometer from Bruker. The chemical shifts are displayed on the *f1* dimension as δ values in units of ppm. The residual protons of the deuterated solvent were used as internal standard for CDCl₃ ($\delta = 7.26$ ppm for the ¹H-NMR experiments and $\delta = 77.2$ ppm for the ¹³C-NMR experiments), CD₂Cl₂ ($\delta = 5.32$ ppm for the ¹H-NMR experiments and $\delta = 54.0$ ppm for the ¹³C-NMR experiments), MeCN-d₃ ($\delta = 1.94$ ppm for the ¹H-NMR experiments and $\delta = 118.3$ ppm for the ¹³C-NMR experiments), C₆D₆ ($\delta = 7.16$ ppm for ¹H-NMR experiments and $\delta = 128.1$ ppm for the ¹³C-NMR experiments), MeOH-d₃ ($\delta = 3.31$ ppm for the ¹H-NMR experiments and $\delta = 49.0$ ppm for the ¹³C-NMR experiments) or DMSO-d₆ ($\delta = 2.50$ ppm for the ¹H-NMR experiments and $\delta = 39.5$ ppm for the ¹³C-NMR experiments).³⁴⁰ The following abbreviations were used for the multiplicity of the NMR signals: s (singlet), d (doublet), t (triplet), q (quartet), m (multiplet). Residual solvent signals are marked with 'X' within the spectra. All spectra were measured at room temperature if not mentioned otherwise. The software EXSYCalc²³⁷ was used to determine the exchange rates from the integrals of the EXSY/NOESY experiments. DOSY-NMR spectra were evaluated with the TopSpin Software from Bruker using the function of the T_1/T_2 relaxation.

Mass spectra were measured on a *Applied Biosystems* API 2000 (ESI), *Finnigan* MAT 8200, *Bruker micrOTOF* (HR-ESI), *Bruker maXis* (HR-ESI), JEOL AccuTOF GCv (LIFDI-ToF) or *Finnigan MAT LCQ* (HR-ESI) instrument.

IR spectra were measured on an ATR Jasco FT/IR-4100 or Vertex 70 from Bruker. The *in situ* IR measurements were performed using a Mettler-Toledo ReactIR 10 flushed with compressed dried air filtered by an adsorption dryer Zander KE 3 or with N₂.

Elemental analyses were submitted to the analytical laboratory of the department of inorganic chemistry at the Georg-August-University Göttingen and performed on an Elementar Vario EL III.

UV-Vis spectra were recorded with an Variant Cary 50 spectrometer.

GPC analysis was performed with a GPC-SEC Analysis Systems 1260 Infinity and HT-GPC analysis on a High-Temperature Gel Permeation Chromatograph by Polymer Char.

Gas chromatography (GC) analyses were performed on a Trace GC Ultra equipped with a CP 9012 VF-5ms (30m) column. Chiral GC analysis was performed on an Agilent Technologies 7890A equipped with a CP-Chirasil-Dex CB column.

EPR spectra were measured with a Bruker E500 ELEXSYS X-band spectrometer with a standard cavity (ER4102ST, 9.45 GHz). The sample temperature was regulated with an Oxford instrument He-flow cryostat (ESP910) and a temperature controller from Oxford (ITC-4). The microwave frequency was measured with the built-in frequency counter, while the magnetic field was calibrated by using a NMR field probe (Bruker ER035M). The simulations were done with xsphe using Gaussian line shapes.

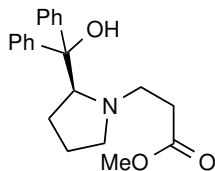
The bis(oxazoline)-pyrazole ligand HL^{BOX} was prepared and provided by Dr. Torben Böhnisch.¹⁷⁸ If not mentioned otherwise all chemicals were acquired from commercial sources (*Acros, Sigma Aldrich, abcr, Deutero, Merck*) and used without further purification.

ChemDraw and ChemOffice Version 16 from CambridgeSoft was used for the chemical drawings.

6.2. Copolymerization of CO₂/CHO

6.2.1. Synthesis of methyl

(*S*)-3-(2-(hydroxydiphenylmethyl)pyrrolidin-1-yl)propanoate



(*S*)-diphenyl(pyrrolidin-2-yl)methanol (1.00 g, 3.95 mmol, 1 eq.) and methyl acrylate (3.6 mL, 39.7 mmol, 10 eq.) were dissolved in 150 mL ethanol and heated to reflux for 3 h. All volatile substrates were removed under vacuum yielding the product as a colorless solid.

Yield: quant.

Sumformula: C₂₁H₂₅NO₃.

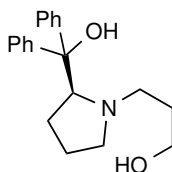
Molar mass: 339.44 g/mol.

¹H-NMR (300 MHz, CDCl₃): δ (ppm) = 7.62 (m, Ph), 7.59 (m, Ph), 7.52 (m, Ph), 7.50 (m, Ph), 7.29 (m, Ph), 7.27 (m, Ph), 7.24 (m, Ph), 7.16 (m, Ph), 7.14 (m, Ph), 7.11 (m, Ph), 4.67 (s, 1H, OH), 3.84 (dd, *J* = 9.1, 4.5 Hz, 1H, CH), 3.60 (s, 3H, OCH₃), 3.20 (m, 1H, CH₂N^{pyrrolidine}), 2.39 (m, 1H, CH₂N^{pyrrolidine}), 2.35 (m, 2H, CH₂N), 2.21 (m, 2H, CH₂COOMe), 1.87 (m, 1H, 3-CH₂^{pyrrolidine}), 1.70 (m, 1H, 3-CH₂^{pyrrolidine}), 1.62 (m, 2H, 4-CH₂^{pyrrolidine}).

MS(ESI) in MeOH *m/z*: 340.4 [M+H]⁺.

The analytical data is in good agreement with literature.¹⁴¹

6.2.2. Synthesis of (*S*)-3-(2-(hydroxydiphenylmethyl)pyrrolidin-1-yl)propan-1-ol (H₂L^{ProOH})



Methyl (*S*)-3-(2-(hydroxydiphenylmethyl)pyrrolidin-1-yl)propanoate (1.28 g, 3.95 mmol) was transferred into a Schlenk tube, dissolved in dry diethyl ether (30 mL) and cooled to 0 °C. Slowly 1.64 mL of a 2.4 M solution of LiAlH₄ in THF were added under vigorous stirring. The reaction solution was allowed to warm to room temperature and left to stir for 3 h. 1 mL of water was added forming a colorless precipitate. All volatile substrates were removed under vacuum and the remaining solid was extracted with DCM (60 mL, 30 mL, 20 mL). The suspensions were each treated with ultrasound for

5 min. before filtration. The solvent was evaporated yielding the product (1.19 g). Single crystals were obtained by slow evaporation of the DCM solution.

Yield: (97 %).

Sumformula: C₂₀H₂₅NO₂.

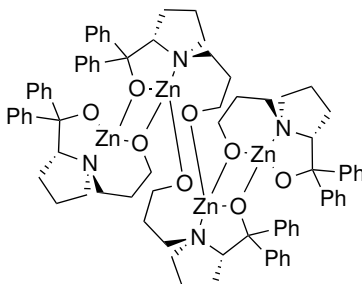
Molar mass: 311.4 g/mol.

¹H-NMR (300 MHz, CDCl₃): δ (ppm) = 7.67-7.12 (m, 10H, Ph), 4.45 (s, 1H, OH), 3.84 (dd, *J* = 9.2, 4.1 Hz, 1H, CH), 3.33 (m, 2H, CH₂OH), 3.26 (m, 1H, CH₂N^{pyrrolidine}), 2.37 (m, 1H, CH₂N^{pyrrolidine}), 2.24 (m, 1H, CH₂N), 2.08 (m, 1H, CH₂N), 1.88 (m, 1H, 3-CH₂^{pyrrolidine}), 1.70 (m, 3H, 4-CH₂^{pyrrolidine}, 3-CH₂^{pyrrolidine}), 1.48 (m, 2H, CH₂CH₂OH).

¹³C-NMR (75 MHz, CDCl₃): δ (ppm) = 148.1 (Ph), 146.4 (Ph), 128.3 (Ph), 128.2 (Ph), 126.5 (Ph), 126.4 (Ph), 125.8 (Ph), 125.7 (Ph), 78.2 (CPh₂), 71.7 (CH), 60.9 (CH₂OH), 55.6 (CH₂N^{pyrrolidine}), 53.9 (CH₂N), 31.6 (CH₂CH₂OH), 29.6 (3-CH₂^{pyrrolidine}), 24.7 (4-CH₂^{pyrrolidine}).

MS(ESI) in MeOH *m/z*: 312.2 [M+H]⁺.

6.2.3. Synthesis of [L^{ProOH}Zn]₂



(*S*)-3-(2-(hydroxydiphenylmethyl)-pyrrolidin-1-yl)propan-1-ol (178.2 mg, 0.572 mmol) was dissolved in 7 mL dry DCM and 231 μL of zinc bis[bis(trimethylsilyl)amide] were added. The solution was stirred overnight. All volatile substrates were removed under vacuum, yielding the desired product (214.5 mg, quant.) as a colorless solid. Single crystals could be obtained from diffusion of pentane or diethyl ether into a DCM solution.

Yield: quant.

Sumformula: C₈₈H₁₀₈N₄O₁₀Zn₄ (L₄Zn₄)

Molar mass: 749.58 g/mol (L₂Zn₂), 1499.16 g/mol (L₄Zn₄).

¹H-NMR (300 MHz, THF-d₈, 239 K): δ (ppm) = 8.82–6.78 (m, 10 H, Ph), 4.99 (m, CHCPh₂), 4.67 (m, CHCPh₂), 4.52 (m, CHCPh₂), 4.44 (m, CHCPh₂), 4.19 (m, CHCPh₂), 4.01–3.55 (m), 3.40–3.25 (m), 3.06 (t, *J* = 10.6 Hz), 2.92 (t, *J* = 12.4 Hz), 2.71–2.20 (m), 2.05–1.96 (m), 1.91–1.11 (m).

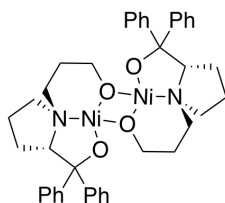
¹³C-NMR (126 MHz, THF-d₈, 239 K): δ (ppm) = 156.41, 155.75, 154.76, 154.63,

154.39, 154.26, 154.15, 153.08, 152.26, 151.89, 129.87, 129.13, 128.93, 128.82, 128.76, 128.51, 128.00, 127.74, 127.57, 127.48, 127.39, 127.31, 127.25, 126.94, 126.79, 126.48, 126.35, 126.21, 126.07, 125.91, 125.76, 125.71, 125.44, 125.33, 80.69, 79.39, 77.86, 77.65, 76.76, 76.40, 76.30, 75.40, 74.89, 70.72, 69.22, 68.82, 68.39, 68.10, 63.07, 60.73, 60.52, 60.09, 59.11, 58.78, 58.19, 57.48, 33.74, 33.10, 32.41, 32.18, 31.11, 30.79, 29.87, 29.48, 29.21, 27.87, 26.56, 25.98, 23.71, 23.20, 22.84, 21.63, 14.88, 14.21.

Elemental analysis (%): found: C 64.19, H 6.62, N 3.52; calculated (C₈₈H₁₀₈N₄O₁₀Zn₄): C 64.32, H 6.62, N 3.41.

MS(LIFDI) in toluene *m/z* (%): 747 (100) [L₂Zn₂+H]⁺.

6.2.4. Synthesis of [L^{ProOH}Ni]₂



(*S*)-3-(2-(hydroxydiphenylmethyl)-pyrrolidin-1-yl)propan-1-ol (200 mg, 0.642 mmol) and KH (51.5 mg, 1.28 mmol) were suspended in 5 mL dry THF and the reaction mixture was stirred for 30 min until no further formation of gas was observed. The suspension was added to a suspension of NiBr₂(dme) (198.1 mg, 0.642 mmol) in dry THF (5 mL) and left to stir for 3 days. The purple suspension was filtered through a WHATMAN filter and the purple solution layered with pentane. Single crystals could be obtained.

Yield: 60%

Sumformula: C₄₀H₄₆N₂O₄Ni₂

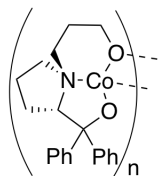
Molar mass: 736.21 g/mol.

¹H-NMR (300 MHz, CDCl₃): δ (ppm) = 8.78 (m, 4H, Ph), 7.80 (m, 4H, Ph), 7.52 (m, 2H, Ph), 7.06 (m, 4H, Ph), 6.99 (m, 4H, Ph), 6.92 (m, 2H, Ph), 4.40 (m, 2H, 4-CH₂^{pyrrolidine}), 4.21 (m, 2H, NiN-CH₂(CH₂)₂O), 4.01 (m, 2H, CH₂N^{pyrrolidine}), 2.98 (m, 2H, CHCPh₂), 2.63 (m, 2H, CH₂ONi), 2.37 (m, 2H, NiN-CH₂(CH₂)₂O), 2.10 (m, 2H, 4-CH₂^{pyrrolidine}), 1.77 (m, 2H, 3-CH₂^{pyrrolidine}), 1.65 (m, 2H, 3-CH₂^{pyrrolidine}), 1.60 (m, 2H, CH₂N^{pyrrolidine}), 1.54 (m, 2H, CH₂ONi), 1.00 (m, 2H, CH₂(CH₂)ONi).

¹³C-NMR (126 MHz, CDCl₃): δ (ppm) = 153.2 (Ph), 148.9 (Ph), 128.3 (Ph), 127.6 (Ph), 127.0 (Ph), 126.5 (Ph), 125.8 (Ph), 125.2 (Ph), 85.0 (CPh₂), 79.7 (CHCPh₂), 63.6 (NiN-CH₂(CH₂)₂ONi), 59.8 (CH₂N^{pyrrolidine}), 57.9 (CH₂ONi), 29.2 (3-CH₂^{pyrrolidine}), 27.5 (CH₂(CH₂)ONi), 24.8 (4-CH₂^{pyrrolidine}).

MS(MALDI) in a DCTB A 4-5 matrix m/z : 735.6 [L₂Ni₂+H]⁺.

6.2.5. Synthesis of [L^{ProOH}Co]₂



(*S*)-3-(2-(hydroxydiphenylmethyl)-pyrrolidin-1-yl)propan-1-ol (50 mg, 0.161 mmol) and KH (13.3 mg, 0.332 mmol) were suspended in 5 mL dry THF and the reaction mixture was stirred for 30 min until no further formation of gas was observed. The suspension was added to a suspension of CoBr₂ (35.1 mg, 0.161 mmol) in dry THF (5 mL) and left to stir for 3 days. The solvent was removed under vacuum and the obtained solid was extracted with dry DCM (3 × 3 mL), filtered and the solvent was removed, yielding the complex as blue solid.

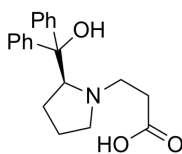
Yield: 50 %

Sumformula: (C₂₀H₂₃N₁O₂Co)_n

Molar mass: (368.34)_n g/mol.

para ¹H-NMR (300 MHz, CDCl₃): 194.32, 150.66, 130.66, 80.59, 29.08, 23.14, 5.14, 1.22, 0.83, -8.36, -14.44, -65.38, -72.72, -115.73.

6.2.6. Synthesis of H₂L^{ProO₂H}



Methyl (*S*)-3-(2-(hydroxydiphenylmethyl)pyrrolidin-1-yl)propanoate (556.7 mg, 1.640 mmol) and NaOH (0.777 mg, 19.4 mmol) were dissolved in ethanol (30 mL) and water (5 mL). The reaction was heated to reflux for 2 h. The reaction solution was reduced to 5 mL under vacuum and a HCl solution was added until pH 7 was reached. DCM (3 × 20 mL) was added to extract the target compound. The DCM was removed from the combined organic phases yielding the product (150 mg).

Yield: 28 %

Sumformula: C₂₀H₂₃NO₃

Molar mass: 325.4 g/mol.

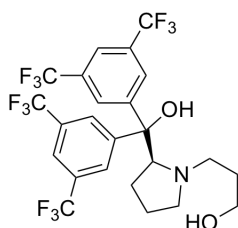
¹H-NMR (300 MHz, CDCl₃): δ (ppm) = 7.66–7.09 (m, 10H, Ph), 4.42 (t, *J* = 7.6 Hz,

1H, CH), 3.65–3.40 (m, 1H, CH₂N^{pyrrolidine}), 2.88 (m, 1H, CH₂N^{pyrrolidine}), 2.83 (m, 2H, CH₂COOH), 2.52–2.31 (m, 2H, CH₂N), 2.20–1.93 (m, 2H, 3-CH₂^{pyrrolidine}), 1.82 (tt, *J* = 13.4, 6.6 Hz, 2H, 4-CH₂^{pyrrolidine}).

¹³C-NMR (126 MHz, CDCl₃): δ (ppm) = 175.1 (COOH), 145.5 (ipso-C-Ph), 144.8 (ipso-C-Ph), 128.6 (Ph), 128.5 (Ph), 127.5 (Ph), 127.1 (Ph), 126.0 (Ph), 125.8 (Ph), 78.3 (CPh₂), 74.3 (CHN), 54.6 (CH₂N^{pyrrolidine}), 52.8 (CH₂N), 32.2 (CH₂COOH), 28.6 (3-CH₂^{pyrrolidine}), 23.3 (4-CH₂^{pyrrolidine}).

MS(ESI) in MeOH *m/z*: 348.2 [H₂L^{ProO₂H}+Na]⁺, 326.2 [H₂L^{ProO₂H}+H]⁺.

6.2.7. Synthesis of H₂L^{F₁₂ProOH}



(*S*)-bis(3,5-bis(trifluoromethyl)phenyl)(pyrrolidin-2-yl)methanol (98.7 mg, 0.188 mmol) and methyl acrylate (0.17 mL, 18.8 mmol) were dissolved in 10 mL ethanol and heated to reflux for 72 h in a Schlenk tube (product formation monitored by NMR spectroscopy). All volatile substrates were removed under vacuum yielding the intermediate product as colorless solid. The obtained solid was dissolved in dry diethyl ether (7 mL) and cooled to 0 °C. Slowly 0.08 mL of a 2.4 M solution of LiAlH₄ in THF were added under vigorous stirring. The reaction solution was allowed to warm to room temperature and left to stir overnight. 1 mL of water was added. All volatile substrates were removed under vacuum and the remaining solid was extracted with DCM (2 × 15 mL), applying ultrasound for 5 min. before filtration. The DCM phase was evaporated yielding the product (107 mg).

Yield: 98 %.

Sumformula: C₂₄H₂₁F₁₂NO₂.

Molar mass: 583.4 g/mol.

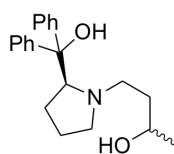
¹H-NMR (300 MHz, CDCl₃): δ (ppm) = 8.11 (s, 2H, Ph), 8.00 (s, 2H, Ph), 7.75 (s, 2H, Ph), 3.90 (dd, *J* = 8.7, 5.4 Hz, 1H, CH), 3.37 (t, *J* = 6.1 Hz, 2H, CH₂OH), 3.26 (ddd, *J* = 9.9, 6.2, 4.0 Hz, 1H, CH₂N^{pyrrolidine}), 2.50 (td, *J* = 9.0, 7.0 Hz, 1H, CH₂N^{pyrrolidine}), 2.27 (dt, *J* = 12.1, 6.0 Hz, 1H, CH₂N), 2.02 (dt, *J* = 12.4, 7.9 Hz, 1H, CH₂N), 1.92–1.81 (m, 1H, 3-CH₂^{pyrrolidine}), 1.78–1.62 (m, 2H, 4-CH₂^{pyrrolidine}), 1.57–1.43 (m, 3H, CH₂CH₂OH and 3-CH₂^{pyrrolidine}).

¹³C-NMR (75 MHz, CDCl₃): δ (ppm) = 149.8 (Ph), 147.9 (Ph), 132.0 (dq, *J* =

33.3, 6.4 Hz, CF₃), 128.8 (Ph), 126.0 (dq, $J = 15.3, 3.2$ Hz, CF₃), 125.2 (Ph), 121.6 (Ph), 121.3 (dq, $J = 7.7, 3.7$ Hz, CF₃), 77.4 (CPh₂), 71.2 (CH), 60.6 (CH₂OH), 55.1 (CH₂N^{pyrrolidine}), 53.1 (CH₂N), 31.1 (CH₂CH₂OH), 29.8 (3-CH₂^{pyrrolidine}), 24.2 (4-CH₂^{pyrrolidine}).

¹⁹F-NMR (282 MHz, CDCl₃): δ (ppm) = -62.9.

6.2.8. Synthesis of H₂L^{ProOHMe}



(*S*)-diphenyl(pyrrolidin-2-yl)methanol (0.405 g, 1.60 mmol) and but-3-en-2-one (1.45 mL, 17.2 mmol) were dissolved in 50 mL ethanol and heated to reflux for 4 h. All volatile substrates were removed under vacuum. To the obtained solid was dissolved in 40 mL of dry diethyl ether, cooled to 0 °C and 0.7 mL of a 2.4 M solution of LiAlH₄ in THF were added slowly under vigorous stirring. The reaction solution was allowed to warm to room temperature and left to stir overnight. 1 mL of water was added. All volatile substrates were removed under vacuum and the remaining solid was extracted with DCM (2 × 20 mL), applying ultrasound for 5 min. before filtration. The DCM phase was evaporated yielding the target compound.

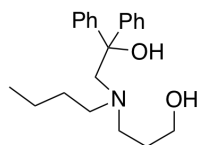
Yield: 92 %.

Sumformula: C₂₁H₂₇NO₂.

Molar mass: 325.5 g/mol.

¹H-NMR (300 MHz, CDCl₃): 7.68–7.07 (m, 10H, Ph), 4.67 (s, 1H, OH), 3.86 (dd, $J = 9.0, 4.3$ Hz, 1H, CH), 3.79 (dd, $J = 9.4, 4.3$ Hz, 1H, CH'), 3.63–3.48 (m, 1H, CHMe), 3.39–3.26 (m, 1H, CHMe'), 3.22–3.14 (m, 1H, CH₂N^{pyrrolidine}), 2.41–2.29 (m, 1H, CH₂N^{pyrrolidine}), 2.25–2.13 (m, 1H, CH₂N), 2.13–2.01 (m, 1H, CH₂N), 1.96–1.83 (m, 1H, 3-CH₂^{pyrrolidine}), 1.76–1.68 (m, 1H, 3-CH₂^{pyrrolidine}), 1.68–1.62 (m, 1H, 4-CH₂^{pyrrolidine}), 1.43–1.33 (m, 1H, 4-CH₂^{pyrrolidine}), 1.32–1.25 (m, 2H, CH₂COH), 0.95 (d, $J = 6.3$ Hz, 3H, CH₃), 0.93 (d, $J = 6.2$ Hz, 3H, CH₃).

MS(ESI) in MeOH m/z : 326.2 [H₂L^{ProOHMe}+H]⁺.

6.2.9. Synthesis of $\text{H}_2\text{L}^{\text{OC}^3\text{NO}^{\text{Ph}}}$ 

2,2-Diphenyloxirane (999 mg, 5.09 mmol, 1 eq.) and 3-(butylamino)propan-1-ol (668 mg, 5.09 mmol, 1 eq.) were filled in a flask and the reaction mixture was stirred for 7 days at 60 °C (71 % conversion determined by $^1\text{H-NMR}$ spectroscopy), 5 days at 80 °C (90 % conversion determined by $^1\text{H-NMR}$ spectroscopy) and 5 days at 120 °C. The crude product was obtained as an oil.

Yield: 90 % ($^1\text{H-NMR}$).

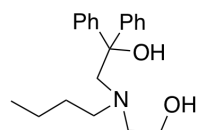
Sumformula: $\text{C}_{21}\text{H}_{29}\text{NO}_2$.

Molar mass: 327.5 g/mol.

$^1\text{H-NMR}$ (300 MHz, CDCl_3): δ (ppm) = 7.54 – 7.15 (m, Ph), 3.51 (t, $J = 6.1$ Hz, 2H, CH_2OH), 3.35 (s, 2H, CH_2CPh_2), 2.44 (t, $J = 7.0$ Hz, 2H, NCH_2CCOH), 2.32 (t, $J = 7.6$ Hz, 2H, $\text{NCH}_2^{n\text{Bu}}$), 1.59 (dt, $J = 12.7, 6.2$ Hz, 2H, NCCH_2COH), 1.34 (dtd, $J = 10.1, 7.3, 5.4$ Hz, 2H, CH_2CCH_3), 1.12 (dq, $J = 14.2, 7.2$ Hz, 2H, CH_2CH_3), 0.80 (t, $J = 7.3$ Hz, 3H, CH_3).

$^{13}\text{C-NMR}$ (75 MHz, CDCl_3): δ (ppm) = 147.3 (Ph), 128.4 (Ph), 128.3 (Ph), 127.6 (Ph), 126.8 (Ph), 125.9 (Ph), 74.7 (CPh_2), 65.5 (CH_2CPh_2), 61.4 (COH), 55.1 (NCH_2 of $n\text{Bu}$), 52.2 (NCH_2CCOH), 30.0 (NCCH_2COH), 29.0 (CH_2CCH_3), 20.5 (CH_2CH_3), 14.1 CH_3 .

MS(ESI) in MeOH m/z (%): 328.2 (100) $[\text{M}+\text{H}]^+$, 350.2 (3) $[\text{M}+\text{Na}]^+$.

6.2.10. Synthesis of $\text{H}_2\text{L}^{\text{OC}^2\text{NO}^{\text{Ph}}}$ 

2-(Butylamino)ethan-1-ol (600.2 mg, 5.12 mmol) and 2,2-diphenyloxirane (1005 mg, 5.12 mmol) were filled in a flask and the reaction mixture was stirred for 7 days at 60 °C (71 % conversion determined by $^1\text{H-NMR}$ spectroscopy), 5 days at 80 °C (90 % conversion determined by $^1\text{H-NMR}$ spectroscopy) and 5 days at 120 °C. The crude product was obtained as an oil.

Yield: 95 % ($^1\text{H-NMR}$).

Sumformula: $\text{C}_{20}\text{H}_{27}\text{NO}_2$.

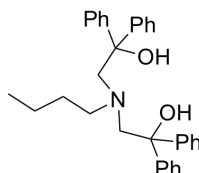
Molar mass: 313.4 g/mol.

$^1\text{H-NMR}$ (300 MHz, CDCl_3): δ (ppm) = 7.53 – 7.16 (m, Ph), 3.53 (t, $J = 5.5$ Hz,

2H, CH₂OH), 3.41 (s, 2H, CH₂CPh₂), 2.60 (t, *J* = 5.5 Hz, 2H, NCH₂COH), 2.37 – 2.29 (m, 2H, NCH₂^{*n*}Bu), 1.31 (dt, *J* = 15.1, 7.2 Hz, 2H, CH₂CCH₃), 1.08 (tq, *J* = 14.1, 7.3 Hz, 2H, CH₂CH₃), 0.77 (t, *J* = 7.2 Hz, 2H, CH₃).

MS(ESI) in MeOH *m/z*: 314.2 [M+H]⁺.

6.2.11. Synthesis of H₂L^{O^{Ph}NO^{Ph}}



2,2-Diphenyloxirane (1.441 g, 7.34 mmol) and butan-1-amine (268.4 mg, 3.67 mmol) were filled in a flask and the reaction mixture was stirred for 7 days at 60 °C (71 % conversion determined by ¹H-NMR spectroscopy), 5 days at 80 °C (90 % conversion determined by ¹H-NMR spectroscopy) and 5 days at 120 °C. The crude product was obtained as an oil.

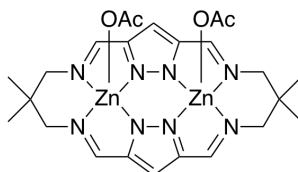
Yield: 52 % (¹H-NMR).

Sumformula: C₃₂H₃₅NO₂.

Molar mass: 465.6 g/mol.

¹H-NMR (300 MHz, CDCl₃): δ (ppm) = 7.50 – 7.17 (m, Ph), 3.50 (s, 4H, CH₂CPh₂), 2.07 (m, 2H, NCH₂^{*n*}Bu), 1.28 (m, 2H, CH₂CCH₃), 1.17 (m, 2H, CH₂CH₃), 0.65 (t, *J* = 7.2 Hz, 2H, CH₃).

6.2.12. Synthesis of [L^{CPI}(Zn-OAc)₂]



Pyrazole-3,5-dicarbaldehyde (101 mg, 0.814 mmol) and Zn(OAc)₂ (149 mg, 0.814 mmol) were suspended in dry ethanol (12 mL) and heated to 73 °C for 15 min., to form a solution. 2,2-Dimethylpropane-1,3-diamine (83.2 mg, 0.814 mmol) in dry ethanol (4 mL) was added drop-wise and the reaction mixture was stirred at 73 °C for 2 h. All volatile compounds were removed under reduced pressure, leaving a beige solid. The solid was dissolved in DCM and layered/precipitated with hexane to yield the target compound.

Yield: 53 %

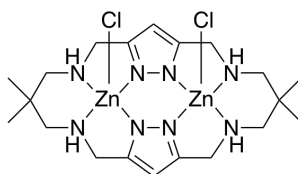
Sumformula: $C_{24}H_{32}N_8O_4Zn_2$

Molar mass: 627.33 g/mol.

1H -NMR (300 MHz, $CDCl_3$): δ (ppm) = 7.99 (s, 4H, CH=N), 6.42 (s, 2H, H-Pz), 4.61 (d, $J = 12.0$ Hz, 4H, CH_2N), 3.20 (d, $J = 11.3$ Hz, 4H, CH_2N), 2.06 (s, 6H, OAc), 1.14 (s, 6H, CH_3), 0.61 (s, 6H, CH_3).

^{13}C -NMR (75 MHz, $CDCl_3$): δ (ppm) = 177.7 (COO), 155.2 (C=N), 148.3 (C-NN), 105.4 (CH-CNN), 69.3 (CH_2-N), 37.6 (CMe_2), 26.8 (CH_3), 22.9 (CH_3), 22.6 (CH_3-COO).

6.2.13. Synthesis of $[L^{CPA}(Zn-Cl)_2]$



$[L^{CPI}(Zn-OAc)_2]$ (81.5 mg, 0.130 mmol) was dissolved in dry THF (16 mL) and $LiAlH_4$ (61 mg, 1.62 mmol) was added in small portions. The suspension was left to stir for 24 h. The reaction was quenched by the addition of methanol (p.a.). All volatile compounds were removed under reduces pressure. The obtained solid was extracted with DCM. The removal of the volatile compound gave the target complex. Layers of a DCM solution and hexanes yielded single crystals suitable for X-ray diffraction experiment.

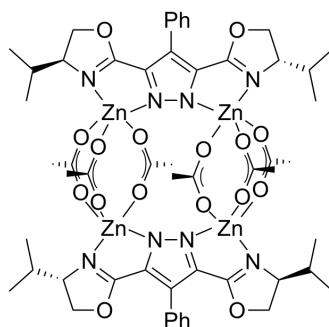
Yield: 10%

Sumformula: $C_{40}H_{34}N_8Zn_2Cl_2$

Molar mass: 588.21 g/mol.

1H -NMR (300 MHz, $CDCl_3$): δ (ppm) = 6.21 (s, 2H, H-Pz), 3.77 (s, 8H, CH_2-Pz), 2.48 (s, 8H, $CH_2C(CH_3)_2$), 1.25 (s, 4H, NH), 0.92 (s, 12H, CH_3).

^{13}C -NMR (75 MHz, $CDCl_3$): δ (ppm) = 102.6 (HC-Pz), 59.0 ($CH_2C(CH_3)_2$), 46.5 (CH_2-Pz), 34.6 ($C(CH_3)_2$), 25.6 (CH_3).

6.2.14. Synthesis of [L^{BOX}Zn₂-OAc₃]₂

The ligand HL^{BOX} (150.0 mg, 0.409 mmol) and Zn(OAc)₂ (150.2 mg, 0.819 mmol) were suspended in dry DCM (10 mL) and the reaction mixture stirred overnight, forming a colorless solution. All volatile compounds were removed under vacuum, yielding the target compound as colorless solid. Layers of a DCM solution and hexanes yielded single crystals suitable for X-ray diffraction experiment.

Yield: >90%

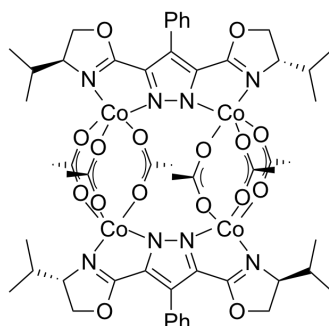
Sumformula: C₅₄H₆₈N₈O₁₆Zn₄

Molar mass: 1346.70 g/mol.

¹H-NMR (300 MHz, CDCl₃): δ (ppm) = 7.48 – 7.29 (m, 10H, Ph), 4.54 (dd, *J* = 9.4 Hz, 4H, CH₂), 4.40 (dd, *J* = 9.4 Hz, 4H, CH₂), 4.28 (m, 4H, CHN), 2.16 (m, 4H, CHMe₂), 1.97 (s, 9H, OAc), 0.92 (d, *J* = 6.7 Hz, 12H, CH₃), 0.86 (d, *J* = 6.8 Hz, 4H).

¹³C-NMR (75 MHz, CD₂Cl₂): δ (ppm) = 179.2 (CO-O), 165.3 (O-C=N), 137.6 (Ph), 131.4 (Ph), 130.8 (Ph), 128.3 (NN-C), 128.1 (Ph), 122.9 (C-Ph), 73.0 (CH₂), 68.0 (C-*i*Pr), 31.1 (CHMe₂), 22.6 (CH₃^{OAc}), 19.0 (CH₃), 16.0 (CH₃).

ESI-MS in THF *m/z* (%): 1281.2 [M-OAc]⁺ (2.5).

6.2.15. Synthesis of [L^{BOX}Co₂-OAc₃]₂

The ligand HL^{BOX} (151.3 mg, 0.414 mmol) and Co(OAc)₂ (146.2 mg, 0.826 mmol) were suspended in dry DCM (15 mL), forming a thick gel. After stirring overnight a purple solution formed. All volatile compounds were removed under vacuum, yielding the

target compound as purple solid. **Yield:** >90 %

Sumformula: C₅₄H₆₈N₈O₁₆Co₄

Molar mass: 1320.91 g/mol.

Analytic: see section 2.6.2.

6.2.16. General remarks regarding the CO₂ cyclohexene oxide copolymerization

The CHO was dried over CaH₂ (reflux for 48 h) and fractionally distilled (collect the main CHO-fraction only after the thermometer shows 136 °C and the distill bridge was rinsed properly with the clean CHO during the distillation process) several times until it was sufficiently dry (usually 2–3 times). The remaining water content was measured by *Karl-Fischer* titration. The storage of the dried CHO should be done in hydrophobic glassware equipped with a Young valve. It was observed, that after thoroughly drying of the glassware (overnight at 140 °C, then attaching to the vacuum and three times heating to ca. 400 °C) traces of water remain on the surface, that will slowly desorb from the surface into the CHO. When working with epoxides the use of silicon grease (Dow Corning high vacuum grease) should be avoided since it was found to be active for the homopolymerization, likely due to the thickener that it contains. Instead, PTFE paste should be used. For the same reason, molecular sieve and/or other medium/strong Lewis acids should be avoided.^{76,341,342}

The polymerizations that needed a pressure higher than 1 bar in CO₂ were performed in a stainless steel *Picoclave* of the company BuchiGlasUster AG with a stainless steel 100 mL reactor chamber for pressures up to 60 bar and temperatures up to 260 °C (s. Figure 104). A Pt-100-Element inside the reactor chamber allowed the measurement and recording of the temperature. A photo of the setup can be found in Figure 105.

The polymerizations were performed in glass vials with a steering bar which were placed inside of the reaction chamber. The solution of the catalyst (in neat CHO if not mentioned differently) was inserted through three thin Teflon tubes into the glass vials (up to three) inside of the reaction chamber. The Teflon tubes were connected on one side to a cannula with parafilm and guided through a septum on valve B (Figure 104) into the glass vials inside of the reactor, when preparing the reactor (vials were sealed with a multiply pierced plastic lid, to avoid spillage but allow pressure equalization). To free the reactor of water and air it was heated under vacuum overnight. In order to seal the open valve B (with the Teflon tubes passing through it) an adapter device was designed allowing to cover the valve B (with the Teflon tubes and cannulas hanging out of it), with a standard 100 mL one-neck round flask.

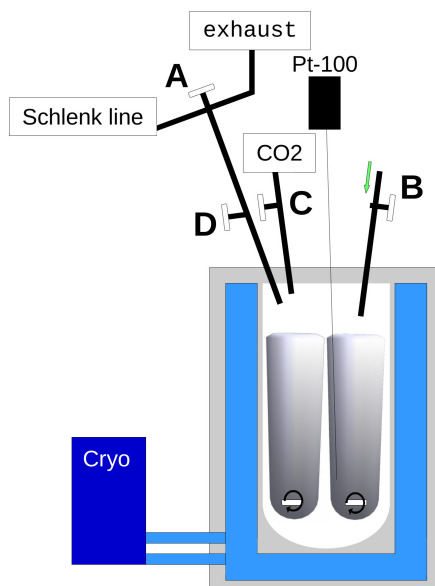


Figure 104: Sketch of the reactor that was used for higher pressures. Valve A: three way valve between the Schlenk line and the exhaust. Valve B: Inlet to the reaction chamber through which the Teflon tubes are directed into the glass vials inside of the reaction chamber. Valve C: Needle valve to the CO₂ supply. Valve D: Needle valve. Cryo: Cryostat or recuperator.



Figure 105: Foto of the reactor setup that was used for higher pressures.

The connected cannula to the Teflon tube allowed to fill the glass vials with a syringe in an inert fashion, by connecting the syringe (filled with CHO/catalyst solution and >10 mL of argon atmosphere, held upside down and slowly squeezing out the argon atmosphere during the connecting process) to the cannula under counter-current flow of argon. Once the syringe is connected to the cannula, both are turned around and the reaction solution is injected (make sure to keep ca. 2 mL of argon inside the syringe after connecting the cannula to the syringe, to flush the remaining CHO-solution, standing in the Teflon tubes, into the reactor). [ATTENTION: Do not remove the Teflon tubes or the syringes from the cannulas, the slight over pressure inside the reactor will press out your reaction solution through the tubes.] All Teflon tubes were pulled out of the reactor together (use tongs) and the reactor was sealed by closing valve B. Control experiments were performed with $\text{Zn}(\text{OAc})_2$, ZnBr_2 , ZnCl_2 and $\text{Zn}(\text{HMDS})_2$. $\text{Zn}(\text{HMDS})_2$ formed very fast the undesired polyether poly(cyclohexene oxide).

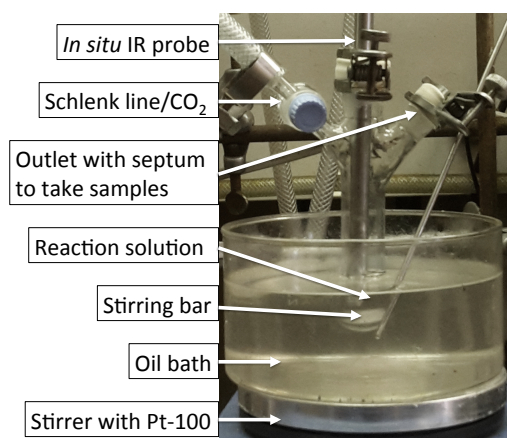


Figure 106: Setup that was used for the CO_2 /epoxide copolymerization at 1 bar.

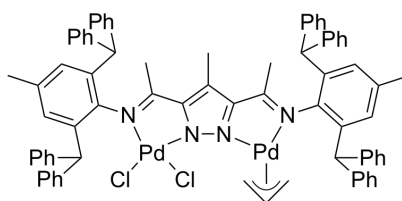
Polymerizations that were performed at 1 bar of CO_2 pressure were performed in a Schlenk tube. If an *in situ* IR measurement was performed of the reaction, a two necked Schlenk tube was used (s. Figure 106). Glassware that was described as hydrophobic was treated with trimethylsilyl chloride prior to use. The glassware was stored overnight at 140 °C, directly put into a dessicator containing ca. 10 mL trimethylsilyl chloride, the pressure was reduced to ca. 60 mbar and the dessicator was sealed. After the glassware was cooled to RT the process was repeated two more times.

6.3. Allyl Palladium Chemistry

The ligand $\text{HL}^{\text{PI}^{\text{iPr}}}$ was taken from a batch that was used during my Master Thesis,¹⁸¹ which was prepared according to literature.²³⁶

The ligand $\text{HL}^{\text{PI}^{\text{Ph}}}$, the complexes $[\text{L}^{\text{PI}^{\text{Ph}}}\text{PdBr}_2\text{Pd}(\text{C}_3\text{H}_5)]$ and $[\text{L}^{\text{PI}^{\text{iPr}}}\text{PdBr}_2\text{Pd}(\text{C}_3\text{H}_5)]$ were prepared according to the synthetic route established during my Master Thesis.¹⁸¹

6.3.1. Synthesis of $[\text{L}^{\text{PI}^{\text{Ph}}}\text{PdCl}_2\text{Pd}(\text{C}_3\text{H}_5)]$



Allyl chloride (0.24 ml, 2.97 mmol) was injected into a Schlenk tube under inert conditions and *freeze-pump-thaw* degassing was performed three times. To the frozen allyl chloride, palladium(0)-1,3-divinyl-1,1,3,3-tetramethyldisiloxane (294 mg of a 10.74 % Pd(0) solution) was added and *freeze-pump-thaw* degassing was repeated. At room temperature a yellow solid form was dissolved by the addition of dry DCM (10 ml). A solution of $\text{HL}^{\text{PI}^{\text{Ph}}}$ (150 mg, 0.149 mmol) in dry DCM (10 ml) was added drop-wise. The solution was stirred overnight. The volatile substances were removed *in vacuo* and the crude solid was washed with diethyl ether (4×5 ml). The product (175 mg, 0.131 mmol) was obtained after drying *in vacuo* as an orange solid. Single crystals were obtained by layering a DCM solution with hexanes.

Yield: 88 %.

Sumformula: $\text{C}_{77}\text{H}_{68}\text{Cl}_2\text{N}_4\text{Pd}_2$.

Molar mass: 1333.2 g/mol.

$^1\text{H-NMR}$ (500 MHz, CD_2Cl_2 , 237 K): δ (ppm) = 7.42–6.97 (m, 40H, Ph), 6.83 (d, $J = 1.4$ Hz, 1H, $\text{HC}^{\text{aniline, allyl-side}}$), 6.77 (d, $J = 1.4$ Hz, 1H, $\text{HC}^{\text{aniline, allyl-side}}$), 6.61 (s, 2H, $\text{HC}^{\text{aniline, Cl-side}}$), 6.22 (s, 1H, $\text{CHPh}_2^{\text{Cl-side}}$), 6.18 (s, 1H, $\text{CHPh}_2^{\text{Cl-side}}$), 5.48 (s, 1H, $\text{CHPh}_2^{\text{allyl-side}}$), 5.33 (s, 1H, $\text{CHPh}_2^{\text{allyl-side}}$), 5.13 (tt, $J = 12.8, 6.8$ Hz, 1H, CH^{allyl}), 4.99 (dd, $J = 6.8, 1.4$ Hz, 1H, $\text{H}_{\text{inside, syn}}^{\text{allyl}}$), 3.23 (d, $J = 12.8$ Hz, 1H, $\text{H}_{\text{inside, anti}}^{\text{allyl}}$), 2.53 (dd, $J = 6.8, 1.9$ Hz, 1H, $\text{H}_{\text{outside, syn}}^{\text{allyl}}$), 2.21 (s, 3H, $\text{CH}_3\text{-aniline}^{\text{Cl-side}}$), 2.13 (s, 3H, $\text{CH}_3\text{-aniline}^{\text{allyl-side}}$), 1.61 (d, $J = 12.1$ Hz, 1H, $\text{H}_{\text{outside, anti}}^{\text{allyl}}$), 1.55 (s, 3H, $\text{CH}_3\text{-Pz}$), 1.03 (s, 3H, $\text{CH}_3\text{-CN}^{\text{allyl-side}}$), -0.44 (s, 3H, $\text{CH}_3\text{-CN}^{\text{Cl-side}}$).

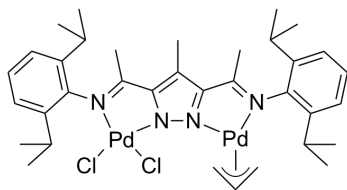
$^{13}\text{C-NMR}$ (126 MHz, CD_2Cl_2 , 237 K): δ (ppm) = 175.0 ($\text{C}=\text{N}^{\text{allyl-side}}$), 172.7 ($\text{C}=\text{N}^{\text{Cl-side}}$), 152.0 ($\text{C}-\text{NN}^{\text{Cl-side}}$), 150.2 ($\text{C}-\text{NN}^{\text{allyl-side}}$), 143.3 ($\text{C}^{\text{aniline}}-\text{N}^{\text{allyl-side}}$), 143.2 ($\text{C}^{\text{aniline}}-\text{N}^{\text{Cl-side}}$), 142.1 (Ph), 142.0 (Ph), 140.9 (Ph), 140.7 (Ph), 140.1 ($\text{C}^{\text{aniline}}-\text{CPh}_2^{\text{allyl-side}}$),

138.3 (C^{aniline}-C Ph₂^{Cl-side}), 138.3 (C^{aniline}-CH₃^{Cl-side}), 136.4 (Ph), 135.9 (Ph), 135.6 (Ph), 135.3 (Ph), 130.6 (Ph), 129.9 (Ph), 129.8 (Ph), 129.7 (Ph), 129.6 (Ph), 129.6 (Ph), 129.6 (Ph), 129.1 (Ph), 129.0 (Ph), 128.7 (CH^{aniline, allyl-side}), 128.7 (Ph), 128.6 (CH^{aniline, Cl-side}), 128.5 (Ph), 128.2 (Ph), 126.9 (Ph), 126.8 (Ph), 126.7 (Ph), 126.6 (Ph), 126.3 (Ph), 120.6 (C^{Pz}-CH₃), 115.7 (CH^{allyl}), 68.6 (C^{allyl}_{inside}), 60.7 (C^{allyl}_{outside}), 52.2 (HCPH₂^{Cl-side}), 52.1 (HCPH₂^{Cl-side}), 52.0 (HCPH₂^{allyl-side}), 51.9 (HCPH₂^{allyl-side}), 21.5 (CH₃-aniline^{allyl-side}), 21.4 (CH₃-aniline^{Cl-side}), 18.6 (CH₃-CN), 18.0 (CH₃-CN), 9.7 (CH₃-Pz).

MS(ESI) m/z : 2638, 1297 [M-Cl]⁺, 1303, 1969.

IR (ATR): $\tilde{\nu}$ (cm⁻¹) = 3448 (m), 3024 (m), 2922 (m), 1599 (s), 1572 (s), 1494 (s), 1448 (s), 1424 (m), 1384 (w), 1363 (w), 1316 (m), 1258 (w), 1209 (w), 1078 (m), 1032 (m), 869 (w), 769 (m), 749 (w), 702 (s).

6.3.2. Synthesis of [L^{PIⁱPr}PdCl₂Pd(C₃H₅)]



Allyl chloride (0.168 ml, 2.34 mmol) was injected into a Schlenk tube under inert conditions and *freeze-pump-thaw* degassing was performed three times. To the frozen allyl chloride, palladium(0)1,3-divinyl1,1,3,3-tetramethyldisiloxane (204 mg of a 10.74 % Pd(0) solution) was added and *freeze-pump-thaw* degassing was repeated one more time. The reaction flask was allowed to reach room temperature and a yellow solid formed which was dissolved by the addition of dry DCM (5 ml). A solution of HL^{PIⁱPr} (50 mg, 0.103 mmol) in dry DCM (10 ml) was added drop-wise. The solution was stirred overnight and turned orange. The volatile substances were removed *in vacuo* and the crude solid was washed with diethyl ether (4×5 ml). The product (68 mg, 0.084 mmol) was obtained after drying *in vacuo* as an orange solid. Single crystals were obtained by layering a DCM solution with hexane.

Yield: 82 %.

Sumformula: C₇₇H₆₈Cl₂N₄Pd₂.

Molar mass: 1333.2 g/mol.

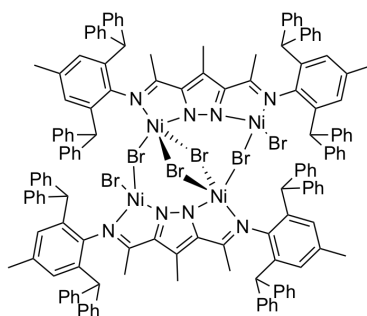
¹H-NMR (500 MHz, CD₂Cl₂, 237 K): δ (ppm) = 7.32–7.16 (m, 6 H, HC-aniline), 5.55 (tt, J = 12.9, 6.8 Hz, 1H, CH^{allyl}), 5.06 (d, J = 6.8 Hz, 1H, H^{allyl}_{inside, syn}), 3.52 (d, J = 12.9 Hz, 1H, H^{allyl}_{inside, anti}), 3.18 (sep, J = 6.7 Hz, 1H, CHCH₃^{Cl-side}), 3.14 (sep, J = 6.7 Hz, 1H, CHCH₃^{Cl-side}), 3.11 (sep, J = 6.7 Hz, 1H, CHCH₃^{allyl-side}), 2.82 (sep, J

= 6.7 Hz, 1H, CHCH₃^{allyl-side}), 2.82 (d, $J = 6.8$ Hz, 1H, allyl-H_{syn,outside}), 2.71 (d, $J = 12.2$ Hz, 1H, allyl-H_{anti,outside}), 2.53 (s, 3H, CHCH₃-Pz), 2.20 (s, 3 H, CH₃-C=N_{allyl-side}), 2.17 (s, 3 H, CH₃-C=N_{Cl-side}), 1.36 (d, $J = 6.8$ Hz, 3H, CH₃CH_{Cl-side}), 1.34 (d, $J = 6.8$ Hz, 3H, CH₃CH_{Cl-side}), 1.24 (d, $J = 6.8$ Hz, 3H, CH₃CH_{allyl-side}), 1.15 (d, $J = 6.8$ Hz, 3H, CH₃CH_{allyl-side}), 1.13 (d, $J = 6.8$ Hz, 3H, CH₃CH_{allyl-side}), 1.10 (d, $J = 6.8$ Hz, 3H, CH₃CH_{allyl-side}), 1.09 (d, $J = 6.8$ Hz, 3H, CH₃CH_{Cl-side}), 1.08 (d, $J = 6.8$ Hz, 3H, CH₃CH_{Cl-side}).

¹³C-NMR (126 MHz, CD₂Cl₂, 237 K): δ (ppm) = 171.1 (N=C_{allyl-side}), 169.8 (N=C_{Cl-side}), 152.5 (NN-C_{allyl-side}), 150.9 (NN-C_{Cl-side}), 144.2 (N-C_{allyl-side}-aniline), 141.2 (*i*Pr-C_{Cl-side}), 141.1 (*i*Pr-CC_{Cl-side}), 140.4 (N-C_{Cl-side}-aniline), 138.6 (*i*Pr-C_{allyl-side}), 138.4 (*i*Pr-CC_{allyl-side}), 127.7 (HC_{allyl-side}-aniline), 127.0 (HC_{Cl-side}-aniline), 124.1 (HC_{allyl-side}-aniline), 124.0 (H-C_{allyl-side}-aniline), 123.4 (HC_{Cl-side}-aniline), 123.4 (HC_{Cl-side}-aniline), 122.2 (CH₃-C-Pz), 116.4 (H-C_{allyl}), 69.1 (allyl-CH₂^{inside}), 62.0 (allyl-CH₂^{outside}), 28.7 (Me₂C_{Cl-side}), 28.7 (Me₂C_{Cl-side}), 28.6 (Me₂C_{allyl-side}), 28.3 (Me₂C_{allyl-side}), 24.1 (CH₃CH), 23.9 (CH₃CH), 23.8 (CH₃CH), 23.6 (CH₃CH), 23.5 (CH₃CH), 23.5 (CH₃CH), 23.5 (CH₃CH), 23.3 (CH₃CH), 20.1 (CH₃-CN_{Cl-side}), 19.8 (CH₃-CN_{allyl-side}), 11.0 (CH₃-Pz). MS(ESI) m/z : 773 [M-Cl]⁺. IR (KBr): 3468 (m), 3064 (w), 2961 (s), 2926 (m), 2868 (m), 1592 (s), 1570 (s), 1491 (m), 1458 (s), 1437 (s), 1384 (m), 1364 (m), 1325 (s), 1256 (w), 1241 (w), 1180 (w), 1100 (w), 1056 (w), 801 (m), 775 (m), 732 (m) cm⁻¹.

6.4. Copolymerization of ethylene and methyl methacrylate

6.4.1. Synthesis of [L^{PI^{Ph}}Ni₂Br₃]₂



The Ligand HL^{PI^{Ph}} (150.0 mg, 0.149 mmol) and potassium *tert*-butanolate (18.3 mg, 0.163 mmol) were suspended in DCM (15 ml) and the reaction mixture was stirred for 30 min. The suspension was filtered and dropwise added to a solution of [NiBr₂(dme)] (91.73 mg, 0.297 mmol) in DCM (20 ml) and the reaction mixture was stirred overnight. The solvent was removed *in vacuo* in order to obtain the orange product and redissolved in DCM (20 ml), washed with water (15 ml) and the *aqueous* phase was extracted with DCM (2×20 ml). The combined organic phases were dried over MgSO₄, filtered and the solvent was removed. The product was dissolved in DCM, and hexane and diethyl

ether were diffused into the solution to obtain yellow crystals. The synthesis was first described during my master thesis.¹⁸¹

Yield: 90 %

Sumformula: C₇₄H₆₃Br₃N₄Ni₂.

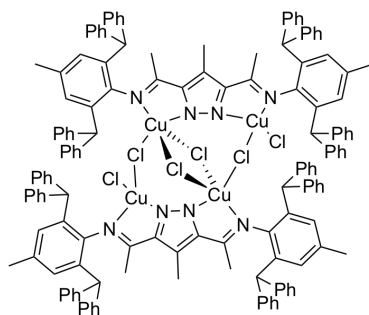
Molar mass: 1365.42 g/mol.

para-¹H-NMR: see Figure 125.

DOSY-NMR: see Figure 126.

MS(ESI) in MeOH *m/z*: 1281.2 [L^{PI^{Ph}}Ni₂Br₂]⁺.

6.4.2. Synthesis of [L^{PI^{Ph}}Cu₂Cl₃]₂



The Ligand HL^{PI^{Ph}} (30.3 mg, 0.030 mmol) and potassium *tert*-butanolate (4.6 mg, 0.041 mmol) were suspended in DCM (10 ml) and the reaction mixture was stirred for 30 min. The suspension was filtered and drop-wise added to a solution of CuCl₂·H₂O (10.6 mg, 0.062 mmol) in THF (10 ml) and the reaction mixture was stirred overnight. The solvent was removed *in vacuo* in order to obtain the red product and redissolved in toluene (12 ml), filtered and layered with hexanes. Single crystals were obtained.

Yield: 82 %

Sumformula: C₁₄₈H₁₂₆Cl₆N₈Cu₄.

Molar mass: 2483.54 g/mol.

MS(ESI) in MeOH *m/z*: 2241.57 [L^{PI^{Ph}}Cu₄Cl₅]⁺ (tetranuclear).

6.4.3. General remarks regarding the ethylene polymerization

The polymerization reactions of ethylene were performed in a BüchiGlasUster pressure vessel (200 mL) equipped with a Pt-100 element and a Cyclone stirrer drive. The reaction vial was freed of moisture and air using standard Schlenk techniques. The solvent (toluene) and catalyst were entered through a septum attached to a ball-valve into the autoclave. The reactor was closed, the Cyclone stirrer drive was set to 1000 rpm and ethylene was pressed into the reaction chamber until the desired pressure was

reached. The reactions were run for 1 h and then quenched by the addition of methanol and 1 M HCl solution. The precipitated polymer was filtered off and dried to constant weight.

6.4.4. General remarks regarding the MMA polymerization

The polymerization reactions of methyl methacrylate were performed in a Schlenk vial equipped with a stirring bar. The methyl methacrylate was freed of air using the freeze-pump-thaw degassing technique, then DCM and MAO were added, followed by the catalyst as a DCM solution. After the desired reaction time a 1 M HCl solution was added, the phases separated and the solvent of the organic phase was removed, yielding the PMMA.

6.4.5. General remarks regarding the ethylene and methyl methacrylate copolymerization

The copolymerizations were performed according to section 6.4.3. In the step when the catalyst was added, dried methyl methacrylate (dried over CaH_2) was added as well. The reaction time was increased to >15 h. The stabilizer of the MMA can be removed by filtration over basic aluminum oxide.

A fast removal of the MMA from the reaction solution, ideally under inert conditions, after the polymerization is recommended, because auto-polymerization of the MMA can be mistaken for a false positive.

A. Appendix

A.1. Mass Spectrometry

A.1.1. Complex $[L^{\text{ProOH}}\text{Zn}]_2$

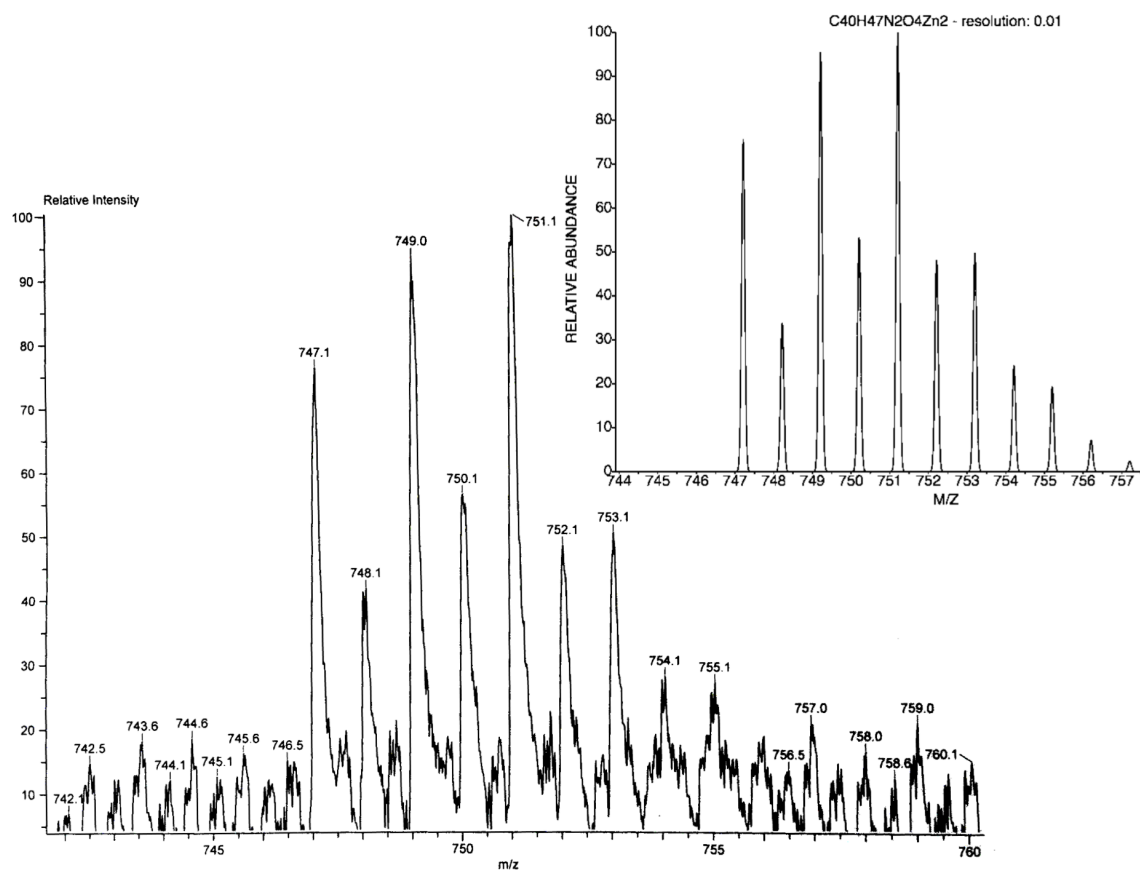
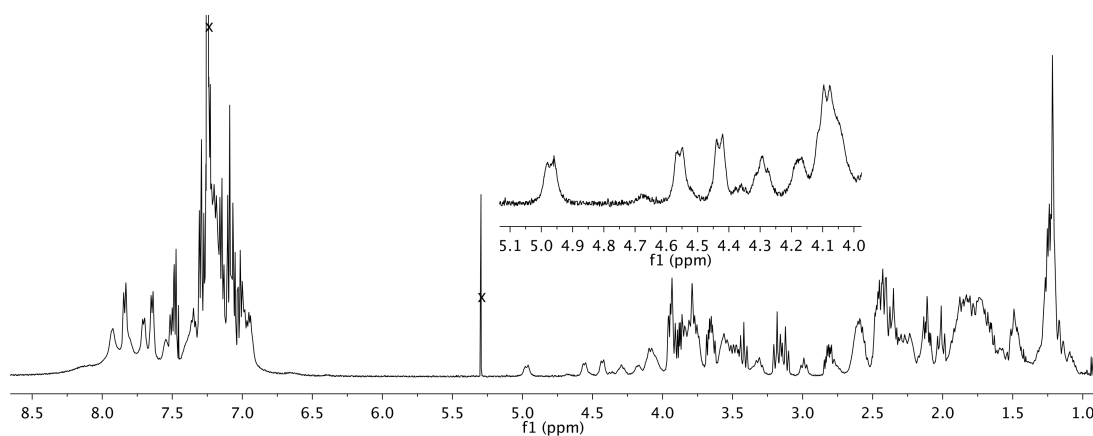
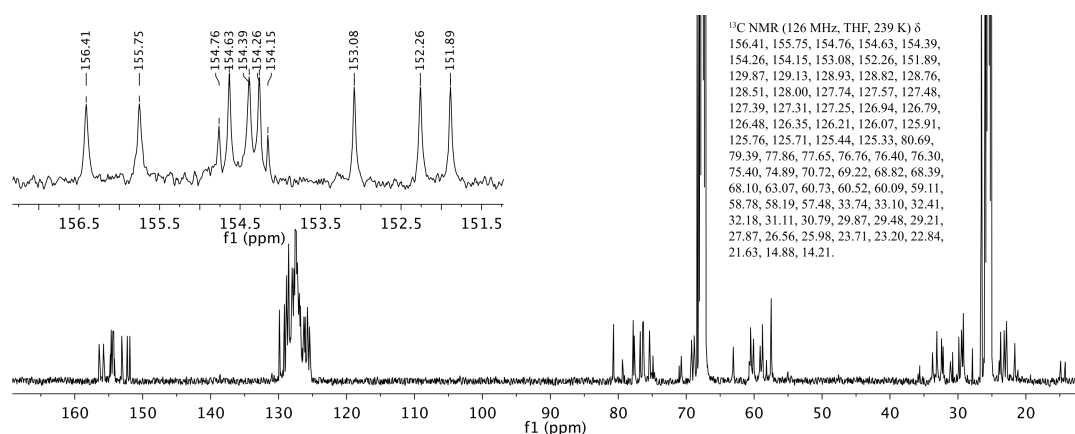
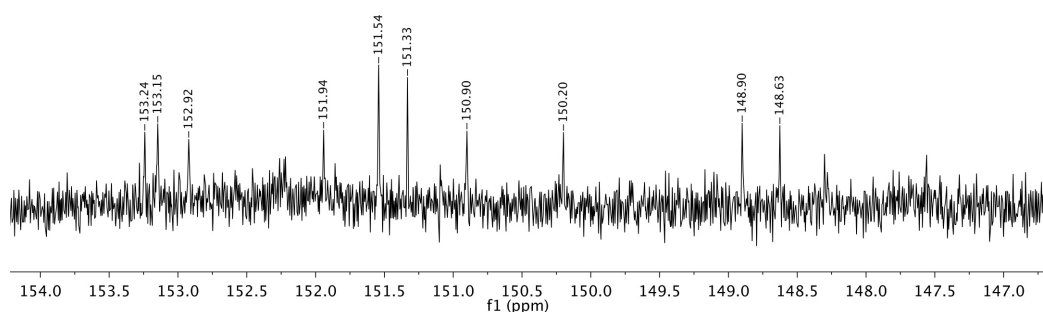


Figure 107: LIFDI-MS (positive mode) of $[L^{\text{ProOH}}\text{Zn}]_2$ in toluene.

A.2. NMR Spectroscopy

A.2.1. Complex $[L^{\text{ProOH}}\text{Zn}]_2$ Figure 108: ^1H -NMR spectrum of $[L^{\text{ProOH}}\text{Zn}]_2$ in CDCl_3 at 238 K.Figure 109: ^{13}C -NMR spectrum of $[L^{\text{ProOH}}\text{Zn}]_2$ in THF at 239 K.Figure 110: Section from 154.0–147 ppm of the ^{13}C -NMR spectrum of $[L^{\text{ProOH}}\text{Zn}]_2$ in CDCl_3 at 238 K. Sample contained $\text{Si}(\text{TMS})_4$ as internal standard from the DOSY measurements.

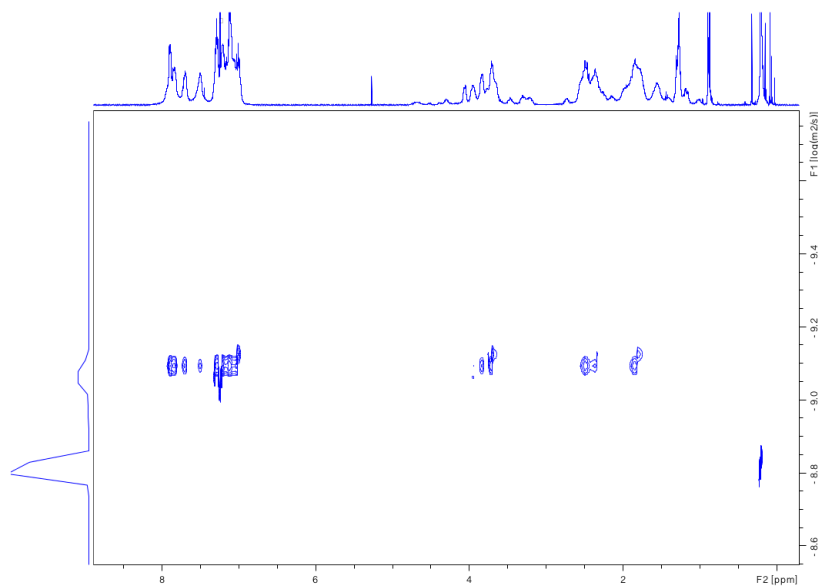


Figure 111: DOSY-NMR spectrum of $[\text{L}^{\text{ProOH}}\text{Zn}]_2$ in CDCl_3 at 323 K. $\text{Si}(\text{TMS})_4$ as internal standard. Processing was performed with TopSpin NMR software from Bruker.

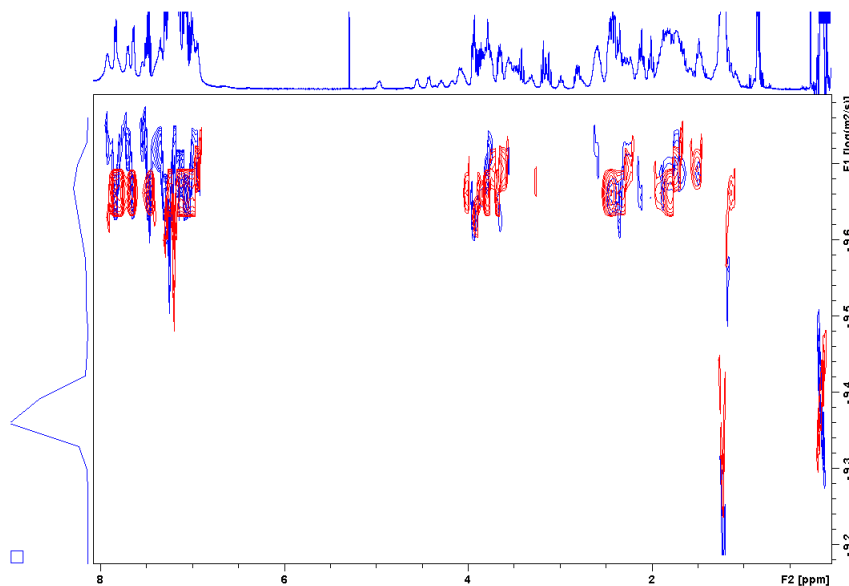


Figure 112: Overlay of the DOSY-NMR spectra of $[\text{L}^{\text{ProOH}}\text{Zn}]_2$ in CDCl_3 at 238 K (blue) and 323 K (red). $\text{Si}(\text{TMS})_4$ as internal standard. Processing was performed with TopSpin NMR software from Bruker.

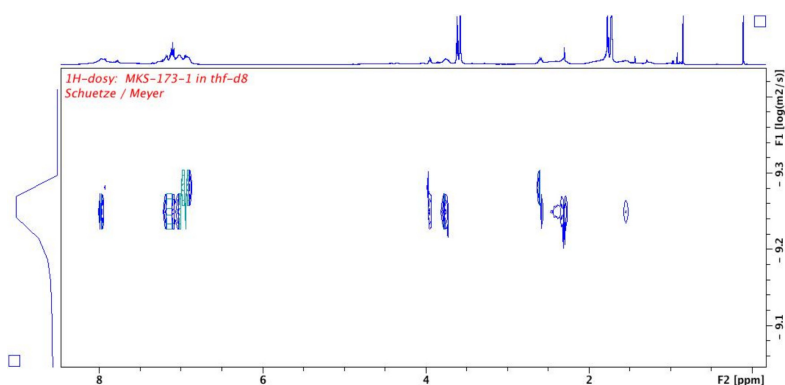


Figure 113: DOSY-NMR spectra of $[\text{L}^{\text{ProOH}}\text{Zn}]_2$ in THF at 298 K. Processing was performed with TopSpin NMR software from Bruker.

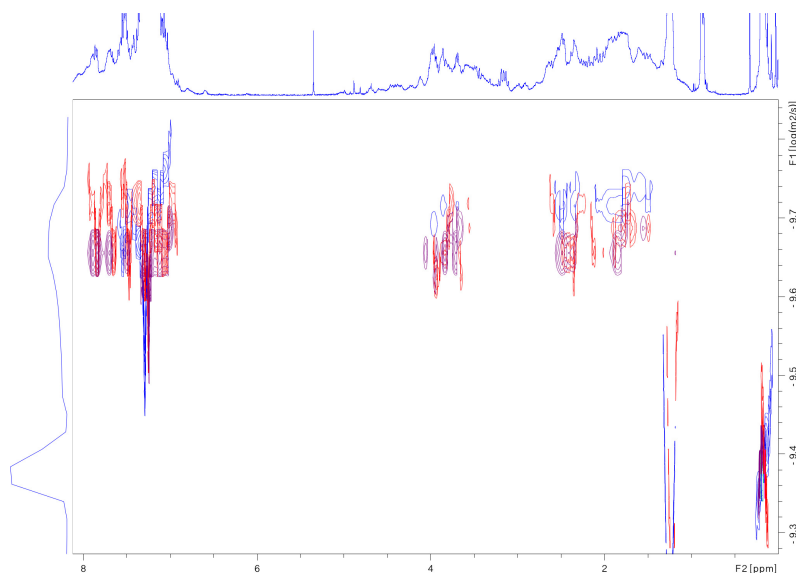
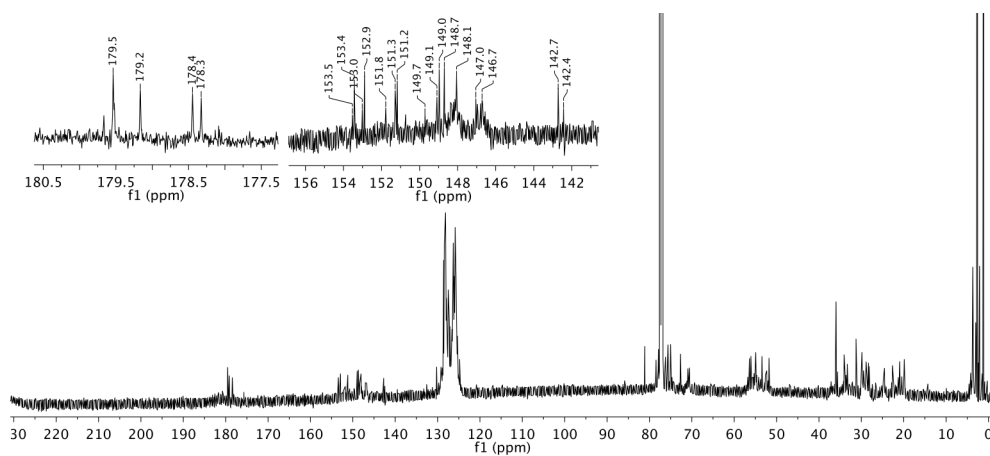
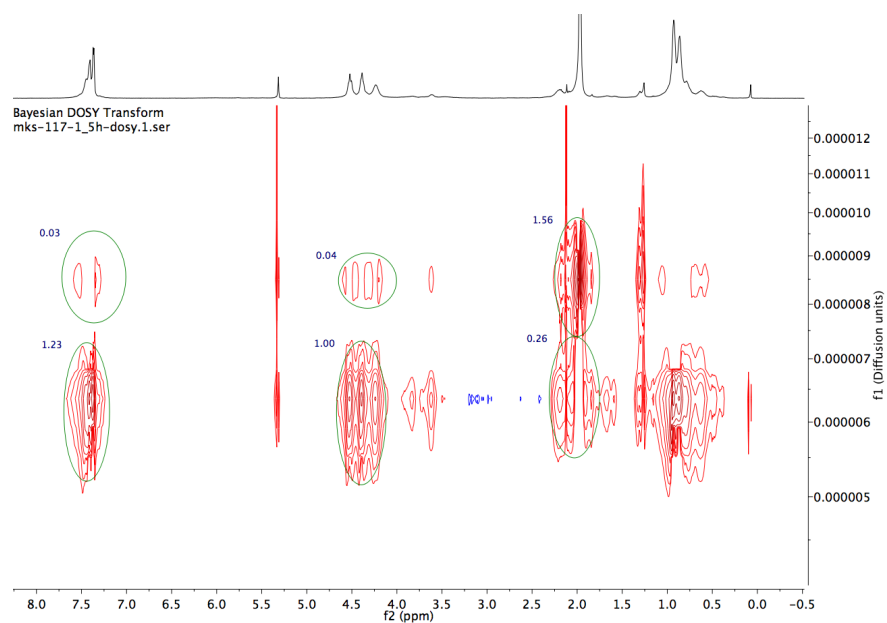


Figure 114: Overlay of the DOSY-NMR spectra of $[\text{L}^{\text{ProOH}}\text{Zn}]_2$ in CDCl_3 at 223 K (blue), 238 K (red) and 323 K (purple). $\text{Si}(\text{TMS})_4$ as internal standard and used as reference for the overlay, thus the values of the y-axis should be disregarded. Processing was performed with TopSpin NMR software from Bruker.

A.2.2. Complex $[L^{\text{ProO}_2\text{H}}\text{Zn}]_2$ Figure 115: ^{13}C -NMR spectrum of $[L^{\text{ProO}_2\text{H}}\text{Zn}]_2$ in CDCl_3 .A.2.3. Complex $[L^{\text{BOX}}\text{Zn}_2(\text{OAc})_3]_2$ Figure 116: DOSY-NMR spectrum of $[L^{\text{BOX}}\text{Zn}_2(\text{OAc})_3]_2$ in CD_2Cl_2 . Displayed with MestReNova.

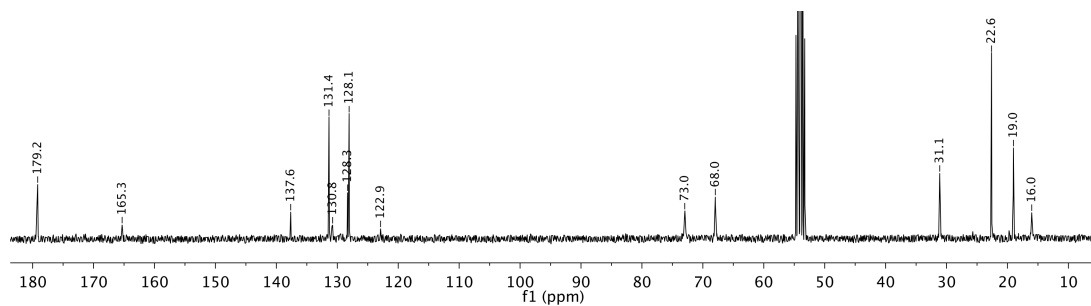


Figure 117: ^{13}C -NMR spectrum of $[\text{L}^{\text{BOX}}\text{Zn}_2(\text{OAc})_3]_2$ in CD_2Cl_2 .

A.2.4. Complex $[\text{L}^{\text{BOX}}\text{Co}_2(\text{OAc})_3]_2$

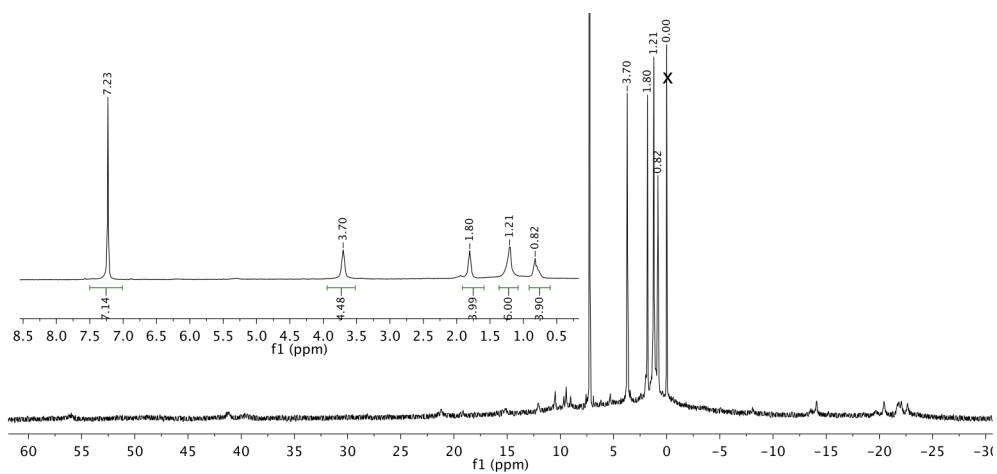


Figure 118: Para-magnetic ^1H -NMR spectrum of $[\text{L}^{\text{BOX}}\text{Co}_2(\text{OAc})_3]_2$ in CDCl_3 .

A.2.5. Determined exchange constants by EXSY experiments

A.2.6. Further Information on the evaluation of the ^1H -EXSY-NMR spectra

In the ^1H -EXSY-NMR spectra of the complexes $[\text{L}^{\text{PI}^{\text{Pr}}}\text{PdCl}_2\text{Pd}(\text{C}_3\text{H}_5)]$ and $[\text{L}^{\text{PI}^{\text{Pr}}}\text{PdBr}_2\text{Pd}(\text{C}_3\text{H}_5)]$, the diagonal signal of the *syn*-positioned allyl proton on the outside is overlapped by one of the CHR_2 signals of the allyl-side of the complexes. In order to obtain a full exchange matrix, which is needed to calculate the exchange constants, the integral of the diagonal signal was assumed to be equal to the integral of the *anti*-positioned allyl proton on the outside. The same was done for the complexes $[\text{L}^{\text{PI}^{\text{Ph}}}\text{PdCl}_2\text{Pd}(\text{C}_3\text{H}_5)]$ and $[\text{L}^{\text{PI}^{\text{Ph}}}\text{PdBr}_2\text{Pd}(\text{C}_3\text{H}_5)]$, since the signal of the *syn* positioned allyl proton on the inside is overlaid with the allyl-CH signal. As a result, the integrated diagonal signal was assumed to be equal to the integral of the *anti* positioned allyl proton on the inside.

The maximum and the minimum temperatures for performing the experiments were determined by the lowest temperature where an allyl exchange can be observed and the highest temperature at which, even with low mixing times ($d8$), the cross relaxation rates become extremely high, rendering the evaluation difficult and accuracy low. Furthermore, and specially at high temperatures, it has to be considered that in order to evaluate the spectra, the cross signals need to be smaller than the diagonal ones. When evaluating the spectra it has to be kept in mind that the exchange signals of protons are influenced by the *Nuclear Overhauser Effect* (NOE) (distance dependency of r^{-6}). This changes the integrated values for protons in close proximity. The cross peak signals are positive at low temperatures and approach a negative constant value at higher temperatures, while the exchange constant starts at zero and increases with the temperature. Additionally to the temperature dependency, the cross peak signals depend on the molecular weight of the observed molecule in a direct manner, due to an increase of the double-quantum relaxation relative to the zero-quantum relaxation. Regarding the *syn/syn* exchange displayed in section 3, every value is displayed as the averaged value of the determined exchange constants from the cross signals of the *syn/syn* and the *anti/anti* exchange, since both describe the same exchange process. Errors of the determined exchange constants were estimated based on the quality of the spectra and the estimated accuracy of the integration. A phase correction of the spectra has been done for all of them. However, the correction of the spectra remained an issue during the integration of the spectra. This applies strongly to cross and diagonal signals, which are in close proximity regarding their chemical shift. For spectra recorded at the upper and the lower temperature limits the resulting error was more pronounced. At the low temperature edge the integrated values are very small, resulting in larger error values since the background noise is relatively high. At high

Table 31: Determined exchange constants obtained for complexes $[L^{Pt^{2+}}PdCl_2Pd(C_3H_5)]$ (top) and $[L^{Pt^{2+}}PdBr_2Pd(C_3H_5)]$ (bottom).

Entry	$T / ^\circ C$	$d\delta / s^{-1}$	$k_{sym/anti}^{outside} / s^{-1}$	$k_{sym/anti}^{inside} / s^{-1}$	$k_{sym/anti}^{corrected} / s^{-1}$	$k_{sym/sgn} / s^{-1}$	$k_{anti/anti} / s^{-1}$	$c / mmol/l$
1	-37	0.5	-0.10	-0.13	0.033	0.12	0.11	30*
2	-30	0.2	-0.24	-0.33	0.083	0.31	0.26	30*
3	-25	0.1	-0.27	-0.34	0.072	0.47	0.42	30*
4	-20	0.1	-0.24	-0.36	0.12	0.66	0.61	30*
5	0	0.1	0.71	-0.38	1.1	2.3	2.2	37
6	0	0.1	0.87	-0.36	1.2	3.0	2.8	20
7	5	0.1	1.7	-0.36	2.0	3.2	3.2	37
8	5	0.1	1.5	-0.35	1.9	3.9	3.7	20
9	5	0.1	1.6	-0.35	1.9	3.4	3.4	15
10	5	0.1	1.6	-0.35	1.9	3.0	2.9	10
11	5	0.1	1.4	-0.33	1.8	2.5	2.4	5.0
12	10	0.1	3.0	-0.36	3.3	4.6	4.6	37
13	10	0.1	2.8	-0.36	3.1	5.4	5.2	20
14	15	0.1	4.8	-0.39	5.2	6.4	6.5	37
15	15	0.1	4.3	-0.42	4.7	7.2	7.3	20
16	20	0.1	5.9	-0.70	6.6	9.4	9.5	20
17	20	0.1	5.7	-0.53	6.3	7.3	6.8	10
Entry	$T / ^\circ C$	$d\delta / s^{-1}$	$k_{sym/anti}^{outside} / s^{-1}$	$k_{sym/anti}^{inside} / s^{-1}$	$k_{sym/anti}^{corrected} / s^{-1}$	$k_{sym/sgn} / s^{-1}$	$k_{anti/anti} / s^{-1}$	$c / mmol/l$
1	-37	0.5	1.6	-0.3	1.8	0.3	0.3	8.5*
2	-37	0.5	1.3	-0.2	1.5	0.5	0.5	17*
3	-30	0.2	4.0	-0.3	4.3	0.5	0.4	17*
4	-25	0.1	7.3	-0.3	7.6	0.7	0.6	17*
5	-20	0.1	11.8	-0.3	12	1.0	0.9	13*
6	-20	0.1	10.2	-0.4	11	2.6	2.4	20
7	-20	0.1	10.4	-0.4	11	2.4	2.2	19
8	-20	0.1	9.7	-0.4	10	1.5	1.5	10
9	-20	0.1	9.3	-0.4	9.7	1.7	1.4	10
10	-20	0.1	9.1	-0.4	9.5	1.1	1.1	4.8

*: complex concentration determined by integration of the 1H NMR spectrum. **: determined by an ^{13}C -EXSY-NMR experiment.

Table 32: Determined exchange constants obtained for complexes $[\text{L}^{\text{Pr}^{\text{th}}}\text{PdCl}_2\text{Pd}(\text{C}_3\text{H}_5)]$ (top) and $[\text{L}^{\text{Pr}^{\text{th}}}\text{PdB}_2\text{Pd}(\text{C}_3\text{H}_5)]$ (bottom).

Entry	$T / ^\circ\text{C}$	$d\delta / \text{s}^{-1}$	$k_{\text{syn}/\text{anti}}$ outside / s^{-1}	$k_{\text{syn}/\text{anti}}$ inside / s^{-1}	$k_{\text{syn}/\text{anti}}$ corrected / s^{-1}	$k_{\text{syn}/\text{syn}}$ / s^{-1}	$k_{\text{anti}/\text{anti}}$ / s^{-1}	$c / \text{mmol/l}$
1	-37	0.5	0.41	0.42	-0.01	0.05	0.14	12*
2	-37	0.5	0.45	0.44	0.01	0.07	0.15	22*
3	-30	0.2	0.33	0.30	0.04	0.09	0.16	12*
4	-30	0.2	0.35	0.32	0.02	0.11	0.18	22*
5	-25	0.1	0.21	0.21	0.00	0.14	0.20	12*
6	-25	0.1	0.37	0.25	0.12	0.2	0.23	22*
7	-20	0.1	0.15	0.14	0.01	0.24	0.28	12*
8	-20	0.1	0.17	0.17	0.01	0.33	0.34	22*
9	-20	0.1	0.27	0.26	0.01	0.48	0.54	44
10**	20	0.10				0.53		44
11	0	0.1	0.21	0.00	0.22	2.9	3.0	44
12***	0	0.1				3.3		44
13	0	0.1	0.16	-0.09	0.25	3.1	2.9	20
14	5	0.1	0.29	-0.13	0.42	4.5	4.2	20
15	10	0.1	0.48	-0.18	0.67	6.3	6.0	20
16	15	0.1	0.78	-0.26	1.00	8.9	8.6	20
Entry	$T / ^\circ\text{C}$	$d\delta / \text{s}^{-1}$	$k_{\text{syn}/\text{anti}}$ outside / s^{-1}	$k_{\text{syn}/\text{anti}}$ inside / s^{-1}	$k_{\text{syn}/\text{anti}}$ corrected / s^{-1}	$k_{\text{syn}/\text{syn}}$ / s^{-1}	$k_{\text{anti}/\text{anti}}$ / s^{-1}	$c / \text{mmol/l}$
1	-30	0.2	1.0	0.36	0.64	0.18	0.17	14*
2	-30	0.2	1.0	0.34	0.67	0.17	0.19	20
3	-25	0.1	1.5	0.26	1.3	0.22	0.22	14*
4	-25	0.1	1.7	0.25	1.4	0.24	0.23	20
5	-20	0.1	2.5	0.16	2.4	0.35	0.30	14*
6	-20	0.1	2.8	0.17	2.7	0.35	0.36	20
7	-15	0.05	4.2	-0.32	4.5	0.33	0.25	18
8	-10	0.05	7.3	-0.30	7.6	0.46	0.56	18
9	-5	0.02	12	-1.2	13	0.7	0.89	18
10	0	0.02	19	-1.4	20	1.3	1.3	18

*: complex concentration determined by integration of the ^1H NMR spectrum. **: determined by an ^{13}C -EXSY-NMR experiment.

Table 33: Determined exchange constants obtained for complexes $[\text{L}^{\text{PtPr}}\text{PdCl}_2\text{Pd}(\text{C}_3\text{H}_5)]$ with 0.5 eq. of Bu_4NCl .

Entry	$T / ^\circ\text{C}$	$d\delta / \text{s}^{-1}$	$k_{\text{sym}/\text{anti}}^{\text{outside}} / \text{s}^{-1}$	$k_{\text{sym}/\text{anti}}^{\text{inside}} / \text{s}^{-1}$	$k_{\text{sym}/\text{anti}}^{\text{corrected}} / \text{s}^{-1}$	$k_{\text{sym}/\text{sym}} / \text{s}^{-1}$	$k_{\text{anti}/\text{anti}} / \text{s}^{-1}$	$c / \text{mmol/l}$
1	-20	0.1	-0.19	-0.48	0.29	10	10	20*
2	-10	0.1	0.47	-0.20	0.68	13	12	20*
3	0	0.1	1.29	0.00	1.3	14	18	20*
4	10	0.05	4.25	0.71	3.5	33	31	20*

*: concentration in $[\text{L}^{\text{PtPr}}\text{PdCl}_2\text{Pd}(\text{C}_3\text{H}_5)]$ referring to weighted sample.

temperatures the mixing times $d\delta$ had to be lowered to be able to evaluate the spectra despite the fast exchanges (e.g. in the case where chloride ions were added). As a result, the signal of the not dominant exchange processes became very small relative to the background noise.

A.2.7. Plots associated to the allyl exchanges within the palladium complexes

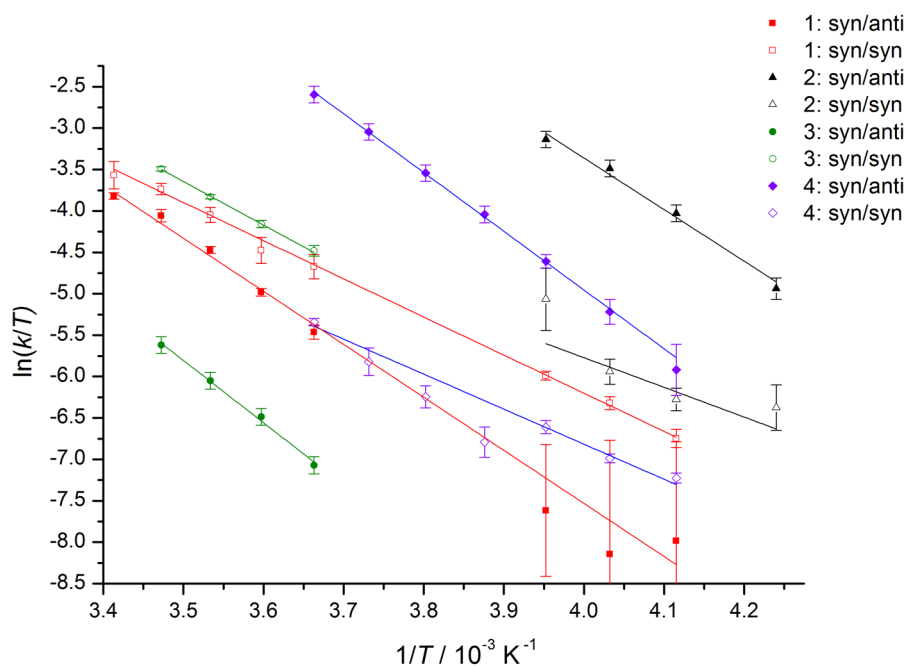


Figure 119: Eyring plots for the allyl complexes **1**–**4**. $[\text{L}^{\text{PI}^{\text{iPr}}}\text{PdCl}_2\text{Pd}(\text{C}_3\text{H}_5)]$ is **1**, $[\text{L}^{\text{PI}^{\text{iPr}}}\text{PdBr}_2\text{Pd}(\text{C}_3\text{H}_5)]$ is **2**, $[\text{L}^{\text{PI}^{\text{Ph}}}\text{PdCl}_2\text{Pd}(\text{C}_3\text{H}_5)]$ is **3** and $[\text{L}^{\text{PI}^{\text{Ph}}}\text{PdBr}_2\text{Pd}(\text{C}_3\text{H}_5)]$ is **4**.

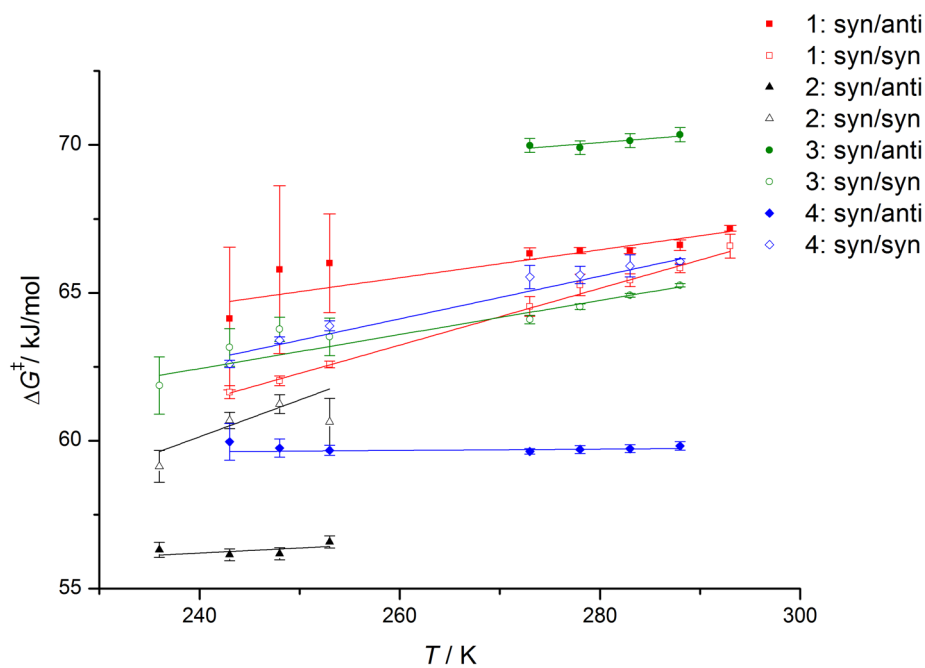


Figure 120: Plots of ΔG^\ddagger against T of the allyl complexes **1**–**4**. $[\text{L}^{\text{PI}^{\text{iPr}}}\text{PdCl}_2\text{Pd}(\text{C}_3\text{H}_5)]$ is **1**, $[\text{L}^{\text{PI}^{\text{iPr}}}\text{PdBr}_2\text{Pd}(\text{C}_3\text{H}_5)]$ is **2**, $[\text{L}^{\text{PI}^{\text{Ph}}}\text{PdCl}_2\text{Pd}(\text{C}_3\text{H}_5)]$ is **3** and $[\text{L}^{\text{PI}^{\text{Ph}}}\text{PdBr}_2\text{Pd}(\text{C}_3\text{H}_5)]$ is **4**.

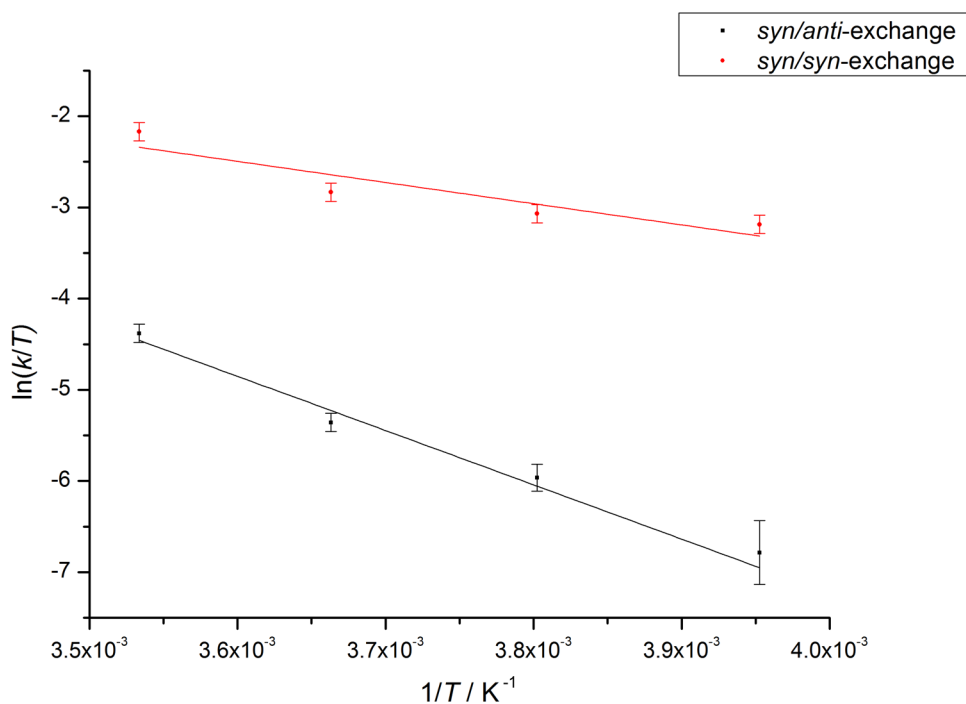


Figure 121: Eyring plot of the allyl exchange of $[\text{L}^{\text{PI}^{\text{iPr}}}\text{PdCl}_2\text{Pd}(\text{C}_3\text{H}_5)]$ (**1**) with 0.5 eq. of Bu_4NCl .

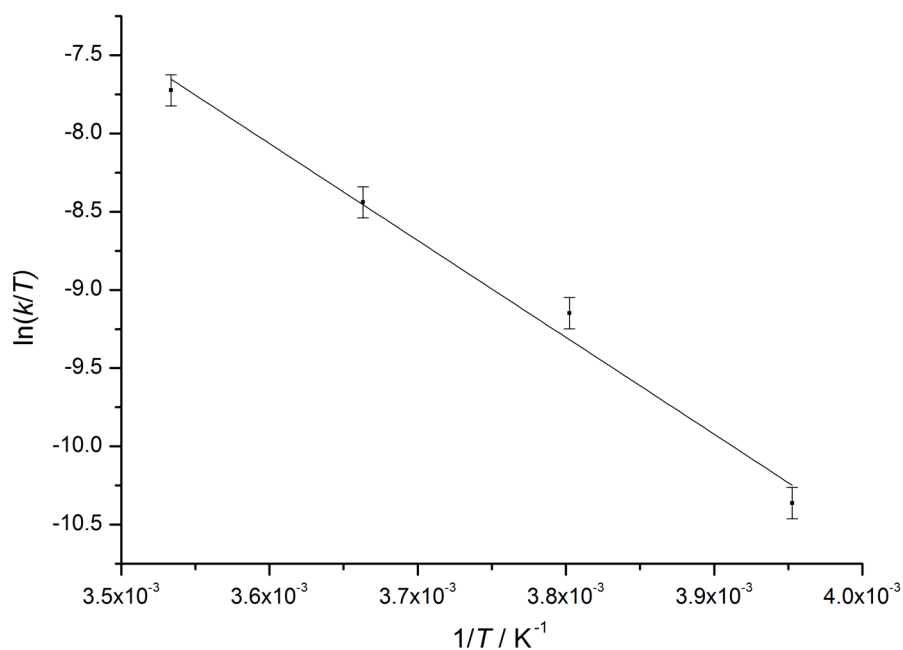


Figure 122: Eyring plot of the complex exchange between $[\text{L}^{\text{PI}^i\text{Pr}}\text{PdCl}_2\text{Pd}(\text{C}_3\text{H}_5)]$ (**1**) and $[(\text{C}_3\text{H}_5)\text{PdCl}]_2$.

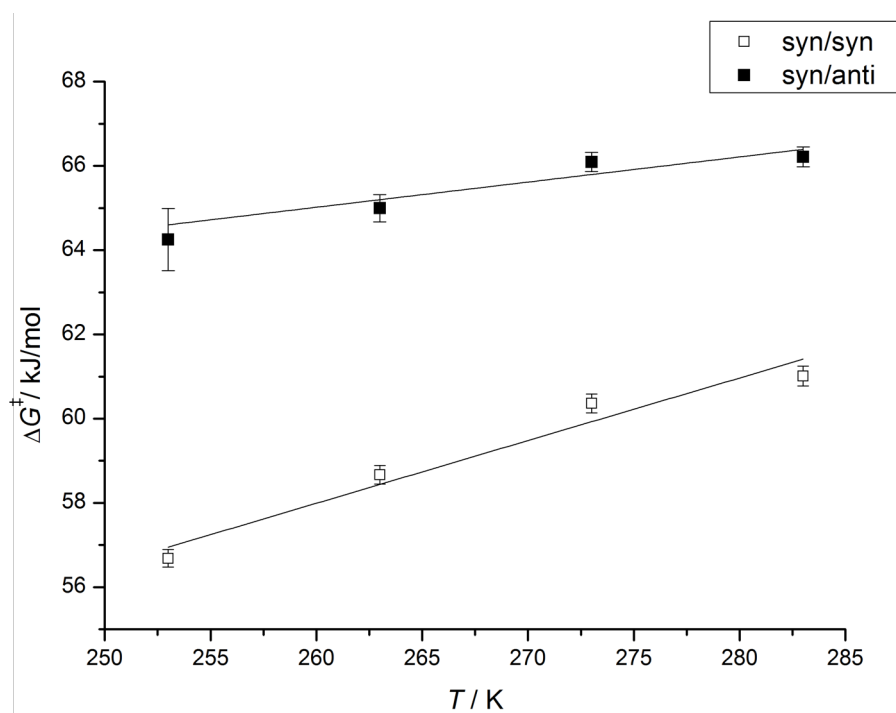


Figure 123: Plot of ΔG^\ddagger vs. T of $[\text{L}^{\text{PI}^i\text{Pr}}\text{PdCl}_2\text{Pd}(\text{C}_3\text{H}_5)]$ (**1**) with 0.5 eq. of Bu_4NCl .

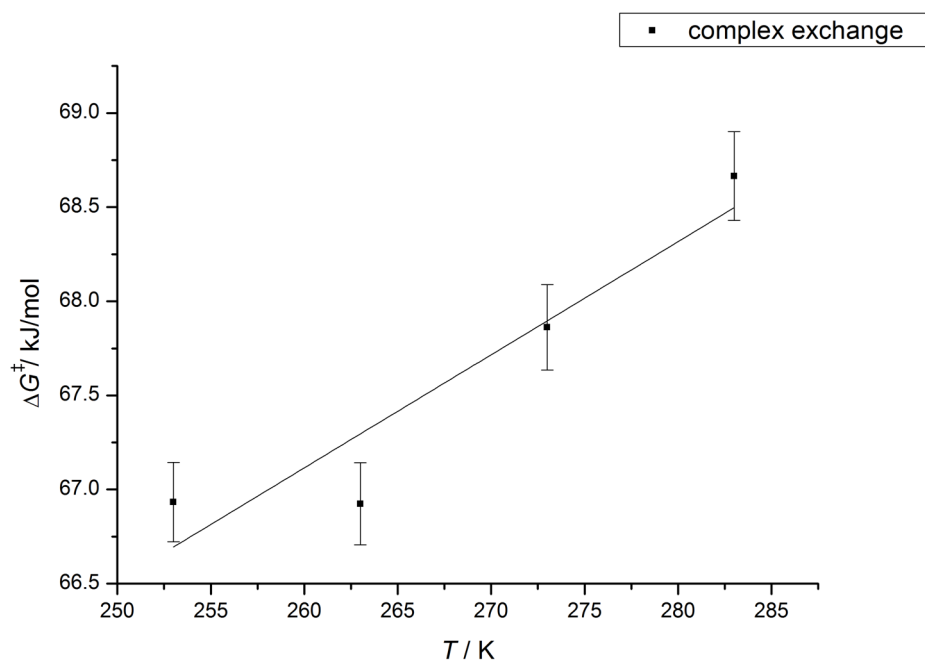


Figure 124: Plot of ΔG^\ddagger vs. T of the complex exchange between $[\text{L}^{\text{PI}^{\text{Pr}}}\text{PdCl}_2\text{Pd}(\text{C}_3\text{H}_5)]$ (1) and $[(\text{C}_3\text{H}_5)\text{PdCl}]_2$.

A.2.8. Complex $[\text{L}^{\text{PI}^{\text{Ph}}}\text{Ni}_2\text{Br}_3]_2$

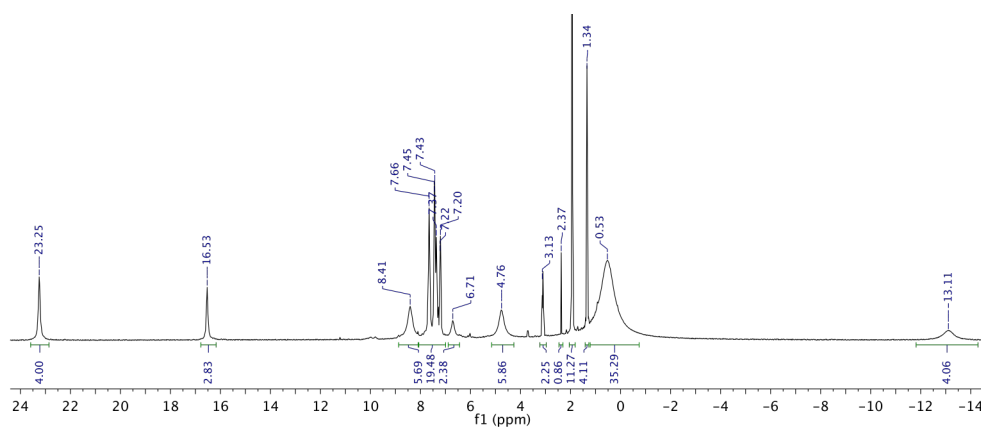


Figure 125: Para- ^1H -NMR spectrum of $[\text{L}^{\text{PI}^{\text{Ph}}}\text{Ni}_2\text{Br}_3]_2$ in CD_3CN .

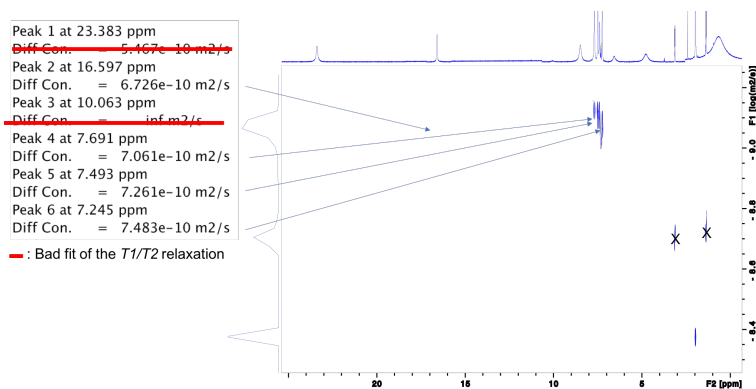


Figure 126: Para-DOSY-NMR spectrum of $[\text{L}^{\text{PI}^{\text{Ph}}}\text{Ni}_2\text{Br}_3]_2$ in CD_3CN . The residual signals of diethyl ether are visible in the spectrum at $D = 1.825 \times 10^{-9} \text{ m}^2/\text{s}$ (crossed out by an “X”). Processing was performed with TopSpin NMR software from Bruker.

A.3. Polymerization reactions

A.3.1. CO_2/CHO polymerizations with complex $[\text{L}^{\text{ProOH}}\text{Zn}]_2$

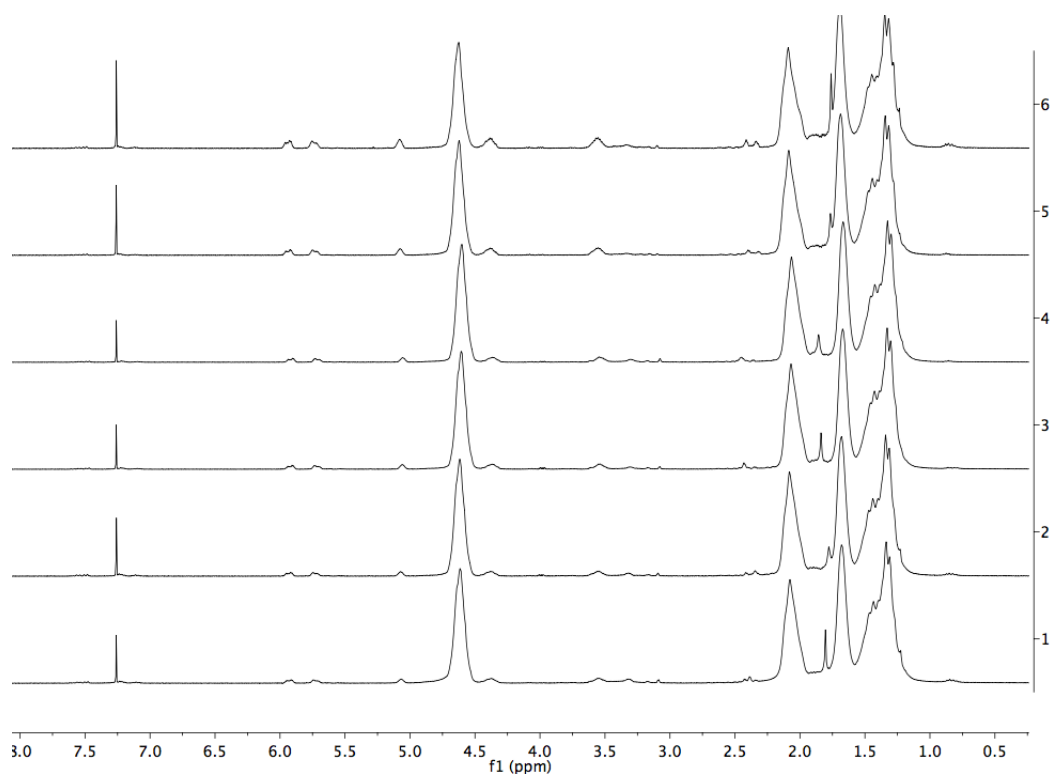


Figure 127: ^1H -NMR spectra in CDCl_3 of the products obtained from the polymerization reactions summarized in Table 5 with hydrophobic glassware. The entries from Table 5 correspond to the spectra in the figure as following: Spec. 1 to entry 3, spec. 2 to entry 4, spec. 3 to entry 7, spec. 4 to entry 8, spec. 5 to entry 9, spec. 6 to Entry 10.

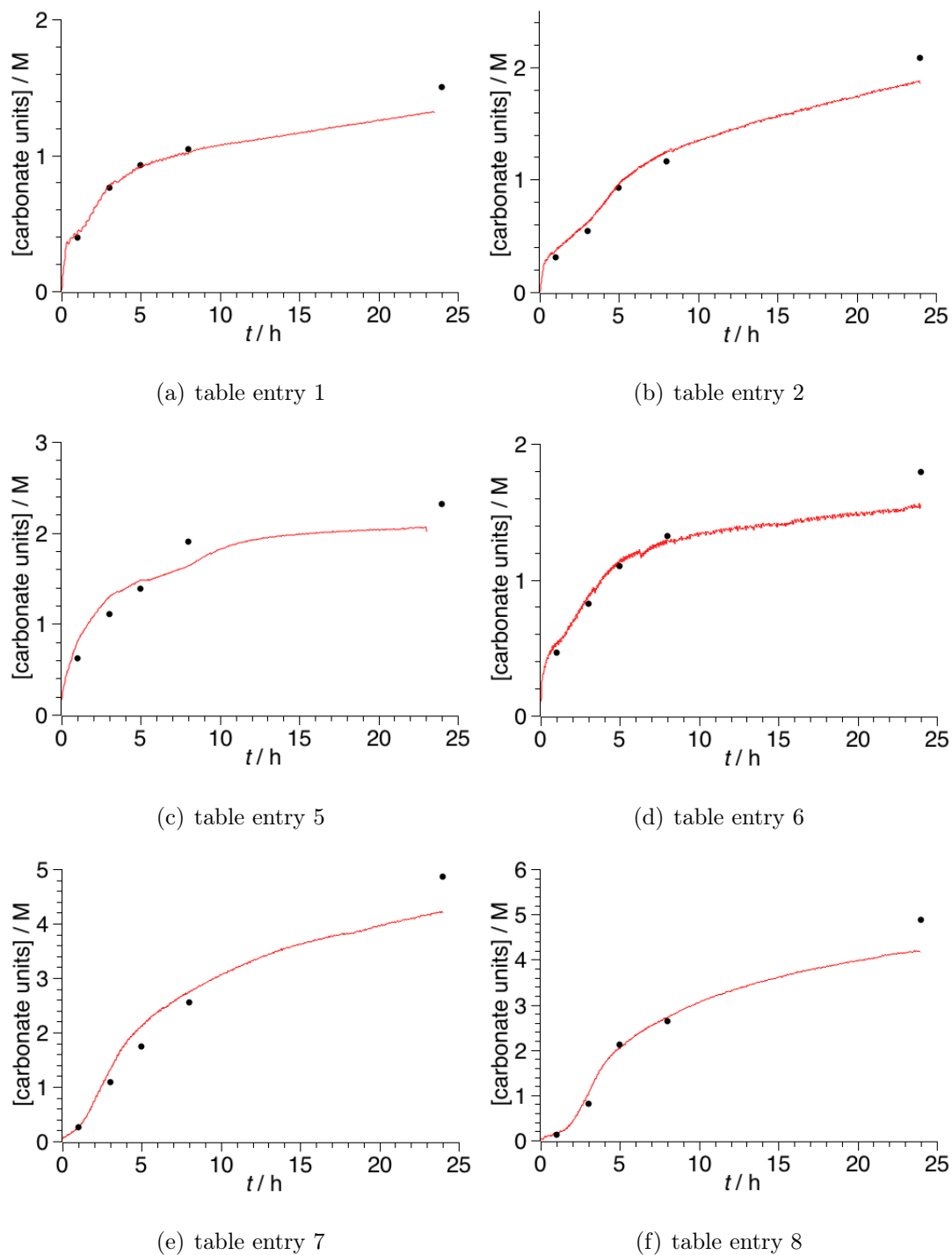


Figure 128: Plot of the PCHC formation against time. PCHC formation monitored by *in situ* IR measurement at the increase of the band at 1750 cm^{-1} and correlated with the PCHC product found in samples taken from the reaction solution. Referring to the polymerizations within Table 5.

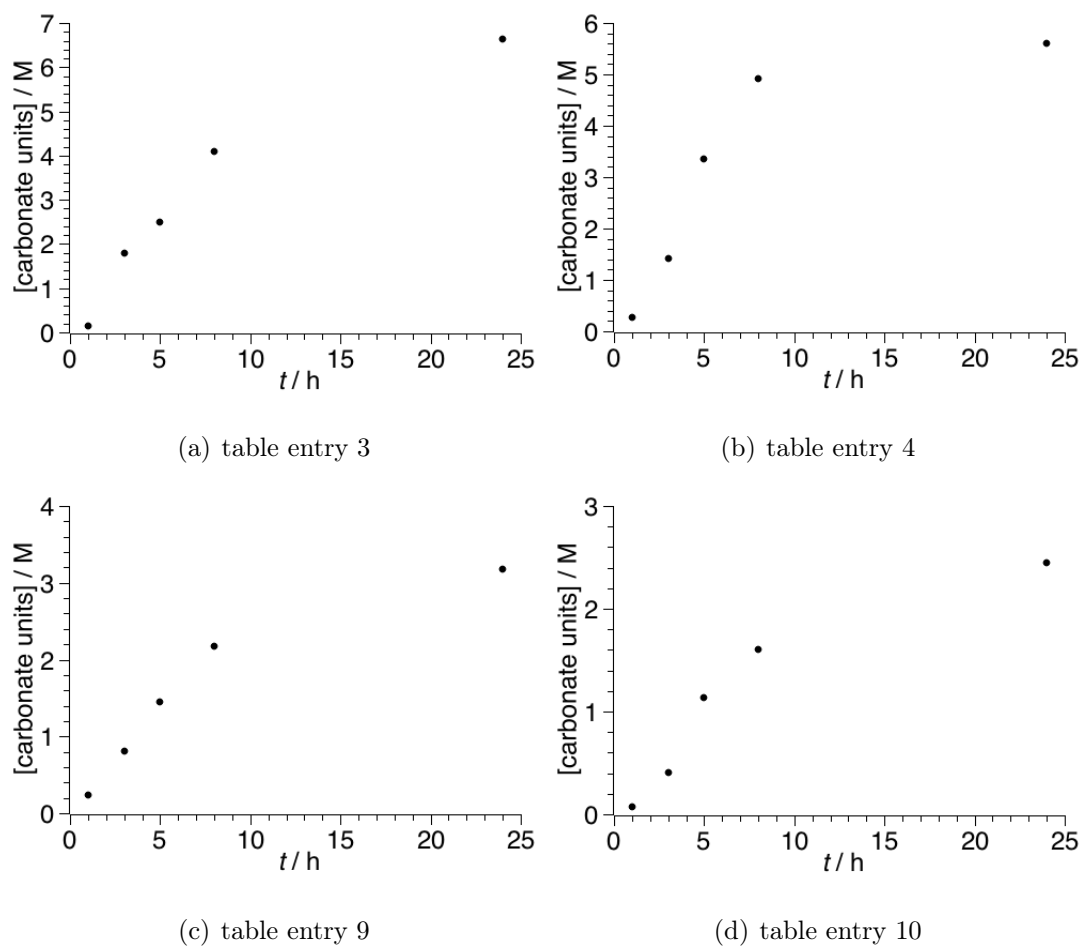


Figure 129: Plot of the PCHC formation against time. PCHC formation monitored by analyzing samples taken from the reaction solution. Referring to the polymerizations within Table 5.

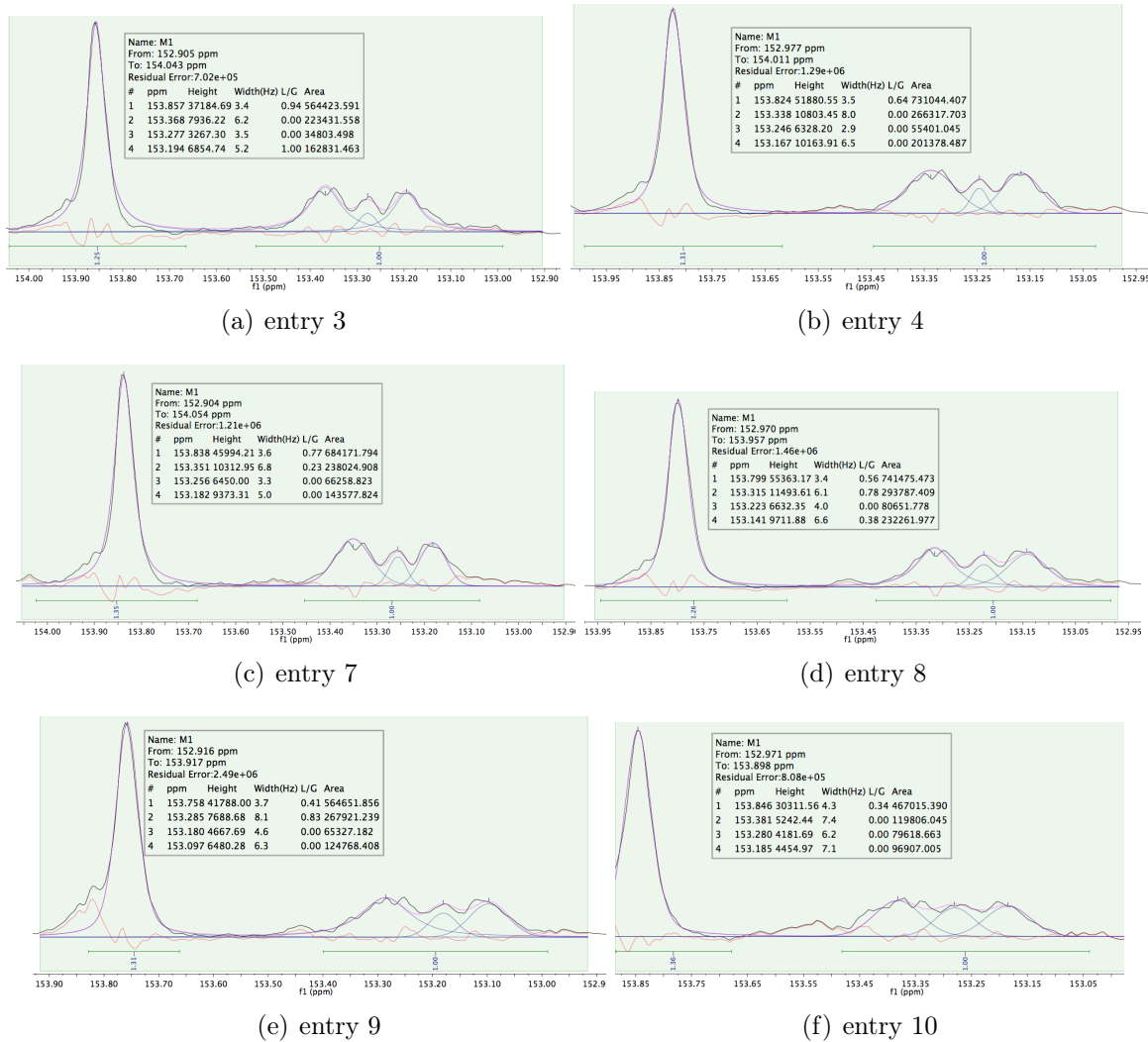


Figure 130: Carbonyl section of the ^{13}C -NMR spectra in CDCl_3 of the products obtained from the polymerization runs within Table 5 applying hydrophobic glassware. The fit (purple line) of the region and assignment of the tetrad-sequences are displayed. ^{103}C Black line: experimental data, blue line: fit of the according peak, red line: visualization of the error. The entries from Table 5 correspond to the spectra in the figure as depicted under each graphic.

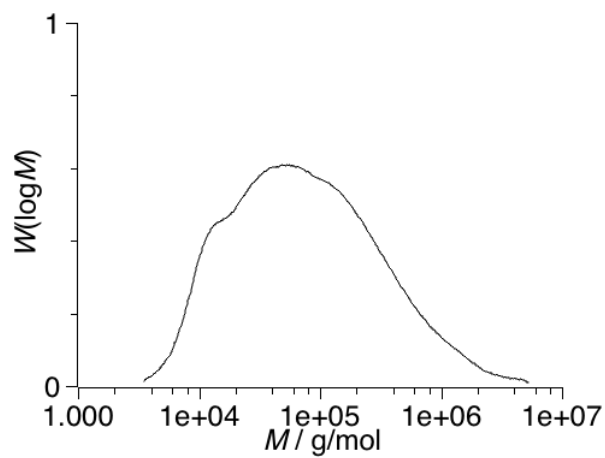
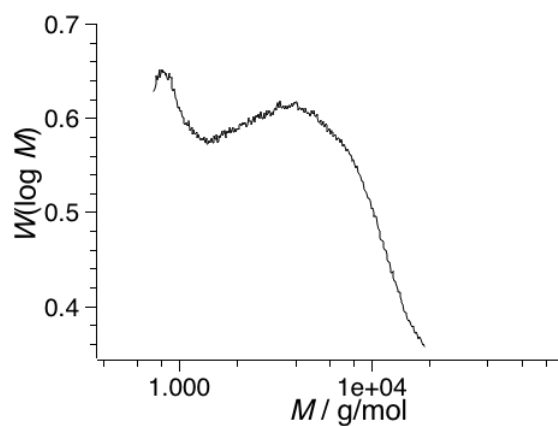
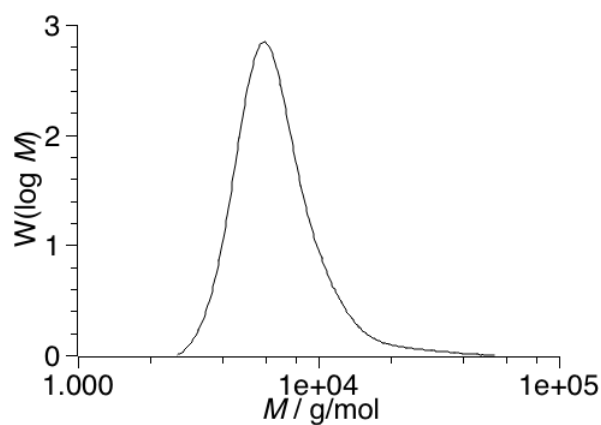
A.3.2. CO₂/CHO polymerizations with complex [L^{ProOH}_nCo_n]

Figure 131: Molecular mass distribution determined by GPC analysis. GPC analysis was performed in THF, calibrated with polystyrene, and toluene was added as internal standard.

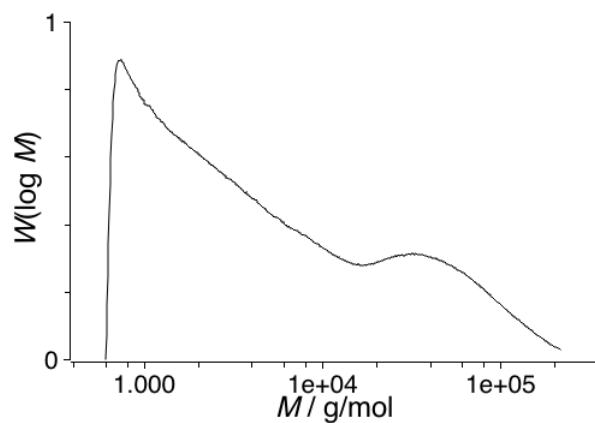
A.3.3. CO₂/CHO polymerizations with complex [L^{BOX}Zn₂(OAc)₃]₂ and [L^{BOX}Co₂(OAc)₃]₂

(a) table entry 1

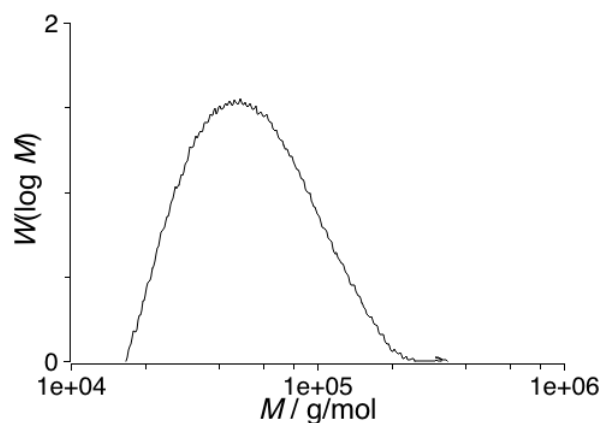


(b) table entry 6

Figure 132: Molecular mass distribution determined by GPC analysis. GPC analysis was performed in THF, calibrated with polystyrene, and toluene was added as internal standard.



(a) Table 17, entry 3.



(b) Table 17, entry 3, magnification of the signal suspected to origin form PCO. PDI = 1.32

Figure 133: Molecular mass distribution determined by GPC analysis. GPC analysis was performed in THF, calibrated with polystyrene, and toluene was added as internal standard.

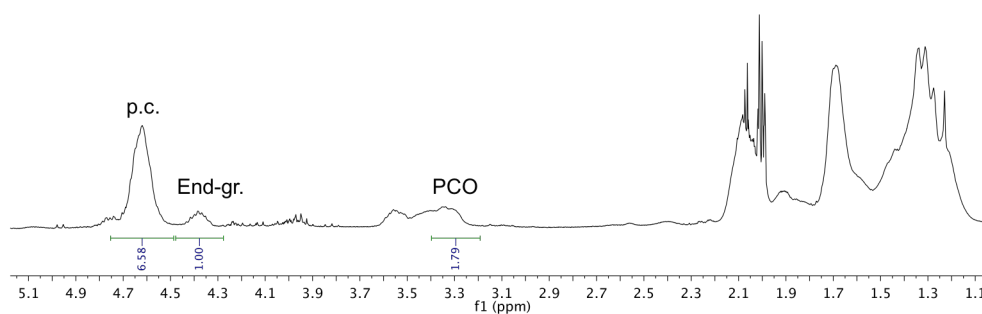


Figure 134: Section of the $^1\text{H-NMR}$ spectrum of the product of Table 17, entry 3 in CDCl_3 .

A.3.4. Further information on the data analysis for determination of the tacticity of the polymers

An assignment of the tetrad signals of the PCHC can be found in the publication of Coates *et al.* from 2006 and the referenced literature within.¹⁰³

The main problem of the precise determination of the tacticity and the associated P_r value (racemic diad probability) is, besides the accuracy of the performed fit, that the signals of the $[mmm]$ and $[mmr]$ overlap at a chemical shift of 153.9 ppm (in CDCl_3). For the determination of the relative abundance of the P_r tetrad concentration the following steps were performed to obtain reliable P_r values:

From the Bernoullian method assuming the Bovey's formalism¹⁰⁵ the following expressions for $[mmm]$ and $[mmr]$ were combined giving:

$$[mmr] + [mmm] = 2((1 - P_r)^2 P_r) + (1 - P_r)^3$$

For a zero-point determination the equation was rearranged to from:

$$0 = P_r^3 - P_r^2 - P_r + 1 - [mmm + mmr]$$

From the fit of the tetrad signals the relative surface areas were determined and the obtained values were filled in for $[mmm + mmr]$. From the solutions of the latter equation a provisional P_r' value was obtained. To minimize the error from the fitted regions, since so far only one signal of the carbonly region was accounted for, the $[r]$ contribution of the mixed $[mmm + mmr]$ signal were summed up with the $[r]$ contributions of the remaining tetrad signals at higher fields to from the final P_r value.

However, a fast approximated determination is also possible, by when making the assumption that the low-field signals at 153.9 ppm exclusively originate from the m -centered tetrads and the high-field signals from ca. 153.0-153.5 ppm exclusively originate from the r -centered tetrads. This assumption neglects the $[rmr]$ tetrads, that could not be assigned or found in the polymer probes at the proposed chemical shift of 152.9 ppm in CDCl_3 .¹⁰³ Furthermore, the assignment of the $[rmr]$ tetrads even after the publication of Coates *et al.* in 2006 is not certain.¹⁰³ Under the taken assumption, m - and r -centered tetrad regions can be integrated do determine an approximated P_r^a value.

A.4. X-ray crystallography

The X-ray data were collected on a STOE IPDS II diffractometer (graphite monochromated Mo-K α radiation, $\lambda = 0.71073 \text{ \AA}$) by use of ω scans. The structures were solved with SHELXT³⁴³ and refined on F^2 accounting for all reflections with SHELXL-2014, SHELXL-2016 or SHELXL-2017.³⁴⁴ All non-hydrogen atoms were refined anisotropically. Most hydrogen atoms were placed in calculated positions and assigned to an isotropic displacement parameter of 1.2 / 1.5 $U_{eq}(\text{C})$. Face-indexed absorption corrections were performed numerically with the program X-RED.³⁴⁵

This short summary of the data from the X-ray measurements was composed together with Dr. Sebastian Dechert.

Table 34: Crystal data and refinement details for $\text{H}_2\text{L}^{\text{ProOH}}$, $[\text{L}^{\text{ProOH}}\text{Zn}]_2$, $[\text{L}^{\text{ProOH}}\text{Zn}]_2'$ and $[(\text{L}^{\text{ProOH}}\text{Zn})_6(\text{Zn}_3\text{CO}_3)]$.

compound	$\text{H}_2\text{L}^{\text{ProOH}}$	$[\text{L}^{\text{ProOH}}\text{Zn}]_2$	$[\text{L}^{\text{ProOH}}\text{Zn}]_2'$	$[(\text{L}^{\text{ProOH}}\text{Zn})_6(\text{Zn}_3\text{CO}_3)]$
empirical formula	$\text{C}_{20}\text{H}_{25}\text{NO}_2$	$\text{C}_{80}\text{H}_{92}\text{N}_4\text{O}_8\text{Zn}_4$	$\text{C}_{86}\text{H}_{106}\text{Cl}_2\text{N}_4\text{O}_8\text{Zn}_4$	$\text{C}_{123}\text{H}_{138}\text{N}_6\text{O}_{21}\text{Zn}_9$
formula weight	311.41	1499.05	1656.12	2624.72
T [K]	133(2)	133(2)	133(2)	133(2)
crystal size [mm ³]	$0.500 \times 0.390 \times 0.290$	$0.500 \times 0.490 \times 0.470$	$0.500 \times 0.490 \times 0.470$	$0.500 \times 0.490 \times 0.480$
crystal system	tetragonal	tetragonal	monoclinic	cubic
space group	$P4_12_12$ (No. 92)	$P4_32_12$ (No. 96)	$P2_1$ (No. 4)	$P2_13$ (No. 198)
a [Å]	7.9941(2)	17.1821(2)	14.3365(3)	26.0397(2)
b [Å]	7.9941(2)	17.1821(2)	19.4694(3)	26.0397(2)
c [Å]	53.9524(19)	23.3762(4)	14.5663(3)	26.0397(2)
α [°]	90	90	90	90
β [°]	90	90	97.852(2)	90
γ [°]	90	90	90	90
V [Å ³]	3447.9(2)	6901.2(2)	4027.67(13)	17656.6(4)
Z	8	4	2	4
ρ [g·cm ⁻³]	1.200	1.443	1.366	0.987
$F(000)$	1344	3136	1736	5424
μ [mm ⁻¹]	0.077	1.435	1.300	1.247
$T_{\text{min}} / T_{\text{max}}$	0.8143 / 0.9562	0.5399 / 0.6062	0.4251 / 0.9543	0.6246 / 0.6990
θ -range [°]	1.510 - 25.681	1.471 - 26.779	1.411 - 26.734	1.354 - 25.948
hkl -range	$-9 \leq h \leq 9$ $-9 \leq k \leq 9$ $-65 \leq l \leq 9$	$-19 \leq h \leq 21$ $-21 \leq k \leq 21$ $-29 \leq l \leq 29$	$-18 \leq h \leq 18$ $-24 \leq k \leq 24$ $-18 \leq l \leq 18$	$-32 \leq h \leq 31$ $-31 \leq k \leq 31$ $-31 \leq l \leq 31$
measured refl.	20784	72872	58959	217874
unique refl. [R_{int}]	3266 [0.0571]	7335 [0.0372]	17037 [0.0699]	11245 [0.0689]
obs. refl. ($I > 2\sigma(I)$)	2809	7155	15993	10078
data / restr. / param.	3266 / 0 / 216	7335 / 0 / 433	17037 / 54 / 983	11245 / 0 / 478
goodness-of-fit (F^2)	1.034	1.055	1.017	1.089
$R1, wR2$ ($I > 2\sigma(I)$)	0.0304 / 0.0712	0.0187 / 0.0460	0.0344 / 0.0853	0.0300 / 0.0728
$R1, wR2$ (all data)	0.0369 / 0.0733	0.0197 / 0.0464	0.0373 / 0.0865	0.0380 / 0.0792
res. el. dens. [e·Å ⁻³]	-0.102 / 0.110	-0.259 / 0.246	-0.291 / 0.451	-0.384 / 0.238

Table 35: Crystal data and refinement details for $[\text{L}^{\text{ProOH}}\text{Ni}]_2$, $[\text{L}^{\text{ProOH}}\text{Co}]_n$, $[\text{L}^{\text{CP1}}(\text{Zn-OAc})_2]$, and $[\text{L}^{\text{CPA}}(\text{Zn-Cl})_2]$.

compound	$[\text{L}^{\text{ProOH}}\text{Ni}]_2$	$[\text{L}^{\text{ProOH}}\text{Co}]_n$	$[\text{L}^{\text{CP1}}(\text{Zn-OAc})_2]$	$[\text{L}^{\text{CPA}}(\text{Zn-Cl})_2]$
empirical formula	$\text{C}_{48.40}\text{H}_{63.60}\text{N}_2\text{Ni}_2\text{O}_{5.60}$	$\text{C}_{122}\text{H}_{144}\text{Cl}_4\text{Co}_7\text{N}_6\text{O}_{14}$	$\text{C}_{26.50}\text{H}_{37}\text{Cl}_5\text{N}_8\text{O}_4\text{Zn}_2$	$\text{C}_{23}\text{H}_{40}\text{Cl}_8\text{N}_8\text{Zn}_2$
formula weight	880.43	2472.73	839.63	842.97
T [K]	133(2)	133(2)	133(2)	133(2)
crystal size [mm ³]	$0.480 \times 0.450 \times 0.200$	$0.500 \times 0.280 \times 0.210$	$0.500 \times 0.360 \times 0.190$	$0.210 \times 0.200 \times 0.180$
crystal system	monoclinic	monoclinic	monoclinic	monoclinic
space group	$P2_1$ (No. 4)	$P2_1$ (No. 4)	$P2_1/n$ (No. 14)	$P2_1/n$ (No. 14)
a [Å]	8.7811(3)	15.0677(3)	13.1268(4)	12.9512(3)
b [Å]	19.3047(5)	18.0883(5)	12.7160(3)	13.3785(3)
c [Å]	13.0409(4)	23.4340(6)	22.4372(7)	21.0557(5)
α [°]	90	90	90	90
β [°]	94.927(3)	91.067(2)	102.592(3)	95.794(2)
γ [°]	90	90	90	90
V [Å ³]	2202.48(12)	6385.8(3)	3655.14(19)	3629.63(15)
Z	2	2	4	4
ρ [g·cm ⁻³]	1.328	1.286	1.526	1.543
$F(000)$	938	2574	1716	1720
μ [mm ⁻¹]	0.904	1.029	1.721	1.939
T_{\min} / T_{\max}	0.6265 / 0.8824	0.4743 / 0.7565	0.3690 / 0.8428	0.5881 / 0.7378
θ -range [°]	1.567 - 27.043	1.422 - 25.759	1.657 - 26.950	1.806 - 26.863
hkl -range	-11 $\leq h \leq$ 11 -24 $\leq k \leq$ 24 -16 $\leq l \leq$ 24	-15 $\leq h \leq$ 18 -21 $\leq k \leq$ 21 -28 $\leq l \leq$ 28	-16 $\leq h \leq$ 16 -16 $\leq k \leq$ 14 -28 $\leq l \leq$ 28	-16 $\leq h \leq$ 13 -16 $\leq k \leq$ 16 -26 $\leq l \leq$ 26
measured refl.	30892	76765	36925	39659
unique refl. $[R_{\text{int}}]$	9327 [0.0281]	24105 [0.1044]	7764 [0.0275]	7713 [0.0395]
obs. refl. ($I > 2\sigma(I)$)	8853	20060	6644	6126
data / restr. / param.	9327 / 52 / 570	24105 / 3 / 1385	7764 / 30 / 480	7713 / 91 / 433
goodness-of-fit (F^2)	1.046	1.024	1.081	1.065
$R1, wR2$ ($I > 2\sigma(I)$)	0.0273 / 0.0656	0.0549 / 0.1280	0.0325 / 0.0820	0.0382 / 0.0944
$R1, wR2$ (all data)	0.0305 / 0.0675	0.0664 / 0.1335	0.0423 / 0.0893	0.0564 / 0.1053
res. el. dens. [e·Å ⁻³]	-0.230 / 0.376	-0.572 / 0.609	-0.663 / 0.833	-0.928 / 0.849

Table 36: Crystal data and refinement details for $[\text{L}^{\text{O}^{\text{Ph}}\text{N}^{\text{H}}}\text{ZnEt}]_2$, $[\text{L}^{\text{BOX}}\text{Zn}_2(\text{OAc})_3]_2$, $[\text{L}^{\text{BOX}}\text{Co}_2(\text{OAc})_3]_2$ and $[\text{L}^{\text{PzImineCPh}_2}\text{Co}_2(\text{OAc})_3]_2$.

compound	$[\text{L}^{\text{O}^{\text{Ph}}\text{N}^{\text{H}}}\text{ZnEt}]_2$	$[\text{L}^{\text{BOX}}\text{Zn}_2(\text{OAc})_3]_2$	$[\text{L}^{\text{BOX}}\text{Co}_2(\text{OAc})_3]_2$	$[\text{L}^{\text{PzImineCPh}_2}\text{Co}_2(\text{OAc})_3]_2$
empirical formula	$\text{C}_{40}\text{H}_{54}\text{N}_2\text{O}_2\text{Zn}_2$	$\text{C}_{54}\text{H}_{68}\text{N}_8\text{O}_{16}\text{Zn}_4$	$\text{C}_{96}\text{H}_{128}\text{Cl}_8\text{Co}_4\text{N}_{16}\text{O}_{20}$	$\text{C}_{160}\text{H}_{145}\text{Co}_4\text{N}_8\text{O}_{13}$
formula weight	725.59	1346.64	2345.46	2623.55
T [K]	213(2)	133(2)	133(2)	133(2)
crystal size [mm ³]	$0.500 \times 0.490 \times 0.280$	$0.500 \times 0.500 \times 0.380$	$0.440 \times 0.280 \times 0.120$	$0.500 \times 0.190 \times 0.160$
crystal system	monoclinic	orthorhombic	triclinic	monoclinic
space group	$P2_1/c$ (No. 14)	$P2_12_12_1$ (No. 19)	$P1$ (No. 1)	$P2_1/n$ (No. 14)
a [Å]	10.2247(5)	10.8502(2)	11.8595(4)	19.2772(5)
b [Å]	10.6769(3)	14.2425(3)	15.1203(5)	26.5037(8)
c [Å]	17.4364(8)	38.2667(7)	15.8335(5)	31.5386(9)
α [°]	90	90	85.241(3)	90
β [°]	106.065(4)	90	78.868(3)	102.727(2)
γ [°]	90	90	78.711(2)	90
V [Å ³]	1829.16(14)	5913.5(2)	2728.92(16)	15717.7(8)
Z	2	4	1	4
ρ [g·cm ⁻³]	1.317	1.513	1.427	1.109
$F(000)$	768	2784	1220	5492
μ [mm ⁻¹]	1.347	1.676	0.865	0.472
$T_{\text{min}} / T_{\text{max}}$	0.5779 / 0.7438	0.3589 / 0.6305	0.7323 / 0.8811	? / ?
θ -range [°]	2.073 - 26.940	1.064 - 25.667	1.375 - 26.866	1.138 - 25.717
hkl -range	$-13 \leq h \leq 12$ $-13 \leq k \leq 13$ $-20 \leq l \leq 13$	$-13 \leq h \leq 13$ $-17 \leq k \leq 17$ $-46 \leq l \leq 46$	$-15 \leq h \leq 15$ $-19 \leq k \leq 19$ $-20 \leq l \leq 20$	$-21 \leq h \leq 23$ $-32 \leq k \leq 32$ $-38 \leq l \leq 38$
measured refl.	24678	67277	51593	191290
unique refl. $[R_{\text{int}}]$	3887 [0.0278]	11197 [0.0627]	21892 [0.0480]	29771 [0.1391]
obs. refl. ($I > 2\sigma(I)$)	3406	10988	19524	16216
data / restr. / param.	3887 / 7 / 234	11197 / 0 / 753	21892 / 61 / 1357	29771 / 0 / 1683
goodness-of-fit (F^2)	1.074	1.050	1.025	0.945
$R1, wR2$ ($I > 2\sigma(I)$)	0.0252 / 0.0665	0.0285 / 0.0739	0.0437 / 0.1093	0.0735 / 0.1369
$R1, wR2$ (all data)	0.0321 / 0.0728	0.0292 / 0.0744	0.0504 / 0.1124	0.1376 / 0.1592
res. el. dens. [e·Å ⁻³]	-0.348 / 0.324	-0.569 / 0.406	-0.910 / 1.159	-0.291 / 0.521

Table 37: Crystal data and refinement details for $[\text{L}^{\text{Pr}^{\text{III}}}\text{Cu}_2\text{Cl}_3]_2$.

compound	$[\text{L}^{\text{Pr}^{\text{III}}}\text{Cu}_2\text{Cl}_3]_2$
empirical formula	$\text{C}_{169}\text{H}_{150}\text{Cl}_6\text{Cu}_4\text{N}_8$
formula weight	2759.82
T [K]	133(2)
crystal size [mm ³]	$0.390 \times 0.150 \times 0.110$
crystal system	tetragonal
space group	$P4_12_12$ (No. 92)
a [Å]	18.4634(4)
b [Å]	18.4634(4)
c [Å]	41.7871(11)
α [°]	90
β [°]	90
γ [°]	90
V [Å ³]	14245.1(7)
Z	4
ρ [g·cm ⁻³]	1.287
$F(000)$	5752
μ [mm ⁻¹]	0.758
$T_{\text{min}} / T_{\text{max}}$	0.6942 / 0.8701
θ -range [°]	1.206 - 24.665
hkl -range	$-21 \leq h \leq 21$ $-19 \leq k \leq 21$ $-48 \leq l \leq 21$
measured refl.	79443
unique refl. [R_{int}]	11988 [0.0957]
obs. refl. ($I > 2\sigma(I)$)	9777
data / restr. / param.	11988 / 0 / 835
goodness-of-fit (F^2)	1.029
$R1, wR2$ ($I > 2\sigma(I)$)	0.0539 / 0.1055
$R1, wR2$ (all data)	0.0714 / 0.1117
res. el. dens. [e·Å ⁻³]	-0.354 / 0.512

A.4.1. Selected bond lengths and bond angles

Table 38: Selected bond lengths (sorted) [Å] for $\text{H}_2\text{L}^{\text{ProOH}}$.

Atoms	Bond lengths
O1–H1	0.89(2)
O2–H2	0.90(3)
O2–C20	1.414(3)
O2–C20	1.415(2)
O1–C1	1.4205(19)
O2–N1	2.8477(20)
O1–N1	2.9013(19)

Table 39: Selected bond angles (sorted) [°] for $\text{H}_2\text{L}^{\text{ProOH}}$.

Atoms	Bond angles
C20–O2–H2	104.5(16)
O1–C1–C2	105.16(13)
O1–C1–C14	108.75(13)
O2–C20–H20A	109.2
O2–C20–H20B	109.2
O1–C1–C8	111.23(12)
O2–C20–C19	112.05(17)
C1–O1–H1	113.1(16)

Table 40: Selected bond lengths (sorted) [Å] for $[\text{L}^{\text{ProOH}}\text{Zn}]_2$.

Atoms	Bond lengths
Zn2–O11	1.8865(15)
Zn1–O2	1.9568(15)
Zn2–O12	1.9634(15)
Zn2–O1	1.9778(14)
Zn1–O12	1.9830(15)
Zn1–O2'	2.0344(15)
Zn1–O1	2.0565(14)
Zn2–N11	2.1097(18)
Zn1–N1	2.3001(17)
Zn1–Zn2	2.9110(3)
Zn1–Zn1'	3.0855(5)

Table 41: Selected bond angles (sorted) [°] for $[L^{\text{ProOH}}\text{Zn}]_2$.

Atoms	Bond angles	Atoms	Bond angles
O2'-Zn1-Zn1'	38.46(4)	C21-O11-Zn2	112.88(12)
O2-Zn1-Zn1'	40.29(5)	O12-Zn1-O2'	113.17(6)
O12-Zn1-Zn2	42.21(4)	C1-O1-Zn1	114.05(11)
O12-Zn2-Zn1	42.73(4)	C37-N11-Zn2	117.29(14)
O1-Zn1-Zn2	42.76(4)	O12-Zn1-Zn1'	117.71(4)
O1-Zn2-Zn1	44.90(4)	N11-Zn2-Zn1	118.23(5)
O2-Zn1-O2'	77.65(7)	O2-Zn1-O12	119.93(7)
O1-Zn1-N1	79.30(6)	O11-Zn2-O1	121.14(6)
O12-Zn1-O1	84.33(6)	C17-N1-Zn1	121.27(13)
O12-Zn2-O1	86.97(6)	C20-O2-Zn1	121.78(13)
O11-Zn2-N11	88.72(7)	C40-O12-Zn2	123.99(12)
O2-Zn1-N1	90.58(6)	C1-O1-Zn2	126.24(12)
Zn2-O1-Zn1	92.34(6)	N1-Zn1-Zn1'	128.98(4)
N1-Zn1-Zn2	92.63(4)	C40-O12-Zn1	129.03(13)
Zn2-O12-Zn1	95.06(6)	O1-Zn2-N11	132.34(7)
O12-Zn1-N1	96.14(6)	O11-Zn2-O12	133.68(7)
O12-Zn2-N11	98.03(7)	C20-O2-Zn1'	136.07(13)
O2'-Zn1-O1	100.02(6)	O1-Zn1-Zn1'	136.93(4)
C18-N1-Zn1	100.25(12)	Zn2-Zn1-Zn1'	138.204(12)
C34-N11-Zn2	101.02(12)	O2'-Zn1-N1	150.55(6)
Zn1-O2-Zn1'	101.24(7)	O11-Zn2-Zn1	152.44(5)
O2'-Zn1-Zn2	106.88(4)	O2-Zn1-O1	154.81(6)
C14-N1-Zn1	106.94(12)	O2-Zn1-Zn2	162.11(5)
C38-N11-Zn2	111.10(13)		

Table 42: Selected bond lengths (sorted) [Å] for $[L^{\text{ProOH}}\text{Zn}]_2$ (second coordination motif).

Atoms	Bond lengths	Atoms	Bond lengths
Zn4-O31	1.883(3)	Zn2-O22	2.008(3)
Zn1-O1	1.898(3)	Zn2-O12	2.059(3)
Zn3-O21	1.906(3)	Zn2-O11	2.099(3)
Zn4-O32	1.932(3)	Zn1-N1	2.102(4)
Zn3-O22	1.951(3)	Zn4-N31	2.106(3)
Zn4-O12	1.960(3)	Zn3-N21	2.133(3)
Zn1-O11	1.972(3)	Zn2-N11	2.262(3)
Zn1-O2	1.975(3)	Zn3-O12	2.423(3)
Zn2-O2	1.987(3)	Zn1-Zn2	2.9750(6)
Zn3-O32	1.992(3)	Zn3-Zn4	2.9779(6)

Table 43: Selected bond angles (sorted) [°] for $[\text{L}^{\text{ProOH}}\text{Zn}]_2$ (second coordination motif).

Atoms	Bond angles	Atoms	Bond angles
O32–Zn3–Zn4	39.88(8)	C34–N11–Zn2	108.4(2)
O12–Zn3–Zn4	40.95(6)	O22–Zn3–Zn4	109.65(8)
O2–Zn2–Zn1	41.17(8)	C18–N1–Zn1	110.1(3)
O32–Zn4–Zn3	41.38(9)	C1–O1–Zn1	111.3(2)
O11–Zn2–Zn1	41.39(7)	O21–Zn3–O32	111.33(13)
O2–Zn1–Zn2	41.48(8)	O32–Zn3–N21	112.62(13)
O11–Zn1–Zn2	44.75(8)	C40–O12–Zn4	112.9(2)
O12–Zn4–Zn3	54.14(8)	C21–O11–Zn2	113.6(2)
O32–Zn3–O12	75.55(10)	C40–O12–Zn2	114.2(2)
O22–Zn3–O12	75.75(10)	O31–Zn4–O12	114.28(12)
O11–Zn2–N11	78.84(11)	C38–N11–Zn2	114.5(2)
O2–Zn2–O11	82.56(10)	O22–Zn3–O32	115.04(11)
O22–Zn2–O12	83.62(11)	O2–Zn2–O12	115.08(11)
O12–Zn2–N11	84.79(11)	C61–O31–Zn4	115.1(3)
Zn4–O12–Zn3	84.90(9)	C77–N31–Zn4	115.6(3)
O11–Zn1–O2	86.22(11)	C41–O21–Zn3	116.3(2)
O21–Zn3–N21	86.23(12)	C57–N21–Zn3	118.2(3)
O31–Zn4–N31	87.74(14)	C17–N1–Zn1	118.3(4)
O21–Zn3–Zn4	88.38(9)	C80–O32–Zn4	121.0(3)
O1–Zn1–N1	88.60(12)	C20–O2–Zn1	123.3(3)
O32–Zn4–O12	88.92(12)	O1–Zn1–O11	123.51(12)
O21–Zn3–O12	89.62(10)	C60–O22–Zn3	123.6(2)
Zn2–O12–Zn3	90.15(10)	N1–Zn1–Zn2	124.17(9)
Zn1–O11–Zn2	93.86(11)	C20–O2–Zn2	125.0(2)
N11–Zn2–Zn1	94.11(8)	O21–Zn3–O22	125.31(12)
Zn1–O2–Zn2	97.35(12)	O31–Zn4–Zn3	125.53(9)
Zn4–O32–Zn3	98.74(12)	C21–O11–Zn1	125.8(2)
O2–Zn1–N1	100.40(13)	C60–O22–Zn2	129.2(2)
O32–Zn4–N31	100.82(13)	O11–Zn1–N1	130.19(13)
O22–Zn3–N21	100.91(13)	O1–Zn1–O2	131.01(13)
O2–Zn2–O22	101.57(11)	Zn4–O12–Zn2	131.88(13)
C14–N1–Zn1	101.6(2)	O12–Zn4–N31	136.00(11)
C54–N21–Zn3	101.9(2)	O31–Zn4–O32	136.21(13)
C74–N31–Zn4	102.0(2)	C80–O32–Zn3	137.2(3)
O22–Zn2–O11	104.47(11)	N31–Zn4–Zn3	140.65(10)
C78–N31–Zn4	106.1(2)	O1–Zn1–Zn2	145.58(9)
C58–N21–Zn3	106.4(2)	N21–Zn3–Zn4	145.79(11)
C37–N11–Zn2	106.8(2)	O22–Zn2–N11	150.32(12)
Zn3–O22–Zn2	107.08(13)	O12–Zn2–Zn1	154.38(8)
C40–O12–Zn3	107.3(2)	O12–Zn2–O11	159.15(10)
O22–Zn2–Zn1	107.87(8)	N21–Zn3–O12	171.74(12)
O2–Zn2–N11	108.10(12)		

Table 44: Selected bond lengths (sorted) [Å] for $[(\text{L}^{\text{ProOH}}\text{Zn})_3\text{CO}_3]_2(\text{Zn}_3\text{CO}_3)$ (Figure 38).

Atoms	Bond lengths
Zn1–O1	1.892(3)
Zn3–O12	1.919(3)
Zn3–O2	1.933(3)
Zn1–O3	1.942(3)
Zn3–O11''	1.952(3)
Zn1–O2	1.965(3)
Zn2–O13	1.966(3)
Zn2–O12	1.969(3)
Zn2–O11	2.008(3)
Zn3–O21	2.015(3)
Zn2–N11	2.091(3)
Zn1–N1	2.137(4)
Zn2–O21'	2.306(3)

Table 45: Selected bond angles (sorted) [°] for $[(\text{L}^{\text{ProOH}}\text{Zn})_3\text{CO}_3]_2(\text{Zn}_3\text{CO}_3)$ (Figure 38).

Atoms	Bond angles	Atoms	Bond angles
O11–Zn2–O21'	73.16(10)	Zn3–O12–Zn2	111.61(13)
O11''–Zn3–O21	81.22(11)	O12–Zn3–O21	115.29(11)
O11–Zn2–N11	84.30(12)	C1–O1–Zn1	116.6(2)
O1–Zn1–N1	86.63(12)	C51–O13–Zn2	116.8(3)
O12–Zn2–O21'	88.69(10)	C20–O2–Zn3	117.2(2)
O13–Zn2–O21'	92.38(10)	C41–O3–Zn1	118.74(19)
O13–Zn2–O12	93.80(12)	C61–O21–Zn2''	119.2(3)
Zn3–O21–Zn2''	93.81(10)	C61–O21–Zn3	119.60(17)
O2–Zn1–N1	95.38(12)	O3–Zn1–O2	120.36(12)
C14–N1–Zn1	99.6(2)	O12–Zn3–O11''	120.37(12)
O12–Zn2–N11	102.51(12)	C17–N1–Zn1	120.8(3)
O2–Zn3–O21	102.93(11)	O2–Zn3–O11''	121.30(12)
C18–N1–Zn1	104.2(2)	O3–Zn1–N1	121.61(13)
C34–N11–Zn2	105.6(2)	O1–Zn1–O2	121.70(12)
Zn3'–O11–Zn2	105.92(12)	C40–O12–Zn2	122.2(2)
O1–Zn1–O3	106.75(12)	Zn3–O2–Zn1	122.69(14)
O13–Zn2–N11	106.92(12)	C40–O12–Zn3	124.4(2)
C20–O2–Zn1	108.0(2)	O13–Zn2–O11	130.43(11)
C37–N11–Zn2	109.7(2)	O12–Zn2–O11	131.63(12)
O12–Zn3–O2	110.37(12)	C21–O11–Zn3'	141.4(2)
C38–N11–Zn2	110.5(2)	N11–Zn2–O21'	156.74(11)
C21–O11–Zn2	111.6(2)		

Table 46: Selected bond angles (sorted) [°] for [L^{ProOH}Ni]₂ (Figure 40).

Atoms	Bond angles	Atoms	Bond angles
O12–Ni1–Ni2	41.08(6)	C34–N11–Ni2	107.65(17)
O2–Ni1–Ni2	41.09(6)	C1–O1–Ni1	108.16(16)
O2–Ni2–Ni1	41.10(6)	C21–O11–Ni2	109.61(16)
O12–Ni2–Ni1	41.47(6)	C38–N11–Ni2	112.45(18)
O2–Ni1–O12	81.65(9)	C18–N1–Ni1	113.80(18)
O12–Ni2–O2	82.05(9)	C20–O2–Ni1	113.93(17)
O11–Ni2–N11	88.30(10)	C40–O12–Ni2	114.68(17)
O1–Ni1–N1	88.44(10)	C40–O12–Ni1	119.78(17)
O2–Ni1–N1	94.50(9)	C20–O2–Ni2	120.39(17)
O12–Ni2–N11	94.68(10)	O11–Ni2–Ni1	135.52(6)
O11–Ni2–O2	95.64(8)	N1–Ni1–Ni2	135.54(7)
O1–Ni1–O12	96.44(9)	O1–Ni1–Ni2	135.92(6)
Ni2–O12–Ni1	97.45(9)	N11–Ni2–Ni1	136.13(8)
Ni2–O2–Ni1	97.81(9)	O12–Ni1–N1	169.22(10)
C14–N1–Ni1	107.09(16)	O2–Ni2–N11	170.22(10)
C17–N1–Ni1	107.30(18)	O1–Ni1–O2	173.57(9)
C37–N11–Ni2	107.48(18)	O11–Ni2–O12	175.01(10)

Table 47: Selected bond angles (sorted) [°] for [(HO(L^{ProOH}₃Co₃)₂Co)] (Figure 44).

Atoms	Bond angles	Atoms	Bond angles	Atoms	Bond angles
O72-Co2-O62	80.07(19)	Co4-O42-Co3	95.4(2)	C20-O2-Co4	116.1(4)
O9-Co6-O52	80.7(2)	O72-Co7-N7	95.5(2)	C81-O61-Co6	116.3(4)
O2-Co2-O42	80.8(2)	Co2-O52-Co6	95.54(18)	C1-O1-Co1	116.6(4)
O42-Co2-O32	81.06(18)	O42-Co4-N4	95.6(2)	C61-O51-Co5	116.7(4)
O2-Co2-O32	81.14(18)	Co7-O9-Co5	95.6(2)	C101-O71-Co7	117.1(4)
O52-Co2-O62	81.18(18)	Co2-O2-Co4	95.76(19)	C21-O31-Co3	117.5(4)
O42-Co4-O2	81.19(19)	Co2-O42-Co3	95.76(18)	C41-O41-Co4	117.8(5)
O8-Co3-O42	81.4(2)	O71-Co7-O62	95.8(2)	C57-N4-Co4	118.0(5)
O72-Co7-O62	81.4(2)	Co1-O8-Co4	95.8(2)	C20-O2-Co2	118.1(4)
O62-Co6-O52	81.54(18)	Co5-O52-Co6	95.8(2)	C100-O62-Co2	118.2(4)
O52-Co5-O72	81.66(19)	Co2-O62-Co7	96.00(19)	C100-O62-Co7	118.3(4)
O72-Co2-O52	81.78(19)	O61-Co6-O52	96.1(2)	C37-N3-Co3	118.7(4)
O9-Co5-O72	81.95(19)	Co4-O8-Co3	96.8(2)	C60-O42-Co2	118.9(4)
O8-Co4-O2	82.01(19)	Co1-O8-Co3	96.9(2)	C17-N1-Co1	119.4(5)
O8-Co1-O32	82.07(19)	O52-Co5-N5	97.7(2)	C77-N5-Co5	119.6(4)
O2-Co1-O32	82.13(19)	Co6-O9-Co5	97.7(2)	C117-N7-Co7	120.0(4)
O32-Co3-O42	82.29(18)	Co3-O32-Co2	99.95(19)	O1-Co1-O8	120.2(2)
O9-Co7-O62	83.5(2)	Co6-O62-Co2	100.85(19)	C120-O72-Co2	120.2(4)
O31-Co3-N3	84.3(2)	Co5-O52-Co2	100.9(2)	C80-O52-Co2	121.0(4)
O71-Co7-N7	84.4(2)	O9-Co7-N7	101.4(2)	C40-O32-Co2	121.1(4)
O51-Co5-N5	84.9(2)	Co1-O2-Co2	101.4(2)	C97-N6-Co6	121.2(5)
O41-Co4-N4	85.0(2)	Co4-O42-Co2	101.4(2)	O61-Co6-O9	121.5(2)
O61-Co6-N6	85.0(2)	Co7-O72-Co2	102.4(2)	O71-Co7-O9	121.8(2)
O52-Co5-O9	85.2(2)	O2-Co2-O52	102.58(19)	C80-O52-Co5	122.7(4)
O1-Co1-N1	85.4(2)	C14-N1-Co1	102.7(4)	O41-Co4-O8	123.5(2)
O42-Co4-O8	85.40(19)	O8-Co3-N3	102.8(2)	C60-O42-Co4	123.8(4)
O32-Co3-O8	86.1(2)	C114-N7-Co7	102.8(4)	C120-O72-Co7	124.1(4)
O2-Co1-O8	87.25(19)	C118-N7-Co7	103.2(4)	C40-O32-Co3	124.6(4)
O62-Co6-O9	87.4(2)	O62-Co2-O32	103.23(18)	C100-O62-Co6	124.6(4)
O72-Co7-O9	88.23(19)	C54-N4-Co4	103.3(5)	C20-O2-Co1	125.6(4)
O51-Co5-O72	92.6(2)	C94-N6-Co6	103.3(4)	O31-Co3-O8	127.2(2)
Co6-O62-Co7	92.74(19)	O9-Co5-N5	103.4(2)	O51-Co5-O9	127.6(2)
Co7-O72-Co5	93.11(19)	O8-Co4-N4	103.8(2)	O51-Co5-O52	145.8(2)
Co1-O2-Co4	93.63(19)	C34-N3-Co3	103.8(4)	O31-Co3-O32	146.0(2)
O62-Co6-N6	93.7(2)	C74-N5-Co5	103.9(4)	O71-Co7-O72	149.4(2)
O2-Co1-N1	94.0(2)	C58-N4-Co4	104.2(5)	O41-Co4-O42	150.2(2)
Co3-O32-Co1	94.12(19)	O72-Co2-O42	104.5(2)	O61-Co6-O62	150.4(2)
Co2-O72-Co5	94.36(18)	C38-N3-Co3	104.8(4)	O1-Co1-O2	151.8(2)
O1-Co1-O32	94.61(19)	O8-Co1-N1	105.0(2)	N1-Co1-O32	171.9(2)
O41-Co4-O2	94.7(2)	C18-N1-Co1	105.1(5)	N6-Co6-O52	172.3(2)
Co2-O32-Co1	94.71(18)	C98-N6-Co6	105.1(5)	O72-Co2-O2	172.97(19)
O42-Co2-O52	94.89(18)	O9-Co6-N6	105.2(2)	N4-Co4-O2	173.2(2)
O72-Co2-O32	94.99(18)	C78-N5-Co5	105.2(4)	O42-Co2-O62	173.6(2)
O2-Co2-O62	95.04(18)	C80-O52-Co6	115.1(4)	O52-Co2-O32	174.1(2)
Co7-O9-Co6	95.1(2)	C40-O32-Co1	115.7(4)	N7-Co7-O62	174.1(2)
O32-Co3-N3	95.3(2)	C60-O42-Co3	116.0(4)	N5-Co5-O72	174.6(2)
O31-Co3-O42	95.3(2)	C120-O72-Co5	116.0(4)	N3-Co3-O42	175.0(2)

Table 48: Selected bond angles (sorted) [°] for $[L^{O^{Ph}N^H}ZnEt]_2$ (Figure 56).

Atoms	Bond angles	Atoms	Bond angles
O1'-Zn1-Zn1'	43.11(3)	C15-N1-Zn1'	114.46(11)
O1-Zn1-Zn1'	43.86(3)	C1-O1-Zn1	117.97(9)
O1'-Zn1-N1'	82.04(5)	C19A-Zn1-N1'	120.6(3)
O1-Zn1-O1'	86.97(4)	C19A-Zn1-O1	125.8(3)
N1'-Zn1-Zn1'	89.80(4)	C19B-Zn1-N1'	126.5(5)
Zn1-O1-Zn1'	93.03(4)	C19B-Zn1-O1	127.6(5)
O1-Zn1-N1'	97.77(5)	C20A-C19A-Zn1	130.4(7)
C14-N1-Zn1'	107.51(10)	C19A-Zn1-O1'	131.7(3)
C20B-C19B-Zn1	108.5(7)	C19A-Zn1-Zn1'	149.5(3)
C1-O1-Zn1'	110.21(9)		

Table 49: Selected bond angles (sorted) [°] for $[L^{CPI}(Zn-OAc)_2]$ (Figure 58).

Atoms	Bond angles	Atoms	Bond angles
N2-Zn2-N3	76.40(8)	C14-N4-Zn2	115.36(15)
N1-Zn1-N8	76.94(8)	C2-N1-Zn1	115.38(15)
N7-Zn1-N6	77.32(7)	O3-Zn2-N3	115.63(8)
N5-Zn2-N4	77.61(7)	C10-N7-Zn1	115.65(16)
N4-Zn2-N3	84.89(8)	C23-O3-Zn2	117.99(16)
N7-Zn1-N8	85.63(8)	O3-Zn2-N4	118.38(8)
N2-Zn2-N5	87.49(7)	C21-O1-Zn1	120.52(17)
N1-Zn1-N6	88.72(7)	C7-N7-Zn1	122.89(15)
O1-Zn1-N6	105.86(8)	C5-N8-Zn1	123.01(16)
O3-Zn2-N5	106.58(7)	C17-N3-Zn2	123.13(16)
O3-Zn2-N2	109.23(8)	C15-N4-Zn2	123.21(15)
O1-Zn1-N1	112.54(8)	N2-Zn2-N4	132.34(8)
C11-N6-Zn1	112.74(14)	N5-N6-Zn1	132.57(15)
C13-N5-Zn2	113.01(15)	N1-Zn1-N7	133.46(8)
O1-Zn1-N7	113.97(8)	N2-N1-Zn1	133.46(15)
O1-Zn1-N8	114.48(8)	N6-N5-Zn2	133.53(15)
C3-N2-Zn2	115.13(15)	N1-N2-Zn2	134.25(15)
C4-N8-Zn1	115.15(17)	N5-Zn2-N3	137.69(8)
C20-N3-Zn2	115.33(16)	N6-Zn1-N8	139.66(8)

Table 50: Selected bond angles (sorted) [°] for $[L^{\text{CPA}}(\text{Zn-Cl})_2]$ (Figure 63).

Atoms	Bond angles	Atoms	Bond angles
N5–Zn2–N4	75.84(10)	C9–N4–Zn2	111.2(2)
N6–Zn1–N7	76.62(10)	N2–Zn2–Cl2	111.76(8)
N2–Zn2–N3	78.96(11)	C5–N3–Zn2	111.8(2)
N1–Zn1–N8	78.98(10)	N6–Zn1–Cl1	111.84(7)
N3–Zn2–N4	87.70(10)	N1–Zn1–Cl1	115.52(8)
N8–Zn1–N7	88.30(10)	N5–Zn2–Cl2	116.94(8)
N5–Zn2–N2	92.84(10)	C3–N2–Zn2	117.2(2)
N1–Zn1–N6	93.54(10)	C2–N1–Zn1	117.6(2)
N7–Zn1–Cl1	98.61(7)	C13–N6–Zn1	118.9(2)
N4–Zn2–Cl2	102.49(8)	C11–N5–Zn2	119.8(2)
N3–Zn2–Cl2	104.39(8)	N2–N1–Zn1	131.6(2)
N8–Zn1–Cl1	105.60(7)	N6–N5–Zn2	132.1(2)
C10–N4–Zn2	106.1(2)	N5–N6–Zn1	132.9(2)
C14–N7–Zn1	106.73(18)	N1–N2–Zn2	133.1(2)
C20–N8–Zn1	106.84(18)	N5–Zn2–N3	137.78(10)
C4–N3–Zn2	107.03(19)	N6–Zn1–N8	141.19(10)
C15–N7–Zn1	110.10(19)	N2–Zn2–N4	145.32(11)
C19–N8–Zn1	110.62(19)	N1–Zn1–N7	145.61(10)

Table 51: Selected bond angles (sorted) [$^{\circ}$] for $[\text{L}^{\text{BOX}}\text{Zn}_2(\text{OAc})_3]_2$ (see Figure 66).

Atoms	Bond angles	Atoms	Bond angles
O25–Zn4–O26	56.69(10)	C33–N12–Zn4	111.8(2)
N4–Zn2–N2	76.37(12)	C10–N3–Zn1	112.2(2)
N1–Zn1–N3	76.88(12)	C3–N2–Zn2	113.3(2)
N13–Zn3–N11	77.00(12)	C16–N4–Zn2	113.3(3)
N14–Zn4–N12	78.11(12)	C32–N11–Zn3	113.4(2)
O29–Zn2–N4	80.97(12)	C46–N14–Zn4	113.5(2)
C65–O26–Zn4	82.4(2)	O31–Zn2–O29	114.07(12)
N13–Zn3–O30	84.25(12)	O32–Zn3–N13	114.77(13)
O23–Zn1–N3	84.60(11)	C2–N1–Zn1	115.3(2)
O24–Zn4–N14	84.62(12)	C40–N13–Zn3	115.5(3)
O22–Zn4–N12	86.61(13)	O21–Zn1–O23	121.69(11)
O29–Zn2–O27	88.71(11)	C67–O27–Zn2	124.6(2)
O24–Zn4–O26	88.84(15)	C63–O23–Zn1	125.1(2)
O23–Zn1–O25	90.42(11)	C69–O29–Zn2	126.8(2)
O32–Zn3–N11	90.93(12)	C65–O25–Zn1	127.1(2)
O32–Zn3–O30	91.26(12)	O23–Zn1–N1	128.74(12)
O24–Zn4–O25	91.57(11)	C61–O22–Zn4	130.4(3)
O27–Zn3–O30	92.61(10)	C71–O32–Zn3	130.8(3)
O21–Zn1–N3	95.42(12)	C61–O21–Zn1	132.9(3)
O22–Zn4–O24	95.64(17)	C69–O30–Zn3	133.0(3)
N12–Zn4–O26	95.87(12)	O29–Zn2–N2	133.22(12)
O27–Zn2–N2	96.21(11)	C71–O31–Zn2	133.8(3)
O21–Zn1–O25	96.82(11)	N11–N12–Zn4	135.1(2)
O25–Zn1–N1	97.73(11)	C42–N13–Zn3	135.7(3)
O22–Zn4–N14	98.16(14)	N1–N2–Zn2	135.8(2)
C65–O25–Zn4	98.7(2)	N2–N1–Zn1	135.9(2)
O31–Zn2–O27	99.68(11)	C63–O24–Zn4	136.0(3)
O22–Zn4–O25	100.15(11)	C48–N14–Zn4	136.3(2)
O32–Zn3–O27	102.32(11)	C18–N4–Zn2	136.4(3)
O31–Zn2–N4	103.75(13)	C12–N3–Zn1	139.0(2)
C67–O27–Zn3	104.7(2)	N12–N11–Zn3	139.0(2)
O25–Zn4–N12	104.92(11)	O27–Zn3–N13	142.80(12)
N14–Zn4–O26	105.13(13)	O27–Zn2–N4	156.55(12)
Zn1–O25–Zn4	105.89(12)	O22–Zn4–O26	156.60(11)
O27–Zn3–N11	106.10(11)	O30–Zn3–N11	160.22(11)
O21–Zn1–N1	107.48(12)	O25–Zn4–N14	161.58(13)
Zn3–O27–Zn2	107.67(11)	O24–Zn4–N12	162.73(12)
O31–Zn2–N2	110.84(12)	O25–Zn1–N3	167.64(12)

Table 52: Selected bond lengths (sorted) [Å] for the degradation product of $[\text{L}^{\text{BOX}}\text{Co}_2(\text{OAc})_3]_2$ (see Figure 68).

Atoms	Bond lengths	Atoms	Bond lengths
Co2–O44	2.043(4)	Co3–O46	2.123(4)
Co2–N2	2.055(5)	Co1–N1	2.132(5)
Co3–N22	2.062(5)	Co1–O46	2.136(4)
Co3–N32	2.065(4)	Co1–N33	2.153(5)
Co1–O41	2.070(4)	Co1–N3	2.154(5)
Co4–O45	2.071(4)	Co4–N23	2.159(5)
Co1–N31	2.079(5)	Co4–N13	2.162(4)
Co3–O47	2.081(5)	Co3–O22	2.210(4)
Co4–N11	2.088(4)	Co2–O2	2.221(4)
Co4–O42	2.101(4)	Co3–O48	2.282(5)
Co2–N12	2.110(4)	Co2–O43	2.351(4)
Co2–O42	2.114(4)	Co3–C208	2.501(7)

Table 53: Selected bond angles (sorted) [°] for the degradation product of $[L^{\text{BOX}}\text{Co}_2(\text{OAc})_3]_2$ (see Figure 68).

Atoms	Bond angles	Atoms	Bond angles	Atoms	Bond angles
O47-Co3-C208	29.3(2)	O44-Co2-O2	93.90(16)	Co4-O42-Co2	116.84(16)
O48-Co3-C208	30.2(2)	C208-O47-Co3	94.7(4)	C3-N2-Co2	117.5(4)
O47-C208-Co3	56.0(3)	N1-Co1-O46	95.53(16)	C92-N31-Co1	117.5(4)
O44-Co2-O43	58.71(15)	N2-Co2-O43	96.02(16)	C201-O42-Co4	118.7(3)
O47-Co3-O48	59.46(18)	N11-Co4-N23	96.24(17)	C205-O46-Co3	122.7(4)
O48-C208-Co3	65.2(3)	O46-Co3-C208	97.0(2)	C205-O46-Co1	124.1(4)
N2-Co2-O2	75.60(16)	O42-Co4-N21	97.38(16)	C201-O42-Co2	124.2(3)
N31-Co1-N33	76.64(18)	C203-O44-Co2	97.6(4)	N22-Co3-C208	131.0(2)
N11-Co4-N13	76.89(17)	O41-Co1-O46	98.42(16)	C205-O45-Co4	131.9(3)
N22-Co3-O22	76.99(16)	O22-Co3-C208	98.5(2)	N12-N11-Co4	132.0(3)
N21-Co4-N23	77.31(17)	O45-Co4-N21	98.76(17)	N32-N31-Co1	132.0(3)
N1-Co1-N3	77.53(18)	O45-Co4-O42	100.19(16)	C201-O41-Co1	132.4(4)
N23-Co4-N13	80.78(17)	N21-Co4-N13	100.50(17)	N1-N2-Co2	133.1(4)
O41-Co1-N33	83.29(17)	O44-Co2-O42	100.75(17)	C72-N23-Co4	134.5(3)
N11-Co4-O42	84.17(15)	O47-Co3-O46	101.0(2)	N21-N22-Co3	135.8(4)
C203-O43-Co2	84.4(3)	O2-Co2-O43	101.12(15)	C12-N3-Co1	137.2(4)
C208-O48-Co3	84.6(4)	O41-Co1-N1	101.35(17)	N2-N1-Co1	137.4(4)
N31-Co1-O46	85.27(16)	N22-Co3-O47	101.72(19)	C102-N33-Co1	137.4(3)
N32-Co3-O22	85.44(17)	N1-Co1-N33	101.93(18)	C42-N13-Co4	139.0(3)
O46-Co1-N3	85.90(17)	O22-Co3-O48	103.01(16)	N22-N21-Co4	139.1(4)
N32-Co3-O48	86.25(17)	N31-N32-Co3	111.4(3)	C93-N32-Co3	139.7(4)
N12-Co2-O2	86.60(16)	N11-N12-Co2	111.6(3)	C33-N12-Co2	140.1(4)
O45-Co4-N11	87.23(17)	C70-N23-Co4	111.9(3)	N32-Co3-O47	143.5(2)
O45-Co4-N13	87.59(16)	C76-O22-Co3	111.9(3)	N12-Co2-O43	150.39(16)
O41-Co1-N31	88.28(17)	C40-N13-Co4	112.2(4)	O44-Co2-N2	150.75(18)
O42-Co2-O43	89.12(15)	C10-N3-Co1	112.3(4)	O42-Co4-N13	159.17(16)
N22-Co3-O46	89.13(17)	N22-Co3-N32	112.47(18)	N22-Co3-O48	161.10(16)
N12-Co2-O42	89.79(16)	C62-N21-Co4	112.9(3)	O46-Co1-N33	161.79(16)
O47-Co3-O22	90.3(2)	C100-N33-Co1	113.0(4)	O46-Co3-O22	163.73(15)
N32-Co3-O46	92.22(17)	Co3-O46-Co1	113.05(15)	C29B-C208-Co3	164.0(10)
O44-Co2-N12	92.52(17)	N2-Co2-N12	113.58(17)	O42-Co2-O2	165.06(15)
N2-Co2-O42	92.67(17)	C2-N1-Co1	113.9(3)	O45-Co4-N23	166.74(17)
N31-Co1-N3	92.69(18)	C16-O2-Co2	113.9(3)	C29A-C208-Co3	169.0(10)
N33-Co1-N3	92.79(18)	N32-Co3-C208	115.8(2)	N31-Co1-N1	170.08(18)
O46-Co3-O48	92.88(17)	C32-N11-Co4	116.0(4)	N11-Co4-N21	173.42(18)
O42-Co4-N23	92.90(16)	C63-N22-Co3	116.2(4)	O41-Co1-N3	175.64(18)

Table 54: Selected bond angles (sorted) [°] for $[L^{PI^Ph}Co_2(OAc)_3(OH)_{0.5}]_2$ (see Figure 70).

Atoms	Bond angles	Atoms	Bond angles	Atoms	Bond angles
O5-Co4-O6	58.76(12)	O1-Co1-O5	95.05(13)	C123-N14-Co4	123.3(3)
N2-Co2-N4	75.57(13)	O10-Co2-N4	95.30(12)	C87-N13-Co3	124.3(3)
N11-Co3-N13	76.49(14)	O9-Co3-N13	96.40(13)	C211-O12-Co3	124.3(3)
N12-Co4-N14	76.64(14)	O10-Co2-O7	96.69(13)	C203-O3-Co1	126.8(3)
N1-Co1-N3	76.99(13)	O11-Co3-O9	98.35(14)	C42-N4-Co2	127.4(3)
O8-Co2-N4	85.25(11)	N14-Co4-O6	99.05(13)	C205-O5-Co1	129.2(3)
O9-Co3-O12	85.63(12)	N2-Co2-O7	99.06(12)	C207-O9-Co3	130.2(3)
O4-Co4-N14	86.00(14)	O1-Co1-N3	100.77(14)	C207-O8-Co2	130.3(3)
O4-Co4-O5	86.26(12)	N11-Co3-O7	100.87(13)	N1-N2-Co2	133.8(3)
O9-Co3-O7	86.43(12)	O1-Co1-O3	105.34(13)	C201-O2-Co4	134.6(3)
O8-Co2-O7	86.59(12)	Co2-O7-Co3	107.82(13)	N2-N1-Co1	135.2(3)
N11-Co3-O12	87.04(13)	O8-Co2-N2	110.02(13)	O8-Co2-O10	135.23(14)
O11-Co3-O7	87.10(13)	N12-Co4-O5	111.26(13)	N12-N11-Co3	135.3(3)
O3-Co1-N3	88.96(13)	O2-Co4-N14	111.44(14)	C201-O1-Co1	137.0(3)
O3-Co1-O5	89.29(13)	C40-N4-Co2	111.6(3)	N11-N12-Co4	137.6(3)
N11-Co3-O11	89.46(15)	O1-Co1-N1	111.71(13)	C209-O11-Co3	138.5(3)
O12-Co3-O7	89.58(12)	Co1-O5-Co4	113.27(14)	O3-Co1-N1	142.13(14)
O2-Co4-N12	89.92(14)	O10-Co2-N2	113.43(13)	C203-O4-Co4	142.3(3)
C205-O6-Co4	90.0(3)	C83-N12-Co4	113.8(3)	O2-Co4-O6	149.26(13)
C205-O5-Co4	90.4(3)	C85-N13-Co3	115.1(3)	N14-Co4-O5	155.98(13)
O11-Co3-N13	91.22(13)	C5-N3-Co1	115.5(3)	O4-Co4-N12	162.19(13)
O2-Co4-O5	91.62(12)	C82-N11-Co3	115.9(3)	O5-Co1-N3	163.98(13)
O12-Co3-N13	91.89(13)	C3-N2-Co2	116.0(3)	O7-Co2-N4	167.99(13)
O2-Co4-O4	92.80(14)	C2-N1-Co1	116.1(3)	N11-Co3-O9	169.61(13)
O4-Co4-O6	93.16(14)	C121-N14-Co4	116.9(3)	O11-Co3-O12	174.65(14)
N12-Co4-O6	93.46(14)	C209-O10-Co2	120.3(3)	O7-Co3-N13	176.90(13)
N1-Co1-O5	94.88(13)	C7-N3-Co1	123.2(3)		

Table 55: Selected bond angles (sorted) [°] for $[L^{PI^Pr}PdCl_2Pd(C_3H_5)]$ (see Figure 77, a).

Atoms	Bond angles	Atoms	Bond angles
C35-Pd1-C34	38.14(13)	C2-N1-Pd1	113.85(17)
C36-Pd1-C35	38.65(14)	C3-N2-Pd2	113.92(18)
C36-Pd1-C34	69.05(13)	C19-N4-Pd2	115.23(18)
C35-C34-Pd1	69.82(18)	C5-N3-Pd1	115.93(18)
C36-C35-Pd1	70.50(18)	C7-N3-Pd1	122.53(17)
C35-C36-Pd1	70.85(18)	C21-N4-Pd2	124.31(17)
C34-C35-Pd1	72.04(18)	N1-N2-Pd2	135.38(18)
N1-Pd1-N3	76.99(9)	N2-N1-Pd1	137.13(18)
N2-Pd2-N4	78.86(9)	N1-Pd1-C35	139.23(12)
Cl2-Pd2-Cl1	90.89(3)	N3-Pd1-C35	142.90(11)
N4-Pd2-Cl2	94.74(7)	N3-Pd1-C34	163.53(11)
N2-Pd2-Cl1	96.03(6)	N4-Pd2-Cl1	167.06(6)
N3-Pd1-C36	105.76(11)	N2-Pd2-Cl2	172.85(6)
N1-Pd1-C34	107.48(11)	N1-Pd1-C36	175.98(12)

Table 56: Selected bond angles (sorted) [°] for [L^{PI^{Pr}}PdBr₂Pd(C₃H₅)] (see Figure 77, b).

Atoms	Bond angles	Atoms	Bond angles	Atoms	Bond angles
C35A-Pd1-C36A	37.7(6)	N1-Pd1-N3	76.7(2)	C21-N4-Pd2	124.7(5)
C35A-Pd1-C34A	37.9(6)	N2-Pd2-N4	78.3(2)	N3-Pd1-C35B	133.7(8)
C35B-Pd1-C34B	39.4(9)	Br2-Pd2-Br1	91.36(4)	N2-N1-Pd1	135.1(5)
C36B-Pd1-C35B	40.2(9)	N2-Pd2-Br1	94.28(17)	N1-N2-Pd2	135.5(5)
C36B-C35B-Pd1	67.8(17)	N4-Pd2-Br2	96.58(18)	N1-Pd1-C35A	139.6(4)
C34A-Pd1-C36A	67.9(8)	C36B-Pd1-N3	104.1(9)	N1-Pd1-C35B	142.9(6)
C35A-C36A-Pd1	68.7(10)	N1-Pd1-C34A	104.8(5)	C35A-Pd1-N3	143.7(4)
C36B-Pd1-C34B	69.0(13)	N3-Pd1-C36A	107.6(6)	N3-Pd1-C34A	163.9(6)
C35A-C34A-Pd1	69.1(11)	N1-Pd1-C34B	110.4(8)	N4-Pd2-Br1	166.97(18)
C35B-C34B-Pd1	69.1(16)	C2-N1-Pd1	111.8(5)	N1-Pd1-C36A	167.9(6)
C34B-C35B-Pd1	71.4(19)	C19-N4-Pd2	114.4(5)	N3-Pd1-C34B	172.8(8)
C35B-C36B-Pd1	72.0(16)	C5-N3-Pd1	114.7(5)	N1-Pd1-C36B	173.0(10)
C34A-C35A-Pd1	73.0(12)	C3-N2-Pd2	114.8(5)	N2-Pd2-Br2	173.90(18)
C36A-C35A-Pd1	73.6(11)	C7-N3-Pd1	124.7(5)		

Table 57: Selected bond angles (sorted) [°] for [L^{PI^{Ph}}PdBr₂Pd(C₃H₅)] (see Figure 77, c).

Atoms	Bond angles	Atoms	Bond angles
C82-Pd1-C83	38.02(17)	N1-Pd1-C83	112.17(15)
C81-Pd1-C82	38.33(17)	C3-N2-Pd2	112.9(2)
C81-Pd1-C83	67.96(17)	C41-N4-Pd2	114.1(2)
C82-C83-Pd1	69.9(2)	C5-N3-Pd1	115.4(3)
C81-C82-Pd1	70.2(2)	C7-N3-Pd1	122.9(2)
C82-C81-Pd1	71.5(2)	C43-N4-Pd2	125.2(2)
C83-C82-Pd1	72.1(2)	N3-Pd1-C82	133.58(15)
N3-Pd1-N1	78.13(12)	N2-N1-Pd1	135.9(2)
N2-Pd2-N4	79.76(12)	N1-N2-Pd2	137.1(2)
Br2-Pd2-Br1	90.491(16)	C82-Pd1-N1	140.36(15)
N4-Pd2-Br2	92.96(9)	N3-Pd1-C83	169.66(15)
N2-Pd2-Br1	97.12(8)	N4-Pd2-Br1	170.91(8)
C81-Pd1-N3	101.80(15)	N2-Pd2-Br2	172.20(8)
C2-N1-Pd1	110.1(2)	C81-Pd1-N1	177.30(14)

Table 58: Selected bond angles (sorted) [°] for $[L^{PI^h}Cu_2Cl_3]_2$ (see Figure 89).

Atoms	Bond angles	Atoms	Bond angles
N2–Cu2–N4	79.2(2)	N3–Cu1–Cl1	101.20(16)
N1–Cu1–N3	79.8(2)	N3–Cu1–Cl3'	107.29(15)
N2–Cu2–Cl2	88.77(15)	C5–N3–Cu1	114.7(4)
Cu2'–Cl2–Cu2	88.80(8)	C40–N4–Cu2	115.0(4)
Cu2'–Cl4–Cu2	89.20(8)	C3–N2–Cu2	116.6(4)
Cl4–Cu2–Cl2	91.00(6)	C2–N1–Cu1	116.7(4)
Cl3–Cu2–Cl2	94.01(5)	C42–N4–Cu2	122.3(4)
N2–Cu2–Cl4	94.88(15)	C7–N3–Cu1	125.3(4)
N4–Cu2–Cl3	95.05(14)	N1–N2–Cu2	133.7(4)
N1–Cu1–Cl3'	97.66(16)	N2–N1–Cu1	134.5(4)
Cu2–Cl3–Cu1'	99.40(6)	N1–Cu1–Cl1	161.40(16)
Cl1–Cu1–Cl3'	99.71(7)	N4–Cu2–Cl2	164.28(14)
N4–Cu2–Cl4	99.96(14)	N2–Cu2–Cl3	164.48(16)
Cl3–Cu2–Cl4	100.32(5)		

A.5. Abbreviations

bio-PE	bio-sourced polyethylene
bio-PET	bio-sourced polyethylene terephthalate
CHO	cyclohexene oxide
CPA	Cyclic-Pyrazole-Amine
CPI	Cyclic-Pyrazole-Imine
<i>d</i> ₈	mixing time
DCM	dichloromethane, CH ₂ Cl ₂
DIPP	2,6-diisopropyl
DMAP	4-dimethylaminopyridine
dme	1,2-dimethoxyethane
dmsO	dimethylsulfoxide
DOSY	Diffusion Ordered Spectroscopy
eq.	equivalents
EXSY	EXchange Spectroscopy
g	gramm
h	hours
HMDS	hexamethyldisilazane
LIFDI	liquid injection field desorption ionization
<i>i</i> Pr	isopropyl
L	liter
liq.	liquid
MA	methyl acrylate
MAO	methylaluminumoxane
MeCN	acetonitrile
mg	milligramm
min	minute(s)
mL	milliliter
MMA	methyl methacrylate
MMAO	modified methylaluminumoxane
NMR	nuclear magnetic resonance
PC	polycarbonate
PCHC	poly(cyclohexene carbonate)
PE-HD	high-density polyethylene
PE-LD	low-density polyethylene
PE-LLD	linear low-density polyethylene
PE-MD	medium-density polyethylene

PE-VLD	very-low-density polyethylene (VLDPE)
PLA	polylactide
PP	polypropylene
PS	poly(1-phenylethylene), polystyrene
PTSA	<i>p</i> -toluenesulfonic acid
PUR	polyurethane
PVC	poly(1-chloroethylene), polyvinyl chloride
Pz	pyrazolate
RT	room temperature
THF	tetrahydrofuran
TON	turnover number
TOF	turnover frequency
VMS	1,3-divinyltetramethyldisiloxane
X (within a NMR spectrum)	solvent/impurity

B. References

- [1] Peters, R. *Cooperative Catalysis: Designing Efficient Catalysts for Synthesis*; Wiley, 2015.
- [2] Kalck, P. *Homo- and Heterobimetallic Complexes in Catalysis: Cooperative Catalysis*, 59th ed.; Topics in Organometallic Chemistry; Springer International Publishing, 2016; p 277.
- [3] Gunanathan, C.; Milstein, D. In *Bifunctional Mol. Catal.*; Ikariya, T., Shibasaki, M., Eds.; Springer Berlin Heidelberg: Berlin, Heidelberg, 2011; pp 55–84.
- [4] Grützmacher, H. *Angew. Chem. Int. Ed.* **2008**, *47*, 1814–1818.
- [5] Olah, G. A.; Prakash, G. K. S.; Goepfert, A. *J. Am. Chem. Soc.* **2011**, *133*, 12881–12898.
- [6] Kishna, M.; Niesten, E.; Negro, S.; Hekkert, M. P. *J. Clean. Prod.* **2017**, *155*, 7–16.
- [7] Zhang, X.; Fevre, M.; Jones, G. O.; Waymouth, R. M. *Chem. Rev.* **2018**, *118*, 839–885.
- [8] PlasticsEurope EPRO, *Plastics - the Facts*; 2016; p <http://www.plasticseurope.org>.

- [9] Storz, H.; Vorlop, K.-D. *Appl Agric For. Res* **2013**, *63*, 321–332.
- [10] Schneiderman, D. K.; Hillmyer, M. A. *Macromolecules* **2017**, *50*, 3733–3749.
- [11] Gandini, A.; Lacerda, T. M. *Prog. Polym. Sci.* **2015**, *48*, 1–39.
- [12] Mathers, R. T. *J. Polym. Sci. Part A Polym. Chem.* **2012**, *50*, 1–15.
- [13] Ragauskas, A. J.; Williams, C. K.; Davison, B. H.; Britovsek, G.; Cairney, J.; Eckert, C. A.; Frederick Jr, W. J.; Hallett, J. P.; Leak, D. J.; Liotta, C. L.; Mielenz, J. R.; Murphy, R.; Templer, R.; Tschaplinski, T. *Science* **2006**, *311*, 484–489.
- [14] Yao, K.; Tang, C. *Macromolecules* **2013**, *46*, 1689–1712.
- [15] Schroder, K.; Matyjaszewski, K.; Noonan, K. J. T.; Mathers, R. T. *Green Chem.* **2014**, *16*, 1673–1686.
- [16] Hong, M.; Chen, E. Y.-X. *Green Chem.* **2017**, *19*, 3692–3706.
- [17] Thakur, V. K.; Thakur, M. K. *Handbook of Sustainable Polymers: Structure and Chemistry*; Pan Stanford Publishing CRC, 2016.
- [18] Saibuatrong, W.; Cheroennet, N.; Suwanmanee, U. *J. Clean. Prod.* **2017**, *158*, 319–334.
- [19] Zhu, Y.; Romain, C.; Williams, C. K. *Nature* **2016**, *540*, 354–362.
- [20] Lettner, M.; Schöggel, J.-P.; Stern, T. *J. Clean. Prod.* **2017**, *157*, 289–298.
- [21] Shen, L.; Worrell, E.; Patel, M. *Biofuels, Bioprod. Biorefining* **2010**, *4*, 25–40.
- [22] Technavio, *Global Biodegradable Polymers Market 2017-2021*; 2016; p 83.
- [23] Brockhaus, S.; Petersen, M.; Kersten, W. *J. Clean. Prod.* **2016**, *127*, 84–95.
- [24] Kleij, A. W.; Sci, C. *Catal. Sci. Technol.* **2014**, *4*, 1481.
- [25] Maeda, C.; Miyazaki, Y.; Ema, T. *Catal. Sci. Technol.* **2014**, *4*, 1482.
- [26] Lu, X. B. *Carbon Dioxide and Organometallics*, toporgan, ed.; Springer International Publishing, 2016; pp 1–308.
- [27] Liu, Q.; Wu, L.; Jackstell, R.; Beller, M. *Nat. Commun.* **2015**, *6*, 1–15.
- [28] Markewitz, P.; Kuckshinrichs, W.; Leitner, W.; Linssen, J.; Zapp, P.; Bongartz, R.; Schreiber, A.; Müller, T. E. *Energy Environ. Sci.* **2012**, *5*, 7281–7305.

- [29] Peters, M.; Köhler, B.; Kuckshinrichs, W.; Leitner, W.; Markewitz, P.; Müller, T. E. *ChemSusChem* **2011**, *4*, 1216–1240.
- [30] Arakawa, H. *et al. Chem. Rev.* **2001**, *101*, 953–996.
- [31] Olajire, A. A. *J. CO₂ Util.* **2013**, *3-4*, 74–92.
- [32] Mleczko, L.; Wolf, A.; Lolli, G. *ChemBioEng Rev* **2016**, 204–218.
- [33] Beckman, E. J. *Nature* **2016**, *531*, 180–181.
- [34] Schnell, H. D.; Bottenbruch, L. D.; Krimm, H. D. Verfahren zur Herstellung thermoplastischer Kunststoffe. 1959; encrypted.google.com/patents/DE971790C?cl=it.
- [35] Christopher, W. F.; Fox, D. *Polycarbonates*; 1962.
- [36] Elvers, B., Ed. *Ullmann's Polymers and Plastics: Products and Processes*; Wiley: Weinheim, 2016.
- [37] Keim, W. *Kunststoffe*, 1st ed.; Wiley-VCH Verlag GmbH & Co. KGaA: Weinheim, 2006.
- [38] Rubin, B. S. *J. Steroid Biochem. Mol. Biol.* **2011**, *127*, 27–34.
- [39] Taherimehr, M.; Pescarmona, P. P. *J. Appl. Polym. Sci.* **2014**, *131*, 1–17.
- [40] Prieto, A. *Microb. Biotechnol.* **2016**, *9*, 652–657.
- [41] Xu, J.; Feng, E.; Song, J. *J. Appl. Polym. Sci.* **2014**, *131*, 1–29.
- [42] Luinstra, G. *Polym. Rev.* **2008**, *48*, 192–219.
- [43] Mecking, S. *Angew. Chem. Int. Ed.* **2004**, *43*, 1078–1085.
- [44] Zhou, M.; Takayanagi, M.; Yoshida, Y.; Ishii, S.; Noguchi, H. *Polym. Bull.* **1999**, *42*, 419–424.
- [45] Jambeck, J. R.; Geyer, R.; Wilcox, C.; Siegler, T. R.; Perryman, M.; Andrady, A.; Narayan, R.; Law, K. L. *Science* **2015**, *347*, 768–771.
- [46] Poland, S. J.; Darensbourg, D. J. *Green Chem.* **2017**, *19*, 4990–5011.
- [47] Paul, S.; Zhu, Y.; Romain, C.; Brooks, R.; Saini, P. K.; Williams, C. K. *Chem. Commun.* **2015**, *51*, 6459–6479.

- [48] Inoue, S.; Koinuma, H.; Tsuruta, T. *J. Polym. Sci. Part B Polym. Lett.* **1969**, *7*, 287–292.
- [49] Chapman, A. M.; Keyworth, C.; Kember, M. R.; Lennox, A. J. J.; Williams, C. K. *ACS Catal.* **2015**, *5*, 1581–1588.
- [50] Wu, G.-P.; Darensbourg, D. J. *Macromolecules* **2016**, *49*, 807–814.
- [51] Gürtler, C. From Dream Reaction to Dream Production: CO₂-based Polyols. UTECH Europe, Exhibition Program, 2012.
- [52] *Bayer Res.* **2008**, *12*, 74–78.
- [53] Covestro, Carbon Dioxide is revolutionizing plastics production. 2017; <https://co2-dreams.covestro.com>.
- [54] Langanke, J.; Wolf, A.; Peters, M. *Carbon Dioxide Util.*; Elsevier B.V., 2015; pp 59–71.
- [55] Hou, Q.; Grijpma, D. W.; Feijen, J. *Acta Biomater.* **2009**, *5*, 1543–1551.
- [56] Bat, E.; Feijen, J.; Grijpma, D. W. *Biomacromolecules* **2010**, *11*, 2692–2699.
- [57] Bat, E.; Kothman, B. H. M.; Higuera, G. A.; van Blitterswijk, C. A.; Feijen, J.; Grijpma, D. W. *Biomaterials* **2010**, *31*, 8696–8705.
- [58] Seow, W. Y.; Yang, Y. Y. *J. Control. Release* **2009**, *139*, 40–47.
- [59] Chiu, F.-C.; Lai, C.-S.; Lee, R.-S. *J. Appl. Polym. Sci.* **2007**, *106*, 283–292.
- [60] Chen, W.; Meng, F.; Li, F.; Ji, S.-J.; Zhong, Z. *Biomacromolecules* **2009**, *10*, 1727–1735.
- [61] Attia, A. B. E.; Yang, C.; Tan, J. P. K.; Gao, S.; Williams, D. F.; Hedrick, J. L.; Yang, Y.-Y. *Biomaterials* **2013**, *34*, 3132–3140.
- [62] Koning, C. E.; Sablong, R. J.; Nejad, E. H.; Duchateau, R.; Buijsen, P. *Prog. Org. Coatings* **2013**, *76*, 1704–1711.
- [63] Sanson, C.; Diou, O.; Thévenot, J.; Ibarboure, E.; Soum, A.; Brûlet, A.; Miraux, S.; Thiaudière, E.; Tan, S.; Brisson, A.; Dupuis, V.; Sandre, O.; Lecommandoux, S. *ACS Nano* **2011**, *5*, 1122–1140.
- [64] Sanson, C.; Schatz, C.; Le Meins, J.-F.; Brûlet, A.; Soum, A.; Lecommandoux, S. *Langmuir* **2010**, *26*, 2751–2760.

- [65] Xu, J.; Fillion, T. M.; Prifti, F.; Song, J. *Chem. Asian J.* **2011**, *6*, 2730–2737.
- [66] Bartolini, C.; Mespouille, L.; Verbruggen, I.; Willem, R.; Dubois, P. *Soft Matter* **2011**, *7*, 9628–9637.
- [67] Kim, S. Y.; Kim, H. J.; Lee, K. E.; Han, S. S.; Sohn, Y. S.; Jeong, B. *Macromolecules* **2007**, *40*, 5519–5525.
- [68] Fan, C.; Zhang, C.; Jing, Y.; Liao, L.; Liu, L. *RSC Adv.* **2013**, *3*, 157–165.
- [69] Winkler, M.; Romain, C.; Meier, A. R.; Williams, C. K. *Green Chem.* **2015**, *17*, 300–306.
- [70] Romain, C.; Thevenon, A.; Saini, P. K.; Williams, C. K. In *Carbon Dioxide and Organometallics*; Lu, X.-B., Ed.; Springer International Publishing: Cham, 2016; Chapter Carbon Dio, pp 101–141.
- [71] Robert, C.; de Montigny, F.; Thomas, C. M. *Nat. Commun.* **2011**, *2*, 586.
- [72] Hauenstein, O.; Reiter, M.; Agarwal, S.; Rieger, B.; Greiner, A. *Green Chem.* **2016**, *18*, 760–770.
- [73] Hauenstein, O.; Agarwal, S.; Greiner, A. *Nat. Commun.* **2016**, *7*, 11862.
- [74] Byrne, C. M.; Allen, S. D.; Lobkovsky, E. B.; Coates, G. W. *J. Am. Chem. Soc.* **2004**, *126*, 11404–11405.
- [75] Peña Carrodegua, L.; González-Fabra, J.; Castro-Gómez, F.; Bo, C.; Kleij, A. W. *Chem. Eur. J.* **2015**, *21*, 6115–6122.
- [76] Yahiaoui, A.; Belbachir, M.; Soutif, J. C.; Fontaine, L. *Mater. Lett.* **2005**, *59*, 759–767.
- [77] Oral, A.; Tasdelen, M. A.; Demirel, A. L.; Yagci, Y. *J. Polym. Sci. Part A Polym. Chem.* **2009**, *47*, 5328–5335.
- [78] Whiteoak, C. J.; Kielland, N.; Laserna, V.; Castro-Gómez, F.; Martin, E.; Escudero-Adán, E. C.; Bo, C.; Kleij, A. W. *Chem. Eur. J.* **2014**, *20*, 2264–2275.
- [79] Decortes, A.; Kleij, A. W. *ChemCatChem* **2011**, *3*, 831–834.
- [80] North, M.; Pasquale, R. *Angew. Chem. Int. Ed.* **2009**, *48*, 2946–2948.
- [81] Coates, G. W.; Moore, D. R. *Angew. Chem. Int. Ed.* **2004**, *43*, 6618–6639.

- [82] Jutz, F.; Buchard, A.; Kember, M. R.; Fredriksen, S. B.; Williams, C. K. *J. Am. Chem. Soc.* **2011**, *133*, 17395–405.
- [83] Klaus, S.; Vagin, S. I.; Lehenmeier, M. W.; Deglmann, P.; Brym, A. K.; Rieger, B. *Macromolecules* **2011**, *44*, 9508–9516.
- [84] Xu, Y.; Lin, L.; He, C.-T.; Qin, J.; Li, Z.; Wang, S.; Xiao, M.; Meng, Y. *Polym. Chem.* **2017**, *8*, 3632–3640.
- [85] González-Fabra, J.; Castro-Gómez, F.; Kleij, A. W.; Bo, C.; Gonzalez-Fabra, J.; Castro-Gómez, F.; Kleij, A. W.; Bo, C.; González-Fabra, J.; Castro-Gómez, F.; Kleij, A. W.; Bo, C. *ChemSusChem* **2017**, *10*, 1233–1240.
- [86] Moore, D. R.; Cheng, M.; Lobkovsky, E. B.; Coates, G. W. *J. Am. Chem. Soc.* **2003**, *125*, 11911–24.
- [87] Xiao, Y.; Wang, Z.; Ding, K. *Macromolecules* **2006**, *39*, 128–137.
- [88] Trott, G.; Saini, P. K.; Williams, C. K. *Philos. Trans. A. Math. Phys. Eng. Sci.* **2016**, *374*, 20150085.
- [89] Darensbourg, D. J.; Niezgoda, S. A.; Draper, J. D.; Reibenspies, J. H. *J. Am. Chem. Soc.* **1998**, *120*, 4690–4698.
- [90] Cheng, M.; Lobkovsky, E. B.; Coates, G. W. *J. Am. Chem. Soc.* **1998**, *120*, 11018–11019.
- [91] Reiter, M.; Vagin, S.; Kronast, A.; Jandl, C.; Rieger, B. *Chem. Sci.* **2017**, *43*, 6618–6639.
- [92] Decortes, A.; Haak, R. M.; Mart, C.; Mart, M.; Martin, E.; Benet-Buchholz, J.; Kleij, A. W. *Macromolecules* **2015**, *48*, 8197–8207.
- [93] Darensbourg, D. J.; Moncada, A. I. *Inorg. Chem.* **2008**, *47*, 10000–10008.
- [94] Darensbourg, D. J.; Yarbrough, J. C.; Ortiz, C.; Fang, C. C. *J. Am. Chem. Soc.* **2003**, *125*, 7586–7591.
- [95] Darensbourg, D. J.; Wei, S. H. *Macromolecules* **2012**, *45*, 5916–5922.
- [96] Darensbourg, D. J.; Yeung, A. D. *Polym. Chem.* **2014**, *5*, 3949–3962.
- [97] Kozak, C. M.; Devaine-Pressing, K. *ChemSusChem* **2017**, *10*, 1266–1273.
- [98] Elmas, S.; Subhani, M. A.; Vogt, H.; Leitner, W.; Müller, T. E. *Green Chem.* **2013**, *15*, 1356–1360.

- [99] Darensbourg, D. J.; Lee, W.-Z.; Phelps, A. L.; Guidry, E. *Organometallics* **2003**, *3*, 5585–5588.
- [100] Kuran, W.; Listoś, T. *Makromol. Chem.* **1992**, *193*, 945–956.
- [101] Wei, S.-H. The Copolymerization of CO₂ and Cyclic Ethers and their Degradation Pathways. Ph.D. thesis, 2013.
- [102] Liu, Y.; Li, R.-R.; Lu, X.-B. *Macromolecules* **2015**, *48*, 6941–6947.
- [103] Cohen, C. T.; Thomas, C. M.; Peretti, K. L.; Lobkovsky, E. B.; Coates, G. W. *Dalton Trans.* **2006**, 237–249.
- [104] Barth, H. G.; Mays, J. W. *Modern methods of polymer characterization*; Wiley: New York, 1991; p 574.
- [105] Kuran, W. *Principles of Coordination Polymerisation*; John Wiley & Sons Ltd: Chichester, 2001; Vol. 9; pp 0–470.
- [106] Nozaki, K.; Nakano, K.; Hiyama, T. *J. Am. Chem. Soc.* **1999**, *121*, 11008–11009.
- [107] Baugh, L. S.; Canich, J. A. M. *Stereoselective Polymerization with Single-Site Catalysts*; CRC Press, Taylor and Francis Group: Boca Raton, 2007.
- [108] Taherimehr, M.; Pescarmona, P. P. *J. Appl. Polym. Sci.* **2014**, *131*, 41141.
- [109] Darensbourg, D. J.; Wilson, S. J. *Green Chem.* **2012**, *14*, 2665.
- [110] Klaus, S.; Lehenmeier, M. W.; Anderson, C. E.; Rieger, B. *Coord. Chem. Rev.* **2011**, *255*, 1460–1479.
- [111] Coates, G. W.; Jeske, R. C. *Handb. Green Chem.*; WILEY-VCH Verlag GmbH & Co. KGaA, Weinheim, 2009; Vol. 1; pp 343–374.
- [112] Nozaki, K. *Pure Appl. Chem.* **2004**, *76*, 541–546.
- [113] Kim, J.-S.; Kim, H.; Ree, M. *Chem. Mater.* **2004**, *16*, 2981–2983.
- [114] Sugimoto, H.; Kuroda, K. *Macromolecules* **2008**, *41*, 312–317.
- [115] S, S.; Min, J. K.; Seong, J. E.; Na, S. J.; Lee, B. Y. *Angew. Chem. Int. Ed.* **2008**, *47*, 7306–7309.
- [116] Kissling, S.; Lehenmeier, M. W.; Altenbuchner, P. T.; Kronast, A.; Reiter, M.; Deglmann, P.; Seemann, U. B.; Rieger, B. *Chem. Commun.* **2015**, *51*, 4579–4582.

- [117] Kissling, S.; Altenbuchner, P. T.; Lehenmeier, M. W.; Herdtweck, E.; Deglmann, P.; Seemann, U. B.; Rieger, B. *Chem. Eur. J.* **2015**, *21*, 8148–8157.
- [118] Kember, M. R.; Knight, P. D.; Reung, P. T. R.; Williams, C. K. *Angew. Chem. Int. Ed.* **2009**, *48*, 931–933.
- [119] Zhang, X.-H. H.; Wei, R.-J. J.; Du, B.-Y. Y.; Fan, Z.-Q. Q.; Zhang, Y. Y.; Du, B.-Y. Y.; Fan, Z.-Q. Q. *Macromolecules* **2015**, *48*, 536–544.
- [120] Chatterjee, C.; Chisholm, M. H. *Inorg. Chem.* **2011**, *50*, 4481–4492.
- [121] Sugimoto, H.; Ohshima, H.; Inoue, S. *J. Polym. Sci. Part A Polym. Chem.* **2003**, *41*, 3549–3555.
- [122] Chatterjee, C.; Chisholm, M. H. *Inorg. Chem.* **2011**, *50*, 4481–4492.
- [123] Chatterjee, C.; Chisholm, M. H.; El-Khaldy, A.; McIntosh, R. D.; Miller, J. T.; Wu, T. *Inorg. Chem.* **2013**, *52*, 4547–4553.
- [124] Nakano, K.; Kamada, T.; Nozaki, K. *Angew. Chem. Int. Ed.* **2006**, *45*, 7274–7277.
- [125] Qin, Z.; Thomas, C. M.; Lee, S.; Coates, G. W. *Angew. Chem. Int. Ed.* **2003**, *42*, 5484–5487.
- [126] Darensbourg, D. J.; Yarbrough, J. C. *J. Am. Chem. Soc.* **2002**, *124*, 6335–6342.
- [127] Romain, C.; Garden, J. A.; Trott, G.; Buchard, A.; White, A. J.; Williams, C. K. *Chem. Eur. J.* **2017**, *23*, 7367–7376.
- [128] Buchard, A.; Kember, M. R.; Sandeman, K. G.; Williams, C. K. *Chem. Commun.* **2011**, *47*, 212–214.
- [129] Kember, M. R.; White, A. J. P.; Williams, C. K. *Macromolecules* **2010**, *43*, 2291–2298.
- [130] Kember, M. R.; Williams, C. K. *J. Am. Chem. Soc.* **2012**, *134*, 15676–15679.
- [131] Nakano, K.; Nozaki, K.; Tamejiro, H. *J. Am. Chem. Soc.* **2003**, *125*, 5501–5510.
- [132] Xiao, Y.; Wang, Z.; Ding, K. *Chem. Eur. J.* **2005**, *11*, 3668–3678.
- [133] Cheng, M.; Darling, N. A.; Lobkovsky, E. B.; Coates, G. W. *Chem. Commun.* **2000**, 2007–2008.

- [134] Ahmed, S. M.; Poater, A.; Childers, M. I.; Widger, P. C. B.; LaPointe, A. M.; Lobkovsky, E. B.; Coates, G. W.; Cavallo, L. *J. Am. Chem. Soc.* **2013**, *135*, 18901–18911.
- [135] Trost, B. M.; Ito, H. *J. Am. Chem. Soc.* **2000**, *122*, 12003–12004.
- [136] Trost, B. M.; Fettes, A.; Shireman, B. T. *J. Am. Chem. Soc.* **2004**, *126*, 2660–2661.
- [137] Hua, Y.-Z.; Lu, L.-J.; Huang, P.-J.; Wei, D.-H.; Tang, M.-S.; Wang, M.-C.; Chang, J.-B. *Chem. Eur. J.* **2014**, *20*, 12394–12398.
- [138] Schütze, M.; Dechert, S.; Meyer, F. *Chem. Eur. J.* **2017**, *23*, 16472–16475.
- [139] Chakraborti, A. K.; Nandi, A. B.; Grover, V. *J. Org. Chem.* **1999**, *64*, 8014–8017.
- [140] Boeckman, R. K.; Biegasiewicz, K. F.; Tusch, D. J.; Miller, J. R. *J. Org. Chem.* **2015**, *80*, 4030–4045.
- [141] Subba Reddy, B. V.; Narsaiah, A. V.; Ramesh Reddy, A.; Gopala Rao, Y.; Yadav., J. S. *Lett. Org. Chem.* **2008**, *5*, 116–119.
- [142] Bandyopadhyay, D.; Mukherjee, S.; Turrubiartes, L. C.; Banik, B. K. *Ultrason. Sonochem.* **2012**, *19*, 969–973.
- [143] Neufeld, R.; Stalke, D. *Chem. Sci.* **2015**, *6*, 3354–3364.
- [144] Bachmann, S.; Neufeld, R.; Dzemski, M.; Stalke, D. *Chem. Eur. J.* **2016**, *22*, 8462–8465.
- [145] Bachmann, S.; Gernertb, B.; Stalke, D.; Gernert, B.; Stalke, D.; Pieper, U.; Stalke, D.; Schleyer, P. V. R.; Koszinowski, K. *Chem. Commun.* **2016**, *52*, 12861–12864.
- [146] Lin, P.-M.; Chang, C.-H.; Chuang, H.-J.; Liu, C.-T.; Ko, B.-T.; Lin, C.-C. *ChemCatChem* **2016**, *8*, 984–991.
- [147] Nakano, K.; Hiyama, T.; Nozaki, K. *Chem. Commun.* **2005**, 1871–1873.
- [148] Ren, W.-M.; Zhang, X.; Liu, Y.; Li, J.-F.; Wang, H.; Lu, X.-B. *Macromolecules* **2010**, *43*, 1396–1402.
- [149] Darensbourg, D. J. *Chem. Rev.* **2007**, *107*, 2388–2410.
- [150] Wu, G.-P.; Wei, S.-H.; Ren, W.-M.; Lu, X.-B.; Xu, T.-Q.; Darensbourg, D. J. *J. Am. Chem. Soc.* **2011**, *133*, 15191–15199.

- [151] Ren, W.-M.; Liu, Z.-W.; Wen, Y.-Q.; Zhang, R.; Lu, X.-B. *J. Am. Chem. Soc.* **2009**, *131*, 11509–11518.
- [152] Lu, X.-B.; Ren, W.-M.; Wu, G.-P. *Acc. Chem. Res.* **2012**, *45*, 1721–1735.
- [153] Rao, D.-Y.; Li, B.; Zhang, R.; Wang, H.; Lu, X.-B. *Inorg. Chem.* **2009**, *48*, 2830–2836.
- [154] Li, H.; Niu, Y. *Polym. J.* **2010**, *43*, 121–125.
- [155] Chung, W.-C. Cobalt and Chromium Salen Complexes Catalyzed Copolymerization of CO₂ and Epoxides: The Scope of Epoxides. Ph.D. thesis, Texas A&M University, 2015.
- [156] Thevenon, A.; Garden, J. A.; White, A. J. P.; Williams, C. K. *Inorg. Chem.* **2015**, *54*, 11906–11915.
- [157] Meng, Q.-Y.; Pepper, K.; Cheng, R.-H.; Howdle, S. M.; Liu, B.-P. *J. Polym. Sci. Part A Polym. Chem.* **2016**, *54*, 2785–2793.
- [158] Lalrempuia, R.; Breivik, F.; Törnroos, K. W.; Le Roux, E. *Dalton Trans.* **2017**, *46*, 8065–8076.
- [159] Burés, J.; Burøs, J. *Angew. Chem. Int. Ed.* **2016**, *55*, 2028–2031.
- [160] Elias, H. G. *Makromoleküle - Set mit 4 Bänden*, 6th ed.; Wiley: New York, 2003.
- [161] Rickborn, B.; P, T. R. *J. Org. Chem.* **1971**, *36*, 1365–1368.
- [162] Patton, P. A.; Lillya, C. P.; McCarthy, T. J. *Macromolecules* **1986**, *19*, 1266–1268.
- [163] Darensbourg, D. J.; Mackiewicz, R. M. *J. Am. Chem. Soc.* **2005**, *127*, 14026–14038.
- [164] Nishioka, G. *J. Non. Cryst. Solids* **1990**, *120*, 34–39.
- [165] Grate, J. W.; Warner, M. G.; Pittman, J. W.; Dehoff, K. J.; Wietsma, T. W.; Zhang, C.; Oostrom, M. *Water Resour. Res.* **2013**, *49*, 4724–4729.
- [166] Notni, J.; Schenk, S.; Görls, H.; Breitzke, H.; Anders, E. *Inorg. Chem.* **2008**, *47*, 1382–1390.
- [167] Bok, T.; Yun, H.; Lee, B. Y. *Inorg. Chem.* **2006**, *45*, 4228–4237.

- [168] Lee, B. Y.; Kwon, H. Y.; Lee, S. Y.; Na, S. J.; Han, S.-I.; Yun, H.; Lee, H.; Park, Y.-W. *J. Am. Chem. Soc.* **2005**, *127*, 3031–3037.
- [169] Enders, D.; Wang, C.; Liebich, J. X. *Chem. Eur. J.* **2009**, *15*, 11058–11076.
- [170] Hayashi, Y.; Gotoh, H.; Hayashi, T.; Shoji, M. *Angew. Chem. Int. Ed.* **2005**, *44*, 4212–4215.
- [171] Zaugg, H. E.; Michaels, R. J. *J. Am. Chem. Soc.* **1958**, *80*, 2770–2773.
- [172] Moussa, G. E. M.; Basyouni, M. N.; Shaban, M. E. *Indian J. Chem. Sect. B Org. Chem. Incl. Med. Chem.* **1980**, *19B(9)*, 798–800.
- [173] Haussener, T. J.; Sebahar, P. R.; Reddy, H. R. K.; Williams, D. L.; Looper, R. E. *Tetrahedron Lett.* **2016**, *57*, 2845–2848.
- [174] Liu, K.; Zhao, C. A preparation of hydroxypropylamine derivatives, useful as modulators of peroxisome proliferator activated receptors (PPARs), patent WO 2004-US10970. 2004.
- [175] Geest, D. J. D.; Noble, A.; Moubaraki, B.; Murray, K. S.; Larsen, S.; Brooker, S. *Dalton Trans.* **2007**, *16*, 467–475.
- [176] Ficks, A.; Sibbald, C.; John, M.; Dechert, S.; Meyer, F. *Organometallics* **2010**, *29*, 1117–1126.
- [177] Wockel, S. Synthetic Models for Zinc Metallohydrolases. Ph.D. thesis, Georg-August-University, 2011.
- [178] Böhnisch, T. C_2 -Symmetric Pyrazole-Bridged Ligands and Their Application in Asymmetric Transition-Metal Catalysis. Ph.D. thesis, Georg-August-Universität Göttingen, 2015.
- [179] Bordwell, F. G. *Acc. Chem. Res.* **1988**, *21*, 456–463.
- [180] Bordwell, F. G.; Algrim, D. *J. Org. Chem.* **1976**, *41*, 2507–2508.
- [181] Schütze, M. Preorganized bimetallic complexes for the cooperative olefin polymerization. Master Thesis, Georg-August-University Göttingen, 2014.
- [182] Rule, G. S.; Hitchens, T. K. *Fundamentals of Protein NMR Spectroscopy; Focus on Structural Biology*; Springer Netherlands, 2006.
- [183] Garden, J. A.; Saini, P. K.; Williams, C. K. *J. Am. Chem. Soc.* **2015**, *137*, 15078–15081.

- [184] Walker, W. K.; Kay, B. M.; Michaelis, S. A.; Anderson, D. L.; Smith, S. J.; Ess, D. H.; Michaelis, D. J. *J. Am. Chem. Soc.* **2015**, *137*, 7371–7378.
- [185] Motta, A.; Fragalà, I. L.; Marks, T. J. *J. Am. Chem. Soc.* **2009**, *131*, 3974–3984.
- [186] Breinbauer, R.; Jacobsen, E. *Angew. Chem. Int. Ed.* **2000**, *39*, 3604–3607.
- [187] Liu, S.; Motta, A.; Mouat, A. R.; Delferro, M.; Marks, T. J. *J. Am. Chem. Soc.* **2014**, *136*, 10460–10469.
- [188] Konsler, R. G.; Karl, J.; Jacobsen, E. N. *J. Am. Chem. Soc.* **1998**, *120*, 10780–10781.
- [189] Lee, S. Y.; Hartwig, J. F. *J. Am. Chem. Soc.* **2016**, *138*, 15278–15284.
- [190] Lin, H. C.; Wang, P. S.; Tao, Z. L.; Chen, Y. G.; Han, Z. Y.; Gong, L. Z. *J. Am. Chem. Soc.* **2016**, *138*, 14354–14361.
- [191] Scattolin, T.; Canovese, L.; Visentin, F.; Paganelli, S.; Canton, P.; Demitri, N. *Appl. Organomet. Chem.* **2018**, *32*, e4034.
- [192] Yagishita, F.; Shimokawa, S.; Uemura, N.; Yoshida, Y.; Mino, T.; Sakamoto, M.; Kawamura, Y. *ChemistrySelect* **2017**, *2*, 10143–10145.
- [193] Guo, C.; Fleige, M.; Janssen-Müller, D.; Daniliuc, C. G.; Glorius, F. *J. Am. Chem. Soc.* **2016**, *138*, 7840–7843.
- [194] Berkessel, A.; Gröger, H. *Asymmetric Organocatalysis – From Biomimetic Concepts to Applications in Asymmetric Synthesis*; Wiley-VCH Verlag GmbH & Co. KGaA: Weinheim, Germany, 2005.
- [195] Brandsma, L.; Vasilevsky, S.; Verkruijsse, H. *Application of Transition Metal Catalysts in Organic Synthesis*; Springer: Heidelberg, Berlin, 1998.
- [196] Steinborn, D. *Grundlagen der metallorganischen Komplexkatalyse*, 2nd ed.; Vieweg + Teubner GWV Fachverlage GmbH: Wiesbaden, 2010.
- [197] Tsuji, J. *Palladium Reagents and Catalysts: New Perspectives for the 21st Century*, 1st ed.; John Wiley & Sons, Ltd.: West Sussex, England, 2004.
- [198] Satake, A.; Nakata, T. *J. Am. Chem. Soc.* **1998**, *120*, 10391–10396.
- [199] Mao, B.; Fañanás-Mastral, M.; Feringa, B. L. *Chem. Rev.* **2017**, *117*, 10502–10566.

- [200] Hirata, G.; Satomura, H.; Kumagae, H.; Shimizu, A.; Onodera, G.; Kimura, M. *Org. Lett.* **2017**, *19*, 6148–6151.
- [201] Butt, N. A.; Zhang, W. *Chem. Soc. Rev.* **2015**, *44*, 7929–7967.
- [202] Trost, B. M. *Chem. Pharm. Bull. (Tokyo)*. **2002**, *50*, 1–14.
- [203] Trost, B. M.; Lee, C. *Catal. Asymmetric Synth.*; John Wiley & Sons, Inc., 2000; pp 593–649.
- [204] Trost, B. M.; Vranken, D. L. V. *Chem. Rev.* **1996**, *96*, 395–422.
- [205] Trost, B. M. *Pure Appl. Chem.* **1981**, *53*, 2357–2370.
- [206] Tsuji, J. *Pure Appl. Chem.* **1982**, *54*, 197–206.
- [207] Ibrahim, I.; Córdova, A. *Angew. Chem. Int. Ed.* **2006**, *45*, 1952–1956.
- [208] Mohr, J. T.; Behenna, D. C.; Harned, A. M.; Stoltz, B. M. *Angew. Chem. Int. Ed.* **2005**, *44*, 6924–6927.
- [209] Gruttadauria, M.; Giacalone, F. *Catalytic Methods in Asymmetric Synthesis: Advanced Materials, Techniques, and Applications*; Wiley, 2011; pp 395–397.
- [210] Pfaltz, A.; Lautens, M. *Allylic substitution reactions. Compr. Asymmetric Catal. I-III*, 2nd ed.; 1999; pp 833–884.
- [211] Trost, B. M.; Machacek, M. R.; Aponick, A. *Acc. Chem. Res.* **2006**, *39*, 747–760.
- [212] Chen, Y.; Turlik, A.; Newhouse, T. R. *J. Am. Chem. Soc.* **2016**, *138*, 1166–1169.
- [213] Carroll, M. F. *J. Chem. Soc.* **1940**, 704–706.
- [214] Shimizu, I.; Yamada, T.; Tsuji, J. *Tetrahedron Lett.* **1980**, *21*, 3199–3202.
- [215] Burger, E. C.; Tunge, J. A. *Org. Lett.* **2004**, *6*, 4113–4115.
- [216] Ito, Y.; Hirao, T.; Saegusa, T. *J. Org. Chem.* **2002**, *43*, 1011–1013.
- [217] Lu, Y.; Nguyen, P. L.; Lévaray, N.; Lebel, H. *J. Org. Chem.* **2013**, *78*, 776–779.
- [218] Diao, T.; Stahl, S. S. *J. Am. Chem. Soc.* **2011**, *133*, 14566–14569.
- [219] Moberg, C. *Org. React.*; John Wiley & Sons, Inc.: Hoboken, NJ, USA, 2014; pp 1–74.

- [220] And, B. M. T.; Hachiya, I.; Trost, B. M.; Hachiya, I. *J. Am. Chem. Soc.* **1998**, *120*, 1104–1105.
- [221] Garza, V. J.; Krische, M. J. *J. Am. Chem. Soc.* **2016**, *138*, 3655–3658.
- [222] Lloyd-Jones, G. C.; Pfaltz, A. *Angew. Chem. Int. Ed.* **1995**, *34*, 462–464.
- [223] Carrion, M. C.; Diaz, A.; Guerrero, A.; Jalon, F. a.; Manzano, B. R.; Rodriguez, A.; Paul, R. L.; Jeffery, J. C. *J. Organomet. Chem.* **2002**, *650*, 210–222.
- [224] Mecking, S.; Keim, W. *Organometallics* **1996**, *15*, 2650–2656.
- [225] Breutel, C.; Pregosin, P. S.; Salzmann, R.; Togni, A. *J. Am. Chem. Soc.* **1994**, *116*, 4067–4068.
- [226] Faller, J. W.; Stokes-huby, H. L.; Albrizzio, M. A. *Helv. Chim. Acta* **2001**, *84*, 3031–3042.
- [227] Ficks, A.; Hiney, R. M.; Harrington, R. W.; Gilheany, D. G.; Higham, L. J. *Dalton Trans.* **2012**, *41*, 3515–3522.
- [228] Albinati, A.; Kunz, R. W.; Ammann, C. J.; Pregosin, P. S. *Organometallics* **1991**, *10*, 1800–1806.
- [229] Hansson, S.; Norrby, P.-O.; Sjögren, M. P. T.; Åkermark, B.; Cucciolito, M. E.; Giordano, F.; Vitagliano, A. *Organometallics* **1993**, *12*, 4940–4948.
- [230] Gogoll, A.; Örnebro, J.; Grennberg, H.; Bäckvall, J.-E. *J. Am. Chem. Soc.* **1994**, *116*, 3631–3632.
- [231] Gogoll, A.; Grennberg, H.; Axén, A. *Organometallics* **1997**, *16*, 1167–1178.
- [232] Guerrero, A.; Jalón, F. A. A.; Manzano, B. R. R.; Rodríguez, A.; Claramunt, R. M. M.; Cornago, P.; Milata, V.; Elguero, J. *Eur. J. Inorg. Chem.* **2004**, *3*, 549–556.
- [233] Crociani, B.; di Bianca, F.; Giovenco, A.; Boschi, T. *Inorganica Chim. Acta* **1987**, *127*, 169–182.
- [234] Montoya, V.; Pons, J.; García-Antón, J.; Solans, X.; Font-Bardía, M.; Ros, J.; García-Antòn, J.; Solans, X.; Font-Bardía, M.; Ros, J. *Organometallics* **2007**, *26*, 3183–3190.
- [235] Montoya, V.; Pons, J.; García-Antón, J.; Solans, X.; Font-Bardía, M.; Ros, J. *J. Fluor. Chem.* **2007**, *128*, 1007–1011.

- [236] Noël, G.; Röder, J. C.; Dechert, S.; Pritzkow, H.; Bolk, L.; Mecking, S.; Meyer, F. *Adv. Synth. Catal.* **2006**, *348*, 887–897.
- [237] Cobas, J. C.; Martín-Pastor, M. EXSYCalc, Mestrelab Research. 2007.
- [238] Neuhaus, D.; Williamson, M. P. *The nuclear overhauser effect in structural and conformational analysis*; VCH Publishers, Inc.: Weinheim, Germany, 1989.
- [239] Wedler, G.; Freund, H.-J. *Lehrbuch der Physikalischen Chemie*; WILEY-VCH Verlag: Weinheim, Germany, 2012.
- [240] Elguero, J.; Fruchier, A.; De La Hoz, A.; Jalón, F. A.; Manzano, B. R.; Otero, A.; Gómez-De La Torre, F. *Chem. Ber.* **1996**, *129*, 589–594.
- [241] Jalón, F. A.; Manzano, B. R.; Moreno-Lara, B. *Eur. J. Inorg. Chem.* **2005**, *1*, 100–109.
- [242] Flory, P. J. *Principles of Polymer Chemistry*; Cornell University Press, 1953; p 672.
- [243] Hungenberg, K.-D. *Handb. Polym. React. Eng.*; Wiley-VCH Verlag GmbH, 2008; pp 323–364.
- [244] Ehrlich, P.; Mortimer, G. A. *Fortschritte der Hochpolym. SE - 2*; Advances in Polymer Science; Springer Verlag. LA - English: Berlin Heidelberg, 1970; Vol. 7/3; pp 386–448.
- [245] Hawker, C. J. *J. Am. Chem. Soc.* **1994**, *116*, 11185–11186.
- [246] Barner-Kowollik, C. In *Handbook of RAFT Polymerization*; Barner-Kowollik, C., Ed.; Wiley-VCH Verlag GmbH & Co. KGaA: Weinheim, Germany, 2008.
- [247] Semsarilar, M.; Perrier, S. *Nat. Chem.* **2010**, *2*, 811–820.
- [248] Barner-Kowollik, C.; Buback, M.; Charleux, B.; Coote, M. L.; Drache, M.; Fukuda, T.; Goto, A.; Klumperman, B.; Lowe, A. B.; Mcleary, J. B.; Moad, G.; Monteiro, M. J.; Sanderson, R. D.; Tonge, M. P.; Vana, P. *J. Polym. Sci. Part A Polym. Chem.* **2006**, *44*, 5809–5831.
- [249] Coates, G. W. *Chem. Rev.* **2000**, *100*, 1223–1252.
- [250] Budagumpi, S.; Kim, K.-H.; Kim, I. *Coord. Chem. Rev.* **2011**, *255*, 2785–2809.
- [251] Alt, H. G.; Köppl, A. *Chem. Rev.* **2000**, *100*, 1205–1222.

- [252] Hoff, R.; Mathers, R. T. *Handbook of Transition Metal Polymerization Catalysts*; Wiley-VCH Verlag GmbH & Co. KGaA: Weinheim, Germany, 2010.
- [253] Ittel, S. D.; Johnson, L. K.; Brookhart, M. *Chem. Rev.* **2000**, *100*, 1169–1204.
- [254] Kamigaito, M.; Ando, T.; Sawamoto, M. *Chem. Rev.* **2001**, *101*, 3689–3746.
- [255] Ouchi, M.; Terashima, T.; Sawamoto, M. *Chem. Rev.* **2009**, *109*, 4963–5050.
- [256] Dubois, P.; Coulembier, O.; Raquez, J. M. *Handbook of Ring-Opening Polymerization*; Wiley-VCH Verlag GmbH & Co. KGaA: Weinheim, Germany, 2008.
- [257] Hartwig, J. F. *Organotransition metal chemistry: from bonding to catalysis*; Univ. Science Books, 2010.
- [258] Cossee, P. *J. Catal.* **1964**, *3*, 80–88.
- [259] McGuinness, D. S.; Davies, N. W.; Horne, J.; Ivanov, I. *Organometallics* **2010**, *29*, 6111–6116.
- [260] Theopold, K. H. *Proc. Natl. Acad. Sci.* **2014**, *111*, 11578–11579.
- [261] Guan, Z. *Metal Catalysts in Olefin Polymerization*; Topics in Organometallic Chemistry; Springer Berlin Heidelberg, 2009.
- [262] Gibson, V. C.; Spitzmesser, S. K. *Chem. Rev.* **2003**, *103*, 283–315.
- [263] Makio, H.; Terao, H.; Iwashita, A.; Fujita, T. *Chem. Rev.* **2011**, *111*, 2363–2449.
- [264] Camacho, D. H.; Guan, Z. *Chem. Commun.* **2010**, *46*, 7879–7893.
- [265] Mecking, S. *Angew. Chem. Int. Ed.* **2001**, *40*, 534–540.
- [266] Bézier, D.; Daugulis, O.; Brookhart, M. *Organometallics* **2017**, *36*, 2947–2951.
- [267] O'Connor, K. S.; Lamb, J. R.; Vaidya, T.; Keresztes, I.; Klimovica, K.; LaPointe, A. M.; Daugulis, O.; Coates, G. W. *Macromolecules* **2017**, *50*, 7010–7027.
- [268] Johnson, L. K.; Killian, C. M.; Brookhart, M. *J. Am. Chem. Soc.* **1995**, *117*, 6414–6415.
- [269] Guan, Z. *Science* **1999**, *283*, 2059–2062.
- [270] Guan, Z. *Chem. Eur. J.* **2002**, *8*, 3086–3092.
- [271] Delferro, M.; Marks, T. J. *Chem. Rev.* **2011**, *111*, 2450–2485.

- [272] Liu, S.; Invergo, A. M.; McInnis, J. P.; Mouat, A. R.; Motta, A.; Lohr, T. L.; Delferro, M.; Marks, T. J. *Organometallics* **2017**, *36*, 4403–4421.
- [273] Liu, S.; Motta, A.; Mouat, A. R.; Delferro, M.; Marks, T. J. *J. Am. Chem. Soc.* **2014**, *136*, 10460–10469.
- [274] McInnis, J. P.; Delferro, M.; Marks, T. J. *Acc. Chem. Res.* **2014**, *47*, 2545–2557.
- [275] Li, H.; Marks, T. J. *Proc. Natl. Acad. Sci. U. S. A.* **2006**, *103*, 15295–15302.
- [276] Marques, M. M.; Correia, S. G.; Ascenso, J. R.; Ribeiro, A. F. G.; Gomes, P. T.; Dias, A. R.; Foster, P.; Rausch, M. D.; Chien, J. C. W. *J. Polym. Sci. Part A Polym. Chem.* **1999**, *37*, 2457–2469.
- [277] Chung, T. C.; Rhubright, D. *Macromolecules* **1993**, *26*, 3019–3025.
- [278] McLain, S. J.; McCord, E. F.; Arthur, S. D.; Hauptman, E.; Feldman, J.; Nugent, W. A.; Johnson, L. K.; Mecking, S.; Brookhart, M. *Polym. Mater. Sci. Eng. Div.* **1997**, *76*, 246–247.
- [279] Mecking, S.; Johnson, L. K.; Wang, L.; Brookhart, M. *J. Am. Chem. Soc.* **1998**, *120*, 888–899.
- [280] Johnson, L. K.; Mecking, S.; Brookhart, M. *J. Am. Chem. Soc.* **1996**, *118*, 267–268.
- [281] Xin, B. S.; Sato, N.; Tanna, A.; Oishi, Y.; Konishi, Y.; Shimizu, F. *J. Am. Chem. Soc.* **2017**, *139*, 3611–3614.
- [282] Tao, W.-j.; Nakano, R.; Ito, S.; Nozaki, K. *Angew. Chem. Int. Ed.* **2016**, *55*, 2835–2839.
- [283] Radlauer, M. R.; Buckley, A. K.; Henling, L. M.; Agapie, T. *J. Am. Chem. Soc.* **2013**, *135*, 3784–3787.
- [284] Berkefeld, A.; Drexler, M.; Möller, H. M.; Mecking, S. *J. Am. Chem. Soc.* **2009**, *131*, 12613–12622.
- [285] Younkin, T. R. *Science* **2000**, *287*, 460–462.
- [286] Chen, Z.; Leatherman, M. D.; Daugulis, O.; Brookhart, M. *J. Am. Chem. Soc.* **2017**, *139*, 16013–16022.
- [287] Chen, M.; Chen, C. *ACS Catal.* **2017**, *7*, 1308–1312.

- [288] Williams, B. S.; Leatherman, M. D.; White, P. S.; Brookhart, M. *J. Am. Chem. Soc.* **2005**, *127*, 5132–5146.
- [289] Long, B. K.; Eagan, J. M.; Mulzer, M.; Coates, G. W. *Angew. Chem. Int. Ed.* **2016**, *55*, 7106–7110.
- [290] Li, M.; Wang, X.; Luo, Y.; Chen, C. *Angew. Chem. Int. Ed.* **2017**, *56*, 11604–11609.
- [291] Philipp, D. M.; Muller, R. P.; Goddard, W.; Storer, J.; McAdon, M.; Mullins, M. *J. Am. Chem. Soc.* **2002**, *124*, 10198–10210.
- [292] Nakamura, A.; Ito, S.; Nozaki, K. *Chem. Rev.* **2009**, *109*, 5215–5244.
- [293] von Schenck, H.; Strömberg, S.; Zetterberg, K.; Ludwig, M.; Åkermark, B.; Svensson, M. *Organometallics* **2001**, *20*, 2813–2819.
- [294] Mitsushige, Y.; Carrow, B. P.; Ito, S.; Nozaki, K. *Chem. Sci.* **2016**, *7*, 737–744.
- [295] Sen, A.; Borkar, S. *J. Organomet. Chem.* **2007**, *692*, 3291–3299.
- [296] Michalak, A.; Ziegler, T. *J. Am. Chem. Soc.* **2001**, *123*, 12266–12278.
- [297] Guan, Z.; Carnahan, E. M. *Metal Catalysts in Olefin Polymerization*; Topics in Organometallic Chemistry; Springer: Berlin-Heidelberg, 2009; p 256.
- [298] Wucher, P.; Caporaso, L.; Roesle, P.; Ragone, F.; Cavallo, L.; Mecking, S.; Göttker-Schnetmann, I. *Proc. Natl. Acad. Sci. U. S. A.* **2011**, *108*, 8955–8959.
- [299] Babushkin, D. E.; Semikolenova, N. V.; Zakharov, V.; Talsi, E. P. *Macromol. Chem. Phys.* **2000**, *201*, 558–567.
- [300] Negureanu, L.; Hall, R. W.; Butler, L. G.; Simeral, L. *J. Am. Chem. Soc.* **2006**, *128*, 16816–26.
- [301] Sinn, H. *Macromol. Symp.* **1995**, *97*, 27–52.
- [302] Chen, E. Y.; Marks, T. J. *Chem. Rev.* **2000**, *100*, 1391–1434.
- [303] Ystenes, M.; Eilertsen, J. L.; Liu, J.; Ott, M.; Rytter, E.; Stovngeng, J. a. *J. Polym. Sci. Part A Polym. Chem.* **2000**, *38*, 3450–3450.
- [304] Bullock, R. M. *Catalysis Without Precious Metals*; Wiley, 2010; p 290.
- [305] Zohuri, G. H.; Damavandi, S.; Ahmadjo, S.; Sandaroos, R.; Shamekhi, M. A. *Polyolefins J.* **2014**, *1*, 25–32.

- [306] Boffa, L. S.; Novak, B. M. *Chem. Rev.* **2000**, *100*, 1479–1493.
- [307] Mu, H.; Pan, L.; Song, D.; Li, Y. *Chem. Rev.* **2015**, *115*, 12091–12137.
- [308] Guo, L.; Liu, W.; Chen, C. *Mater. Chem. Front.* **2017**, *1*, 2487–2494.
- [309] Dong, Z.; Ye, Z. *Polym. Chem.* **2012**, *3*, 286–301.
- [310] Chen, Y.; Wang, L.; Yu, H.; Zhao, Y.; Sun, R.; Jing, G.; Huang, J.; Khalid, H.; Abbasi, N. M.; Akram, M. *Prog. Polym. Sci.* **2015**, *45*, 23–43.
- [311] Dai, S.; Zhou, S.; Zhang, W.; Chen, C. *Macromolecules* **2016**, *49*, 8855–8862.
- [312] Zou, W.; Chen, C. *Organometallics* **2016**, *35*, 1794–1801.
- [313] Wang, R.; Zhao, M.; Chen, C. *Polym. Chem.* **2016**, *7*, 3933–3938.
- [314] Chen, Z.; Leatherman, M. D.; Daugulis, O.; Brookhart, M. *J. Am. Chem. Soc.* **2017**, *139*, 16013–16022.
- [315] Chen, Z.; Liu, W.; Daugulis, O.; Brookhart, M. *J. Am. Chem. Soc.* **2016**, *138*, 16120–16129.
- [316] Li, X.-F.; Li, Y.-G.; Li, Y.-S.; Chen, Y.-X.; Hu, N.-H. *Organometallics* **2005**, *24*, 2502–2510.
- [317] Leblanc, A.; Grau, E.; Broyer, J.-P.; Boisson, C.; Spitz, R.; Monteil, V. *Macromolecules* **2011**, *44*, 3293–3301.
- [318] Tian, G.; Boone, H. W.; Novak, B. M. *Macromolecules* **2001**, *34*, 7656–7663.
- [319] Kermagoret, A.; Debuigne, A.; Jérôme, C.; Detrembleur, C. *Nat. Chem.* **2014**, *6*, 179–187.
- [320] Na, S. J.; Joe, D. J.; S, S.; Han, W.-S.; Kang, S. O.; Lee, B. Y. *J. Organomet. Chem.* **2006**, *691*, 611–620.
- [321] Takeuchi, D.; Chiba, Y.; Takano, S.; Osakada, K. *Angew. Chem. Int. Ed.* **2013**, *52*, 12536–12540.
- [322] Chen, Z.; Yao, E.; Wang, J.; Gong, X.; Ma, Y. *Macromolecules* **2016**, *49*, 8848–8854.
- [323] Wang, R.; Sui, X.; Pang, W.; Chen, C. *ChemCatChem* **2016**, *8*, 434–440.
- [324] Na, Y.; Wang, X.; Lian, K.; Zhu, Y.; Li, W.; Luo, Y.; Chen, C. *ChemCatChem* **2017**, *9*, 1062–1066.

- [325] Stephenson, C. J.; McInnis, J. P.; Chen, C.; Weberski, M. P.; Motta, A.; Delferro, M.; Marks, T. J. *ACS Catal.* **2014**, *4*, 999–1003.
- [326] Liang, T.; Chen, C. *Organometallics* **2017**, *36*, 2338–2344.
- [327] Zhai, F.; Solomon, J. B.; Jordan, R. F. *Organometallics* **2017**, *36*, 1873–1879.
- [328] Delferro, M.; McInnis, J. P.; Marks, T. J. *Organometallics* **2010**, *29*, 5040–5049.
- [329] Takeuchi, D.; Chiba, Y.; Takano, S.; Kurihara, H.; Kobayashi, M.; Osakada, K. *Polym. Chem.* **2017**, *8*, 5112–5119.
- [330] Xu, D.; Zhao, X.-X.; Chen, Z.-T.; Ma, Y.-G. *Chinese J. Polym. Sci.* **2018**, *36*, 244–251.
- [331] Li, W.-W.; Mu, H.-L.; Liu, J.-Y.; Li, Y.-S. *J. Organomet. Chem.* **2017**, *836-837*, 34–43.
- [332] Sachse, A.; Demeshko, S.; Dechert, S.; Daebel, V.; Meyer, F. *Dalton Trans.* **2010**, *39*, 3903–3914.
- [333] Chen, C.-T.; Liao, S.-Y.; Lin, K.-J.; Chen, C.-H.; Lin, T.-Y. *J. Inorg. Chem.* **1999**, *38*, 2734–2741.
- [334] Usami, T.; Takayama, S. *Macromolecules* **1984**, *17*, 1756–1761.
- [335] Galland, G. B.; de Souza, R. F.; Mauler, R. S.; Nunes, F. F. *Macromolecules* **1999**, *32*, 1620–1625.
- [336] Sachse, A.; John, M.; Meyer, F. *Angew. Chemie* **2010**, *49*, 1986–9.
- [337] Bruch, M. D.; Schilling, F. C.; Bovev, F. A.; Kozlowski, S. A. *Macromolecules* **1985**, *18*, 1418–1422.
- [338] Ghorbel, E.; Hadriche, I.; Casalino, G.; Masmoudi, N. *Materials (Basel)*. **2014**, *7*, 375–398.
- [339] Krimm, S.; Liang, C.; Sutherland, G. *J. Chem. Phys.* **1956**, *25*, 549–562.
- [340] Fulmer, G. R.; Miller, A. J. M.; Sherden, N. H.; Gottlieb, H. E.; Nudelman, A.; Stoltz, B. M.; Bercaw, J. E.; Goldberg, K. I. *Organometallics* **2010**, *29*, 2176–2179.
- [341] Billouard, C.; Carlotti, S.; Desbois, P.; Deffieux, A. *Macromolecules* **2004**, *37*, 4038–4043.

- [342] Brocas, A.-L.; Mantzaridis, C.; Tunc, D.; Carlotti, S. *Prog. Polym. Sci.* **2013**, *38*, 845–873.
- [343] Sheldrick, G. M. *Acta Cryst.* **2015**, *A71*, 3–8.
- [344] Sheldrick, G. M. *Acta Cryst.* **2015**, *C71*, 3–8.
- [345] X-RED; STOE & CIE GmbH: Darmstadt, Germany. 2002.

Eidesstattliche Erklärung

Ich erkläre, dass diese Arbeit mit dem Titel “Bimetallic Complexes for Cooperative Polymerization Catalysis” selbstständig und ohne Benutzung anderer als der angegebenen Hilfsmittel angefertigt habe und dass ich alle Stellen, die ich wörtlich oder sinngemäß aus Veröffentlichungen entnommen habe, als solche kenntlich gemacht habe. Die Arbeit hat bisher in gleicher oder ähnlicher Form oder auszugsweise noch keiner Prüfungsbehörde vorgelegen.

Göttingen, den 15.04.2018

Mike Schütze

Danksagung

An erster Stelle danke ich Prof. Dr. Franc Meyer für die spannenden Themen sowie für die gute Betreuung und die Freiheit beim Forschen.

Bei Prof. Dr. Phillipp Vana und Dr. Marc Walter möchte ich mich für die Übernahme des Korreferats bedanken und die hilfreichen Tipps bei den Jahresgesprächen.

Prof. Dr. Selvan Demir, Dr. Matthias Otte und Dr. Shoubhik Das danke ich für den Prüfungsbeisitz.

Meinen Kollegen Thomas Kothe, Mauricio Cattaneo, Claudia Schremmer, Torben Böhnisch, Hendrik Stevens, Michael Ainooson, Kristian Dalle, Marten Seeba und Anne Bretschneider gilt ein besonderer Dank für die gute Zusammenarbeit und die tolle Atmosphäre im Labor: It was awesome. Tolle Leute und Musik haben die Arbeit zu einem Vergnügen gemacht. It was awesome! Weiterhin danke ich Sebastian Dechert für die zahlreichen Röntgenstrukturanalysen und Hilfestellungen. Michael John danke ich für die Unterstützung bei den NMR-Messungen. Bei Ralf Schöne möchte ich mich ebenfalls für die Unterstützung bedanken. Des Weiteren möchte ich meinen Dank aussprechen bei Sandra Lotze, Annika von Roden, Hans-Joachim Heymel, Mariusz Burzynski, Bernd Wichmann, Frank Hambloch, Uwe Beckmann und Joachim Hille. Ich danke Alexander Hecht, Jerome Günes, Lars Hoffmann, Nils Hertl, Sven Richter und Torsten Fornefeld für die gute Arbeit im Rahmen ihrer Abteilungspraktika und Moritz Joswig für die gute Arbeit im Rahmen seiner Bachelorarbeit.

Dem Land Niedersachsen danke ich für das Georg-Christoph-Lichtenberg-Stipendium.

Für das Korrekturlesen dieser Arbeit gilt mein Dank Marie Bergner Thomas Kothe, Jerome Günes, Munmun Ghosh, Christine Schiewer, Hendrik Stevens, Nora Cascante Estepa und Joanne Wong. Erneut möchte ich dem gesamten AK Meyer für die klasse Arbeitsatmosphäre und die Hilfsbereitschaft danken.

Abschließend danke ich meinen Freunden und meiner Familie für die Unterstützung und aufregende und schöne Zeit die wir verbracht haben und verbringen werden. Dabei möchte ich besonders Nora Cascante Estepa hervorheben, für ihre Liebe, selbstlose Hilfe und ihre positive Art. Ich möchte meiner Mutter, Iris Friedrich-Schütze, für ihre Geduld und die ununterbrochene Unterstützung. Danke für alles, was Du für mich getan hast. Martin Dzemski, Thomas Kothe, Sonja Schmidt und Nicolas Lemus Diaz, ihr seid die Besten und Danke nochmal für die unvergessliche Zeit.

Mike K. Schütze

Curriculum Vitae

Personal Information

Name Mike K. Schütze
Nationality German
Date of birth January 22nd 1988, in Kassel (Germany)

Education

- 10/2014 – 06/2018 **International Ph.D. program "Catalysis for Sustainable Synthesis"**, Georg-August-University Göttingen.
PhD Thesis: *Bimetallic Complexes for Cooperative Polymerization Catalysis*, supervisor: Prof. Dr. Franc Meyer.
- 10/2011 – 05/2014 **Master of Science in Chemistry**, Georg-August-University Göttingen.
Final grade 1.4 with distinction.
Master Thesis: *Preorganized bimetallic complexes for the cooperative olefin polymerization*, grade 1.0, supervisor: Prof. Dr. Franc Meyer.
- 10/2008 – 08/2011 **Bachelor of Science in Chemistry**, Georg-August-University Göttingen .
Final grade 1.6.
Bachelor Thesis: *Silylens from Chlorosilan-derivatives*, grade 1.3, supervisor: Prof. Dr. Dietmar Stalke.

Work and International Experience

- 01/2018 – today **Process Researcher** at Covestro Deutschland AG.
- 04/2016 – 12/2017 **Coordinator** of the international Ph.D. program "Catalysis for Sustainable Synthesis".
- 11/2014 – 04/2016 **Elected speaker** of the doctoral students of the international Ph.D. program "Catalysis for Sustainable Synthesis".
- 11/2013 – 11/2015 **Voluntary work** for the Studentenwerk Göttingen (internet tutor for student housing with over 400 inhabitants).
- 10/2012 – 01/2013 **Research stay** at the University of Barcelona, Department of Inorganic Chemistry in the group of Prof. Dr. Guillem Aromí.
- 06/2008 – 07/2008 **Industrial placement** at the B. Braun Melsungen AG, Department of Pharmaceutical Development.
- 02/2008 – 05/2008 **Voluntary work** in the Jatun Sacha project in Ecuador (San Cristóbal and Quito).
- 08/2004 – 06/2005 **Exchange student** in Salem, OR, USA - Recipient of the Achievement Award.

Publications, certificates and fellowships

- Patent Pending patent for "New tridentate polymerization catalysts".
- Publication **M. Schütze**, S. Dechert and F. Meyer "Highly Active and Readily Accessible Proline-Based Dizinc Catalyst for CO₂/Epoxide Copolymerization" *Chem. Eur. J.* **2017**, *23*, 16472-16475.
- G.A. Craig, **M. Schütze**, D. Aguilà, O. Roubeau, J. Ribas-Ariño, S. Vela, S.J. Teat and G. Aromì "Linear or Cyclic Clusters of Cu(II) with a Hierarchical Relationship" *Inorg. Chem.* **2014**, *54*, 3290–3297.
- Certificates **European Business Competence Licence** - EBC*L - Levels A and B.
- Social competence and management skills** certificate by the ZESS of the Georg-August-University Göttingen.
- Scholarships **Georg Christoph Lichtenberg Scholarship**, 10/2014 – 12/2017.
- Mix-It Scholarship**, 10/2012 – 01/2013.

May 10, 2018